SPARCLE

An instrument for aerosol size and refractive index measurement

Mochammad Syarif Romadhon

Wolfson College

University of Oxford

A thesis submitted for the degree of

Doctor of Philosophy

Hilary 2021

Abstract

In the last few decades, there is an increasing need to improve *in situ* aerosol measurements. The improved measurements can provide a better understanding of the role of atmospheric aerosol on the Earth climate change. The improved measurement can also help to indicate the quality of ambient air to prevent health problems caused by aerosol exposure. Most *in situ* optically based aerosol photometer assume the refractive index of measured particles to give size-estimate. This type of instrument can have a bias when measuring a particle whose refractive index is different from the assumed value. SPARCLE was designed with two measurement goals. First, SPARCLE measures both the size and refractive index of a particle provided that the particle is a homogeneous sphere. Second, SPARCLE is able to measure particles whose sizes range from 500 nm to 2,500 nm. This size range is within the range of the accumulation mode of tropospheric size distribution.

The purpose of this work is to investigate the feasibility of SPARCLE. A threshold level to detect particles was applied to differentiate between background and scattering signals and it was found that applying the threshold level can limit SPARCLE to detect particles smaller than 640 nm. SPARCLE was calibrated using four monodisperse aerosols containing Polystyrene latex (PSL) beads. The mean size of the aerosols are 1,100 nm, 1,800 nm, 2,000 nm and 3,000 nm. The refractive index of PSL is 1.59. The results indicate that SPARCLE can measure the aerosols with the deviation of the measured size and refractive index less than 2.2% and 1.05%, respectively, of the size and refractive index specified by the aerosol manufacturers.

SPARCLE was used to measure a test aerosol. The test aerosol was a mixture of water and liquid soap. The refractive index of the liquid soap is 1.37. One of the main ingredient of the liquid soap is sodium dodecyl sulphate whose the refractive index is 1.44. The refractive index

of the test aerosol measured by SPARCLE is 1.47. This value is close to the refractive index of the sulphate suggesting that the test aerosol was quickly dried and, then, a solid aerosol was formed which mainly composed of the sulphate.

Acknowledgements

This study was supported by generous funding from Indonesian Endowment Fund (LPDP). The funding covers all I need during the study including an allowance to take my family with me. I've never heard of other funding more generous than that.

I'm so grateful that I had been supervised by a very dedicated supervisor team: Don Grainger, Dan Peters and Simon Proud. Don had been so supportive that I didn't need to worry if I did silly mistakes. I did it more than once and one of them was breaking up pricey components. Dan had inspired me to keep curious even for a small glimpse in measurements graphs. The devils were really in detail. Simon had always been there if I need some practical help in the Lab even for a thing as simple as plugging an electrical cord. Together, they helped me to shape my critical thinking.

The environment I worked in was wonderful. The First Thursday pub had increased my English significantly and helped me to blend into the English culture thanks to the member of the Earth Observation Data Group: Isabelle, Adam, Simon, Anu, Lucy, Elisa, and Rob. To note, as a graduate student I always got free drinks. Isabelle had been very helpful with a brief chit-chat during working time to refresh my mind. I couldn't think of any better office mate. I learnt how to think quickly from Adam Povey, the man who is really a quick thinker and always uses efficient words to describe things. Anu Dudia showed me another job of graduate students: lab demonstrating, a good way to distract myself from my research work and to earn easy money at the same time. The AOPP were also very supportive. They are David Marshal, Philip Stier and Andrew Wells as AOPP head department and graduate director and also Lucy Li and Man-sun as AOPP admin and computation staff. Not to forget is the English Centre, the place I learnt English in the first two years. The instructors there were so well experienced. I still can mention them: Deborah, George and Michael.

Oxford city itself was so lovely that my study time felt so exciting. I thank Chiara and Henry for being a good walk company in Port Meadow. I also thank Wolfson College especially for the punts they provided, it was a really good way to escape. I spent the wonderful first year of my study in the college with Frank, Nora and Elly as flatmates. A million thanks as well for Mahmood, a caretaker in the Castle Mills accommodation where I lived there for about three years. So far, Oxford is the best place I've lived in.

My family was essential to keep my spirit to finish my study. Thanks to my wife: Mirda Ahsfiani Husna, and my son: Abid Dharma Syarif for a never-ending stream of love. Unfortunately, my mother: Siti Musyarofah passed away during my study and couldn't see me finishing my study. However, I can still remember how proud she was when I was admitted to the University of Oxford. It can be understood because my late mother and father: Moch Zaenuri spent only less than a year in their elementary school. They had to leave school to earn some money to survive. I want to use this space to thank all of my siblings: Abdurrahim, Mustain, Siti Mutiah, Siti Musyarofah, Siti Nur Khasanah, Moch Nur Hidayatullah, Siti Nur Laily Safitri, Moch Nur Alimi Zen, and Moch Farkhan Shobirin. We are ten brothers sisters and I had to check those names twice to ensure that I didn't miss one. I thank also my parent-in-law: Muhammad Nasir and Choiriyah for all their support.

This study was made possible by the permission from the office I work at: Balai Besar Teknologi Pencegahan Pencemaran Industri (BBTPPI). Thanks to Ibu Titik Purwati Widowati who, as the head of BBTPPI, had given me permission to leave the office to study here. And also Bapak Wibowo Dwi Hartoto as the head of Tata Usaha BBTPPI who supported me to continue my study. And then, I should thank Nur Zen for helping me deal with any technical and administrative matters while I'm in Oxford. And also for the Employee Team: Agung Budiarto and Mbak Soemarlina.

Finally, I want to thank everyone I couldn't mention here.

This thesis is dedicated to my parents and family. They have sacrificed so much so I could reach this stage.

My parents worked as garbage collectors and did the job manually in the harsh weather of Semarang city, Indonesia. No one could expect that one of their son could go through and finish PhD here in Oxford.

My wife did unpaid leave to accompany me here, three and half of her career had been sacrificed to my work.

Finally, to my son, He deserved more family time with me and those time was deduced by the intensity of my work.

Dedicated to

Mother	Father	Wife	Son
Siti Musyarofah	Moch Zaenuri	Mirda Ashfiani Husna	Abid Dharma Syarif

Contents

List of Figures

List of Tables

List of Acronyms

SPARCLE Stratospheric Aerosol Composition and Loading Experiment

OPC Optical Particle Counter

PMT Photo Multiplier Tube

CCD Charge-coupled Device

PLC Particle Loss Calculator

SMPS Scanning mobility Particle Sizer

DMPS Differential mobility Particle Sizer

List of Mathematical Notation

Symbol	Description	Units	Def.
α	size parameter	-	Eq. 1.11
γ	surface tension	$\mathrm{N\,m^{-1}}$	Eq. 1.7
δ	delta Dirac function	-	Eq. A.47
ϵ	measurement error	-	-
ϵ_{PMT}	the PMT measurement error	V	p. 139
$\boldsymbol{\epsilon}$	an error vector	-	Eq. 5.4
$\boldsymbol{\epsilon}_{\mathrm{meas}}$	an error vector of measured scattering light	-	Eq. 5.12
$\boldsymbol{\epsilon}_{\mathrm{back}}$	an error vector of the background	-	p. 140
$\boldsymbol{\epsilon}_{\mathrm{CCD}}$	an error vector of the CCD camera measurement	-	Eq. 5.10
ϵ_j	the j^{th} element of an error vector $\boldsymbol{\epsilon}$	-	Eq. 5.6
ϵ'_j	the j^{th} element of an error vector $\boldsymbol{\epsilon}_{\mathrm{CCD}}$	-	Eq. 5.10
$\epsilon_i^{\mathrm{back}}$	the i^{th} element of an error vector $\boldsymbol{\epsilon}_{\mathrm{back}}$	-	Eq. 5.14
$\epsilon_i^{\mathrm{meas}}$	the i^{th} element of an error vector $\boldsymbol{\epsilon}_{\mathrm{meas}}$	-	Eq. 5.13
$\epsilon_{i,\ell}^{\mathrm{back}}$	the errors in ℓ^{th} background measurement associated with $(i-6)^{\mathrm{th}}$ and $(j-6)^{\mathrm{th}}$ pixels, respectively	-	Eq. 5.16
ζ_n	Ricatti-Bessel functions	-	Eq. A.40
ζ'_n	derivative of Ricatti-Bessel functions	-	Eq. A.40
$\eta_{\mathrm{S}}(d)$	particle loss during transported in the SPARCLE line	%	Eq. 3.11
$\eta_{\mathrm{O}}(d)$	particle loss during transported in the OPC line	%	Eq. 3.11
$\eta_{\mathrm{s}}(d)$	the sampling efficiency of the SPARCLE sampling pipe	%	Eq. 3.21
$\eta_{\mathrm{t}}(d)$	transport efficiency of the SPARCLE sampling pipe	%	Eq. 3.21
η_{PMT}	the quantum efficiency of the photo-cathode on the PMT window	%	Eq. A.11
θ	scattering angles	-	Eq. 1.11
θ_p	the scattering angle of light which falls on pixel indexed p	-	Eq. A.30
θ'_p	the corrected scattering angle of light which falls on pixel indexed p due to lateral displacement	-	Eq. A.30
θ_p^{i}	the incident angle of scattered light on a pixel indexed p	-	Eq. A.31
κ	a parameter in error functions	mm	Eq. 3.1
ξ	a parameter in error functions	mm	Eq. 3.1
λ	wavelength of light	nm	Fig. 1.2
π_n	Legendre polynomials	-	Eq. A.39

Symbol	Description	Units	Def.
ρ	mass density	$\mathrm{kg\,m^{3}}$	Eq. 1.7
ρ_{o}	the size distribution of an air sample	-	Eq. 3.20
ρ_{O}	the size distribution measured by the OPC	-	Eq. 3.20
ρ_{N}	particle number concentration	$\mathrm{particles\,cm^{-3}}$	Eq. 1.5
ρ_{N_0}	initial particle number concentration	s	Eq. 1.8
ρ_{R}	the ratio between integrated CCD camera reading and accumulated PMT signal	-	Eq. 2.4
ρ_{S}	particle number density measured by SPARCLE	$\mathrm{m^{-3}}$	Eq. 3.22
σ_{v}	the standard deviation of single particle speed in the sensing volume	$\mathrm{m\,s^{-1}}$	Eq. A.7
σ_{d}	the standard deviation of retrieved size	nm	p. 155
σ_{m}	the standard deviation of retrieved refractive index	-	p. 155
σ_{g}	geometric standard deviation of size distributions	-	Eq. 1.2
σ_{y}	the standard deviation of the laser intensity distribution along the **y** axis	mm	Eq. 3.1
τ_{n}	Legendre polynomials	-	Eq. A.39
υ	degree of freedom	-	Eq. 5.8
ϕ	azimuth angles	-	Eq. 1.11
χ^{2}	a cost function to fit a forward function to a measurement vector	-	Eq. 5.5
χ_{υ}^{2}	a reduced cost function	-	Eq. 5.7
$*\chi_{\upsilon}^{2}$	a minimum reduced cost function	-	Eq. 5.20
χ_{D}^{2}	a cost function to fit the forward model of PMT pulse depth to a measured PMT pulse depth	-	Eq. 5.18
ψ_{n}	Ricatti-Bessel functions	-	Eq. A.40
ψ_{n}'	derivative of Ricatti-Bessel functions	-	Eq. A.40
Ψ_{S}	the detection rate of SPARLCE	$\mathrm{s^{-1}}$	Eq. 3.27

Symbol	Description	Units	Def.
a_n	Mie coefficients	-	Eq. A.38
a_{v}	the maximum speed of single particles in the sensing volume	$\mathrm{m\,s^{-1}}$	Eq. A.7
b_n	Mie coefficients	-	Eq. A.38
d	particle size in diameter	nm	-
$\bar{d}$	averaged retrieved size	nm	p. 155
d_0	initial droplet size	nm	Eq. 1.10
d_{d}	the diameter of droplets	nm	Eq. 3.2
d_{d0}	the initial size of “empty” droplets	nm	Eq. 3.7
d_{g}	geometric mean diameter of size distributions	nm	Eq. 1.1
d_i	the size at the midpoint of i^{th} size interval	nm	Eq. 1.1
d_{p}	the diameter of solid particles	nm	Eq. 1.11
d_{PSL}	the diameter of PSLs particles	nm	p. 155
d_{res}	the size of residual particles	nm	Eq. 3.7
$d(t)$	droplet size at time t	nm	Eq. 1.10
d_{v}	median diameter of size distributios	nm	Eq. 3.5
$d^{-}_{95\%}$	the lower limit of the size range of 95% of the particle number of size distributions	nm	Eq. 1.3
$d^{+}_{95\%}$	the upper limit of the size range of 95% of the particle number of size distributions	nm	Eq. 1.3
$\hat{e}_r$	the unit vector of spherical coordinate in radial direction	m	Eq. A.45
$\hat{e}_\theta$	the unit vector of spherical coordinate in radial direction	θ	Eq. A.45
$\hat{e}_\phi$	the unit vector of spherical coordinate in ϕ direction	-	Eq. A.45
$erf(y)$	an error function to describe the laser intensity distribution along the **y** axis	mm	Eq. 3.1
h	laser beam height	m	Eq. 2.1
h	the number of measurand	-	p. 5.2
h_{D}	the length of the dryers	m	Eq. 3.9
i	speed of single particles	-	Eq. A.36
j^{mid}	the middle pixel $j^{\mathrm{mid}} = 1500$	-	Eq. A.23
k	wavenumber defined as $k = \frac{2\pi}{\lambda}$	$\mathrm{nm^{-1}}$	Eq. A.3
$\mathfrak{k}$	imaginary part of refractive index	-	Fig. 1.5
m	refractive index	-	Eq. 1.5
$\bar{m}$	averaged retrieved refractive index	-	p. 155
m^{g}	the refractive index of the slab of glass	-	Eq. A.32
m_{PSL}	the refractive index of PSLs as specified by manufacturers	-	p. 155
n	in general are dummy indices	-	Eq. A.40
n_i	particle number at i^{th} size interval	-	Eq. 1.1
$\mathfrak{n}$	real part of refractive index	-	Fig. 1.5
p	index for measured PMT signals	-	p. 176

Symbol	Description	Units	Def.
p_a	partial pressure of substance a	Pa	Eq. 1.6
$\bar{p}_a$	saturation pressure of substance a	Pa	Eq. 1.6
$p(x,z)$	the probability density of particles traversing a point whose coordinate is (x,z)	m^{-2}	Eq. 3.15
q	index for simulated PMT signals	-	Eq. A.12
q_{T}	the index when a simulated PMT signal starts to trigger the CCD camera	-	Eq. A.12
r	SPARCLE inlet radius	m	Eq. 2.1
$\hat{r}$	the radial direction of scattered light	mm	Eq. A.3
r_{D}	the radius of the dryers	m	Eq. 3.9
$\vec{r_p}$	the radial distant of pixel indexed p	mm	Eq. A.22
r_{s}	the radius of SPARCLE sampling pipe	m	Eq. 2.5
s	the number of measurand	-	p. 5.2
t	time	s	Eq. 1.8
t_{d}	the time of flight of droplets in the dryers	s	Eq. 3.9
t_{dead}	the dead time of SPARCLE acquisition system	s	Eq. 2.7
t_{int}	integration time of the CCD camera	s	Eq. A.19
t_p	sampling time of a PMT signal indexed p	s	p. 176
t'_q	simulated sampling time of PMT signals	-	Eq. A.12
t_{s}	sampling time	s	Eq. 3.23
t_{samp}	SPARCLE sampling time	s	Eq. 2.7
t_{T}	the time when a PMT signal starts to trigger the CCD camera	s	p. 176
u	set of integer numbers that simulated PMT signals at $t'_{q\in u}$ are less than V_T	-	Eq. A.13
v	is general is speed	$\mathrm{m\,s^{-1}}$	-
$v(x,z)$	the speed of single particle traversing a point whose coordinate is (x,z)	$\mathrm{m\,s^{-1}}$	Eq. 3.15
v_{a}	the speed of air	$\mathrm{m\,s^{-1}}$	Eq. 2.5
x, y, z	particle position in the sensing volume in Cartesian coordinate	mm	Eq. 3.1
$\mathbf{x}$	a state vector	-	Eq. 5.2
$\hat{\mathbf{x}}$	a state vector considered as a retrieval solution	-	Eq. 136
$\mathbf{y}$	a measurement vector	-	Eq. 5.2
$\mathbf{y}_{\mathrm{back}}$	a vector of measured background intensity	-	Eq. 5.11
$\mathbf{y}_{\mathrm{meas}}$	a vector of measured light intensity	-	Eq. 5.11
x_i	the i^{th} element of $\mathbf{x}$	-	Eq. 5.2
y_i	the i^{th} element of $\mathbf{y}$	-	Eq. 5.2
y_i^{meas}	the i^{th} element of $\mathbf{y}_{\mathrm{meas}}$	-	Eq. 5.13
y_i^{back}	the i^{th} element of $\mathbf{y}_{\mathrm{back}}$	-	Eq. 5.13
y_{p}	the position of single particles along the $\mathbf{y}$ axis during its travelling in the sensing volume	µm	Eq. A.50

Symbol	Description	Units	Def.
A_{b}	$\int I(x,y)\,dx\,dy$	W	Eq. A.6
A_{d}	detector's photo-active area	m^2	Eq. A.1
A_{p}	the area of a pixel in the CCD camera line sensor	m^2	Eq. A.21
D	the thickness of the slab of glass	mm	Eq. A.35
E_{o}	the scalar value of the electric field of illuminating light	$\mathrm{V\,m^{-1}}$	Eq. A.36
$\vec{E}_{\mathrm{s}}$	the electric field of scattered light	$\mathrm{V\,m{-}1}$	Eq. A.2
$E_{s\theta}$	The component of the electric field of scattered light on θ direction	$\mathrm{V\,m^{-1}}$	Eq. A.36
$E_{s\phi}$	The component of the electric field of scattered light on ϕ direction	$\mathrm{V\,m^{-1}}$	Eq. A.36
F	the volume fraction of the spheres in suspensions	-	Eq. 3.2
F_{stc}	the volume fraction of the spheres in stock suspensions	-	Eq. 3.3
$\mathbf{F}$	the forward function of SPARCLE measurements	-	Eq. 5.3
F_i	the i^{th} element of $\mathbf{F}$	-	-
$G(\theta,\phi)$	geometrical factor specific to instrument's design	-	Eq. 1.11
G_{amp}	the amplification factor of the amplifier	-	Eq. A.11
G_{PMT}	the gain of the PMT	-	Eq. A.11
$H_{n+\frac{1}{2}}$	half-integral-order Hankel functions of the second kind	-	Eq. A.42
$\vec{H}^*_{\mathrm{s}}$	the conjugate of the magnetic field of scattered light	T	Eq. A.2
$H_{s\theta}$	The component of the electric field of scattered light on θ direction	T	Eq. A.36
$H_{s\phi}$	The component of the magnetic field of scattered light on ϕ direction	T	Eq. A.36
I	light intensity	$\mathrm{W\,m^{-2}}$	Eq. 1.11
$I_{\perp}$	the intensity of light which its propagation is perpendicular to its electric vector oscillation plane	$\mathrm{W\,m^{-2}}$	Eq. 1.11
$I_{\parallel}$	the intensity of light which its propagation is parallel to its electric vector oscillation plane	$\mathrm{W\,m^{-2}}$	Eq. 1.11
$I_{\mathrm{x}}(x)$	the distribution of light intensity along the $\mathbf{x}$ axis	-	Eq. A.15
$I_{\mathrm{y}}(y)$	the distribution of light intensity along the $\mathbf{y}$ axis	-	Eq. A.15
$J_{n+\frac{1}{2}}$	half-integral-order spherical Bessel functions	-	Eq. A.42
K	coagulation coefficient	$\mathrm{m^3\,s^{-1}}$	Eq. 1.8

Symbol	Description	Units	Def.
$K(\lambda)$	photopic luminous efficacy	lumens W^{-1}	Eq. A.21
$\mathcal{K}$	the ratio between air sample volume and SPARCLE sensing volume	-	Eq. 2.2
M	molecular weight of substance a	$\mathrm{kg\,kmol}^{-1}$	Eq. 1.7
N	total number of particles	-	Eq. 1.1
$N(t)$	particle number at time t	-	Eq. 1.10
N_0	initial particle number	-	Eq. 1.10
$N_{\mathrm{A}}(d)$	the size distribution at the line before the split line to the OPC and SPARCLE	-	Eq. 3.11
N_{s}	the number of spheres in droplets	-	Eq. 3.4
$\bar{N}_{\mathrm{s}}$	average number of spheres	-	Eq. 3.2
N_{o}	the number of particle in an air sample	-	Eq. 3.20
$N_{\mathrm{O}}(d)$	the size distribution at the end of the OPC line	-	Eq. 3.11
$N_{\mathrm{S}}(d)$	the size distribution at the end of SPARCLE line	-	Eq. 3.11
N_{S}	the number of particles detected by SPARCLE	-	Eq. 3.23
n	the normalisation factor of the CCD camera	-	Eq. A.21
$\mathcal{N}$	observed count by SPARCLE	-	Eq. 2.2
n	the normalisation factor of the CCD camera	V	Eq. 2.3
P_n^1	Legendre polynomials	-	Eq. A.38
$P(d,m)$	the probability of SPARCLE detecting particles whose size is d and refractive index is m	-	Eq. 3.18
$P(\mathrm{d}A)$	the probability of single particles passing through an element area $\mathrm{d}A$	-	Eq. 3.17
P_{b}	measured power of the laser beam	W	Eq. A.4
$P_{\mathrm{d}}(N_{\mathrm{s}})$	the probability of having N_{s} number of spheres in a droplet	-	Eq. 3.4
P_j	the power of scattered light falls over square indexed j	W	Eq. A.15
P_{PMT}	the power of scattered light over the PMT window	W	Eq. A.15
P_{s}	scattered light power	W	Eq. A.1
P_{sum}	the power of scattered light over the PMT window with the light is scattered by particles located at the center of reference	W	Eq. A.18
$\mathcal{P}$	$\mathcal{P} = k\,r$	-	Eq. A.36
Q_{a}	the flowrate of sampled air	$\mathrm{m}^3\,\mathrm{s}^{-1}$	Eq. 2.6
Q_{S}	the sampling flowrate of SPARCLE	$\mathrm{m}^3\,\mathrm{s}^{-1}$	Eq. 3.23
$\mathcal{Q}$	the normalisation factor of SPARCLE probability density	-	Eq. 3.15
$\mathcal{Q}_{\mathrm{depth}}$	the normalisation factor in the probability PMT pulse depth generated by single particles	-	Eq. A.47
$\mathcal{Q}_{\mathrm{width}}$	the normalisation factor in the probability PMT pulse width generated by single particles	-	Eq. A.50

Symbol	Description	Units	Def.
R	gas constant	$\mathrm{J\,K^{-1}\,mol^{-1}}$	Eq. 1.7
R_0	singlet ratio	-	Eq. 3.6
R_1	singlet ratio	-	Eq. 3.5
R_f	The Reynold number of an air flow	-	Eq. 2.5
R_{lo}	the load resistor installed on the PMT outlet	Ω	Eq. A.11
R_{x}	the projection of pixel position on the $\mathbf{x}$ axis	mm	Eq. A.22
R_{y}	the projection of pixel position on the $\mathbf{y}$ axis	mm	Eq. A.22
R_{z}	the projection of pixel position on the $\mathbf{z}$ axis	mm	Eq. A.22
$\mathscr{R}$	lateral displacement of scattered light due to the slab of glass	mm	Eq. A.30
S	total scattered light measured by the CCD camera	-	Eq. 3.13
S_a	saturation ratio of substance a	-	Eq. 1.6
$S_1\&S_2$	Mie scattering amplitudes	-	Eq. A.3
$\mathring{S}_a$	saturation ratio of substance a when in an equilibrium with droplets of substance a	-	Eq. 1.7
$\vec{S}_{\mathrm{b}}$	the Poynting vector of the laser beam	$\mathrm{W\,m^{-2}}$	Eq. A.3
$\mathcal{S}^{\mathrm{CCD}}$	the sensitivity of the line sensor in the CCD camera	$\mathrm{V\,lux^{-1}\,s^{-1}}$	Eq. A.21
$\vec{S}_{\mathrm{s}}$	the Poynting vector of scattered light	$\mathrm{W\,m^{-2}}$	Eq. A.1
T	temperature	K	Eq. 1.7
T_{width}	PMT pulse width	µs	Eq. A.50
$\mathcal{T}$	the transmittance of scattered light through the slab of glass	-	Eq. A.29
V	in general is electrical voltage	V	-
V_{CCD}	the voltage of the sensor line in the CCD camera	V	Eq. 2.3
V_{depth}	the depth of PMT pulses	V	Eq. 3.18
V_{o}	the volume of an air sample	$\mathrm{m^3}$	Eq. 3.20
V_{PMT}	the voltage output of the PMT	V	Eq. 2.4
V_{S}	The volume of air sample that being evaluated by SPARCLE at particular time period	$\mathrm{m^3}$	Eq. 3.23
V_{T}	SPARCLE threshold level to detect particles	V	Eq. 3.18
$\mathcal{V}_{\mathrm{CCD}}$	normalised output of the CCD camera	-	Eq. 2.3
$\mathcal{V}_{\mathrm{back}}$	An average CCD camera reading in measuring the scattering chamber background	-	Eq. 3.13
$\mathcal{V}'_{\mathrm{back}}$	Single CCD camera reading in measuring the scattering chamber background	-	Eq. 3.14
$\mathcal{V}(p_j)$	CCD camera readings at pixel p_j	-	Eq. 3.13
$\mathcal{V}^{\mathrm{tr}}_{\mathrm{sim}}$	the corrected simulated CCD camera readings due to transmittance in the propagation through the slab of glass	-	Eq. A.29
$\mathcal{V}_{\mathrm{sv}}$	SPARCLE sensing volume	$\mathrm{m^3}$	Eq. 2.1

Symbol	Description	Units	Def.
$W(p)$	the energy of scattered light integrated by pixel p	J	Eq. A.21
Y	dilution factor	-	Eq. 3.3

Symbol	Description	Units	Def.
$Re(..)$	the real part of the element inside brackets	-	Eq. A.44
$\Big\|...\Big\|$	operator referring to the absolute values of functions between the bars	-	-
$\mathrm{Cov}(.,.)$	the operator to calculate the covariance of the elements inside the bracket	-	

Chapter 1

Introduction

This study is motivated by the increasing need to improve *in situ* aerosol measurements in the last few decades [IPCC, 2014; WHO, 2013]. One example that drives this need is the growing awareness of health problems caused by aerosol pollution. Peters et al. showed that a few hours of exposure to particulate matters of sizes less than 2.5 µm and concentrations higher than 25 µg m^{-3} may elevate the risk of heart attack [Peters et al., 2001]. Other studies confirm the link between particulate matter exposure and cardiovascular morbidity and mortality [Brook et al., 2010, 2004; IARC, 2013]. Additionally, measurements of particle refractive index are needed to have a better understanding of the Earth climate change by improving the estimation of the radiative forcing caused by atmospheric aerosols in the Earth's atmosphere [Valenzuela et al., 2018]. In the clear-sky conditions, atmospheric aerosols scatter and absorb solar radiation [Boucher and Lohmann, 1995]. The magnitude of the solar radiation being scattered or absorbed is still uncertain and contributes to the high uncertainty in the Earth's radiative forcing estimation [IPCC, 2014; Myhre et al., 2013]. Recent studies show that the uncertainty can be attributed partly to the uncertainty of the refractive indices of tropospheric particles. [Erlick et al., 2011; Zarzana et al., 2014; Valenzuela et al., 2018].

The purpose of this study is to investigate the feasibility of SPARCLE, an *in situ* aerosol photometer capable of determining the particle size distribution and number density of an aerosol population as well as the refractive index of the particles. This capability makes SPARCLE a unique instrument, since most of *in situ* optically based instruments assume the refractive index of measured particles to give size-estimates [Szymanski et al., 2009].

SPARCLE has two measurement goals. The first goal is to provide size-resolved measurements of particles whose sizes range from 500 nm to 2,500 nm. This size range is within the range of the accumulation mode of tropospheric size distribution. The second goal is to retrieve both the size and refractive index of measured particles based on the pattern of light they scatter. The retrieval uses Mie scattering theory [Mie, 1908] and deduces unambiguous results, assuming that the measured particles are homogeneous spheres. SPARCLE is suitable for ambient measurement since large proportions of the ambient particles with sizes between 500 nm and 2,000 nm are either liquid droplets or particles with morphologies that have a dominant liquid phase [Sullivan and Prather, 2005; Pinnick et al., 2011; Prospero et al., 1983].

The instrument used in this study is the second generation of SPARCLE [Peters et al., 2009] which transformed the original design from a stratospheric instrument [Thomas, 2003] into one suitable for use in troposphere studies. With the dimension of 60 cm× 30 cm ×20 cm and weight of up to 15 kg, SPARCLE is a field-deployable instrument.

1.1 What is an aerosol

An aerosol is a suspension of solid or liquid particles in a gas. The size of the particles spans from a few nanometers to tens of microns. An aerosol can be generated either naturally or from anthropogenic sources. Some examples of naturally generated aerosols are mineral dusts, volcanic emissions and sea spray. Some instances of anthropogenic aerosols are the products of fuel combustion and dust from mining.

Aerosols can be subdivided based on two general criteria: their physical form and method of generation [Hinds, 1999]. There is no rigorous scientific classification for these two criteria. Some common classifications refer to the appearance or source of particles such as smoke and fog, while others are based on arbitrary conventions such as nanoparticles. Table 1.1 lists a few common definitions of aerosols.

Table 1.1: Common aerosols found in the troposphere. These classifications are based on either the physical form or the method of generation of the aerosol particles. These classification are taken from [Colbeck and Lazaridis, 2014]. Note that the reference use the term *aerosol* ambiguously to refer both an individual particle and a suspension of particles.

Particle	Definition
Bioaerosol	The aerosol of biological systems and products of organisms, such as viruses, bacteria and pollen. The size range of viruses, bacteria and pollen are roughly 5–50 nm, 500–50,000 nm and 10,000–100,000 nm, respectively.
Dust	A solid-particle aerosol produced from crushing or other physical actions resulting in the mechanical breakup of parent materials. The size of dust ranges from few nanometer to more than 100,000 nm. The shape of dust is usually irregular.
Fume	A solid aerosol of condensed vapours or any gaseous products from combustion. Typically, these particles are a complex chain of primary particles and less than 50 nm in size.
Haze	An aerosol in the atmosphere that reduces visibility. The size range is between 500–10,000 nm.
Mist and Fog	Spherical liquid aerosols produced from condensation or atomisation processes. The size of these particles range from submicrometer to about 200,000 nm.
Smog	A solid-liquid aerosol produced by the interaction between sunlight and vapours in the atmosphere. The size of these particles are generally less than 1,000 or 2,000 nm. The term *smog* is derived from the combination of the terms *smoke* and *fog*.
Smoke	A solid or liquid aerosol generated either from condensation of supersaturated vapours or incomplete combustion. The size of these particles are usually less than 1,000 nm.
Spray	A droplet aerosol formed by the physical or electrostatic breakup of a liquid. Particle size is larger than a few micrometers.
Nanoparticle	A particle in the size range of 1–100 nm.

1.2 Aerosol properties

Aerosol properties can be distinguished into two categories. The first is single particle properties, such as particle size, shape, composition and refractive index. The second is collective aerosol properties, such as particle size distribution, the scattering and absorption coefficient of atmospheric aerosols. Single particle and collective aerosol properties relevant to this study are particle shape, size, refractive index and size distribution.

1.2.1 Shape and size

Aerosol particles vary in shape. Liquid particles are nearly always spherical while solid particles have complex shapes and can be coated by other particles. Some examples of the shapes of various solid particles are shown in Figure 1.1. The figure shows the scanning electron microscope image of minerals, fly ash, organics and biogenic particles. The shapes of the particles vary from irregular shape such as that of the mineral particles to nearly spherical such as that of the organic particle. The figure also indicates that almost all of the particles are coated by particles such as soot and $Ca(NO_3)_2$ particles.

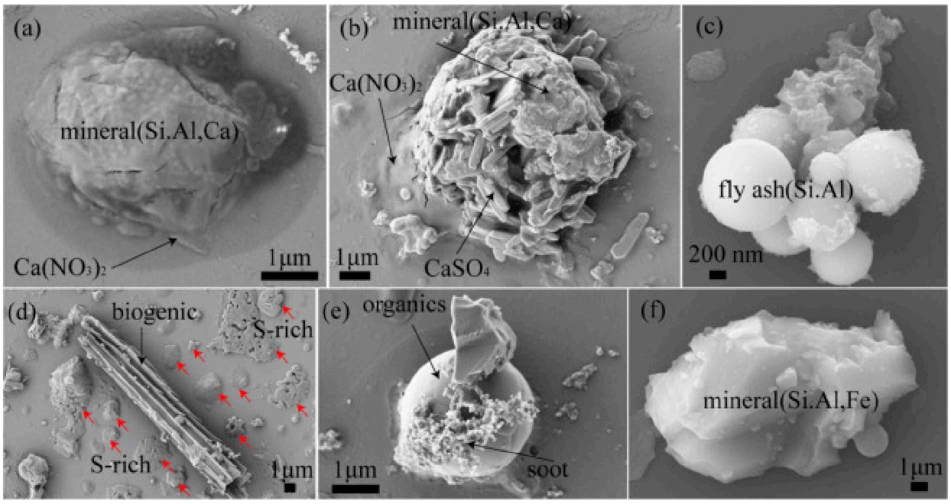

Figure 1.1: The scanning electron microscope images of particles collected from haze episodes in Jinan city of North China. The composition of particles are shown in each image. (a) A mineral particle composed of Si, Al and Ca and coated by $Ca(NO_3)_2$. (b) A mixture of rod-shape $CaSO_4$ and mineral particles coated by $Ca(NO_3)_2$. (c) An aggregate of nearly spherical fly ash. (d) A biogenic particle and S-rich particles indicated by red arrows. (e) A spherical organic partly covered by soot particles. (f) An irregular mineral particle.

Particle size is defined in various ways. The definitions can be based on either a particular aerosol property or the behaviour of interest in a specific system [McMurry, 2000]. Some examples of the definitions are:

1. Geometric diameters.
   A geometric diameter is the diameter of a spherical aerosol.

2. Aerodynamic diameters.
   An aerodynamic diameter is the diameter that specifies the response of particles to air flow. It is defined as the diameter of a sphere of density $1\,\mathrm{g\,cm^{-3}}$ settling due to gravity at the same terminal velocity as the particle of interest, regardless of the particle's shape and density. This definition can be used to analyse data from an aerodynamic particle sizer.

3. Electrical mobility diameters.
   An electrical mobility diameter is defined as the diameter of a sphere with the same electrical mobility as the particle of interest. This definition can be applied to measurement data taken by a differential mobility analyser (DMA).

4. Optical diameters.
   An optical diameter is defined as the diameter of a standard particle generating the same response as the particle of interest in an aerosol photometer. Standard particles widely used in the calibration of aerosol photometers are Polystyrene latex (PSL) beads.

1.2.2 Size distribution

Knowledge of the size distribution of aerosol particles is essential; it may offer an explanation of aerosol particle's sources and formation. For example, the size distribution of ambient air has three distinct modes and each mode can be related to both different modes of aerosol formation processes and different particle characteristics [Whitby, 1978].

Aerosols can be classified based on their particle size distribution. Monodisperse aerosols are aerosols which particles are nearly the same size. Aerosols whose particles vary widely in size are called polydisperse aerosols. Most types of aerosols found in nature are polydisperse aerosols. Monodisperse aerosols are commonly generated in laboratory settings.

The simplest depiction of particle size distribution is a histogram of the number of particles in successive size intervals. For the distribution that covers a large range of particle size, it is useful to describe the distribution using lognormal distribution. The distribution can be characterised by two parameters derived from lognormal distribution: geometric mean diameter, d_{g}, and geometric standard deviation, σ_{g} [Hinds, 1999]. Geometric mean can be calculated as

$$\ln d_{\mathrm{g}} = \frac{\Sigma n_i \ln d_i}{N}, \tag{1.1}$$

where N is the total number of particles, n_i is the number of particles at the i^{th} size interval, and d_i is the size at the midpoint of the i^{th} size interval. Geometric standard deviation can be calculated as

$$\ln \sigma_{\mathrm{g}} = \left[\frac{\Sigma n_i (\ln d_i - \ln d_{\mathrm{g}})^2}{N-1}\right]^{1/2}. \tag{1.2}$$

The sizes of 95% of particles are between $d^{-}_{95\%}$ and $d^{+}_{95\%}$ where

$$d^{-}_{95\%} = \frac{d_{\mathrm{g}}}{\sigma_{\mathrm{g}}^{\;2}}, \tag{1.3}$$

$$d^{+}_{95\%} = d_{\mathrm{g}}\,\sigma_{\mathrm{g}}^{2}. \tag{1.4}$$

Conventionally, size distributions with σ_{g} between 1.1 to 1.2 is considered to be monodisperse aerosols. Aerosols that have bigger σ_g are considered to be polydisperse aerosols.

1.2.3 Refractive index

Optical properties of aerosols describe the interaction between aerosol and light. One of the properties is the refractive index of particles, m, expressed as

$$m = n + ik, \tag{1.5}$$

where n and k are the real and the imaginary part of particle refractive index, respectively. Both parts affect the propagation of light in materials differently; the real part determines the speed of the light while the imaginary part determine the decay of the light intensity [Mischenko, 2004]. As a result, the refractive index of particles modifies the proportion of light being absorbed or scattered as it illuminates the particles.

Particle refractive index depends on both the material of particles and the wavelength of the light propagating in particles. Some examples of refractive indices of common materials evaluated at $\lambda = 589\,\mathrm{nm}$ of yellow sodium light are listed in Table

1.2. Most materials shown in the table are non-absorptive materials indicated by zero values of the imaginary part. The examples of particle refractive index as a function of light wavelength are depicted in Figure 1.2. The samples are volcanic ash taken from Mount Aso, Japan [Reed et al., 2018] and composite clay made of $\frac{1}{3}$ by weight of Montmorillonite, Illite and Kaolinite [Querry, 1987]. As can be seen in the figure, both of the real and the imaginary part vary as a function of light wavelength.

Table 1.2: Refractive indices of some common materials [Lide, 2005]. The refractive indices were measured using Yellow Sodium light at $\lambda = 589\,\text{nm}$ except for Carbons which were measured at $\lambda = 491\,\text{nm}$. The table is adapted from [Hinds, 1999]

Material	Refractive index	Material	Refractive index
Vacuum	1.0 + 0i	Quartz (SiO_2)	1.544 +0i
Water vapor	1.00025 + 0i	Polystyrene latex	1.590 +0i
Air	1.00028 +0i	Glycerine	1.4730 +0i
Water	1.3330 +0i	Benzene	1.501 +0i
Ice (H_2O)	1.305 +0i	Soot	1.96+0.66i
Sodium Chloride	1.544 +0i	Carbon	2.0+1.0i

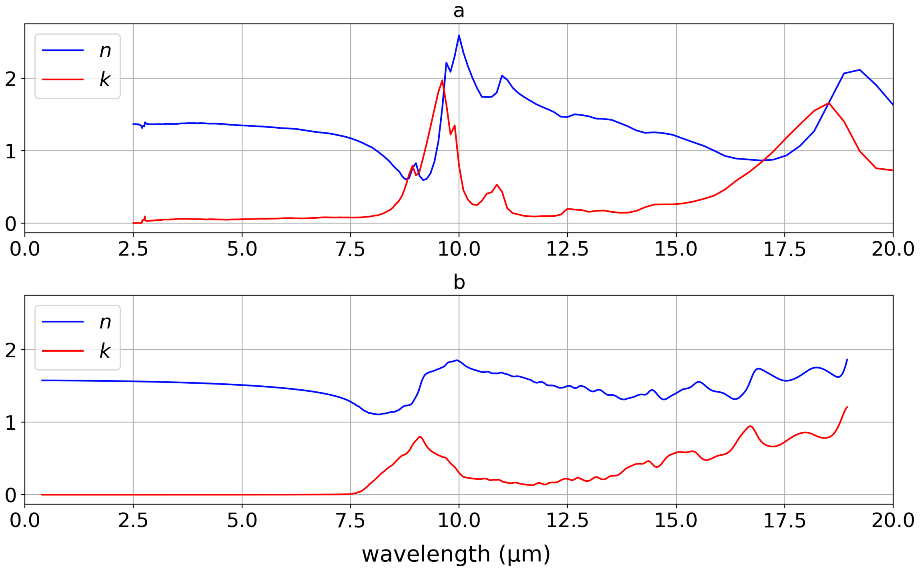

Figure 1.2: The refractive indices of two materials: clay (a) and volcanic ash (b). In the figure, two components of the refractive indices are plotted: the real part, n, and the imaginary part, k. The data were produced by [Querry, 1987] and [Reed et al., 2018] and available in Aerosol Refractive Index Archive compiled by [Grainger et al., 2020]

1.3 Physical and chemical processes in aerosol system

Physical and chemical processes can change the properties of aerosols. They all involve mass transfer to or from particles. This transfer can be the result of molecular transfer between particles and gas molecules such as in: condensation, evaporation, nucleation and chemical reaction, or it may a result of inter-particle mass transfer such as in coagulation.

1.3.1 Condensation and evaporation

The size of droplets can change by the condensation of vapour on droplets surface or by the evaporation of droplets. The condition that determine the condensation or the evaporation depends on the partial pressure of vapour around droplets as well as the size, the temperature and the substance of droplets. This condition can be derived using the condition of both vapour condensation on flat-surface liquid and flat-surface liquid evaporation and then modifying the condition based on the spherical shape of droplets [Seinfeld and Pandis, 2006].

In a simple case of flat-surface liquid comprised of pure substance a, the saturation ratio of vapour a determines the rate of both vapour a condensation and liquid a evaporation. The saturation ratio is expressed as:

$$S_a = p_a \,/\, \bar{p}_a\,, \tag{1.6}$$

where S_a is the saturation ratio of vapour a; p_a and $\bar{p}_a$ are the partial pressure and the saturation pressure of vapour a, respectively. The equilibrium of the liquid-vapour system, defined as saturated, can be achieved when S_a is equal to one. In this condition, the rates of the condensation and the evaporation are equal. When the level of S_a is either lower or greater than one, it leads to the greater rate of either the evaporation or the condensation, respectively. The saturation ratio levels of $S_a > 1$ and $S_a < 1$ are known as supersaturated and unsaturated, respectively.

Since droplets are spherical, the condition based on the saturation ratio needs to be modified [Seinfeld and Pandis, 2006]. In a simple case of droplets comprised of pure substance a, the level of the saturation ratio of vapour a around the droplets required for the equilibrium of the vapour-droplets system, denoted as $\mathring{S}_a$, in the environment with temperature T is given by Kelvin equation:

$$\mathring{S}_a = e^{\frac{4\,\gamma\, M}{\rho\, R\, T\, d}}, \tag{1.7}$$

where γ and ρ, are the surface tension and the mass density of the liquid phase of substance a, respectively; M is the molecular weight of substance a; R is the gas constant; d is the diameter of the droplets. When the level of S_a is either lower or greater than $\mathring{S}_a$, it leads to the greater rate of either droplets a evaporation or vapour a condensation, respectively.

1.3.2 Nucleation

Nucleation refers to particle formation from vapour either in the absence or the presence of foreign particles [Seinfeld and Pandis, 2006]. In the absence of foreign particles, nucleation can occur on embryos comprised of vapor molecules, a process called homogeneous nucleation. Nucleation can also occur by the nucleation of vapor on the surface of foreign particles, a process called heterogeneous nucleation. The main different between those two nucleation paths is the level of vapour saturation ratio required to trigger nucleation. Homogeneous nucleation requires large vapour saturation ratio typically larger than two. For example, homogeneous nucleation of pure water vapour with temperature 293 K into water droplets is predicted to occur at water vapour saturation ratio larger than 3.5. This level of saturation ratio is, normally, conditioned at laboratory. In the atmosphere, typically, particles are formed heterogeneously. Heterogeneous nucleation requires nuclei with a wettable surface in a supersaturated environment. In this condition, vapour molecules will be adsorbed on nuclei surface forming a layer of liquid coating the nuclei. Then, this newly-formed particles can grow and the rate of its growing is a complex function which depends on the type of the nuclei. For solid insoluble nuclei, the liquid layer can be approximated as droplets of pure liquid and grow through condensation. In the case of soluble nuclei, the dissolved nucleus, typically, tend to make the newly-formed particles grow in lower saturation ratios than that required by particles formed with insoluble nuclei.

1.3.3 Coagulation

Coagulation is an aerosol growth as a result of particle collision with other particles. The collision can be caused by either Brownian motion or external forces. Brownian-induced coagulation differs from condensation in a way that particles diffuse to other particles' surface and this mechanism doesn't require a saturated environment. One simplified example of Brownian-induced coagulation is the coagulation of monodisperse aerosols resulted in both decreasing particle number concentration, ρ_N, over a period of time, t, modelled as:

$$\frac{\mathrm{d}\rho_N}{\mathrm{d}t} = -K\,{\rho_N}^2, \tag{1.8}$$

where K is the coagulation coefficient of particles [Hinds, 1999]. The evolution of particle number concentration as a function of time can be achieved by integrating Equation 1.8 resulted in:

$$\rho_N(t) = \frac{\rho_{N_0}}{1+\rho_{N_0}\,K\,t}. \tag{1.9}$$

If monodisperse aerosols are in a contained system, the decreasing of particle number concentration due to coagulation results in the increasing of particle size. In the case of monodisperse aerosols comprised of droplets, the increase of droplet size as a function of time and initial number concentration can be expressed as:

$$d(t) = d_0\left[\frac{\rho_{N_0}}{\rho_N(t)}\right]^{1/3}, \tag{1.10}$$

where d_0 and $d(t)$ are initial droplet size and droplet size at time t, respectively; ρ_{N_0} and $\rho_N(t)$ are initial droplet number concentration and droplet number concentration at time t, respectively. Based on Equations 1.9 and 1.10, the time required for droplets to halve their initial number concentration and double their initial droplets size can be calculated and the results are listed in Table 1.3. According to the table, a larger initial aerosol number concentration leads to a shorter time to halve the initial concentrations and to double their particle size. In the calibration of aerosol instruments, where standard aerosols are generated and measured, the effect of coagulation can be neglected if the coagulation takes a much longer time to change the aerosol concentration and particle size compare to the time interval between aerosol generations and measurements.

Table 1.3: The calculated time required to halve the initial number concentration of monodisperse aerosols comprised of droplets and to double their initial droplets size. In this calculation, the coagulation coefficient of droplet, K, is assumed to be $5 \times 10^{-16}\,\mathrm{m^3\,s^{-1}}$. Source: [Hinds, 1999]

Initial number concentration ($\mathrm{m^{-3}}$)	Time to halve initial number concentration (s)	Time to double particle size (s)
10^{18}	0.002	0.014
10^{16}	0.2	1.4
10^{14}	20	140
10^{12}	2000	14,000
10^{10}	200,000	1,400,000

1.3.4 Reactions

Aerosol particles have a high surface area to mass ratio. This property allows aerosol particles to participate actively in many kinds of chemical interaction between gas molecules and aerosol particles. A specific example of this interaction is the chemical conversion of SO_2 to sulphuric acid or sulphates taking place inside cloud droplets. This chemical conversion can lead to the growth of cloud droplets in a short period of time around 10–30 minutes [Smith et al., 1996].

1.4 Tropospheric aerosol

Aerosols are generated either naturally or anthropologically and can be introduced into the troposphere either directly or indirectly. The major natural aerosols are terrestrial dust, volcanic ash, and sea spray. The main anthropogenic aerosols are combustion products and industrial dust. Aerosols such as dust, fly ash and combustion products are directly introduced into the troposphere. These aerosols are called primary aerosols. Another mechanism is indirect routes through gas to particle conversions. Aerosols introduced through indirect routes are called secondary aerosols. An example of secondary aerosols is sulphates in the troposphere that are generated from the oxidation of atmospheric sulphuric gases. The flux of primary and secondary aerosols commonly found in the atmosphere have been estimated globally and listed in Table 1.4.

Table 1.4: The estimation of global emission for principal atmospheric aerosols. The estimations are expressed in total mass of particles introduced into the atmosphere per year. The table is adapted from [Seinfeld and Pandis, 2006].

Source	Route	Particle	Est. Flux ($Tg\ yr^{-1}$)	Reference
Natural	Primary	Mineral dust	1,490	[Zender et al., 2003]
		Sea salt	10,100	[Gong et al., 2003]
		Volcanic dust	30	[Kiehl and H., 1995]
		Biological debris	50	[Kiehl and H., 1995]
	Secondary	Sulphates from (Methylsulfanyl)methane	12.4	[Liao et al., 2003]
		Sulphates from volcanic SO_2	20	[Kiehl and H., 1995]
		Organic aerosol from biogenic volatile organic compounds	11.2	[Chung and Seinfeld, 2002]
Anthropogenic	Primary	Industrial dust	100	[Kiehl and H., 1995]
		Black carbon	12[a]	[Liousse et al., 1996]
		Organic aerosol	81[a]	[Liousse et al., 1996]
	Secondary	Sulphates from SO_2	48.6[b]	[Liao et al., 2003]
		Nitrates from NO_x	21.3[c]	[Liao et al., 2004]

[a] Tg of Carbon; [b] Tg of Sulphur; [c] Tg of $NO^-{}_3$.

1.4.1 Tropospheric residence, transport and removal

In the troposphere, aerosol particles can be suspended for a few days up to a few weeks. The duration depends on their size and composition. For instance, fine-aerosols can reside in the troposphere between approximately 9 and 50 days [Jia, 2014]. Meanwhile, dust resides in the troposphere for two weeks on average [Seinfeld and Pandis, 2006].

While suspended, aerosols can be transported thousands of kilometers. Aerosol transport can be detected by either *in situ* measurements or satellite observations. For example, several *in situ* measurements of dust across the US detected dust originating from Asia [Husar et al., 2001; Griffin et al., 2002] and a satellite observation captured the presence and transport of aerosols from the Sahara desert to the Mediterranian as shown in Figure 1.3.

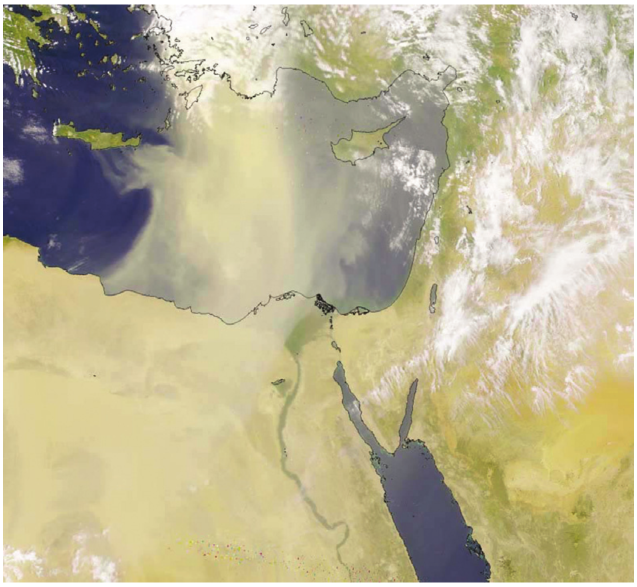

Figure 1.3: Satellite image of a dust plume extending North across the Mediterranean from the Sahara desert. Image acquired on 18 April 2001 and provided by the Sea-WiFS project, NASA/Goddard Space Flight Center and ORBIMAGE. Image taken from [Buseck and Schwartz, 2003]

Aerosol particles are removed from the troposphere through dry and wet deposition [Raes et al., 2000]. These removal mechanisms can be associated with particle size. Particles larger than 1,000 nm settle mainly due to gravity while smaller particles are removed primarily by wet deposition through precipitation or activation of the particles as cloud condensation nuclei to form cloud droplets.

A series of additional processes involving cloud droplets can lead to new particle formation [Seinfeld and Pandis, 2006]. The processes include chemical reactions in the aqueous phase of cloud droplets resulted in products such as sulphates. For example, Walcek estimated that during the passage of a midlatitude storm system, 65% of tropospheric sulphates over the northeastern United States was formed through chemical reactions in cloud droplets [Walcek et al., 1990].

1.4.2 Spatial and temporal variation

Aerosols in the troposphere are distributed heterogeneously in time, location, and altitude. The concentration of tropospheric aerosols in a particular area can change within tens of minutes. Spatially, tropospheric aerosol concentration may vary in the scale of a few kilometers horizontally and a few tens of meters vertically.

An example of temporal variation of aerosols is demonstrated in the aerosol measurements performed at the research station Melpitz Germany [Birmili and Wiedensohler, 2000]. The results are shown in Figure 1.4 . In the figure, the measured number concentrations are plotted as a function of measurement time and particle size. Based on the figure, a sudden rise in the concentration of small particles between 5 nm and 10 nm is detected shortly after 8 am. The concentration remains high for the next two hours and then decreases. The measurement shows that number concentration can vary in the order 10^3 within few hours.

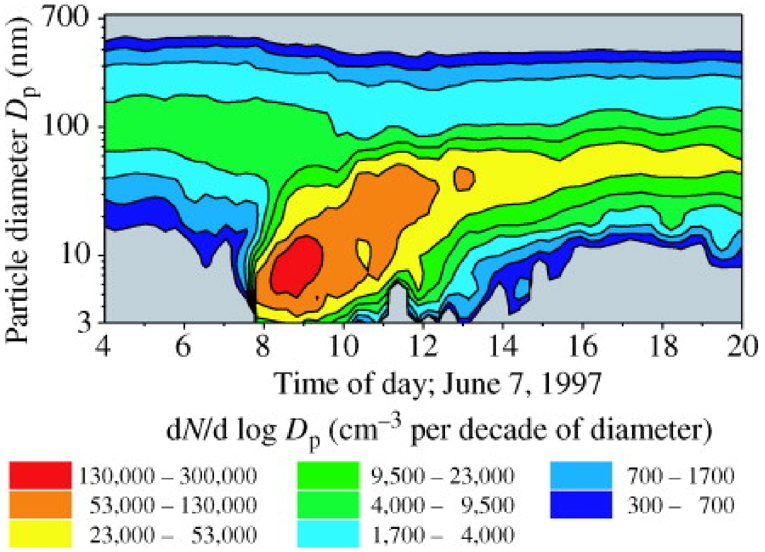

Figure 1.4: Contour plot of the number densities as a function of particle diameter and time of day. The unit of the concentration is cm^{-3} per decade of diameter ($dN/dlogD_p$) and is represented by the colours and contour lines. The measurement was taken at Meltpitz, Germany, 50 km NE of Leipzig, Germany. The image is taken from Source [Birmili and Wiedensohler, 2000]

An example of spatial variation of tropospheric aerosols in horizontal and vertical orientation is demonstrated in aerosols measurements performed at the mountainous terrain of Lower Frase Valley near Vancouver Canada. The results are shown in Figure 1.5. The concentrations of aerosols are inferred from backscatter intensity obtained by a lidar instrument installed on an aircraft. On the horizontal axis, the time of backscatter obtained are plotted. The axis can be converted into a distance based on the aircraft speed of $100\,\mathrm{m\,s^{-1}}$. Approximately, one minute in this axis corresponds to six kilometers. On the vertical axis, the altitudes of the measured aerosols are plotted. The altitudes were inferred based on the duration of backscatter travelling from the measured aerosols to the lidar.

The measurement results shown in Figure 1.5 can be interpreted as follows. The black regions are silhouettes of mountains or mountainous area. In the area above the mountains and valleys, the concentrations are varied, indicating tropospheric layering. In the valleys, the concentrations are high which could be due to accumulating particles from higher regions.

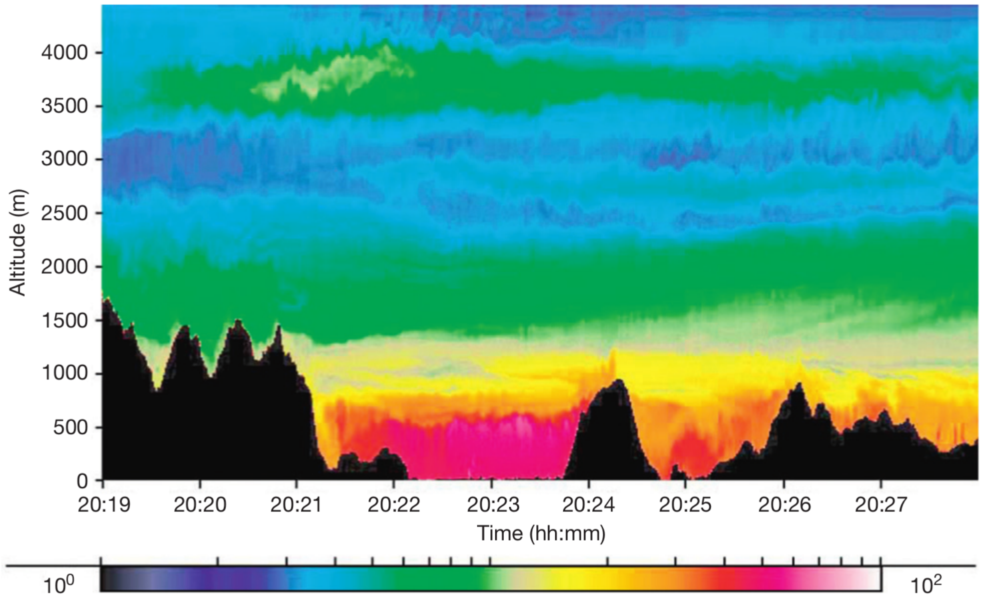

Figure 1.5: Lidar image from an aircraft indicating aerosol density in the eastern part of Lower Fraser Valley, Canada. At the bottom, the colour bar provides colour coded magnitude of aerosol concentration on a logarithmic scale. The horizontal axis is coordinated universal time or UTC, local time is UTC -07.00. This axis can be converted into a distance by using the aircraft speed of $100\,\mathrm{m\,s^{-1}}$. Roughly, one minute correspond to six kilometers. Courtesy of K.Strawbridge, Meteorological Service of Canada, the image is taken from [Buseck and Schwartz, 2003]

1.4.3 Ambient aerosols: urban, marine and rural aerosols

Urban aerosols are mixtures of primary and secondary aerosols. The main sources of the primary aerosols are emission from industries, transportation, power generation and natural sources while the secondary aerosols are mainly formed by gas-to-particle conversion mechanism of combustion products. The size distribution of urban particles varies as a function of the distant to sources. For example, measurements of fine particles whose size less than 100 nm in the regions less than 150 m away from highways showed a variation of fine particle size distributions [Zhu et al., 2002]. The size distribution in the region 30 m away from the highway peaked at particle size of 10 nm with the concentration of nearly 15×10^4 particles cm^{-3}, while that in the region 150 m away from the highway peaked at particle size of 41.3 nm with the concentration of 1×10^4 particles cm^{-3}.

In the absence of aerosols transported from continentals, aerosols over remote oceans mainly consist of marine-originated particles [Savoie and Prospero, 1989]. Typically, 90-95% of marine atmospheric particles are fine particles whose size less than 600 nm and the rest is coarse particles whose size bigger than 600 nm. The fine particles are formed primarily by the gas-to-particle conversion of the products of organosulfur gases oxidation such as (Methylsulfanyl)methane emitted by the ocean [Fitzgerald, 1991]. The coarse particles are composed primarily of sea salt as a result of sea spray evaporation [Blanchard and Woodcock, 1957; Monahan et al., 1983]. Normally, sea spray are produced by bursting bubbles or wind-induced wave breaking. The concentration of marine atmospheric particle are typically in the range of 100 particles cm^{-1} – 300 particles cm^{-1} [Savoie and Prospero, 1989].

Aerosols in rural areas are mainly originated from nature but with a moderate influence of anthropogenic sources [Hobbs et al., 1985]. Plants are the largest sources of secondary aerosols in remote rural area. The example of the secondary aerosols is biogenic aerosols resulted from reactions involving volatile organic compounds emitted by plants [Faiola et al., 2018; Riccobono et al., 2014]. Anthropogenic aerosols can also be transported from urban to neighbouring rural area and can lead to higher particle number concentration compare to that of remote rural area. For example, particle number concentrations in remote area nearby a forest and urban-influence rural area were measured in the level of 1,000 particles cm^{-1} – 4,000 particles cm^{-1} and 3,000 particles cm^{-1} – 10,000 cm^{-1}, respectively [Wiedensohler et al., 2002].

Aerosols in deserts are dominated by mineral dusts. Main components of desert dusts are Si, Al, Fe and Ca [Warneck, 2000]. The size distribution and the particle number concentration of desert dust depend strongly on the wind speed. Typically, the size distribution of desert dust shows three overlapping modes. For example, a measurement of Saharan dust shows that the size distribution of dust has three modes peaked at diameters of 400 nm, 1,000 nm and 2,000 nm [Rocha-Lima et al., 2018].

1.4.4 The Whitby model

The Whitby model describes that the distribution of tropospheric aerosols can be characterised by three main modes: nucleation, accumulation, and coarse mode [Whitby, 1978]. The size range of the nucleation and the accumulation mode are from 5 nm to 100 nm and from 100 nm to 2,000 nm, respectively. The coarse mode consists particles larger than 2,000 nm.

Typically, particle size distribution in the troposphere has a minimum concentration between the accumulation and the coarse mode, roughly at particle size of 2,000 nm. Whitby divided particles with respect to this size into two fractions: fine particles whose size are less than 2,000 nm and coarse particles whose size are greater than 2,000 nm. According to this division, fine particles include nucleation-mode and accumulation-mode particles.

These fractions have major differences in origin as well as in physical and chemical characteristics [Seinfeld and Pandis, 2006]. Particles in the nucleation mode are generated from the condensation of hot vapors during combustion processes and from the nucleation of atmospheric species to form fresh particles. This mode has a transient nature due to rapid coagulation either with larger particles or other particles in the nucleation modes. Particles in the accumulation mode are produced by the coagulation of particles in the nuclei mode and from the condensation of vapors onto existing particles causing them to grow into this size range. In this mode, particle removal mechanism is the least efficient causing particles to accumulate in number. Some examples of fine particles are Sulphates, Nitrates, Organics, Carbon, and Lead. Coarse particles are produced by mechanical processes such as wind erosion. Particles in this mode have high sedimentation rates due to their size and sink quickly by dry deposition. Some examples of coarse particles are crustal materials, sea salt and plant particles. Fine and coarse particles exchange is highly unlikely, due to the differences in particle sources and sink mechanisms. The depiction of particle sources and sinks for fine and coarse particles along with the corresponding modes can be seen in Figure 1.6.

Numerical fittings of lognormal functions to various size distribution in atmosphere was performed by Jaenicke [Jaenicke, 1993]. The lognormal functions were three functions that represent nucleation, accumulation and course modes. The fittings resulted in the parameters of the lognormal functions that lead to best fit between the lognormal functions and the size distributions. The parameters are listed in Table 1.5.

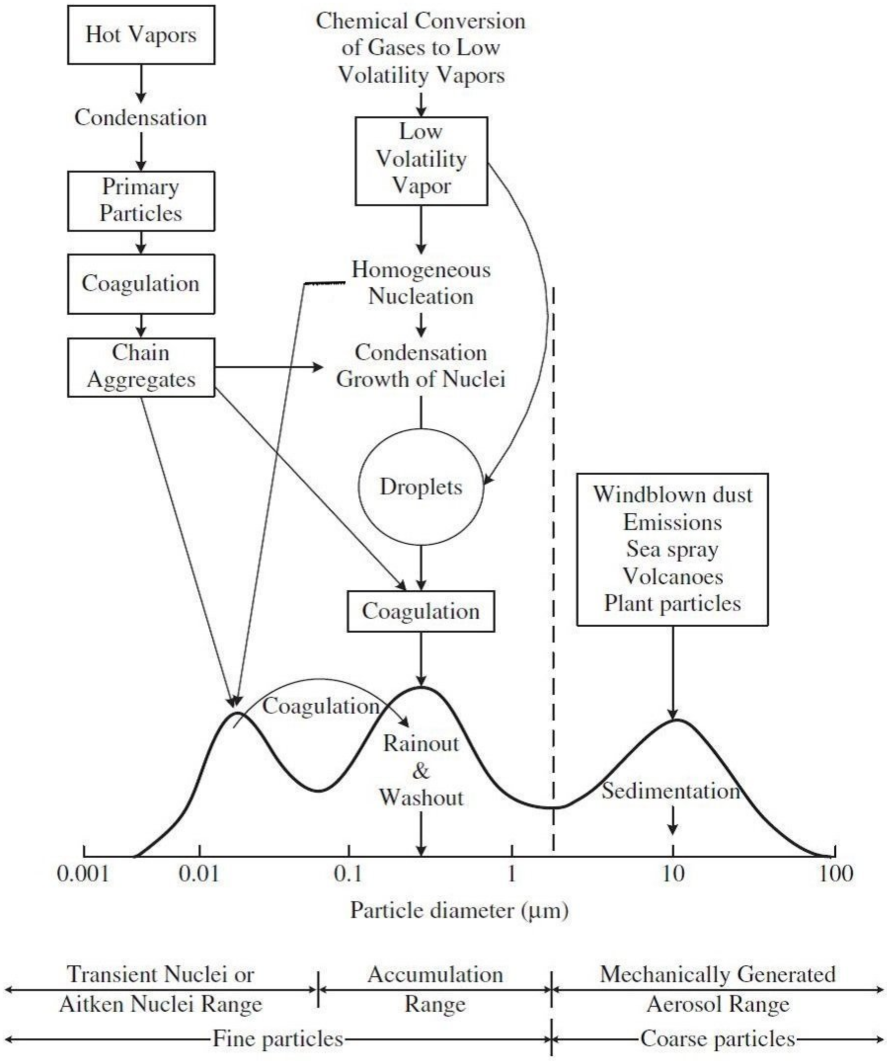

Figure 1.6: Physical and chemical processes related to aerosol size. The size distribution of tropospheric aerosols can be characterised by three main modes: nucleation, accumulation and coarse. Notice that aerosol exchange between coarse mode and the other two modes is unlikely, depicted by a dash line at particle size of 2 µm, due to their differences in sources and sink mechanisms. The picture was taken from [Colbeck and Lazaridis, 2014]

Table 1.5: Parameters to model atmospheric aerosol distribution based on three log-normal functions that represent nucleation, accumulation and coarse modes. Three parameters in the functions to characterise each mode are particle number concentration, ρ_N, geometric mean diameter, d_{g}, and geometric standard deviation, σ_{g}. The parameters are taken from [Jaenicke, 1993]

region type	mode	parameters				
		ρ_N (particles cm^{-3})	d_{g} (nm)	$\ln \sigma_{\mathrm{g}}$	$d^{-}_{95\%}$ (nm)	$d^{+}_{95\%}$ (nm)
urban	nucleation	9.93×10^4	13	0.245	4	40
	acc.	1.11×10^3	14	0.666	1	301
	coarse	3.64×10^4	50	0.337	11	236
marine	Nucleation	1.33×10^2	8	0.657	< 1	165
	acc.	6.66×10^1	266	0.210	101	700
	coarse	3.10×10^0	580	0.396	94	3,593
rural	Nucleation	6.65×10^3	15	0.225	5	42
	acc.	1.47×10^2	54	0.557	4	702
	coarse	1.99×10^3	84	0.266	25	286
remote continental	nucleation	3.20×10^3	20	0.161	10	42
	acc.	2.90×10^3	116	0.217	43	315
	coarse	3.00×10^{-1}	1,800	0.380	313	10,358
free tropospere	nucleation	1.29×10^2	7	0.645	< 1	136
	acc.	5.97×10^1	250	0.253	78	802
	coarse	6.35×10^1	520	0.425	73	3,681
polar	nucleation	2.17×10^1	138	0.245	45	426
	acc.	1.86×10^{-1}	750	0.300	188	2,986
	coarse	3.00×10^{-4}	8,600	0.291	2,252	32,847
desert	nucleation	7.26×10^2	2	0.247	1	6
	acc.	1.14×10^2	38	0.770	1	1318
	coarse	1.78×10^{-1}	21,600	0.438	2,874	162,351

1.5 Approaches to performing aerosol measurements

There are variety of methods and instruments which scientists and engineers can use to perform *in situ* aerosol measurements. Each instrument provides measurements for particular properties and most instruments only operate within a certain particle size range. Due to these limitations, it is common that more than one instrument is used in an aerosol measurement campaign to reach measurement goals.

In selecting their instruments, users should recognise the main principles and limitations of the instruments they are about to use. The instruments can be classified into two general types. The first type is collecting instruments which collect aerosol particles for off-line laboratory analysis. The second is direct-reading instruments which detect aerosol particles and measure the properties of aerosols in near real-time. Some direct-reading instruments also collect measured particles which can be analysed further in the laboratory.

1.5.1 Aerosol collecting instruments and laboratory analysis

The most common sampling technique involves the use of filters to collect aerosol particles. The currently available filters are highly efficient in capturing nearly all sizes of particles. The principle of collection is straightforward. An aerosol is drawn through a filter, and then the filter separates the particles from the gas. The selection of filter depends on the purpose of the measurements. For example, general-purpose air samplings are widely done using fibrous filters due to their price and good mechanical strength. If the purpose is mass and elemental analysis of the sample, then membrane filters made of Teflon are frequently used. This is because Teflon filters absorb only a small amount of water vapour [Chow et al., 1990].

Some sampling instruments are designed to classify particles into various size fractions. Two instruments commonly used are cyclones and impactors. Cyclones make air flow in a swirling motion. This motion results in large particle being deposited onto a surface by centrifugal action. Meanwhile, impactors work by introducing an abrupt change in airflow. The abrupt change causes large particles to be deposited onto a surface or substrate.

Laboratory analysis of particles can be done in various ways. Sample particles attached to the filters can be analysed using electron microscopy, X-ray diffraction, or X-ray fluorescence to study about their size, shape, concentration and composition. Filters containing sample particles can be extracted and analysed through ion chromatographic analysis to quantify the organic species present. The mass concentration of sample aerosols can be calculated by taking the ratio of the increase of filter weight after measurement and the volume of aerosol sample.

Collecting instruments suffer the major drawbacks that they are time consuming and time-integrated measurements. Other drawbacks are measurement artifacts caused by filters, such as adsorption or desorption of water vapour into filter materials [Charell and Hawley, 1981] and loss of volatile particles collected on filters[Eatough et al., 1995].

1.5.2 The aerosol direct-reading instrument

Instruments widely used in the direct-reading aerosol measurement are optical particle counters (OPCs). In OPCs, particles passing through the sensing volumes are illuminated. The size of the particles are inferred from the intensity of light scattered by individual particles [Sorensen et al., 2011]. A commercial OPC with 31 size channels that span between 0.4 µm and 32 µm can process aerosols with concentrations of up to 3,000,000 particles per liter and present measurement results every 6 seconds [GRIMM, 2020]. The main drawback of OPCs is that their accuracy is dependant on particle shape and refractive index [Szymanski et al., 2009].

To detect fine particles, condensation particle counters (CPCs) are widely used. In CPCs, particles are exposed to a supersaturated vapour. This exposure induces the particles to grow to approximately the same size. The particles are then detected by an optical system. CPCs can detect particles down to about 1 nm in size.

Differential mobility analysers (DMAs) are instruments that classify particles according to their electrical mobility. In DMAs, particles are charged and flow through an electric field. The particles with a particular velocity pass through classifiers and can be detected downstream. A CPC can be installed downstream of a DMA to measure the size distribution of fine particles. This combination is frequently called a differential mobility particle sizer (DMPS).

Aerodynamic particle sizers (APS) classify particles based on the velocity of the particles in the sensing zone. In the inlet of APS, particles are accelerated so that their velocity in the sensing zone is a function of the aerodynamic diameter of the particles. The velocity is measured by the “time-of-flight” of particles in the sensing zone. The velocity may need to be corrected as the acceleration can distort liquid particles. A commercial APS measures particles with size ranges from 0.5 µm to 20 µm [TSI, 2020].

1.6 Factors that limit aerosol measurements

Errors in a measurement should be recognised to be able to assess the interpretation and usefulness of the measurement data. Errors can be introduced due to particles lost in sampling and transport lines, the limited sensitivity of sensors deployed in the instruments, or the insufficient number of samples. As a result of these types of errors, measured aerosol properties may not reflect the original aerosol properties.

1.6.1 Particle loss in instrument inlets and transport lines

A general scheme of particle measurements by instruments requires sampling and transporting particles through inlet and transport lines to be sensed in the sensing volume of instruments. During these processes, particles can be lost due to various factors. In the inlets, particle lost is a function of the ratio of ambient air velocity to sampling velocity, the air turbulence, as well as the size, shape and orientation of the inlets [Pramod and Baron, 2011; Vincent J., 2007; Okazaki et al., 1987]. In the transport lines, particle lost is a function of electrostatic attraction, impaction or gravitational settling [Pramod and Baron, 2011; Ye and Pui, 1990].

1.6.2 Detector response and sensitivity

Detectors used in instruments may have a non-ideal responses to the particle property of interest. The non-ideal responses can lead to measurement artefacts. For instance, low sensitivity of detectors to signals correlated with small particles may result in poor detection of small particles and can distort the size distribution of measured particles. This error was demonstrated in the study of a TSI aerosizer performance [Blackford D. et al., 1988]. In the study, the errors due to the detector responses and the inlet of the instrument were measured. Based on this error study, a simulation of aerosol measurement using the instrument can be created and plotted in Figure 1.7. As can be seen in the figure, the distortion of the measured size distribution from the original size distribution is expected in both the lower and higher end of the size range. In the lower size range, the size distribution is distorted due to the poor sensitivity of the detector. At the higher end, the distortion is caused by the inlet losses.

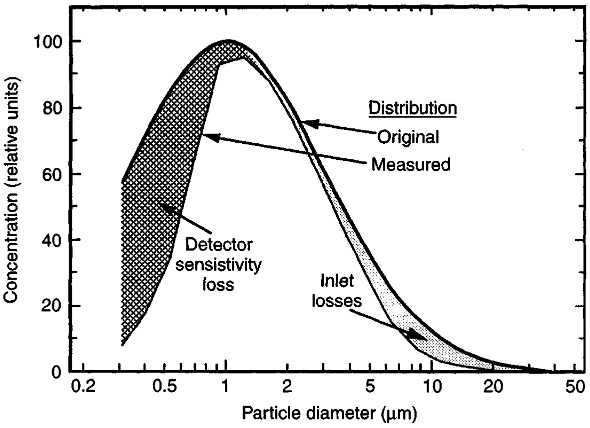

Figure 1.7: A simulation of measurement distortion expected from the measurement of size distribution using the aerodynamic particle sizer (APS3300). The simulation shows that the losses of small particles and big particles, indicated by the grey areas, are due to the detectors' sensitivity and the inlet, respectively. The study was done by [Blackford D. et al., 1988]. The figure is taken from [Pramod and Baron, 2011]

1.6.3 Coincidence errors in instruments sensing volume

In a single particle detecting instrument, coincidence errors take place when two or more particles are in the sensing volume simultaneously. These errors are commonly found in OPC. In OPC, light scattered by two small particles or more simultaneously at the sensing volume can be perceived as that scattered by a single larger particle. This leads to underestimating the sample concentration of sample aerosols.

Coincidence errors limit the maximum level of concentration an instrument can measure. For example, a study shows that the coincidence error in the measurement of OPC A10 increased as the concentration increased [Sachweh et al., 1998]. In the study, the counting error of less than 7% was found when measuring an aerosol with the concentration of 10^6 particle cm^{-3}. The error increased up to 50% as the concentration of the aerosol increased to 10^7 particle cm^{-3}.

1.6.4 Corrections for physical properties

Corrections might be needed due to the specific characteristics of an instrument. For example, most OPCs are calibrated using non-absorbing PSL beads. The refractive index of PSL beads is 1.59 with no imaginary part at the wavelength of 589 nm. A correction will be needed if OPCs are used to measure different sample such as dust coal whose refractive index is $1.54 - 0.5i$. Otherwise, the measurement will provide inaccurate results [Liu et al., 1974].

1.6.5 Aerosol sampling statistics

In the measurement of an aerosol population, the uncertainty of the results is inversely proportional to the number of samples. This is based on the Poisson statistic that the uncertainty can often be assumed to be the square root of the number of samples. For example, to achieve 1% uncertainty, at least 10,000 particles must be sampled. The importance of the sampling statistic is illustrated in Figure 1.8. The figure shows two simulated measurements of the same aerosol population with two different sample size: 10^6 and 10^3 particle number. For the measurement with 10^6 particle number, the result shows a lognormal size distribution with a number median diameter of 2.5 µm and a geometric standard deviation of 2.0. The result is shown in Figure 1.8(a). A different shape of size distribution is expected to be achieved with the lower sample number measurement as shown in Figure 1.8(b). The shape is still approximately lognormal though the increased uncertainty is apparent.

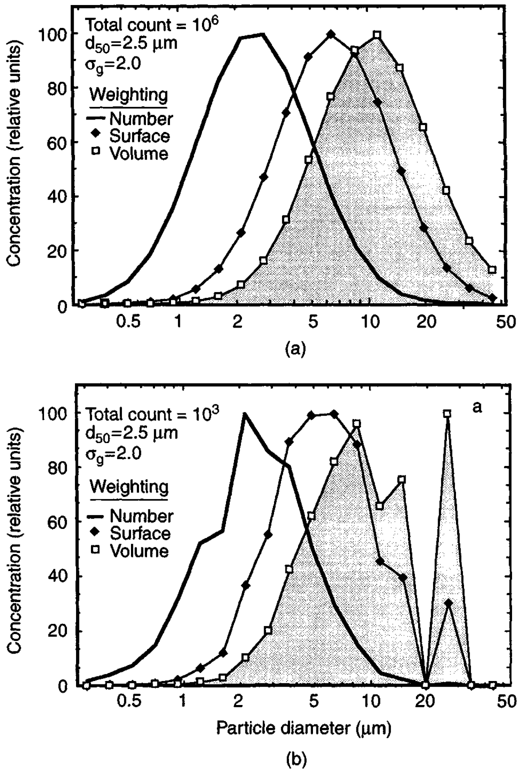

Figure 1.8: Plots of size distribution of the particle number, surface area and volume of two different simulated measurement of the same aerosol population with two different sample size. The plots are normalised to the same height. The study was done by [Liu et al., 1974]. The figure is taken from [Pramod and Baron, 2011]

1.7 OPCs

OPCs are widely used in aerosol and atmospheric research due to their applicability in *in situ*, real time measurement. Despite years of development, OPCs still suffer from ambiguity in particle sizing, mainly due to particle optical properties variations [Cooke and Kerker, 1975; Liu et al., 1986; Szymanski and Liu, 1986; Hinds and Kraske, 1986; Garvey and Pinnick, 1983] and particle shape variations [Chang et al., 2003; Chen and Cheng, 1984; Gebhart and Zerull, 1986; Umhauer and Bottlinger, 1991]. Several designs have been suggested to alleviate this ambiguity. One such design attempting to alleviate the ambiguity due to particle optical properties variations is the instrument used in this work.

1.7.1 Basic types and characteristics of OPC instruments

OPCs infer the size of single particles based on the measured intensity of light elastically scattered by the single particles. In the inversion, it is assumed that the single particles are homogeneous spheres; This assumption puts a limit on the accuracy of OPCs in sizing particles with non-spherical shape. The measurement steps of a typical OPC include transporting a particle to sensing volumes, illuminating the particle by a well-defined light source, collecting the scattered light over a particular solid angles and measuring the collected scattered light. The schematic design of a typical OPC can be seen in Figure 1.9. As shown in the figure, single particles are drawn into a sensing volume through a sampling pipe. In the sensing volume, the particles are illuminated by a laser beam. Then, the scattered light from the illumination over a solid angle is collected by a collecting optic and directed to a detector. The solid angle is represented by an arc of angle ϕ and $\phi + \Delta\phi$ swept around a sphere by θ and $\theta + \Delta\theta$. Finally, the particle exits through a removal pipe.

The intensity of light scattered by a homogeneous spherical particle collected over a particular solid angle can be calculated using Mie theory [Mie, 1908]. Mie calculated the intensity based on the assumption that the spherical particle is illuminated by a linearly polarised light propagating in particular direction. In spherical coordinates with the particle located at the center of reference, the intensity is expressed as

$$I = \frac{\lambda^2}{4\pi^2} \int_{\phi_1}^{\phi_2} \int_{\theta_1}^{\theta_2} \left[I_{\parallel}(\alpha, m, \theta, \phi) + I_{\perp}(\alpha, m, \theta, \phi) \right] G(\theta, \phi)\, d\theta\, d\phi, \tag{1.11}$$

where $I_{\parallel}$ and $I_{\perp}$ are the scattered light intensities propagated in parallel and perpendicular, respectively, relative to the plane oscillation of the electric vector of the

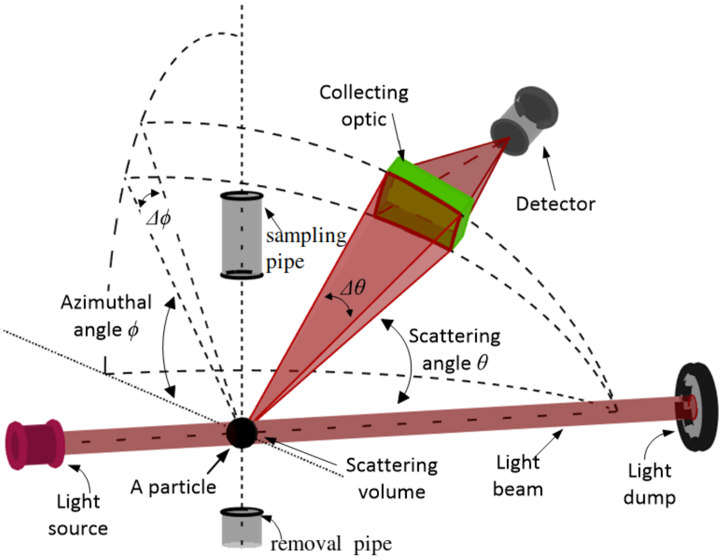

Figure 1.9: The typical design of OPCs.

illuminating light; α is the size parameter defined as $\alpha = \frac{\pi d_\mathrm{p}}{\lambda}$ with d_p as the particle diameter and λ as the wavelength of the illuminating light; θ is scattering angles defined as the angle between the propagation direction of the illuminating light and scattered light directions; ϕ is azimuthal angles defined as the angle between the plane oscillation of the electric vector of the illuminating light and scattered light directions; $G(\theta, \phi)$ is the geometrical factor specific to the instrument's design. The solid angle, over which the scattered light is collected, is represented by an arc of angle $\phi_1 - \phi_2$ swept around a sphere by $\theta_1 - \theta_2$.

There are two types of OPCs based on the range of solid angle over which the total scattered light is collected [Szymanski et al., 2009]. The first type collects scattered light over the forward region, typically within the range of $\theta_1 = 5°$ to $\theta_2 = 25°$. The second type collects scattered light over the broad angular region, typically from $\theta_1 = 25°$ to $\theta_2 \geq 100°$.

A numerical calculation was done to describe the general characteristic of the two types of OPCs [Szymanski et al., 2009]. In the calculation, it was assumed that the range of ϕ is 2π for both types and the range of θ for the first type is from $\theta_1 = 5°$ to $\theta_2 = 25°$ while for the second type is from $\theta_1 = 25°$ to $\theta_2 = 100°$. The calculation was done by setting the wavelength of illuminating light is 630 nm. The results of the calculations for non-absorbing and purely absorbing particles are shown in Figure 1.10. In the figure, the intensities are plotted as a function of particle diameter and particle refractive index. The gradient of the intensities is projected on the horizontal plane of each plot. The range of particle diameters is from 0.1 µm to 3 µm. The range of particle refractive indices for non-absorbing particles is from 1.3 to 1.6 and that for purely absorbing particles is from 0.0 to 0.4. Figure 1.10.a and 1.10.b show the intensities collected from the forward region for non-absorbing and purely absorbing particles, respectively, while Figure 1.10.c and 1.10.d show those collected from the broad-angular region for non-absorbing and purely absorbing particles, respectively.

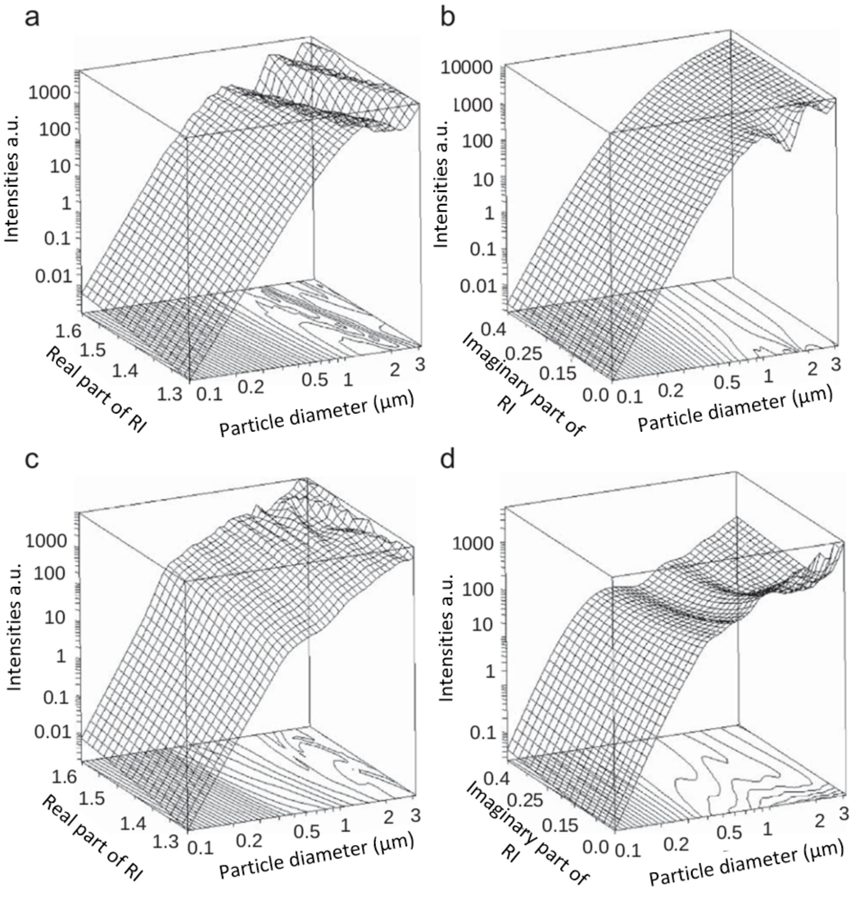

Figure 1.10: The calculations of scattered light intensities as a function of particle diameter and refractive index (RI), $m = n + ik$, collected from two different regions: the forward region and broad-angular region. The calculations were done for non-absorbing and purely absorbing particles. In (a) and (b), the intensities of those collected from the forward region are shown. While in (c) and (d), the intensities of those collected from the broad-angular region are shown. The figure was taken from [Szymanski et al., 2009]

Based on the figure, it is obvious that the intensities are not always a unique function of the particle diameter and refractive index. For the first type of OPCs, unique particle sizing is possible for particle size less than 1,000 nm. If particle sizing is based on a relatively wide channel size, then the second type is the better option since the intensities do not vary drastically.

1.7.2 Early development of OPC instruments

The first OPC instrument was built in 1947 [Gucker et al., 1947a] and later improved in 1954 [Gucker and Rose, 1954]. The OPC collected light scattered between $\theta_1 = 1°$ and $\theta_2 = 20°$. The light was then measured by a PMT. The output signals of the PMT were processed by a pulse height analyser. The maximum counting rate of the OPC was 3000 particles per minute with the coincidence error of less than 1%. The minimum particle diameter that the OPC was able to count is 340 nm. The OPC responded linearly to particles whose diameter between 500 nm and 1,000 nm with the accuracy of 1 nm.

An OPC aimed to measure very dilute aerosols was designed in 1947 [Gucker et al., 1947b]. The OPC collected light scattered at $\theta = 90°$. The main reason for choosing this angle was to ensure a low level of stray light. Stray light intensity as low as 0.03% of light scattered by smoke particles was achieved. This low background noise allowed the OPC to detect dioctyl phthalate smoke particles of diameter 600 nm.

An OPC suitable for balloon-borne measurements was designed in 1964, widely known as the Wyoming OPC [Rosen, 1964]. The design uses a microscope to focus the light scattered by single particles in the forward region to a PMT. The instrument was used to measure the vertical distribution of dust of up to 30 km. The measurement resulted in the concentration of particles with diameter greater than 560 nm and 760 nm as a function of altitude. The uncertainty of the measurements was around 20 %.

The Wyoming OPC was later modified by adding another combination of microscope-PMT [Rosen, 1968]. This addition was aimed to avoid false counts due to cosmic ray striking the PMTs, which improved the lower limit of detection. The modified OPC could detect particles with diameter greater than 300 nm and 500 nm. A calibration showed that the OPC response with respect to particle size became ambiguous for particles with diameter between 1,000 nm and 2,000 nm [Pinnick et al., 1973; Pinnick and Hofmann, 1973]. It was also found that the OPC responses largely varied as a function of refractive index for particles larger than 400 nm in diameter.

Four commercial OPCs responses to various sample types, sizes and shapes were studied [Pinnick and Auvermann, 1979]. The four OPCs are the classical scattering aerosol spectrometer probe (CSASP), the active scattering aerosol spectrometer probe

(ASASP), the forward scattering spectrometer probe (FSSP), and the axially scattering spectrometer probe (ASSP). Some characteristics of the four OPCs as stated by the manufacturers are shown in the table 1.6. The study demonstrated that the responses of the four OPCs were affected by the refractive index and shape of samples so the specifications stated by the manufacturers are no longer valid for particular application. In the measurements of spherical particles, the responses of CSASP and ASASP appear to correspond to the theoretical prediction but FSSP and ASSP generated ambiguous results for particles larger than 1,000 nm in diameter. It was found that slightly irregularly shaped particles generated responses comparable to those of spherical particles for CSASP and ASASP while no corresponding measurements were done for FSSP and ASSP. The study results are summarised in Table 1.7.

Table 1.6: Characteristics of the four OPCs as stated by the manufacturers

instrument	**light source**	**light-collecting optics** $\theta_1 - \theta_2$	**flow rate or active area**	**size range* & recommended use stated by manufacturer**
CSASP	5 mW He-Ne laser	$4° - 22°$	$0.15\,\mathrm{cm^3\,s^{-1}}$	440 nm–32,000 nm; Fog, haze, dust, smoke
ASASP	2 mW He-Ne laser (intra-cavity)	$4° - 22°$	$0.1\,\mathrm{cm^3\,s^{-1}}$	170 nm–3,000 nm; Haze, dust, smoke
FSSP	5 mW He-Ne laser	$3° - 13°$	$0.25\,\mathrm{mm^2}$ **	440 nm–44,000 nm; Fog, cloud, dust
ASSP	5 mW He-Ne laser	$4° - 22°$	$0.4\,\mathrm{mm^2}$ **	440 nm–44,000 nm; Fog, cloud, dust

* Size range is defined for particle diameter. Size resolution is ±10% of the maximum of size range.

** The flow rate can be determined by multiplying the active area with the speed of air passing through the active area.

Table 1.7: The calibration results on the size and the resolution of the instruments with various samples. Source: [Pinnick and Auvermann, 1979]

Instrument	The calibration results		
	homogeneous spherical aerosols of uniform composition	homogeneous spherical aerosols of mixed and unknown composition	Irregular particles
CSASP	Size range varies according to particles refractive index. For water droplets, the size range is 460 nm–28,000 nm in diameter. while for dust is 420 nm–100,000 nm. resolution is less than that stated by manufacturer.	size range: 400 nm–100,000 nm in diameter; resolution severely deteriorated for particles bigger than 1,000 nm in diameter.	size range unknown; the responses of slightly irregular particles are similar to spheres of equal area, in the range from 3,000 nm to 8,000 nm of equivalent diameter.
ASASP	The lower limit of size range varies varies according to particles refractive index. The limit in measuring water droplets is 192 nm in diameter. In measuring dust, the limit is 160 nm, in diameter. The size resolution is poor for particles greater than 1,000 nm in diameter.	size range: 100 nm to between 2,000 nm and 3,000 nm; poor size resolution for particles greater than 1,000 nm in diameter.	size range for slightly irregular particles is similar to that of spheres of equal area; resolution deteriorated significantly.
FSSP and ASSP	Size range varies according to particles refractive index. Multi-valued responses are observed for particles larger than 1,000 nm in diameter; resolution is comparable to CSASP	Resolution deteriorated for particles greater than 1,000 nm in diameter.	unknown

1.8 Current development of OPC instruments

Some attempts has been made to further develop OPC instruments. The first is the development of an OPC that measures scattered light in two-dimensional direction known as two-dimensional angular optical scattering (TAOS). It is expected that the size and shape of sampled particles can be retrieved from measured scattered light. The second is the development of an OPC that measure the scattering of two wavelength of light known as dual wavelength optical particle spectrometer (DWOPS). It is expected that the sizing ambiguity is reduced in retrieving particle size using the measured light. The third is the first generation of SPARCLE that measure the pattern of light scattered by single particles. It is expected that the size and refractive index of the single particles can be retrieved based on the patterns.

1.8.1 TAOS

As the name suggests, TAOS measures two-dimensional pattern of light scattered by single particles over large scattering angles. The instrument illuminates single particles with a pulsed green laser with $\lambda = 532$ nm as the particle passes through one focal point of an ellipsoidal mirror. The angularly scattered light is collected by the mirror and focused into a slit to be sensed by a gated image-intensified charge coupled device (ICCD) camera. The ICCD camera is located beyond the second focal point of the mirror.

An experiment to measure atmospheric aerosols using TAOS was carried out based on the scheme shown in Figure 1.11 [Aptowicz et al., 2006]. In the experiment, aerosols were sampled from the air through an inlet installed on the laboratory roof with the flow rate of 770 liter per minute. A virtual impactor was installed as a particle concentrator to concentrate particles whose sizes range from 1,000 nm to 10,000 nm in diameter. The concentrated particles were drawn into a cubical airtight aluminum box with the flow rate of around 1 liter per minute. In the box, the concentrated particles were aerodynamically focused using a conically shaped aerodynamic nozzle. The nozzle was located slightly above the scattering focal volume where the particles were to be illuminated. The aerosol exited the airtight box through a tube located about 1 cm under the scattering focal volume. The experiment measured scattering patterns of around 6000 ambient aerosol particles. Twenty of them are shown in Figure 1.12. In the figure, the intensity of the patterns has been adjusted for clarity. Some images, such as images 1, 8, 15, and 20, demonstrate recognisable patterns that are likely to be generated from spherical particles. Other patterns had yet to be associated with a particular shape. The retrieval of particle properties based on measured patterns is still under development.

(a) Cross-sectional view

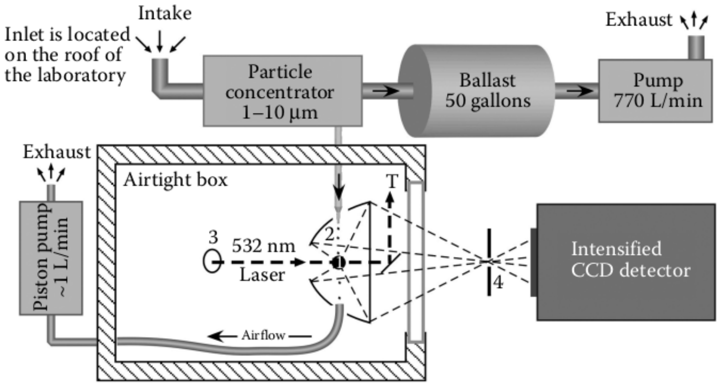

(b) Bird's eye view

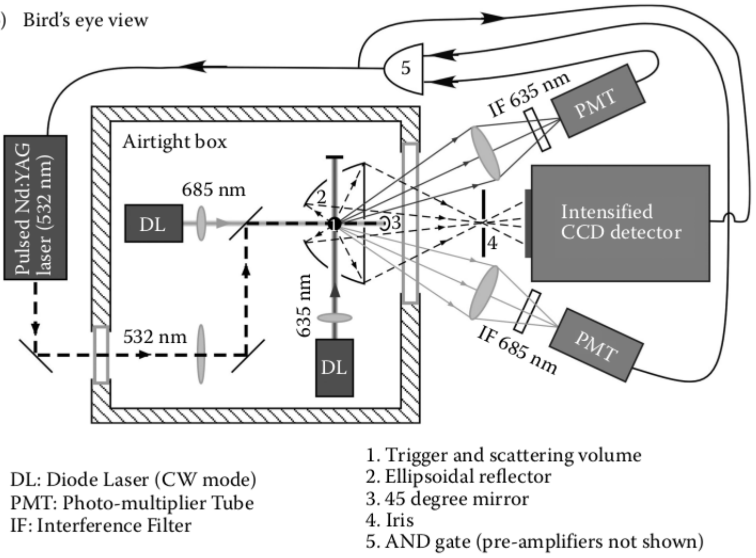

Figure 1.11: Schematic of a TAOS prototype measuring atmospheric aerosol particles. (a) Aerosols are sampled through a concentrator and a small portion of the aerosols flow into an airtight box through an aerodynamic focusing nozzle. (b) Single particles flow from the nozzle, traverse the intersection of crossed laser beams and are subsequently illuminated by a pulsed green laser [Aptowicz et al., 2006]

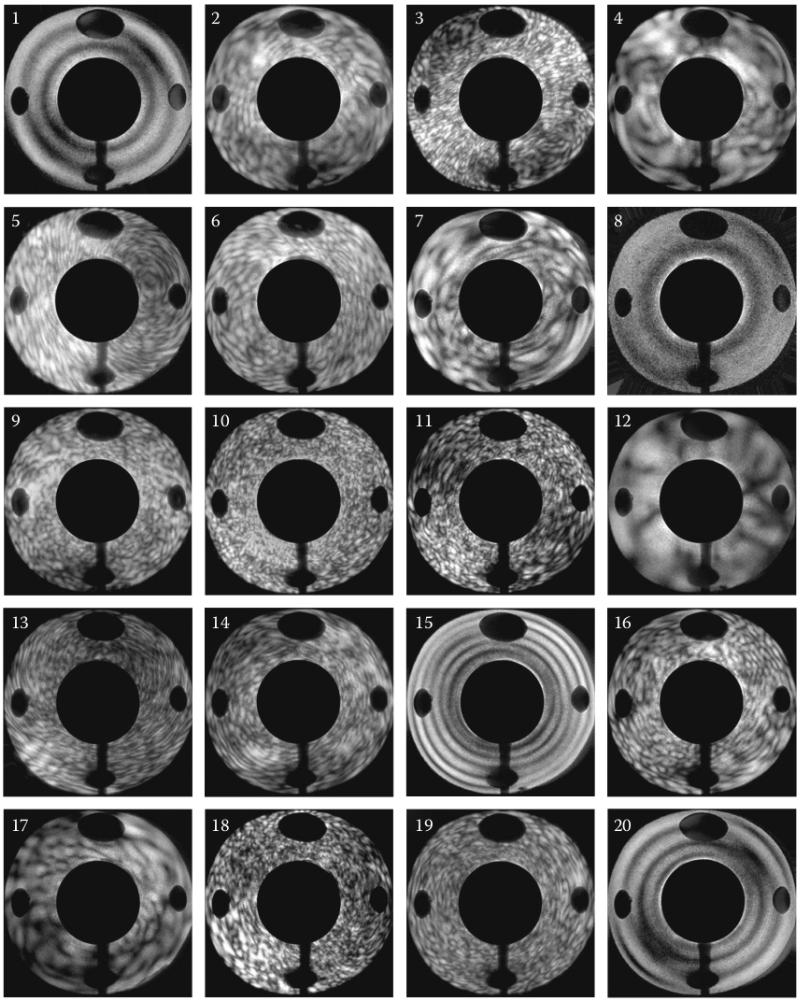

Figure 1.12: TAOS patterns of single atmospheric aerosol particles. The patterns are confined to a circular shape. The black circular shape appeared consistently in all of the patterns related to the regions where the scattered light is not directed into the detector. The images are taken from [Aptowicz et al., 2006]

1.8.2 DWOPS

DWOPS is designed to collect the light scattered by single particles using the forward and backward scattered light from two illumination wavelengths. The scattered light can be used to retrieve the size and refractive index of the single particles [Szymanski et al., 2002]. The design uses two light sources to illuminate single particles and installs beam splitters to split the scattered light according to their wavelengths. A paraboloidal mirror is installed to collect the light scattered in forward and backward region. The schematic of the design is shown in Figure 1.13. Numerical calculations illustrate that the sizing accuracy of the instrument deviates as a function of particle size, with the deviation less than 10% of true sizes, while the determination of complex refractive index distributed around 20% of true refractive index for both real and imaginary parts in the measurement of particles whose size between 100 nm and 10,000 nm in diameter, the real part of the refractive index from 1.2 to 2 and the imaginary part of the refractive index from 0.0 to 1.0 [Nagy et al., 2007]. An experiment to test the numerical calculation was performed. Prior to the experiment, scale factors that link between the light scattered by particles and the instrument responses were built based on the measurement of instruments responses to PSLs whose sizes are 500 nm and 2,000 nm. Then, the experiment proceeded by measuring spherical homogeneous particles whose sizes of between 589 nm and 1,000 nm in diameter, the real part of the refractive index from 1.45 to 1.70, and the imaginary part of the refractive index from 0 to 0.32. It is reported that the results of the experiment confirmed the numerical calculations.

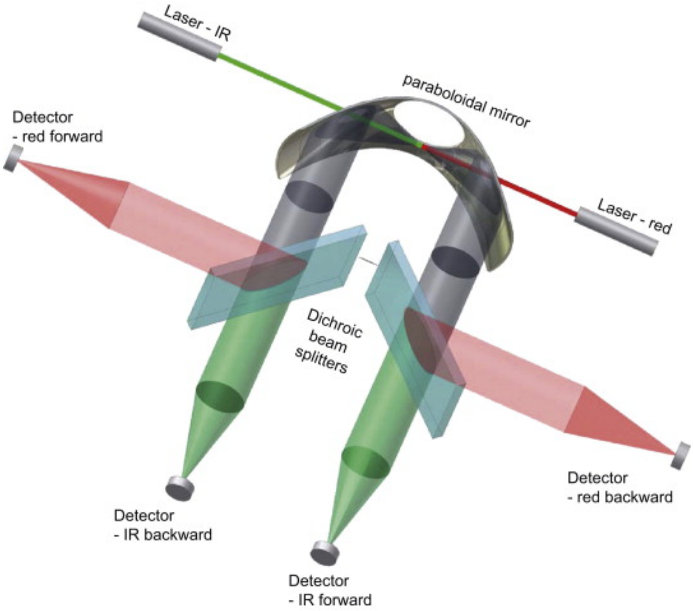

Figure 1.13: Schematic diagram of DWOPS. Two laser sources are used to illuminate a particle. The light scattered on the forward and the backward region is collected by a paraboloidal mirror. The collected light is then split according to the light source wavelengths and measured by detectors. The images are taken from [Szymanski et al., 2009]

1.8.3 The first generation of SPARCLE

The first generation of SPARCLE was designed to determine the size and refractive index of single particles based on the angularly resolved light scattered by the single particles [Thomas, 2003]. The design is suitable for use in small balloon-borne *in situ* measurements. The main target of the first generation instrument is stratospheric aerosols.

The detection system in the instrument has two measurement goals. The goals are to be able to measure the smallest possible single particles and to capture the pattern of light scattered by single particles to a high degree of precision. These goals require the use of two sensors, one devoted to each goal.

The two sensors in the instrument are described as follows. A PMT is used as the first sensor and collects the light scattered across a solid angle of $0.94\,\mathrm{sr}$ centered at 90° in both scattering and azimuth angles. The second sensor is a solid state linear array sensor called linear diode array (LDA). The LDA measures light scattered in 512 points across the scattering angles $45^\circ - 135^\circ$. The schematic of the design can be seen in Figure 1.14.

The measurements by the sensors are done sequentially. The PMT measures the intensity of light in the scattering volume continuously and the measured intensity can indicate the presence of single particles in the scattering volume. Once single particles are detected, the LDA is triggered to start measurements.

The LDA performed three successive measurements. The first and second measurements measure the light scattered by single particles, while the third measures the background signal. The scattering pattern is constructed by adding the first two measurements and subtracting twice of the background signal. An example of the scattering pattern can be seen in Figure 1.15.

The instrument was calibrated to measure aerosol particles which size and refractive index are known. The aerosols used in the calibration are monodisperse aerosols generated by aerosolised glycerol solution. An APS was installed in parallel with the instrument to monitor the size distribution of the monodisperse aerosols. The PMT responses to some of the monodisperse aerosols are shown in Figure 1.16. The numbers shown on top of each plot are the corresponding mean radii of the monodisperse aerosols particles and PMT response.

As shown in the figure, some of the PMT responses are distributed normally such as those shown in Figure 1.16 (a) and (c), while others are not normally distributed such as those shown in Figure 1.16(b) and (d). This variation of distribution might be due to several causes such as noise on the PMT measurements, size variation of the

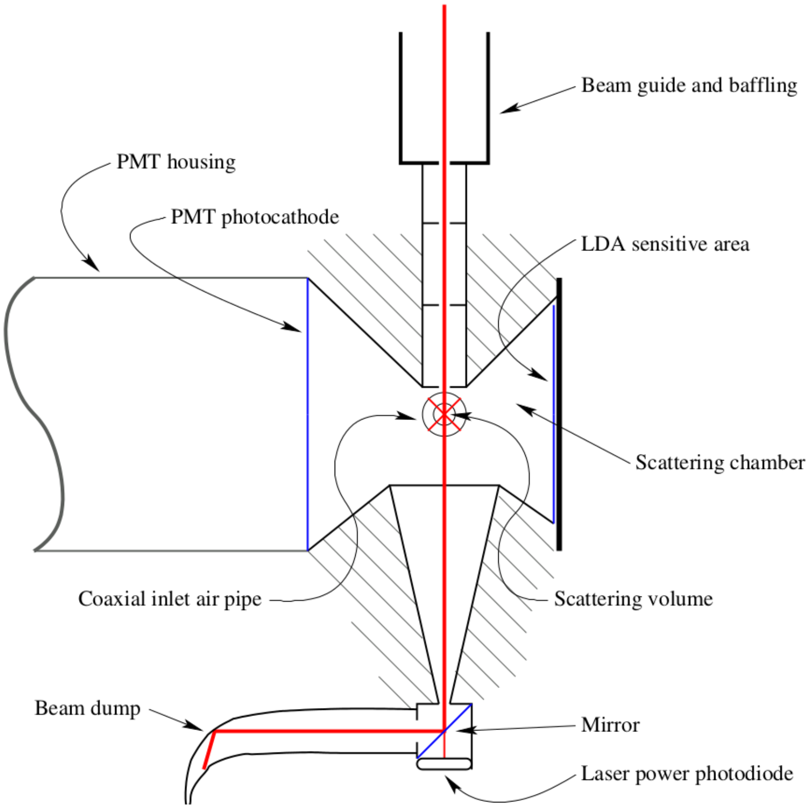

Figure 1.14: Schematic view of the scattering chamber of the first generation of SPARCLE. Aerosol particles are drawn to the scattering volume through coaxial inlet air pipe. In the scattering volume, particles are illuminated by a red laser beam. The light scattered by the particles are measured by the PMT and the LDA. A laser power photodiode is installed to monitor the laser power. At the end of the optical system, the laser beam is directed to the beam dump. The images are taken from [Thomas, 2003]

aerosol particles, non-Gaussian profile of the laser beam, and error caused by circular cross section of the sample air flow.

A new retrieval scheme was developed to retrieve the parameters of the particles size and refractive index. The retrieval scheme is a combination of simulated annealing and the Lavenberg-Marquardt optimal estimation method. At first, simulated annealing is tested for a wide range of parameters. Based on the simulation results, some possible solutions were selected. Then the Lavenberg-Marquardt is applied to these solutions to find the optimal solution.

Two retrievals were done. The purpose of the first retrieval was to obtain two parameters: the particle size and the real part of the particle refractive index. In this retrieval, the imaginary part of the particle refractive index was defined by the

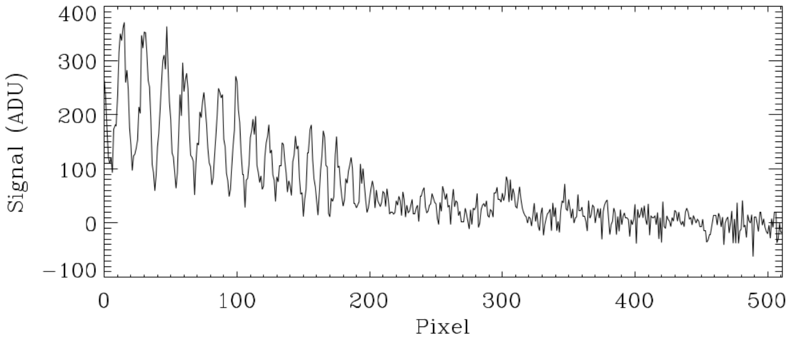

Figure 1.15: One example of an LDA measurement result. The images is taken from [Thomas, 2003]

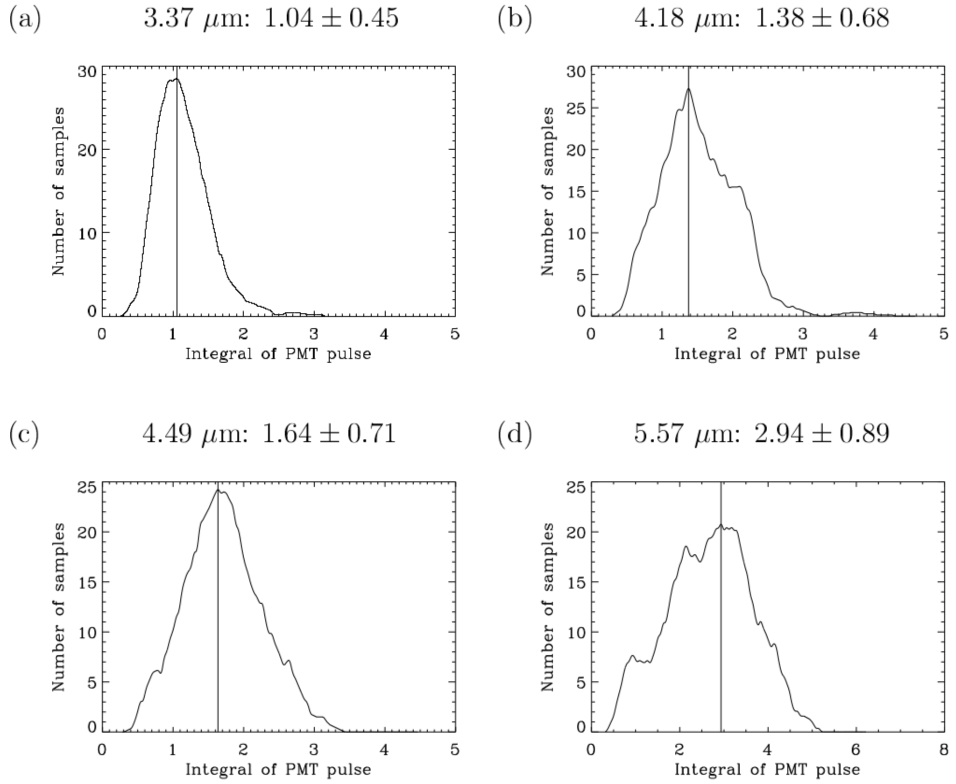
(a) 3.37 μm: 1.04 ± 0.45

(b) 4.18 μm: 1.38 ± 0.68

(c) 4.49 μm: 1.64 ± 0.71

(d) 5.57 μm: 2.94 ± 0.89

Figure 1.16: The distribution of the PMT outputs for the measurement of glycerol particles. On top of each plot, the corresponding particle radii and PMT responses are shown. The images are taken from [Thomas, 2003]

glycerol specification. The second retrieval was to retrieve three parameters: particle size, and both of the real and imaginary part of the particle refractive index. It was found that the second retrieval was less successful than the first.

The first retrieval appears to agree with the expected results. Particle size retrieved from the two retrievals distributed in nearly the same distribution as that of the corresponding particle size measured by the APS. Some of the retrieved sizes are shown in Figure 1.17. Meanwhile, the retrieved refractive index for particles larger than 5.5 µm in radii are distributed around the expected value of 1.473. Below this size, the retrieved refractive index is strongly influenced by the *a priori* estimation used in the retrieval.

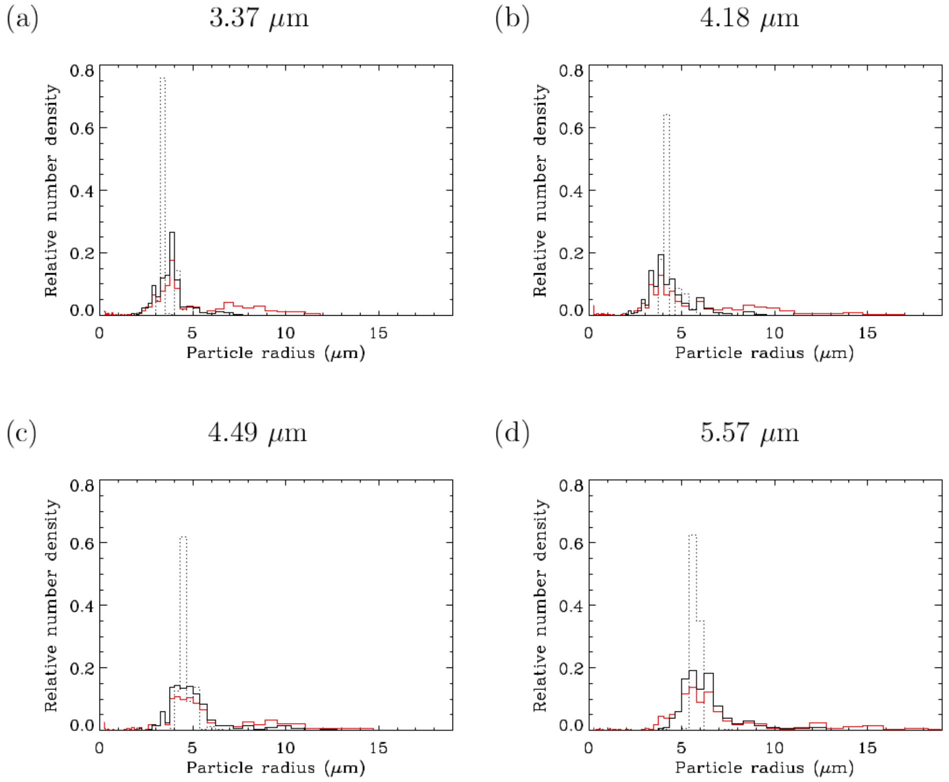

Figure 1.17: The distribution of the retrieval results based on the measurements of glycerol particles with sizes: 3.37 µm, 4.18 µm, 4.49 µm, and 5.57 µm in radii. The retrieval results are plotted in red. Some of the retrieval results with low cost function are selected and plotted in black. The size distribution measured by the APS are shown in dotted lines. The images is taken from [Thomas, 2003]

1.9 Summary

This study investigates the feasibility of the second generation of SPARCLE, an *in situ* instrument to retrieve the size and refractive index of aerosol particles. This feature is unique since most of *in situ* optically based instruments assume the refractive index of measured particles to give size-estimates. It is expected that the *in situ* measurement of particle size and refractive index improves the understanding of the effect of atmospheric aerosols to the Earth's radiative forcing. The measurement is also expected to have higher accuracy in particle sizing than current available particle sizer so that the impact of aerosols to human health can be better studied. SPARCLE measurement goals are to retrieve the size and refractive index of particles whose sizes range from 500 nm to 2,500 nm in diameter. This size range is within the range of the accumulation mode of trophospheric size distribution.

Aerosols is a suspension of solid or liquid particles in a gas. Aerosols can be generated either naturally or from anthropogenic sources. The shape of aerosol particles vary from spherical to arbitrary shapes. The size of aerosol particles spans from a few nanometers to tens of micrometers. The knowledge of aerosol size distribution can offer an explanation of the sources of the aerosols. Another aerosol property is particle refractive index which summarised the interaction between particles and the light which propagating in the particles: the real part of refractive index determines the speed of the light while the imaginary part determines the decay of the light. Physical and chemical processes in the atmosphere can change properties of aerosols. The processes involve mass transfer to or from particles. This transfer can be the result of molecular transfer between particles gas molecules such as in: condensation, evaporation, nucleation and chemical reaction, or it may result of inter-particle mass transfer such as in coagulation. Aerosol particles have a high level of surface area to mass ratio. This property allows aerosol particles to participate actively in many kinds of chemical interaction between gas molecules and aerosol particles.

Aerosols are introduced into the troposphere either directly or indirectly. Main tropospheric aerosols from natural processes such as terrestrial dust, volcanic ash and sea spray are introduced directly to the troposphere. Aerosols can be indirectly introduced into the troposphere through the gas to particle conversion such as in the oxidation of atmospheric sulphuric gases. Tropospheric aerosols are distributed heterogeneously in time, location and altitude. The concentration of tropospheric aerosols in particular area can change within tens of minutes. Spatially, tropospheric aerosol concentration may vary in the scale of a few kilometers horizontally and a few tens of meters vertically. The Whitby model describes that the distribution of tropospheric aerosols can be characterised by three main modes: nucleation, accumulation and coarse mode. Particles in each modes are different in the formation and removal processes.

There are variety of methods and instruments which scientist and engineers can use to perform *in situ* aerosol measurements. Each instrument provides measurements for particular properties and most instruments only operate within a certain particle size range. Due to these limitations, it is common that more than one instrument is used in an aerosol measurement campaign to reach measurement goals. Instruments to measure aerosol can be classified into two general types: aerosol sampling and direct-reading instruments. The most common sampling technique involves the use of filters to collect aerosol particles. Widely used direct reading instrument is optical particle counters which retrieve particle size based on the light scattered by particles.

Errors in aerosol measurements should be recognised to be able to assess the interpretation and usefulness of the measurement data. Errors can be introduced due to particle lost in sampling and transport lines, the limited sensitivity of sensors deployed in instruments, of the insufficient number of samples. As a result of these types of errors, measured aerosol properties may not reflect the original aerosol properties.

Despite years of development, optical particle counters suffer from ambiguity in particle sizing, mainly due to particle optical properties and particle shape variations. Early development of OPCs showed this ambiguity with high ambiguity for particles larger than 1,000 nm. Three types of OPCs with the purpose of overcoming the ambiguity were recently developed. The first is an OPC that measure two-dimensional pattern of light scattered by particles over large scattering angels. Various patterns from ambient measurements had been measured. The retrieval of particle properties based on the patterns is still under development. The second is an OPC that measure light scattered by single particles using the forward and backward scattered light from two illumination wavelengths. The experiments to test the instrument were performed. Prior to the experiment, scale factors were build based on the responses of the instrument to PSLs with the sizes of 500 nm and 2,000 nm. The results suggest that, in general, the uncertainty of retrieved sizes are less than 10% of real particle size. The third is the first generation of SPARCLE. It was designed do determine the size and refractive index of single particles based on the angularly resolved light scattered by the single particles based on the pattern of scattering light. The calibration of the instrument was done by measuring the responses of the instruments to particles whose sizes are larger than 3.37 µm in radii. The retrieval of particle size and refractive index using the responses based on an *a priory* knowledge of the particles. The retrieved sizes showed a good agreement with real particle size. The retrieved refractive indices for particles with radii larger than 5.5 µm were in a good agreement with real refractive index while those retrieved for smaller particles were strongly influenced by the *a priory*.

Chapter 2

SPARCLE design

The calibration of the original SPARCLE instrument has shown that the SPARCLE design can be applied to retrieve particle size and refractive index, although modifications are needed for it to be applicable in a tropospheric environment and to improve its performance. For example, the original SPARCLE was designed to sample air in the stratosphere which particle number concentration is typically less than 100 particles cm^{-3} while the concentration in the troposphere can be higher than 1000 particles cm^{-3}. Another example is that the calibration of the original SPARCLE showed that the ability of the LDA in capturing light scattering patterns was limited to particles larger than 6,000 nm in diameter, much bigger than particles in the accumulation mode of the troposphere. To solve these issues, some modifications are applied to the three systems that compose the original SPARCLE. These three systems are: the detection system, the sample air delivery system and the data recording system.

2.1 The detection system

The detection system is responsible for both the illumination of single particles in the sensing volume and the measurement of the light they scatter. The design of the detection system of the original SPARCLE is still used in the second generation SPARCLE. The system includes a light source, a sensing volume and two detectors. The two detectors are composed of:

- a detector with high sensitivity and high temporal resolution used mainly to detect the presence of single particles in the sensing volume. The sensitivity should enable SPARCLE to detect sub-micron particles while the temporal resolution should be much shorter than the transit time of particles in the scattering volume,

- a detector with high spatial resolution to capture the pattern of scattered light.

The main considerations when designing this system are:

- to match the light source and the two-detectors' performance with the required measurement goals,
- to design the sensing volume which maximise illumination time and minimise coincidence errors.

To achieve the measurement goals, the patterns of scattering light measured by the detection system should be well-resolved. Well-resolved scattering patterns are determined by the ratio between the scattering intensity and the measurement errors introduced by the detection system. When the ratio is higher, the scattering pattern is more likely to be well-resolved. To obtain a high ratio between the scattering intensity and the errors, parameters that need to be considered are:

- the power and the wavelength of illuminating light,
- the duration of illumination time,
- the sensitivity and the measurement errors of the detectors,
- the distance between single particles and the detectors.

In designing a sensing volume, the influence of its dimension to coincidence errors and illumination time should be considered. For example, a smaller sensing volume reduces coincidence errors since the errors are proportional to the dimension. However, the smaller volume might also shorten illumination time.

2.1.1 The light source selection

Several criteria need to be considered in the light source selection. The criteria are:

- the light source should have a narrow wavelength band. This is necessary to ensure high resolution scattering patterns. According to Mie theory, the scattering patterns of light scattered by single particles depend on the wavelength of the light. Illuminating single particles by a broad range of wavelengths results in the accumulation of several scattering patterns each generated due to illuminating the single particles by individual wavelength from the broad range of wavelengths. The accumulation can smear out the fine details of the patterns,

- the light source should produce a high intensity of light. This provides the ability to detect small particles and to generate a strong intensity of light scattering patterns,

- the light source should produce a well-collimated beam. A well-collimated beam can be easily aligned to prevent the beam from reaching the detectors either directly or through the reflection of instrument components. A well collimated beam limits the variation of the scattering angles of light scattered to particular points due to the variation in the direction of the incident light. The small variation of the angles can lead to a good angular resolution of scattering patterns,

- the light source should be compact and require low energy to operate. This feature is crucial in a compact *in situ* instrument.

One type of light source that can satisfy these criteria are laser diodes. Compared with other lasers, laser diodes have unique characteristics which provide several advantages, they are:

- available in various wavelengths from ultraviolet to infrared,

- available in various output powers from mW to several W,

- available with compact size modules that include a laser diode, collimating lens, a circuit board and a housing,

- long lifetime typically up to 10,000 hours of operation.

On the other hand, laser diodes do have some drawbacks, such as the difficulty in having a perfectly collimated beam and the sensitivity of output power to temperature. However, the advantages of laser diodes make them the most suitable for this application. The original SPARCLE didn't use laser diodes due to the high price of laser diodes at that time. A 514.5 nm argon gas laser was used to test the original SPARCLE. Since then, the price of laser diodes has decreased significantly and so it was decided to use laser diodes in the second generation SPARCLE.

The selection for the particular wavelength and output power of laser diodes is based on two main considerations: its ability to produce a high intensity of scattered light and its practicality of alignment with other SPARCLE components. Based on Mie theory, the first consideration requires the use of shorter wavelengths to ensure sensitivity for smaller particles and a higher illuminating power to produce higher

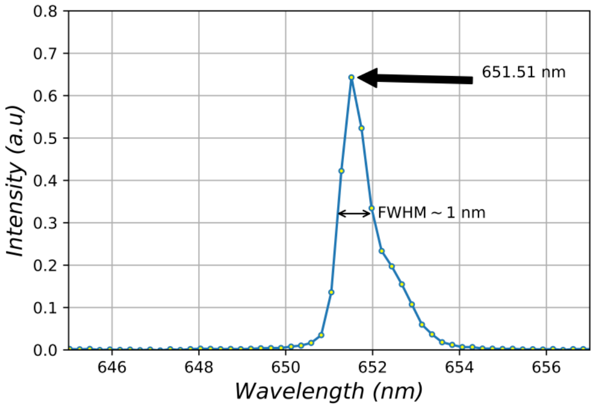

Figure 2.1: The wavelength of the laser diode used in the second generation SPARCLE measured using Thorlabs CCS200M Spectrometer. The wavelength peaked at 651.51 nm with the FWHM around 1 nm.

intensity of scattered light. One option to satisfy this requirement is to select a high output power blue laser diode. However, due to safety reasons, it is more practical to use a red laser diode with a moderate output power. The laser diode used in this work is the CPS65AP05-SE laser diode, emitting light whose wavelength is 650 nm and output power is around 4 mW. The laser comes in a module with pre-installed collimating lens, resulting in a nearly elliptical collimated beam with a major axis of 6 mm and a minor axis of 3 mm. A measurement of the laser diode wavelength using Thorlabs CCS200M Spectrometer shows that the wavelength peaked at 651.51 nm with the full width half maximum (FWHM) being around 1 nm, as depicted in Figure 2.1. The measurement of the laser output power results in 3.9 mW of power, as measured using LaserCheck power meter produced by Coherent Inc. The observation of the beam polarization using Thorlabs Calcite Polarizer GTH10M-A indicates that the beam is polarised in the major axis of the elliptical beam.

2.1.2 The two-detectors selection

The first detector should have both an extremely high sensitivity to measure low level of light scattered by small single particles and a high temporal resolution to indicate the transit time of single particles in the sensing volume. These requirements lead to the selection of a PMT as the detector of choice due to its high conversion efficiency of photons into photoelectrons and its high amplification or gain of the photoelectrons.

In the original SPARCLE, Electron Tubes PMT model 9828B was used and it showed the ability to detect particles transiting in the sensing volume. The PMT can detect light with wavelength between 180 nm and 870 nm with the PMT conversion efficiency at $\lambda = 400\,\text{nm}$ being around 21%. The PMT amplified photoelectrons up to 10^6 times. The PMT has a fast time response: the transit time of photoelectrons to reach the PMT's anode was 80 ns. This features enabled the original SPARCLE to capture light scattering patterns while single particles were still transiting in the sensing volume. The calibration of the original SPARCLE shows that it was capable of capturing the patterns of light scattered by particles whose size is as small as 6,700 nm.

A similar type of detector is used in the second generation SPARCLE. The selected PMT is the Electron Tube PMT model 9124B. The PMT can detect light with wavelength between 280 nm and 680 nm with the conversion efficiency at $\lambda = 400\,\text{nm}$ being around 25%. The amplification is up to 10^6 times. The response time of the PMT is 33 ns.

The second detector should have both a high spatial resolution and high sensitivity to capture fine details of light scattering patterns as well as the ability to integrate scattering light in a relatively short period of time to reduce coincidence errors. The options for this detector are either LDA or charge-coupled devices (CCDs). These devices are in principle very similar: they both collect charges generated from absorbed photons in spatially distributed photosensitive elements. The charges are subsequently read off. The difference between the two sensors is in the design of the photosensitive elements themselves: in a CCD, the charge is collected by a p-n junction within a layer of doped silicon, while an LDA uses a MOS capacitor to generate the required depletion layer within the silicon.

In the original SPARCLE, an LDA series S5461-512Q C-MOS Linear Image Sensor manufactured by Hamamatsu was used and proved to be problematic. The LDA had 512 pixels and each pixel collected charges sequentially. The signal of each pixel was continually sent to an analog-to-digital converter with an indication of the start and the end of the 512-pixels data set. This scheme proved to be problematic since there was no assurance that all the pixels in the 512-pixels data set collected scattered light. As a consequence, a combination of a few sets of 512-pixels-data were needed to reconstruct the scattering light patterns; a combination of some sets coincided with single particles transit in the sensing volume and a set of background only. It was decided that three sets of 512-pixels-data were needed, with the first two containing scattered light patterns and the third containing background only. With each set taking around 5,000 µs, the expected interval between single particles coming to the sensing volume to prevent coincidence errors is 15,000 µs. This was a relatively long period and the calibration showed that the coincidence errors were at least a third of the measured data.

The development of electronic shutters in CCD line sensors offers a solution for the problem described above. Electronic shutters can determine when the pixels in CCD line sensors collect charges simultaneously. Combined with a triggering system to trigger the electronic shutters, a single measurement of light scattering patterns can be realised. In addition, a short integration time, as short as a few µs, can be found in commercial CCDs. For these reasons, a CCD line sensor is selected as a second detector in the second generation SPARCLE. The CCD device selected is LC1-USB CCD camera produced by Thorlabs. The camera contains a CCD linear sensor ILX526A, the number of pixels is 3,000 and the sensitivity to measure light whose wavelength is 660 nm is 3,000 $\mathrm{V\,lux^{-1}\,s^{-1}}$. The integration time of the CCD camera ranges from 1 µs to 200 ms with an electronic shutter function. The manufacturer did not specify the quantum efficiency of the line sensor. The quantum efficiency was measured by Labusov and the result indicates that the efficiency of ILX526A line sensors is about 35% at $\lambda = 650\,\mathrm{nm}$ [Labusov et al., 2008].

2.1.3 Designing the sensing volume

The sensing volume is the volume where single particles are illuminated by the laser beam. The dimensions of a sensing volume can determines the number of coincidence errors and, for this reason, the main consideration in designing the sensing volume is to minimise the errors. The sensing volume in SPARCLE is defined by the volume of the intersection between sample air flow exiting the SPARCLE sampling pipe and laser beam. If the air flow is assumed not to expand or contract as it passes across the sensing volume, it can be described as a cylindrical flow whose radius is the same as the sampling pipe. To illuminate transiting particles in all probable particle flow paths inside this cylindrical flow, it is necessary to have a laser beam which illuminates all parts of the cylinder's cross section. Also, it is advantageous for further analysis to have a rectangular laser beam cross section so all transiting particles have the same path length. The diagram of the sensing volume is shown in Figure 2.2 and, based on the figure, the sensing volume, $\mathcal{V}_{\mathrm{sv}}$, can be calculated as

$$\mathcal{V}_{\mathrm{sv}} = \pi\, r^2\, h, \tag{2.1}$$

where r is the radius of the inlet and h is the height of the laser beam indicated in the figure.

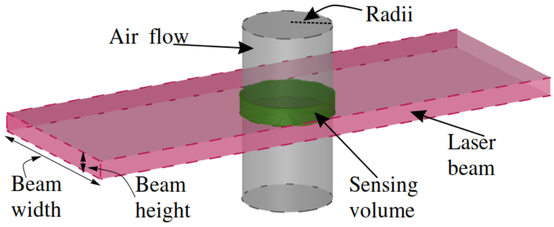

Figure 2.2: The SPARCLE sensing volume governed by the intersection between the SPARCLE sample air flow and laser beam. The beam, air flow and sensing volume are indicated by red, grey and green, respectively.

A statistical model of coincidence errors taking place in sensing volumes has been described by Wales and Wilson [Wales and Wilson, 1961]. Wales and Wilson define the errors as the events when two or more particles transit in sensing volumes simultaneously. They modelled counting operations involving a sensing volume as discrete events where the sensing volume is being filled, counted and emptied. Based on this model, the counting operation of N number particles contained in an air sample with the volume $\mathcal{V}$ can be regarded as the counting operation on $\mathcal{V}$ by sensing volume $\mathcal{V}_{\text{sv}}$ with the number of trials $\frac{\mathcal{V}}{\mathcal{V}_{\text{sv}}}$. Observed counts, $\mathcal{N}$, can deviate from true counts, N, due to the presence of coincidence errors and can be expressed as

$$\mathcal{N} = \frac{1}{\mathcal{K}}\left[1 - e^{-\mathcal{K}N}\right], \tag{2.2}$$

where $\mathcal{K} = \frac{\mathcal{V}_{\text{sv}}}{\mathcal{V}}$. Based on Equation 2.2, coincident errors can be minimised by smaller values of either $\mathcal{K}$ or N.

The sensing volume of the second generation SPARCLE is designed according to Figure 2.2 and the observed counts of SPARCLE in counting particles can be calculated using a combination of equations 2.1 and 2.2. The equations are used to illustrate counts observed by SPARCLE in sampling various particle number concentrations of air samples, with two options of sampling pipe radius: 0.5 mm and 0.1 mm. In the illustration the beam height is set to be 0.4 mm. The results are listed in Table 2.1. According to the table, the coincidence errors of less than 15% of true counts for the bigger sampling pipe can be achieved when the concentration of air sample is 1,000 particles cm^{-3} or less. For the smaller sampling pipe, the coincidence error is still very low even when sampling an air sample with the concentration 10,000 particles cm^{-3}. Understanding coincidence errors is important as it provides a method to correct the measured particle density, i.e. to estimate the true particle density.

The errors expected from the design described above are lower than that of the original SPARCLE. The sensing volume of the original SPARCLE was governed by the intersection of cylinder-shaped air flow and cylinder-shaped laser beam with the radii 1.0 mm and 0.5 mm respectively, resulting in 1.5 mm^3 sensing volume. The calibration of the original SPARCLE showed that more than 30% of coincidence errors were observed in sampling an air sample with the concentration of around 2 particles cm^{-3}.

Table 2.1: The calculation of counts observed by SPARCLE in sampling various concentrations of air samples. The calculation was done for two different sensing volumes. In the calculation, it is assumed that the beam height is 0.4 mm and the volumes of all air samples are 1 cm^3. Each volume contains N number of particles.

sampling pipe radii $r = 0.5\,\text{mm}$ sensing volume $\mathcal{V}_{\text{sv}} \approx 0.3\,\text{mm}^3$ air sample volume = 1 cm^3			
True count N	Observed $\mathcal{N}$	Ratio $\mathcal{N}/N$	Err (%)
10	9.9	0.99	< 1
100	98.4	0.98	< 2
1,000	858.2	0.86	< 15
10,000	3,045.5	0.30	< 70

sampling pipe radii $r = 0.1\,\text{mm}$ sensing volume $\mathcal{V}_{\text{sv}} \approx 0.01\,\text{mm}^3$ air sample volume= 1 cm^3			
True count N	Observed $\mathcal{N}$	Ratio $\mathcal{N}/N$	Err (%)
10	9.9	0.99	< 1
100	99.9	0.99	< 1
1,000	993.7	0.99	< 1
10,000	9,397.2	0.94	< 7

2.1.4 Laser beam manipulation

The elliptical shape of the laser beam is an undesirable characteristic and needs to be manipulated to create the thin rectangular beam described in the previous section. In SPARCLE, the manipulation can be done by using a combination of a rectangular slit and an aspheric lens as shown in Figure 2.3. The manipulation can be described as follows: first, the elliptical beam is arranged such that the major axis of the beam is along the y axis. Second, the beam is directed through the slit whose width is 1.5 mm to stop a portion of the beam on both sides, resulting in a nearly rectangular beam with dimensions of 1.5 mm × 6 mm. Third, an aspheric lens with a focal point of 170 mm is used to compress the beam in the y direction resulting in a thin rectangular beam with dimensions of approximately 1.5 mm × 0.4 mm at around the focal point of the lens. The beam profiles can be seen in the inset of Figure 2.3. The actual beam cross-section used in SPARCLE may deviate from that shown in the figure since laser diode beam diverges along the major and minor axis of the beam. The detail of the cross-section of the beam used in SPARCLE will be discussed in Chapter 3.

Additional settings for the laser manipulations are installed to reduce stray light in the optical system. An optional slit is installed before chamber window 1 to remove unwanted divergent beam. The two window chambers are installed at roughly 45° with respect to the beam propagation direction to prevent the beam from being reflected along the optical axis. Beyond the focal point, the beam diverges and a beam stop is installed to prevent the beam from reflecting back to the sensing volume. The selection of the focal length of the lens is based on the preference to have a thin beam along its propagation inside the scattering chamber in order to reduce the amount of light scattered by the air inside the chamber. A thin beam also ensures that the focused beam illuminating single particles is nearly collimated. In SPARCLE, the beam path in the scattering chamber is around 30 mm and hence, a lens with a focal length longer than 30 mm is essential.

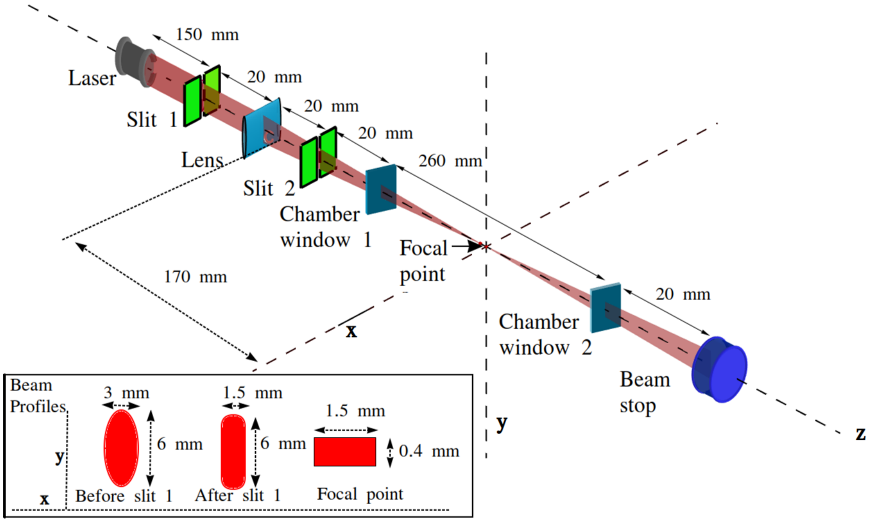

Figure 2.3: The laser beam manipulation in SPARCLE. In the inset, beam profiles in three different positions are shown: before slit 1, after slit 1 and at focal point.

2.1.5 The arrangement of the detection system

In general, the arrangement of the detection system in the second generation SPARCLE follows that of the original SPARCLE: the two detectors are placed close to the sensing volume without the use of additional optics. The arrangement is shown in Figure 2.4. While this approach may be prone to stray light, it is preferable due to its simplicity. The two detectors are located in the opposite direction from the sensing volume with their axis of symmetry crossing the sensing volume, and are at right angles to both the sample air flow and the laser beam. The two-detectors are located at roughly the same distance from the sensing volume, which is around 6 mm. This distance is shorter than that in the detection system of the original SPARCLE. In the original SPARLCE, the PMT and the LDA were located around 21 mm and 12 mm respectively. The shorter distance ensures that higher intensity of scattering light reach the detectors as the intensity is inversely proportional to the square of the distance. The shorter distance also ensures the PMT collects light over a wider solid angle than that collected in the original SPARCLE. The solid angle subtended by the PMT in the current design is around 5.8 sr while that in the original SPARCLE is around 0.94 sr. In the current design, the solid angle is represented by an arc of angles from $\phi_1 = 40°$ to $\phi_2 = 140°$ swept around a sphere from $\theta_1 = 20°$ to $\theta_2 = 160°$ where θ and ϕ are scattering angles and azimuths angles respectively, as defined in the first chapter. The short distance between scattering particles and the CCD camera allow the collection of scattering light over a broad range of scattering angles. The scattering angles subtended by the pixels of the CCD camera is from $\theta_1 = 37°$ to $\theta_2 = 144°$ and the azimuth angle of all pixels is $\phi = 90°$. The values of the azimuth angles are due to the placement of the pixels on the plane perpendicular with the polarisation plane of the laser. The variation of the azimuth angles and the scattering angles over individual pixels is approximated to be extremely small since the solid angle of scattering light subtended by individual pixels is also extremely small.

Another setting shown in the figure is the arrangement of a laser power monitoring unit and a signal processing unit. A laser power monitoring unit is installed to monitor the stability of the laser power by measuring a small portion of laser beam reflected by chamber window 1 indicated in the figure. A signal processing unit is installed to trigger the CCD camera based on the signals continuously sent by the PMT.

The summary of the detection system criteria, selection and design can be seen in Table 2.2.

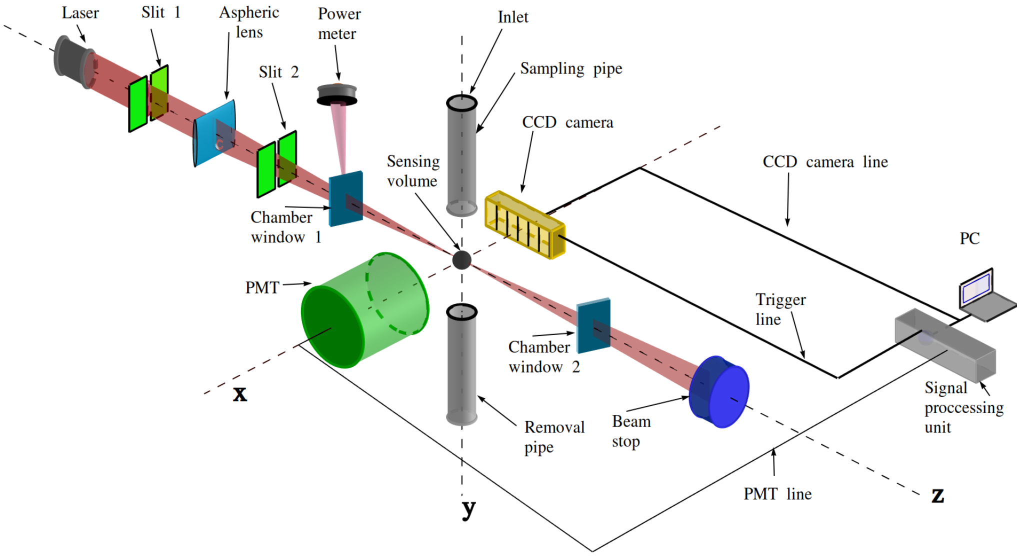

Figure 2.4: The detection system of SPARCLE.

Instruments or parts	Criteria	Instrument selected or parts manipulation
Light source	Output has narrow wavelength bandwidth, high intensity, and well-collimated. Dimension should be compact. Requires low energy to operate	Laser diode modules CPS65AP05-SE $\lambda = 651\,\text{nm}$; Output power : 4 mW; The beam is collimated.
PMT	Should have an extremely high sensitivity and high temporal resolution:	PMT 9124B series produced by Electronic Tube.inc; Quantum efficiency ($\lambda : 650\,\text{nm}$) $\approx 25\%$ Gain is set to nearly 10^5 times.
CCD camera	Should have high sensitivity and high spatial resolution:	LC1-USB CCD camera produced by Thorlabs. Pixel number & pitch : 3000 & $7\,\mu\text{m} \times 200\,\mu\text{m}$ Quantum eff. $\approx 35\%$ Sensitivity : $300\,\text{V lux s}^{-1} - 3000\,\text{V lux s}^{-1}$
Laser beam	The shape should be a thin rectangular beam.	Shaped by slits and cylinder lens. The focal point of the lens is 170 mm. The cross-section of the beam is $0.4\,\text{mm} \times 2\,\text{mm}$
Sensing volume	Dimension should be relatively small The arrangement ensures that all possible particle paths should be illuminated	The dimension is $\pi\, r^2\, h$ where r and h are the sampling pipe radii and beam height, respectively.

Table 2.2: A summary of the detection system selection

2.1.6 The mapping of pixels to scattering angles

Since the variation of scattering angles and azimuth angles over the individual pixels are extremely small, scattering light intensity is modelled homogeneously over a pixel. The variations are $\Delta\theta \approx 10^{-3}$ and $\Delta\phi \approx 30 \times 10^{-3}$ calculated based on the dimensions of each pixel: 7 µm × 200 µm, and the line sensor is located parallel to the z axis with the distance to the z axis around 7 mm. With this model, the individual pixels measure light scattered at particular scattering angles. The individual pixels can be mapped to the corresponding scattering angles since the scattering angles are the angle between the location vector of the individual pixels relative to scattering particles and the propagation direction of illuminating light. The calculation of the location vector is based on the following considerations:

- the distance between the CCD camera's optical window with the z axis is 6 mm and the sensor line within the CCD camera is located around 0.6 mm from the window,
- the variation of the scattering angle and azimuth angle over each pixel,
- there are 3,000 pixels in the CCD camera and these pixels are modelled as 3,000 points with the distance between two consecutive points is 7 µm,
- the pixels were numbered between 0 and 2,999 and they were lined up parallel to the z axis,
- the CCD camera is positioned so a scattering angle of 90° is approximately the 1,500th pixel.

Based on these considerations, the mapping of the individual pixels to the corresponding scattering angles was calculated and it is shown in Figure 2.5. As can be seen in the figure, the mapping is not linear. The light scattered at the forward or back scattering angles are measured with higher spatial resolution than those scattered around the scattering angle of 90°.

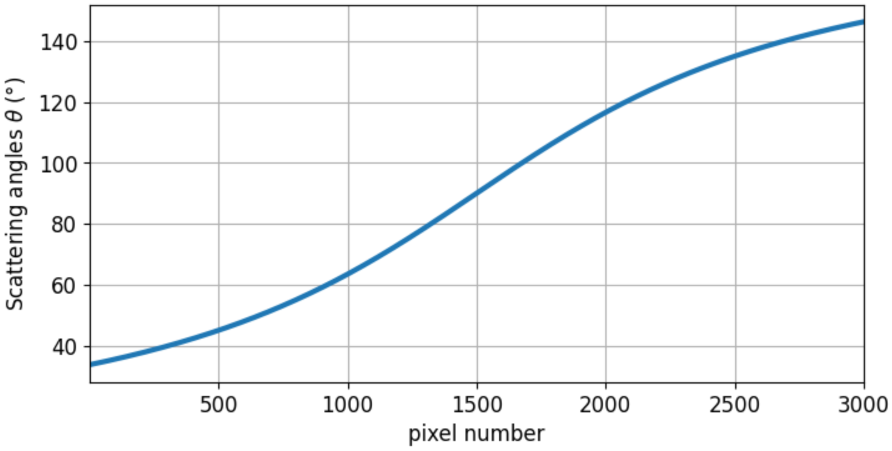

Figure 2.5: The mapping of the pixels to scattering angles

2.1.7 The limit of detection

The limit of the detection system can be determined by the ratio between the detection system responses to the light scattered by various sizes of single particles and noise. The higher ratio increases the likelihood of detecting the scattering light. The responses can be calculated in two steps. First, the power of light scattered by single particles across detectors' photosensitive surfaces are calculated based on Mie theory. Second, the power is converted into an electrical signal based on the detectors' specifications. On the other hand, interfering noise can be estimated by identifying probable noise and quantifying it.

In the design of the SPARCLE detection system, at least two sources of noise are identified: Rayleigh and dark noise. Rayleigh noise is caused by uncertainties in the number of photoelectrons generated by the detectors' photosensitive area due to light scattered by air molecules in the scattering chamber. The uncertainty is described by Poisson statistics as the square root of the amount of expected photoelectrons. Dark noise is caused by detector current incident on the detector. Other noise might exist, such as stray light resulting from the reflection of light from other instruments' components. The quantification of the noise depends on the particular instrument's alignment and, hence, the limit of detection presented in this subsection is only valid for the two cases identified.

Expected PMT responses to light scattered by single particles are calculated by integrating the light across the PMT's photocathode window and then converting it into electrical signals based on the PMT's specification. The electrical signals are then amplified by a factor of 550. To illustrate, the calculation is done for particles with sizes between 1 nm and 3,200 nm, and the refractive index of 1.59. The results of the calculation are shown in Figure 2.6. In the figure, the optical power of the scattered light is shown as a blue line and the corresponding amplified electrical signals are shown as a red line. As can be seen from the figure, the PMT's response is a complex function of particle size. A nearly linear response is observed for the light scattered by particles smaller than 1,000 nm. This feature is advantageous for sizing in that range. The responses to particles bigger than 1,000 nm peak at some particular sizes. The peaks correspond to the high contribution of particular Mie coefficients a and b expressed in Eq. A.40. The high contribution is due to the value of the denominators in the equation that close to zero for particular Mie coefficients. In the figure, the peaks correspond to the Mie coefficients: b_{12}, a_{12} and b_{13} are indicated.

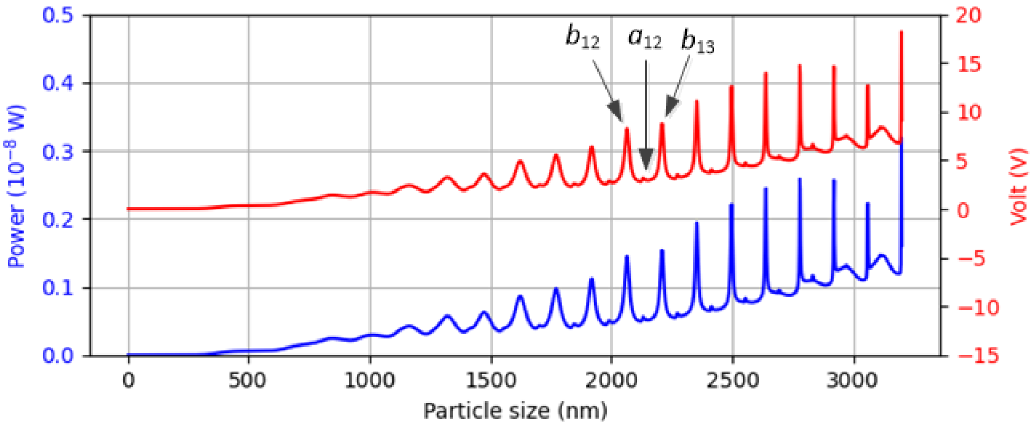

Figure 2.6: The expected responses of the PMT to the light scattered by particles whose sizes vary between 1 nm and 3,200 nm with a refractive index of 1.59. The blue line is the expected optical power of the scattered light across the PMT's photocathode window, and the red line is the corresponding responses of the PMT which has been amplified by a factor of 550. The calculation of converting optical power to electrical voltages is detailed in Appendix A.

The quantification of Rayleigh and dark noise in the SPARCLE detection system is based on the model of how the noise is generated. The Rayleigh noise is generated by light scattered by air molecules which are illuminated by the laser beam. A simplified scattering model is used where the air molecules scatter light directly to the PMT and the CCD camera. The air molecule considered in the model is the molecular size of Nitrogen. Also, the beam intensity is assumed to be constant during its propagation in the scattering chamber. The number of the scattering air molecules can be derived by multiplying air density to the volume of the laser beam in the scattering chamber. The air density is the density of air at atmospheric pressure and a temperature of 20° C. Then, the Rayleigh noise is calculated taking the size and refractive index of air molecules to be 0.3 nm and 1.0003 respectively. The result is shown as a green line in Figure 2.7. On the other hand, the calculation of the Dark noise is straightforward. The current generated by the PMT when no photon falls over the PMT window is specified by the manufacturer. The current then flows into the amplifier used to amplify PMT outputs. The corresponding voltage generated by the current is calculated and shown as a purple line in Figure 2.7. The PMT responses shown in Figure 2.6 are also plotted in Figure 2.7. As can be seen in the figure, the ratio between the responses and the total noise is less than one for particles smaller than 150 nm. While a ratio bigger than 100 is expected for particles bigger than 300 nm.

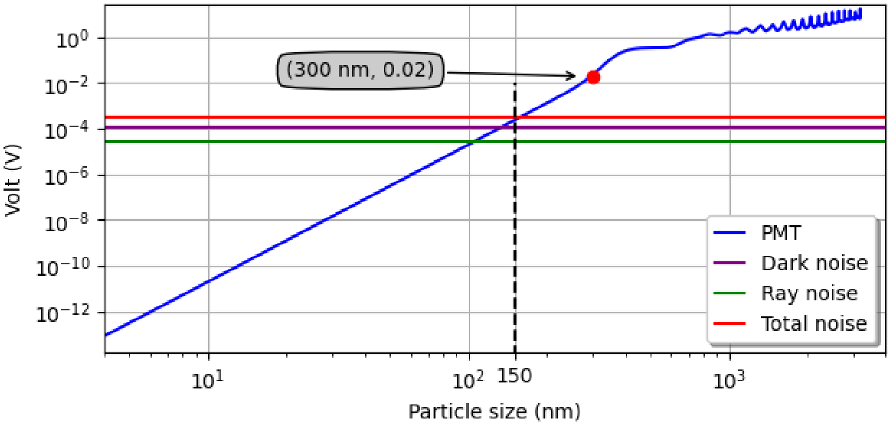

Figure 2.7: The expected responses of the PMT along with Rayleigh and dark noise. The total noise is the summation of the two noises. For clarity, the total noise in the figure is multiplied by a factor of 2. The-signal-to-noise ratio equal to one is indicated by a dashed line while the ratio equal to around 100 is indicated by a red dot. The calculation of PMT responses is detailed in Appendix A.1

Similar calculations were done for the CCD camera. In the calculation, the intensity of scattered light across individual pixels area is integrated over 1,000 µs of exposure time and then converted into electrical signals. To illustrate, three responses of the CCD camera to light scattered by particles with sizes 1,000 nm, 2,000 nm and 3,000 nm and a refractive index of 1.59 are calculated and shown in Figure 2.8. In the figure, the responses are plotted as a function of the scattering angles which are mapped from the individual pixels. In the top figure, the optical power of the scattered light over the scattering angles is shown. The optical power is then converted into volts by the CCD linear sensor with the conversion range between 0 V and -2.3 V. The CCD camera presents the output by normalising the volts into a range from 0 to 1 which linearly corresponds to a range of 0 V down to -2.3 V. The normalisation can be expressed as

$$\mathcal{V}_{\mathrm{CCD}} = -\frac{V_{\mathrm{CCD}}}{n}, \tag{2.3}$$

where $\mathcal{V}_{\mathrm{CCD}}$ is the normalised output of the CCD camera; V_{CCD} is the voltage generated by the CCD line sensors; n is the normalisation factor which is 2.3 V. Note, $\mathcal{V}_{\mathrm{CCD}}$ is dimensionless. The corresponding normalised outputs are shown in the bottom figure. The noise that interferes with these responses is also calculated. The dark noise can be derived from the manufacturer's specification. The manufacturer specifies that typical dark voltage generated by the CCD line sensor is 2.5 mV. The normalised output for this voltage is around 0.001. The Rayleigh noise is calculated based on the scattering model similar to that for the PMT measurements. The calculation is done for a pixel located in the scattering angle of 90°. For simplicity, the Rayleigh noise at this pixel is generalised for all individual pixels. The result indicates that the Rayleigh noise for a pixel is in the order of 10^{-4}. The combination of the two noises is still small so the patterns observed for the three sizes are not disturbed.

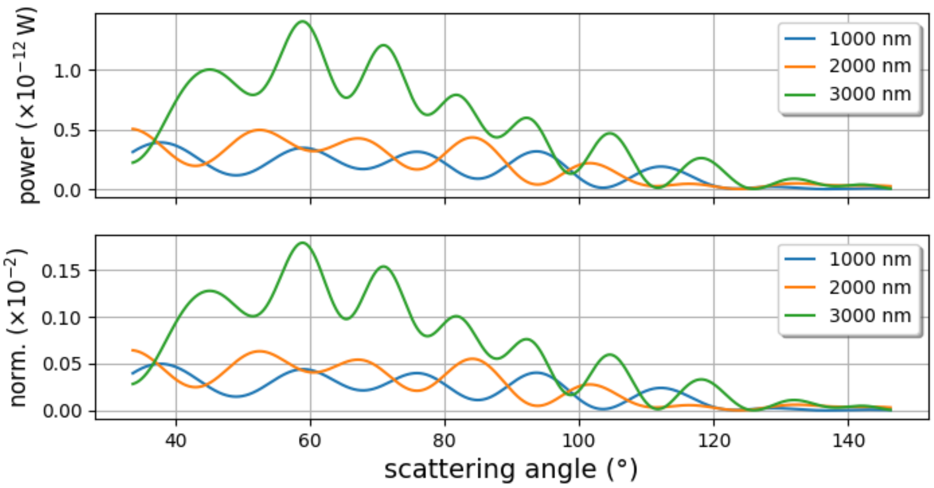

Figure 2.8: The expected responses of the CCD camera to light scattered by particles with three different sizes: 1,000 nm, 2,000 nm and 3,000 nm with the same refractive index of 1.59. The optical power expected across the CCD pixels was calculated and is plotted in the top figure. The CCD camera integrates the optical power over 1,000 µs and converts it into electrical signals. The electrical signals are then normalised and shown in the bottom figure.

The detection limit of the CCD camera can be determined by the ratio between the accumulation of all pixels' readings and the accumulation of noise interfering with all pixels. To illustrate, the CCD camera responses to single particles with the sizes of between 10 nm and 3,200 nm and a refractive index of 1.59 are calculated. Each reading for all the pixels is accumulated and plotted as a function of particle size. The plots are shown in Figure 2.9 with a logarithmic scale. The noise in each pixel calculated in the previous paragraph is accumulated for all the pixels and shown in the figure as well. As can be seen in the figure, the ratio between the expected total readings and the total noise is less than one for particles smaller than 250 nm while the ratio is bigger than 100 for particles bigger than 800 nm.

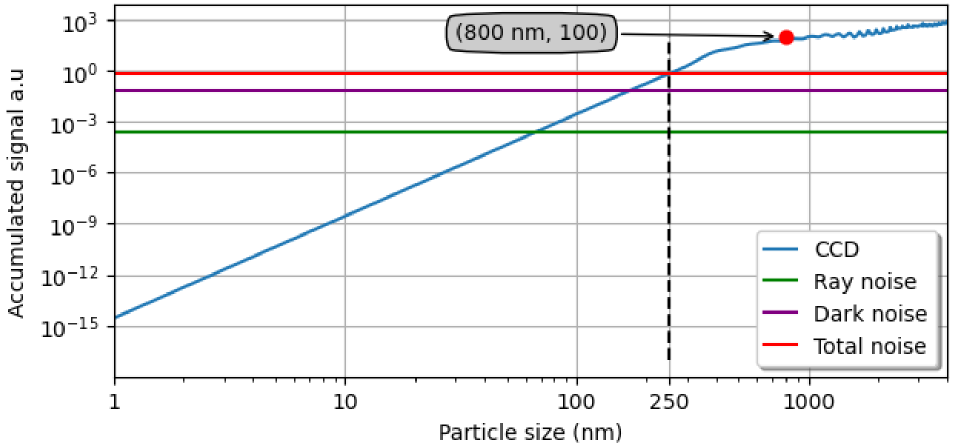

Figure 2.9: The expected responses of the CCD camera along with the noise. The responses are calculated from light scattered by particles whose sizes vary between 1 nm and 3,200 nm with the refractive index of 1.59. The noise sources are Rayleigh and Dark sources. The total noise is the summation of the noise from the two sources. The-signal-to-noise ratio equal to one is indicated by a dashed line while the ratio equal to roughly 100 is indicated by a red dot.

2.1.8 Ratio between PMT signals and CCD camera readings

Visual observation of the PMT signals and the total readings of the CCD camera as shown in Figures 2.7 and 2.9 indicates a similarity between the two. This similarity is expected since the two detectors measure the light scattered by the same single-particle size range. Since the detectors collect the scattering light with different scattering solid angels, the ratio between the outputs of the detectors can provide a characteristic of the SPARCLE design. The ratio is calculated by dividing PMT signals collected for the duration of the CCD camera integration time of 1,000 µs with the total readings of the CCD camera. The ratio can be expressed as

$$\rho_R = \frac{\sum_j \mathcal{V}_{\mathrm{CCD}}(p_j)}{\int_t V_{\mathrm{PMT}}(t)\, dt}, \tag{2.4}$$

where $V_{\text{PMT}}(t)$ is the PMT signals as a function of time t; The integration is evaluated during the integration time of the CCD camera; $\mathcal{V}_{\text{CCD}}(p_j)$ is the CCD camera readings for the pixel p_j; The summation is evaluated for the readings of all pixels; j is the integer number from 1 to 3,000 indicating the the index of the pixels. Note, the dimension of ρ_R is $V^{-1}\,s^{-1}$.

The ratio for particles with sizes between 700 nm and 3,200 nm is shown in the Figure 2.10. As can be seen in the figure, the ratio is a complex function of particle size, where high variation of the ratio is observed for particle size bigger than 1,000 nm. The variation of the ratio as a function of particle size indicates that the measurement of monodisperse aerosols where the variation of particle size is small may result in a linear relationship between $\mathcal{V}_{\text{CCD}}(p_j)$ and $\int_t V_{\text{PMT}}(t)\,dt$ with the slope of the linear relation ρ_R. The measurement of polydisperse aerosols may not lead to the linear relation between $\mathcal{V}_{\text{CCD}}(p_j)$ and $\int_t V_{\text{PMT}}(t)\,dt$.

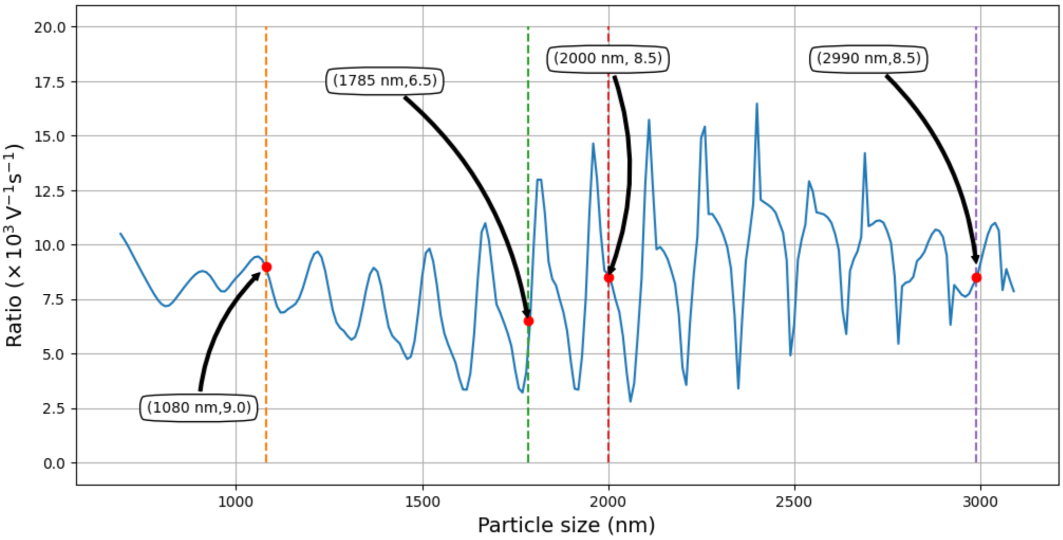

Figure 2.10: The ratio of PMT signals and total CCD camera readings for particle size between 700 nm and 3,200 nm. As shown in the figure, the ratios are highly varied as a function of particle size. As indicated in the figure, the expected ratios in measuring four particle sizes: 1,100 nm, 1,785 nm, 2,000 nm and 3,000 nm are $7.6 \times 10^3\,\text{V}^{-1}\text{s}^{-1}$, $6.5 \times 10^3\,\text{V}^{-1}\text{s}^{-1}$, $8.5 \times 10^3\,\text{V}^{-1}\text{s}^{-1}$ and $9.0 \times 10^3\,\text{V}^{-1}\text{s}^{-1}$, respectively. These particle sizes are the size of particles used in the calibration of SPARLCE.

2.2 Corrections due to a slab of glass in the CCD camera

A slab of glass is installed in front of the sensor line of the CCD camera and this glass affects the intensity as well as the direction of scattering light which propagates through the glass. Using the well-known Snells law and Fresnel equations, the effects introduced by the glass can be calculated. The calculations were done based on the following considerations:

- the polarisation of the electric field of scattering light propagating through the glass is normal to the scattering plane. The scattered light does not have a component of light with the electric field polarised parrallel with the scattering plane since the azimuths angles of the scattering plane is 90°, $\phi = 90°$,
- the refractive index of the glass is 1.5 as specified by the manufacturer,
- the incident angles of scattering light to the glass are measured with respect to the normal of the glass. The incident angles are calculated as the absolute value of the difference between 90° and the scattering angles,
- the thickness of the glass is 0.7 mm as specified by the manufacturer.

Based on Fresnel equations, the transmittance of scattering light propagating through the glass is a function of the polarisation and the incident angle of the scattering light as well as of the refractive index of the glass. The transmittance was calculated and the results are shown in Figure 2.11 as a dashed red line with the scale on the secondary vertical axis. One example of the effect of the transmittance to the light scattered by particles with the size of 3,000 nm and a refractive index of 1.59 is plotted in the same figure. As shown in the figure, the intensity of the scattering light is reduced, with the reduction proportional to the transmittance of the scattering light at particular scattering angles.

Based on Snell's law, the lateral displacement of scattering light when propagating through the glass is a function of the refractive index and the thickness of the glass as well as the incident angles of the scattering light. The lateral displacements were calculated and the results are converted into angular displacements, $\Delta\theta$, which are used to correct the mapping of individual pixels to scattering angles. The results are shown in Figure 2.12 as a dashed red line with the scale on the secondary vertical axis. An illustration of correcting the mapping when measuring light scattered by particles with the size of 3,000 nm and a refractive index of 1.59 is plotted in the

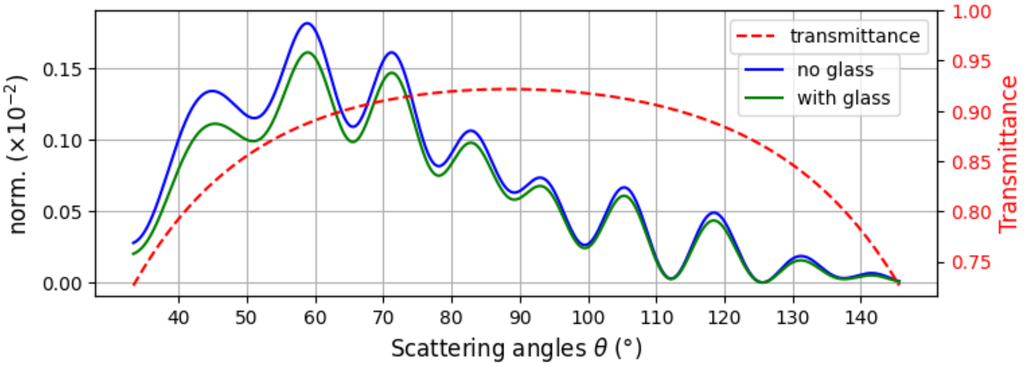

Figure 2.11: The transmittance of scattering light propagating trough the glass installed in the CCD camera. The transmittance is plotted as a dashed red line with their scale is on the secondary vertical axis. The transmittance is peaked at a scattering angle of 90°. The effect of the transmittance to the light scattered by particles with the size of 3,000 nm and the refractive index of 1.59 is shown as a green line with the corresponding intensity without the glass installed is plotted as a blue line.

same figure. As shown in the figure, scattering angles are displaced and the level of displacement is dependant on the scattering angles. At a scattering angle of 90°, the angular displacement is zero.

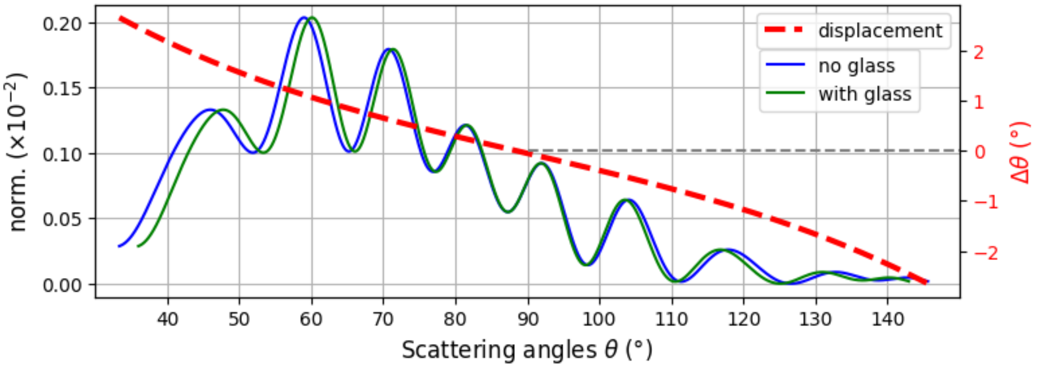

Figure 2.12: Angular displacement in the mapping of individual pixels to scattering angles due to the glass installed in the CCD camera. The displacement is shown as a dashed red line. The blue line is the light scattered by particles with a size of 3,000 nm and a refractive index of 1.59 without the glass installed. With the glass installed, the mapping of pixels to scattering angles is corrected as shown by the green line.

2.3 Air sample delivery system

An air sample delivery system is responsible for sampling ambient air and transporting it into the sensing volume as well as removing it from the instrument. Two main considerations when designing the system were:

1. to ensure that the particle concentration of an air sample that reaches the sensing volume is as close to that of ambient air as possible,
2. to avoid particle contamination in the scattering chamber.

The first consideration requires minimum particle loss in the sampling and transport of air sample. The loss can be minimised by creating a direct route for the air to flow from ambience to the sensing volume and ensuring that the flow is laminar. The second requires removing particles suspended in the air sample immediately after they leave the sensing volume. This requirement led to the design with a narrow gap between the sampling and removal pipe.

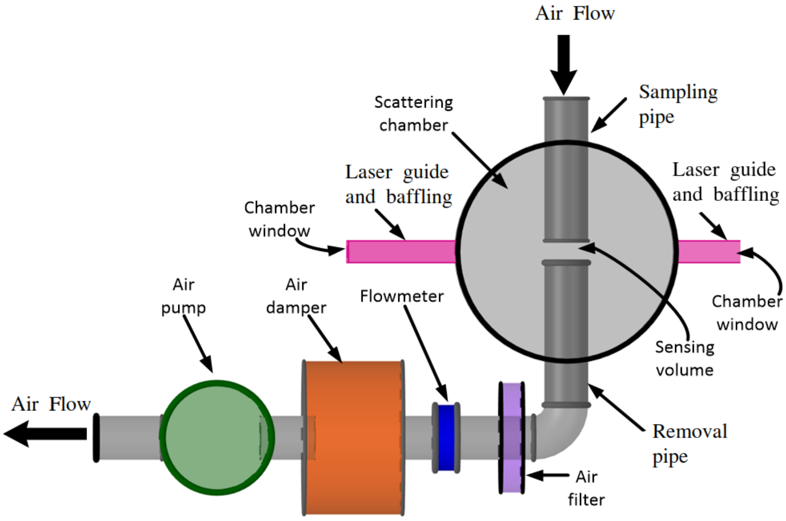

Figure 2.13: The SPARCLE delivery system.

The scheme of the SPARCLE delivery system is shown in Figure 2.13. As can be seen in the figure, the sampling and transport of air sample into the sensing volume is performed through a sampling pipe. The air sample is then removed through a removal pipe. There is a gap between the sampling and the removal pipe in which the sensing volume is located. The gap needs to be set as narrow as possible to reduce the chance of particles drifting into the scattering chamber. The flow of the air sample is controlled by an air pump. The flow rate of the pump can fluctuate as a function of time and to reduce this fluctuation an air damper is installed. The flow rate of air sample is monitored by a flow meter. To protect the flow meter from contamination, an air filter is installed to filter contaminants out of the air sample. Also shown in the figure are two chamber windows through which the laser beam propagates into and out of the scattering chamber. A laser guide and baffling is used to isolate the beam within the scattering chamber.

2.3.1 The type of air flow through the sampling pipe

SPARCLE is designed to have an inlet port which allows for the installation of various sampling pipes whose outer diameter fits the inlet port. The diameter of the port is around 1.4 mm and two options of sampling pipes are available: one with an inner-diameter of 0.5 mm and one with 1 mm, both with the length of 40 mm.

The type of air flow through a pipe can be determined based on the pipe's dimensions. The determination is based on the calculation of the Reynold number of air flowing in the pipe. When the Reynold number is less than 2,000, the flow can be regarded as a laminar flow [Pramod and Baron, 2011]. The Reynold number of an air flow, R_f, can be calculated as

$$R_f = 65,000\, v_a\, r, \tag{2.5}$$

or

$$R_f = 65,000 \frac{Q_a}{\pi\, r} \tag{2.6}$$

where v_a and Q_a is the speed and the flow rate of air, respectively, and r is the radius of the pipe. Calculations based on the above equation were done to illustrate the Reynold number of air flowing with flow rates of less than $500 \times 10^{-9}\,\mathrm{m}^3\,\mathrm{s}^{-1}$ in the two sizes of the sampling pipes: 1 mm and 0.5 mm, and the results are plotted in Figure 2.14. As can be seen from the figure, the Reynold numbers are lower than 40, hence, the flows can be regarded as laminar flows.

2.3.2 Particle loss in the sampling pipe

Particles may be lost while being sampled and transported through the sampling pipe to the sensing volume. The loss can be calculated using a validated software such as the Particle Loss Calculator (PLC) [Von Der Weiden et al., 2009]. In the calculation, users need to specify sampling and transport parameters such as sampling rates and inlet size. The calculator limits sampling rates down to around $1,666 \times 10^{-9}\,\mathrm{m}^3\,\mathrm{s}^{-1}$ and the size of sampling pipe inlet down to 1 mm. However, there are no limits imposed for transport parameters. The parameters used in the calculation are listed in Table 2.3. The results are plotted in Figure 2.15. In the figure, sampling and transport loss in SPARCLE's sampling pipe as functions of particle size are depicted as blue and red

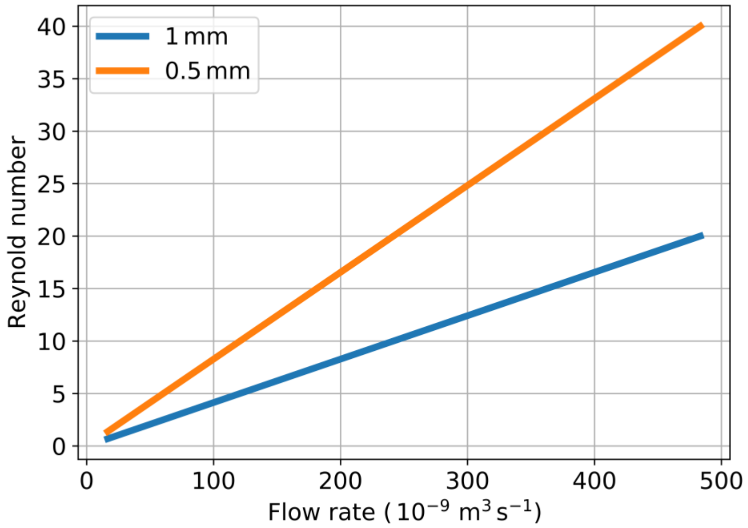

Figure 2.14: Air flow Reynold numbers for various flow rates of air inside two different sizes of sampling pipes:1 mm and 0.5 mm.

lines, respectively. The results are presented as either solid or dashed lines depending on whether the formulae used in the calculation are still in their validity range or not. As can be seen from the figure, more than 10% and 50% of particle losses are expected when sampling particles bigger than 1,800 nm and 6,000 nm, respectively. The calculation for sampling particles smaller than 300 nm is out of the validity range, and therefore indicated by a dashed line. The dashed line can be seen as a projection with low confidence of validity. The calculation of transport loss indicates that less than 10% of particle loss is expected when transporting particles bigger than 50 nm. To conclude, the results of the sampling and transport loss calculations indicate that particle loss in the measurement of particles in the accumulation mode using the sampling and transport parameters listed in Table 2.3 is less than around 10%.

Sampling parameters			**Transport parameters**		
Parameters	**Values**	**Units**	**Parameters**	**Values**	**Unit**
Aspiration angle	90°		Angle of inclination	90°	
Orifice diameter	1	mm	Angle of curvature	0°	
Sampling rate	$1,666 \times 10^{-9}$	m^3s^{-1}	Flow rate	$1,666 \times 10^{-9}$	m^3s^{-1}
Wind velocity	0	$m\,s^{-1}$	Tube length	100	mm
			Tube size	1	mm

Table 2.3: Parameters used in the particle loss calculation.

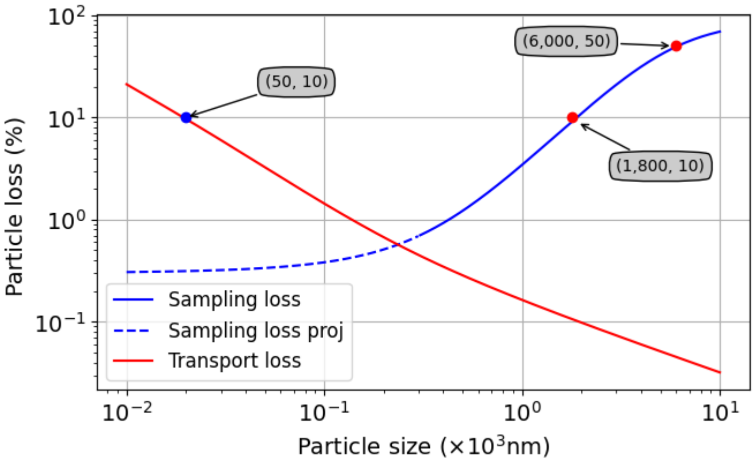

Figure 2.15: Particle loss in sampling and transport of particles through the sampling pipe.

However, sampling and transport rates slower than those used in the aforementioned calculations may be needed and hence, the corresponding particle loss needs to be calculated or estimated. Sampling losses for slower sampling rates are expected to be higher than those shown in Figure 2.15, based on the assumption that slower flow rates are less effective in driving particles into the inlet. While the sampling rates is limited down to $1{,}666\times10^{-9}$ in the calculation using the calculator, there is no limit imposed in the transport rate for the calculation. Transport loss for slower transport rates was calculated for two different transport rates: $300 \times 10^{-9}\,\mathrm{m^3\,s^{-1}}$ and $500 \times 10^{-9}\,\mathrm{m^3\,s^{-1}}$. The results are nearly identical to those shown in Figure 2.15.

2.3.3 Numerical modelling of air flow in the sampling pipe, scattering chamber and removal pipe

To study the velocity profile of air sample flowing in the sampling pipe, the sensing volume and the removal pipe, simple numerical fluid dynamics modelling was done using OpenFoam software [OpenFoam, 2019]. OpenFoam is a collection of various numerical solvers under one interface. In this modelling, a steady-state solver rhoSimpleFoam is used to simulate a turbulent Reynolds-averaged Navier-Stokes air flow of incompressible fluid based on defined boundary conditions. The boundary conditions are:

- the pressure at the sampling pipe inlet is higher than that at the removal pipe outlet. This pressure difference generates air flow from the inlet to the outlet,
- the velocity of air sample is zero at wall boundaries.

Several numerical calculations with various pressure differences between that at the inlet and at the outlet were carried out. One result of the calculation in which the pressure difference was set to be 2 Pa is shown in Figure 2.16. In Figure 2.16.a, the map of the velocity magnitude in the scattering chamber is shown with the magnitude colour-coded from blue to red corresponding to the magnitude from $0.0\,\mathrm{m\,s^{-1}}$ to $1.2\,\mathrm{m\,s^{-1}}$. The figure indicates jet air flow from the sampling pipe to the removal pipe. The flow rate of the jet air can be calculated by integrating the velocity distribution across the sampling pipe cross-section, the result of which is $306 \times 10^{-9}\,\mathrm{m^3\,s^{-1}}$.

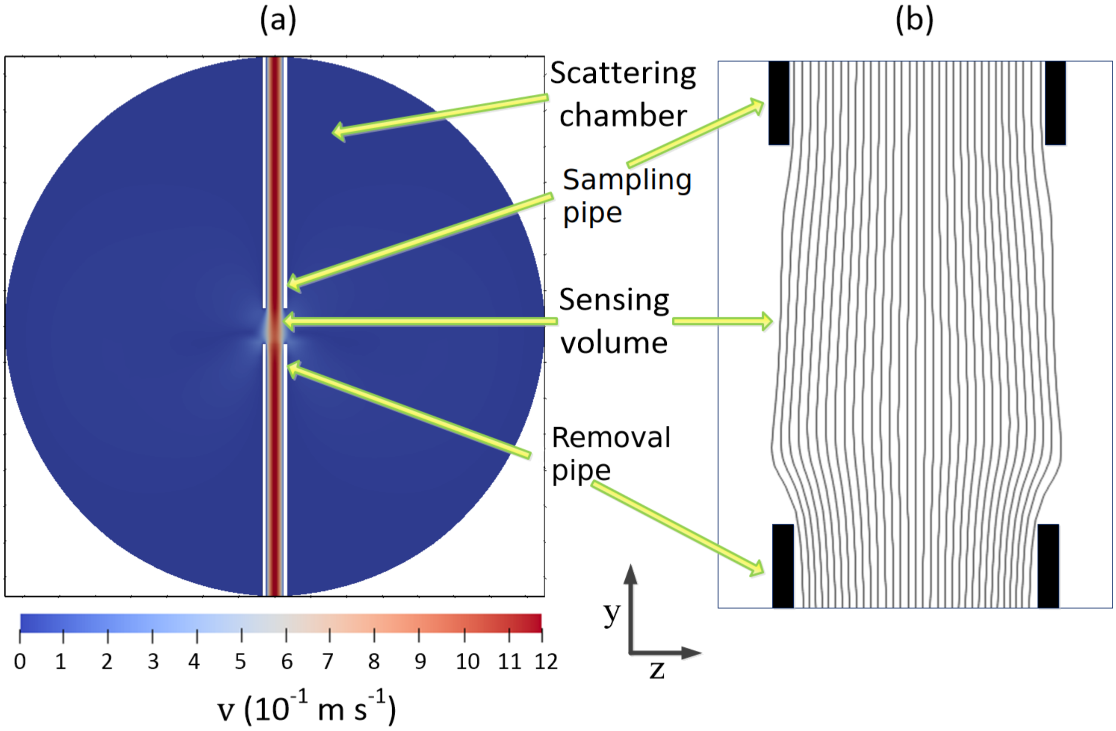

Figure 2.16: The numerical modelling of air inside the scattering chamber. (a) The map of the magnitude of air velocities inside the sampling pipe, sensing volume, and removal pipe. (b). The streamlines of the air in the sensing volume.

Based on the velocity distribution, the streamlines of the jet air that depict lines tangential to the jet air element velocity can be derived. The streamlines are depicted in Figure 2.16(b). They indicate that the jet air in the sensing volume expands slightly. The expansion can be obviously seen by plotting the air velocity magnitudes in the sampling pipe and the sensing volume as a function of the distance from the symmetrical axis of the sampling pipe. The plot is seen at the bottom of Figure 2.17(a). As seen in the figure, the velocity magnitude of air in the sampling pipe is distributed quadratically while that in the sensing volume is distributed normally.

The figure also shows the velocity magnitudes of air circulating in the scattering chamber. This air circulates due to the friction between the air and the jet air in the sensing volume. Another parameter that can be derived based on the distribution is particle transit time in the sensing volume. Since SPARCLE focuses on particles in the accumulation mode with sizes between 500 nm and 2,500 nm, the effect of Brownian and gravitational motions to the dynamic of single-particle motions can be neglected [Tsuda et al., 2013]. As a result, the path lines of single particles can be regarded as the same lines as the streamlines of the air in which the single particles are suspended. Based on the velocity distribution and the height of the sensing volume, a transit time can be calculated. The results are plotted in the top part of Figure 2.17(a). Similar calculations were carried out for two additional sampling flow rates and the results are shown in Figure 2.17(b) and Figure 2.17(c). Based on these figures, it can be concluded that the required flow rates that lead to the transit time longer than or equal to 1,000 µs is less than $170 \times 10^{-9}\,\mathrm{m^3\,s^{-1}}$.

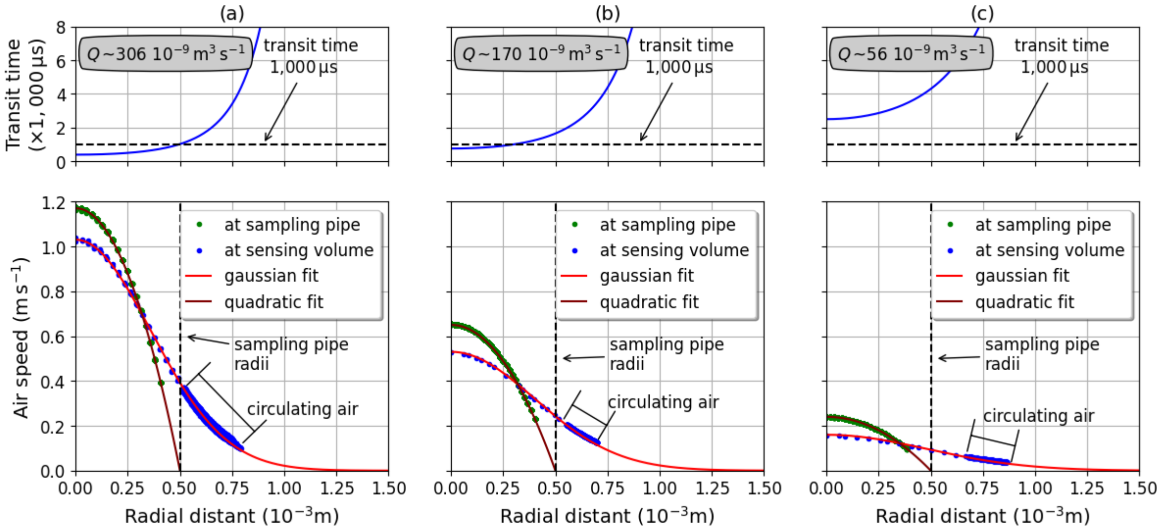

Figure 2.17: The distribution of the magnitude of air velocities in the sampling and sensing volume (bottom) and the corresponding particle transit time in the sensing volume (top) for three different flow rates: $306 \times 10^{-9}\,\mathrm{m^3\,s^{-1}}$, $170 \times 10^{-9}\,\mathrm{m^3\,s^{-1}}$ and $56 \times 10^{-9}\,\mathrm{m^3\,s^{-1}}$. The magnitudes of air velocities circulating in the scattering chamber are also indicated.

2.3.4 Flow meter selection

The flow meter selected is an AWM3100 Series Microbridge Mass Airflow Sensor with a working range between $0\,\mathrm{m^3\,s^{-1}}$ to almost $3,500 \times 10^{-9}\,\mathrm{m^3\,s^{-1}}$ and a measurement uncertainty $2,3 \times 10^{-9}\,\mathrm{m^3\,s^{-1}}$. The working principle is of measuring the power required to keep a constant temperature in an electrical heating element in the air flow. Heater power is measured, and provides a signal proportional the mass air flow. The calibration curve of the flow meter is shown in Figure 2.18.

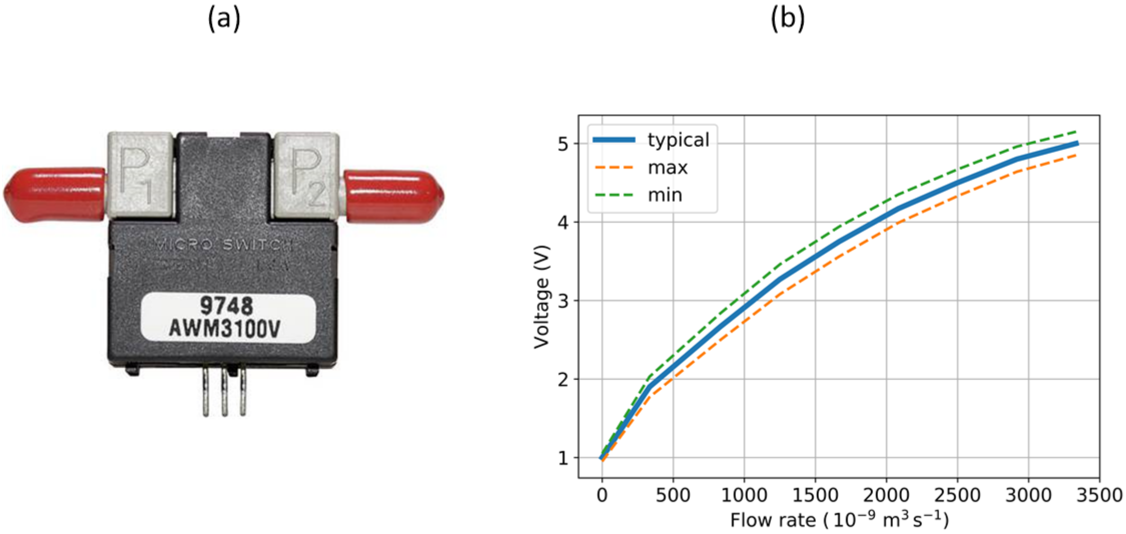

Figure 2.18: The flow meter used in SPARCLE. (a) A picture of a AWM3100V flow meter. (b) The calibration curve of the flow meter. The blue line is the typical value while the orange and green dashed lines are the maximum and minimum values, respectively.

2.3.5 Air pump and air damper selection.

The selected pump is a 100-series peristaltic pump produced by Williamson Pump Ltd shown in Figure 2.19(a) and its working principle is depicted in Figure 2.19(b). The main components of the pump are a flexible tube, a rotor, rollers and a motor. The working principle of the pump is based on air displacement created by the rollers pinching the flexible tube as the rollers rotate. The flexible tube is made of silicon with an inner diameter of 1.6 mm. The rotation of the rollers is controlled by the rotor and the motor. The rotor is attached to a DC powered motor with a maximum rotation of 150 rotations per minute. The setting of the tube's inner diameter and the motor's rotation lead to the maximum flow rate of the pump at around $10^{-6}\,\mathrm{m^3\,s^{-1}}$. However, flow rates generated by the pump vary as a function of time due to the rollers passing the inlet. One example of this variation as measured by the flow meter is plotted as a red line in Figure 2.20. The response time of the flow meter is 1 ms, indicating that the transient shown in the figure is capturing the main transients. In order to smoothen the flow rate, a simple 5-L volume acts as an air damper. The corresponding flow rates with the air damper installed are depicted as a blue line in Figure 2.20. The smoothed air flow has a variability of around $50 \times 10^{-9}\,\mathrm{m^3\,s^{-1}}$.

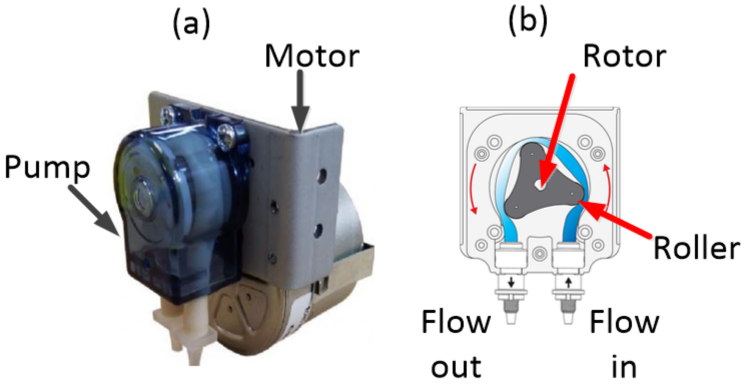

Figure 2.19: The pump used in the second generation SPARCLE. (a) A picture of 100-series peristaltic pump produced by Williamson Pump Ltd. (b) The scheme that shows the working principle of the pump.

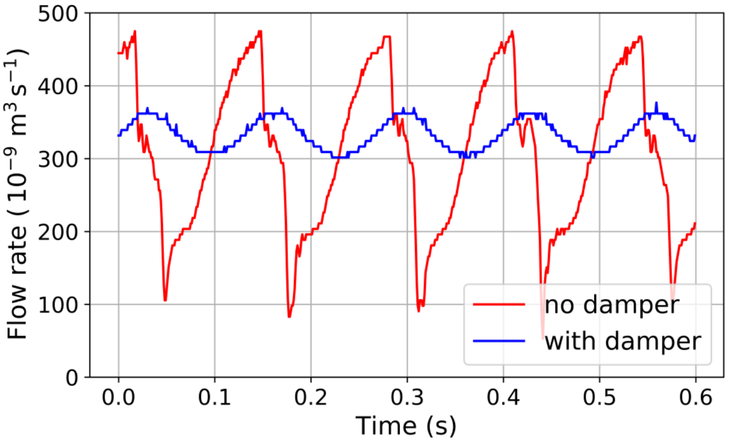

Figure 2.20: Smoothed air by using an air damper. The red line is the flow rate induced by the pump. The flow rate has a high variability from around $100\,10^{-9}\,\mathrm{m^3\,s^{-1}}$ to nearly $500\,10^{-9}\,\mathrm{m^3\,s^{-1}}$. To smooth this flow rate a 5-L air damper is installed. The smoothed flow rate is shown as the blue line.

2.4 Data acquisition system

The final task in designing SPARCLE is creating a data acquisition system to retrieve measurement data. The measurement data are signals from amplified PMT, CCD camera, power meter and flow meter. The main consideration in the design of the data acquisition system is that the system should have minimal impact in the actual measurement process. For example, the CCD camera needs to be triggered immediately single particles enter the sensing volume. In the interest of this, signal delays introduced by each component in the triggering system should be kept to a minimum. Another example is that the rate of particles being measured by SPARCLE per unit time depends on the “dead time” of the acquisition system during which the system is unable to perform measurements. Short “dead time” leads to a high rate of particle measurement per unit time.

The scheme of the SPARCLE data acquisition system is shown in Figure 2.21. As shown in the figure, the signals from the PMT are amplified by an amplifier. The amplified signals are sent to a discriminator which discriminates the amplified signals into background and scattering events. When scattering events are detected, the discriminator generates pulse signals and sends the signals to a gate. The gate determines whether the pulse signals are to be blocked or let through. The determination depends on the readiness of the measuring devices, which are digital oscilloscopes, and the CCD camera, to perform measurements. When the devices are ready, pulse signals are sent by the gate to a buffer, then, the buffer generates trigger signals to trigger the devices to start performing measurements. When the devices are not ready, the pulse signals will be blocked and the scattering events will be overlooked. This scheme allows for the measurement of scattered light by the PMT and the CCD camera as well as the measurement of laser power and air flow rate to be done simultaneously. The digital oscilloscopes and the CCD camera are connected to a PC which controls them as well as storing the data sent by them. The technical specifications of each component of the acquisition system are discussed in Appendix B.

An illustration of the timing diagram of the SPARCLE acquisition system is shown in Figure 2.22. The diagram shows three examples of cases:

1. Amplified PMT signals that are classified by the discriminator as scattering events and lead to triggering of the CCD camera.

2. Amplified PMT signals that are classified by the discriminator as scattering events but do not lead to triggering of the CCD camera.

3. Amplified PMT signals that are not classified as scattering events.

In Figure 2.22.a, three pulses contained in amplified PMT signals are shown to illustrate the three cases. The pulses are identified at the time intervals from t_1 to t_2,

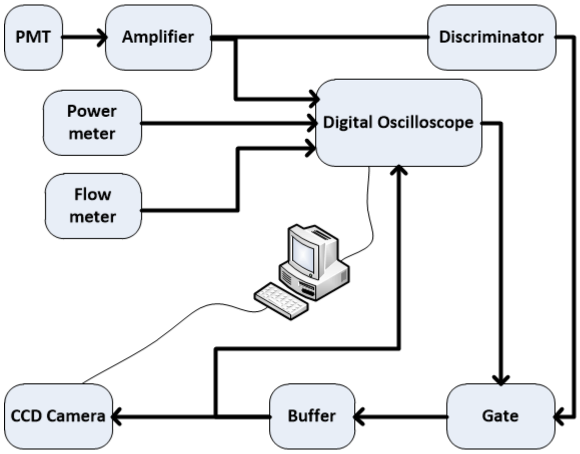

Figure 2.21: SPARCLE data acquisition system.

from t_4 to t_5, and from t_7 to t_8. The discriminator classifies the pulses in two stages: alternating-current (AC) coupling the pulses to remove slow drift in the amplified PMT signals and comparing the AC coupled pulses with a threshold level. The AC coupling of the pulses is illustrated in Figure 2.22.b. In the figure, the threshold level is indicated and the comparator used in the discriminator will generate low outputs when AC coupled pulses are lower or equal to the threshold level. With this scheme, pulses are generated in the outputs of the comparator where the duration is the same as that of AC coupled pulse level that is lower or equal to the threshold. The illustrations for the pulses in comparator outputs are shown in Figure 2.22.c from t_1 to t_2 and from t_4 to t_5. If comparator pulses are generated when the oscilloscope and the CCD camera are ready to perform measurements then trigger pulses will be generated. The readiness is indicated by the level of the signals generated by the oscilloscope. If the signal is low, the oscilloscope and the CCD camera are ready otherwise they are not. The oscilloscope signals are illustrated in Figure 2.22.d. As shown in the figure, the oscilloscope is ready to take a measurement from t_0. When a comparator pulse is generated during the ready time, a corresponding trigger pulse will be generated. The trigger pulse generation is illustrated in Figure 2.22.e which is generated at t_1, the same time a comparator pulse is generated as illustrated in Figure 2.22.c. Once trigger pulses are generated, the oscilloscope and the CCD camera start to perform measurements and during the measurements the oscilloscope generates low signals. The signals are illustrated in Figure 2.22.d. from t_1 to t_3. Once the measurements done, the measurement data are transferred to the PC and then the oscilloscope and the CCD camera are restarted. During the transferring and restarting, the oscilloscope generates high signals. The high signals are illustrated in Figure 2.22.d. at

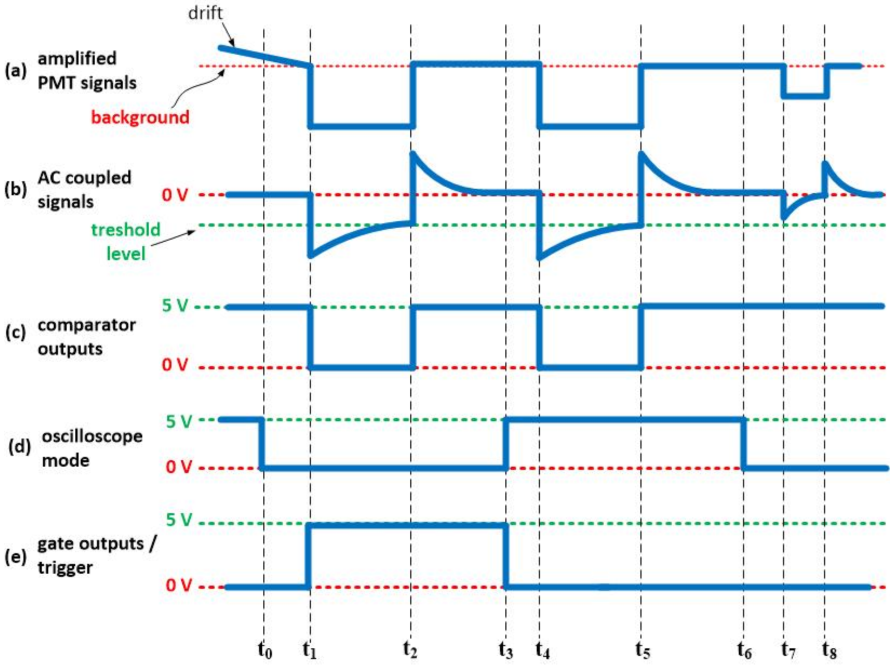

Figure 2.22: The timing diagram of the SPARCLE acquisition system.

the time interval from t_3 to t_6. The duration of trigger pulses is determined by the combination of the levels of comparator outputs and oscilloscope signals. The main goal of the determination is to keep trigger signals stable when the oscilloscope and the CCD camera are performing measurements. Since the oscilloscope and the CCD camera uses a raising edge trigger system, designing a trigger pulse with high signals during the measurements prevents the oscilloscope and the CCD camera being triggered during the measurements. The determination is detailed in Table 2.4.

comparator outputs	oscilloscope signals	trigger signals
high	high	low
low	low	high
low	high	the level of trigger signals does not change
high	low	

Table 2.4: The truth table for trigger signal generation.

The delay of the system can be determined from the delay of each component. The delay of each components can be done in various ways. First, the delay can be evaluated using high temporal measurements of the input and output of each component. Second, the delay can be estimated based on the data sheet of the main parts of each component. Third, an inquiry of the delay information of particular components can be made to the manufacturers. The delay time for each component are listed in Table 2.5.

The total delay time as indicated in Table 2.5 is less than 15 µs. If SPARCLE operates with single-particle transit time in the sensing volume longer than 1,000 µs, then there will be plenty of time for the data acquisition system to measure the light scattered by the single particles.

Component	**Main part or device series**	**Delay time**	**Method**
Amplifier	Four poles Sallen-Key low filters and operational amplifier OP27G	5 µs	Input and output measurement.
Discriminator	Comparator LM311P	<1 µs	Input and output measurement.
Gate	AND logic Gate SN74LS08N and timer NE555	< 80 ns	Data sheet
Buffer	Buffer CD74HCT36	< 80 ns	Data sheet
Digital oscilloscopes	Micro Bitscope BS05	-	Clock timing
CCD camera	LC1-USB CCD camera	< 5 µs	Input and output measurement, personal contact to the manufacturer, and clock timing

Table 2.5: The delay time of the data acquisition system.

The determination of the "dead time" of the system was found by averaging the number of measurements performed by the detection system over a unit of time when the measurements were done with the following conditions:

- the trigger system was disabled and the data acquisition was free running,

- the integration time of the CCD camera was set to the minimum which is at 1 µs,
- the sampling rate of the digital oscilloscope was set to the minimum which is 2 µs per sample and the number of samples sampled by the oscilloscope is 2,000. Hence, the sampling time of the oscilloscope is around 4 ms.

It was found that, on average, 121 measurements were done over a time period of 60 s or 60,000 ms. Since the sampling time in each measurement is 10 ms, the total sampling time for the 121 measurements is

$$t_{\text{samp}} = 121 \times 4\,\text{ms} = 484\,\text{ms}, \tag{2.7}$$

The "dead time" can be estimated by the difference between the time needed to run each measurement and the sampling time for each measurement. The estimation can be expressed as:

$$t_{\text{dead}} = \frac{60,000\,\text{ms} - t_{\text{samp}}}{121} = \frac{60,000\,\text{ms} - 484\,\text{ms}}{121} = 496\,\text{ms}. \tag{2.8}$$

2.5 Summary

The design of the second generation SPARCLE has been discussed. The design is composed of three systems: the detection system, the air delivery system, and the data acquisition system. The air delivery system is responsible for delivering single particles from ambient to the sensing volume. The detection system is responsible for illuminating single particles and measuring the light they scatter. The data acquisition system is responsible for the timing of the measurement and storing the measurements on a personal computer.

It is expected that the PMT in the detection system is able to detect particles bigger than 300 nm and with signal-to-noise ratio bigger than 100. It is also expected that a similar signal-to-noise ratio can be obtained for measurements by the CCD camera when it measures light scattered by particles bigger than 800 nm. However, these expectations are based on few noise sources identified in the design and might not be valid if other noise sources exist.

SPARCLE is expected to measure the pattern of light scattered by single particles. The expected of the pattern of light scattered by three particles with sizes of 1,000 nm, 2,000 nm and 3,000 nm and a refractive index of 1.59 were calculated. The CCD camera responses to these scattering patterns were also calculated. The responses were calculated by integrating the scattering light for about 1,000 µs. The results show that the CCD camera is able to capture the angular resolution of the scattering light with scattering angles between 37° and 144°. The noise identified in the design is low and the patterns of the angular resolution are not disturbed.

If SPARCLE operates with a CCD camera integration time of 1,000 µs, the transit of single particles in the sensing volume should be longer than 1,000 µs. Sampling rates that lead to this condition are the rates slower than $170 \times 10^{-9}\,\mathrm{m^3\,s^{-1}}$. At this level of sampling rate, it is expected that less than 10% of particles with sizes between 50 nm and 1,800 nm are lost while transported through the sampling pipe. The "dead time" in the SPARCLE acquisition system is estimated to be 140 ms. If the sampling time of both the oscilloscope and the CCD camera for each SPARCLE measurement is set to be 10 ms, then the maximum particle per unit time that SPARCLE can measure is 400 particles per minute. It is calculated that the coincidence error when measuring air with concentration less than 100 particles per $\mathrm{cm^3}$ is less than 2% of the concentration for the case of the pipe with the radius of either 0.1 mm or 0.5 mm installed as SPARCLE inlet. Coincidence error around 70% of air sample concentration is expected when measuring air with the concentration of 10,000 particles per $\mathrm{cm^3}$ when sampling pipe with a radius of 0.5 mm is used as the inlet.

Chapter 3

SPARCLE calibration

The aim of the calibration of the second generation SPARCLE was to evaluate whether or not the design described in Chapter 2 works as expected. In preparation for the calibration, the SPARCLE sensing volume was aligned and the spatial distribution of the beam intensity illuminating the sensing volume was measured. The calibration was then performed by measuring SPARCLE responses to four monodisperse aerosols, each containing monodisperse polystyrene latex (PSL) beads, whose particle size and refractive index are known. During the measurements, the size distributions of the aerosols were monitored by a manufacturer calibrated OPC. Additional parameters, such as the relative humidity of the air sample and the power of a fraction of the laser beam, were also measured. Note, the coordinate system described in Chapter 2 is used in this chapter; the coordinate system is centred at a cross-section between the symmetrical axis of the sampling pipe and the horizontal plane of the beam.

3.1 Aligning the sensing volume

As discussed in Chapter 2, the sensing volume is the volume of the intersection between the sample air flow exiting the sampling pipe and the laser beam. The following needs to be considered when aligning the sensing volume:

- the gap between the sampling and the removal pipe needs to be as small as possible to reduce the chance of particles drifting into the scattering chamber,
- a smaller gap risks a higher fraction of the beam being reflected by the pipes,
- the alignment should lead to minimum background noise.

A visual observation of the beam shape when the beam was projected on a paper screen showed that the cross-section of the beam was not a simple rectangular shape as described in Chapter 2. The cross-section's boundaries which were not clearly defined meant the positioning of the sensing volume, which is relative to the pipes and the detectors, affected the background measured by the detectors. The unclear boundary in the y axis might have resulted in the reflection of a beam fraction by the pipes when the gap between the pipes was set to be small. Furthermore, the boundary in the x axis was also not clear as the beam diverged with respect to this axis and the divergence can caused a fraction of the beam to propagate to the detectors. The divergence can be explained as the laser diode produced an elliptical beam which diverged with respect to its major and minor axis and, prior to the sensing volume, the beam was focused in the direction of the major axis only. The beam still diverged with respect to the minor axis which coincided with the x axis. After several attempts, the alignment that led to minimum background was achieved. The alignment can be summarised as follows:

- the divergent beam propagated directly to the CCD line sensor when the beam was positioned such that the CCD line sensor measured scattering light with the azimuth angle of 90°. To avoid the direct propagation, the beam was moved down around 0.4 mm in the y axis direction such that the CCD line sensor measured scattering light with the azimuth angle of around 82°. As indicated in Equation A.3, the difference of scattering intensity at the two azimuth angles measured by the CCD line sensor is negligible. Similarly, the difference between the scattering solid angles subtended by the PMT before and after the beam was moved is also negligible,

- the gap between the sampling and the removal pipe was set around 1 mm. Smaller gaps resulted in higher background. The gap of 1 mm is the gap used in the air flow modelling in the sensing volume as discussed in Chapter 2.

The backgrounds measured by the PMT and the CCD camera are shown in Figure 3.1 along with the output of the PMT and the CCD camera when the beam was switched off. As shown in Figure 3.1.a, the PMT output when the beam was switched off is slightly higher than 4.5 V. When the beam was switched on, a portion of light propagated into the PMT either directly such as the light from the diverged beam or indirectly such as the light from the reflection of the beam by optical components. The light generated background that induced the PMT to generate electrical currents even when there were no particles in the scattering volume. The SPARCLE data acquisition system was designed to convert higher electrical currents generated by the PMT into lower electrical voltages. The mean and the standard deviation of the voltage of PMT outputs that were generated by the background are 3.1 V and 0.07 V, respectively. The readings of the CCD camera when the beam was switched off are nearly zero as shown in Figure 3.1.b. When the beam was switched on, a fraction of light propagated into the CCD line sensor and the readings of the CCD camera were higher with greater variations than the readings when the beam was switched off. The higher reading is the background measured by the CCD camera. Also indicated in the figure are the different levels of background over the pixels of the CCD camera. The high background of pixels 1000 to 2000 may be due to light reflected by the sampling pipe which is located near those pixels

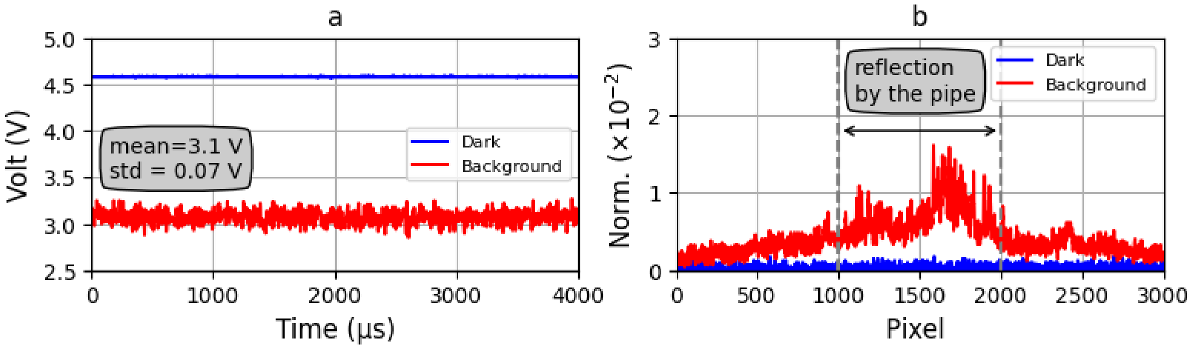

Figure 3.1: The signals measured by the PMT and CCD camera when no particles are in the sensing volume. The blue and the red lines are the signals measured when the laser was switched off and on, respectively.

3.2 The intensity distribution of the laser beam

As mentioned in the previous section, the cross-section of the beam in the sensing volume was not rectangular and hence, the intensity distribution over the cross-section needed to be evaluated. Beam profilers that are able to evaluate the distribution of beam intensity in two dimensional directions are commercially available, but due to their high prices, a decision was made to build an intensity profiler made of an array of photodiodes, instead. A TSL201R-LF photodiode array which consists of 64 photodiodes was used. The dimensions of each photodiode are 120 µm in height and 70 µm in width with the centre-to-centre distance between photodiodes being 125 µm. The width of the beam is around 1.5 mm and the measurement of the intensity distribution across the beam width can be performed by around ten photodiodes.

Meanwhile, the measurement of the intensity distribution across the beam height was not performed since the height is very narrow such that only a limited number of photodiodes can measure the distribution. To illustrate, the height of the beam is around 0.4 mm and this distance corresponds to the distance covered by around three photodiodes. Using only three measurement points, the measurement will not sufficiently capture the distribution. It was decided that the intensity distribution across the beam height is modelled by nearly Gaussian distribution. The nearly Gaussian distribution is expressed as

$$I_{\mathrm{y}}(y) = e^{\frac{-y^2}{2\sigma_y^2}} \left\{ 1 + erf\!\left(\kappa \frac{[y-\xi]}{\sqrt{2}} \right) \right\}, \tag{3.1}$$

where $I_{\mathrm{y}}(y)$ is the distribution of the beam intensity parallel to the y axis; σ_y is the standard deviation of the Gaussian function $e^{\frac{-y^2}{2\sigma_y^2}}$ and is set to 0.1 mm; *erf* is the error function; κ is a parameter in the error function to skew Gaussian function and is set to 10; ξ is a parameter in the error function to set the location in the y axis at which $I_{\mathrm{y}}(y)$ is maximum and it is set to -0.18 mm to set the maximum at $y = 0$.

Three types of measurements were taken to determine the intensity distribution on the x axis across the beam width. The first is to measure the intensity distribution with the beam intensity reduced by a factor of 10^4 by the use of a neutral density filter mounted directly in front of the laser diode. This reduction was necessary to prevent the saturation of the photodiodes. The result is the intensity distribution as a function of photodiode number and is shown as a green line in Figure 3.2. The second and third measurements were undertaken to convert the intensity distribution as a function of positions in the x axis relative to the axis of symmetry of the sampling pipe. The conversion can be done by overlaying the intensity distribution with a shadow created by the pipe when the pipe is moved down along its axis of symmetry to the sensing volume. Based on the shadow, the axis of symmetry relative to the photodiodes can be determined. Since the distances between the photodiodes are known, the relative position of the photodiodes to the axis of symmetry can be developed. In the measurements, the beam intensity was reduced by a factor of 10^2 by the use of a neutral density filter mounted directly in front of the laser diode. The intensity was then measured before and after the sampling pipe had been moved down and the results are shown in Figure 3.2 as red and magenta lines, respectively. The shadow is indicated in the figure by significant differences between the lines. Based on the results, it can be concluded that the high intensity of the beam along the x axis is concentrated within 0.5 mm from the axis of symmetry.

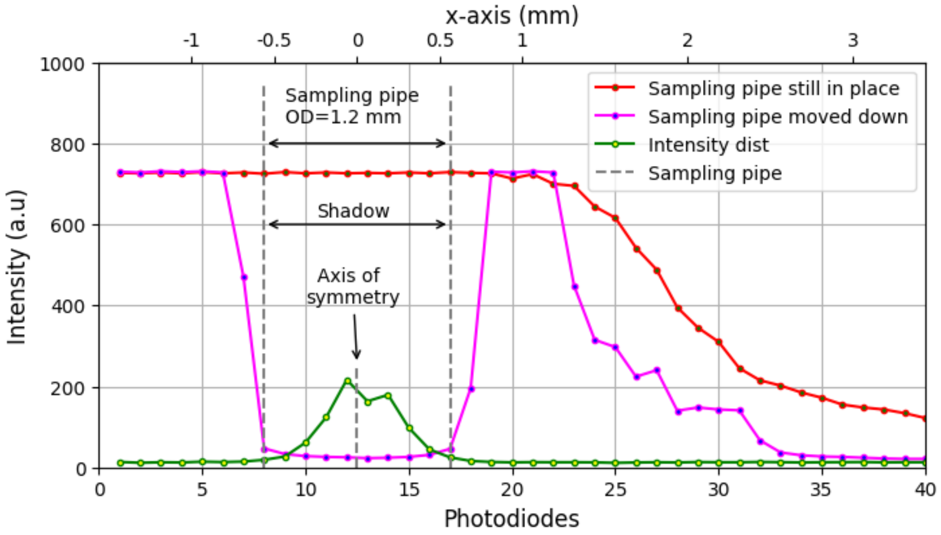

Figure 3.2: The intensity distribution of the beam along the x axis in the sensing volume. The green line is the intensity distribution as a function of the photodiodes. The intensity was measured with the beam reduced by a factor of 10^4. The spatial coordinate of the photodiodes is determined relative to the sampling pipe axis of symmetry. The determination was established by creating a shadow of the sampling pipe as the sampling pipe was moved down to the sensing volume. In the shadow measurement, the beam intensity was reduced by a factor of 10^2. The intensity distribution before and after the sampling pipe was moved down were measured and the results are plotted as the red and magenta lines, respectively. The shadow is indicated by contrast changes between the two lines. Based on the shadow, the axis of symmetry can be indicated and the spatial coordinate of the photodiodes can be determined. The spatial coordinates are shown in the top horizontal axis.

A two-dimensional distribution of the beam intensity can be constructed using the measured distribution across the beam width and the modelled distribution along the beam height. The construction is shown in Figure 3.3, with the x and y axis shown in the figure corresponding to the width and the height direction, respectively. A consequence of this distribution is that the intensity of light scattered by single particles is also a function of the locations where the single particles are being illuminated.

It should be noted that:

- the mid-point of the PMT is located at around +6 mm and the mid-point of the CCD camera is located at around -6 mm in the x axis. The thickness of the glass window in the CCD camera is around 0.7 mm,
- the flow of single particles is parallel with the y axis with the flow direction from -y to +y,

- The propagation of the beam is parallel with the z axis with the propagation direction from -z to +z.

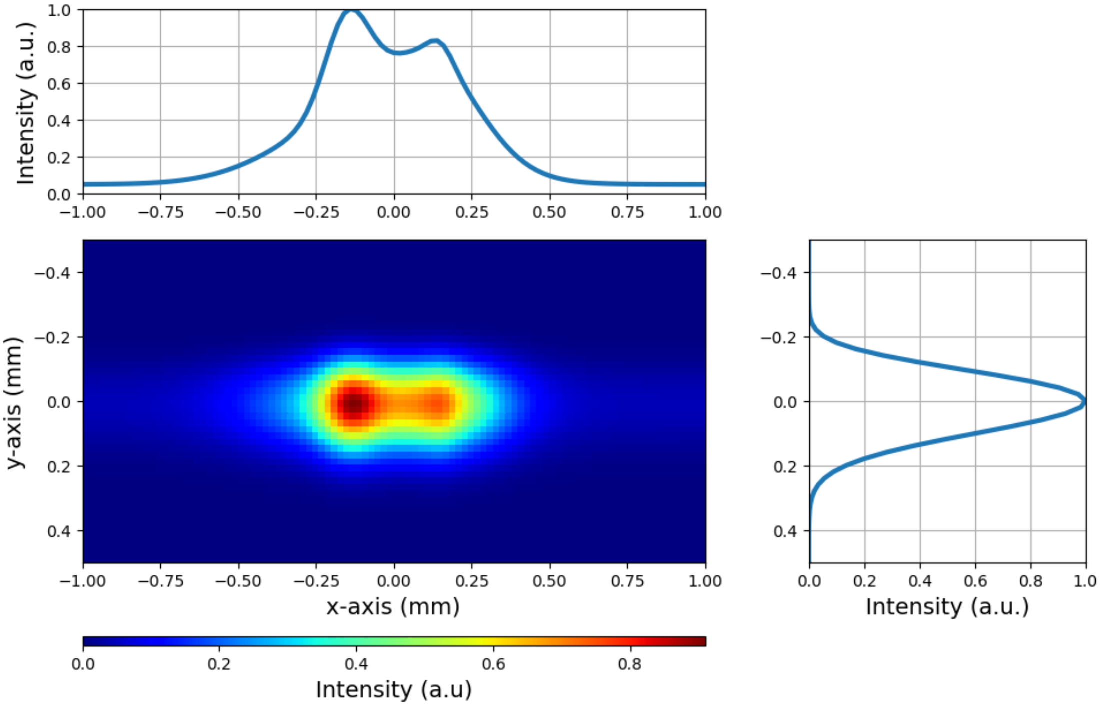

Figure 3.3: The two-dimensional intensity distribution across the x-y plane in the scattering volume. The projections of the intensity at the x and y axis are shown at the top and left figure, respectively. The beam propagates through the plane.

3.3 Monodisperse aerosol generation

The ideal aerosols to test particle size measuring instruments are monodisperse aerosols whose particles are of known stable size and refractive index. A simple way to generate this type of aerosol is by nebulising suspensions containing monodisperse spheres with known chemical and physical properties. Droplets generated from the nebulisation may contain a number of these spheres. These droplets are called “non-empty” droplets. “Non-empty” droplets which contain single spheres are called singlets and, when these droplets evaporate, spherical solid particles remain. Other “non-empty” droplets may contain multiple spheres and, when the droplets evaporate, clusters of spherical particles are formed. The nebulisation can also produce droplets which do not contain any sphere. These droplets are called “empty” droplets. The term “empty” does not imply that the droplets do not contain any particles: they are likely to contain substances other than the spheres, such as surfactants added by suspension manufacturers to stabilise the suspensions, the impurities from water in the suspensions, or particles due to the leaching of the suspension storage container wall [Krarnes et al., 1991; LaFranchi et al., 2003]. When “empty” droplets evaporate, substances they contain solidify and form particles called residual particles. Residual particles can cause a background of small particles in the size distribution of generated monodisperse aerosols. When generating monodisperse aerosols by nebulisation, it is important to have:

- a high ratio of the number of singlets to the number of “non-empty” droplets, otherwise known as the singlet ratio;
- residual particles whose sizes do not overlap with the size of the spheres.

The expected singlet ratio and the expected size distribution of residual particles in nebulising suspensions can be calculated from the probability of generating singlets as well as “empty” and “non-empty” droplets. Raabe modelled the probability of the number of spheres being in a nebulising droplet using the Poisson distribution, with the expected number of spheres in the droplet as the average number of spheres contained in the volume of the droplet [Raabe, 1968]. If the volume fraction of the spheres in the suspensions is F then the average number of spheres with the size d_s contained in a droplet with the size d_d can be calculated as

$$\bar{N}_\mathrm{s} = F\left(\frac{d_\mathrm{d}}{d_\mathrm{s}}\right)^3, \tag{3.2}$$

where $\bar{N}_\mathrm{d}$ is the average number of spheres. When suspensions are prepared by diluting stock suspensions with the dilution factor Y, then Equation 3.2 can be modified into

$$\bar{N}_\mathrm{s} = \frac{F_\mathrm{stc}}{Y}\left(\frac{d_\mathrm{d}}{d_\mathrm{s}}\right)^3, \tag{3.3}$$

where F_stc is the volume fraction of the spheres in stock suspensions. The probability of having N_s number of spheres in a droplet can then be expressed as

$$P_\mathrm{d}(N_\mathrm{s}) = \frac{\bar{N}_\mathrm{s}^{N_\mathrm{s}}\, e^{-\bar{N}_\mathrm{s}}}{N_\mathrm{s}!}. \tag{3.4}$$

Raabe further formulated the dilution factor needed to generate more than 90% of singlet ratio as

$$R_1 \cong 1 - \frac{F_\mathrm{stc}\, d_\mathrm{v}^3\, e^{13.5 \ln^2 \sigma_\mathrm{g}} (1 - 0.5\, e^{\ln^2 \sigma_\mathrm{g}})}{Y\, d_\mathrm{p}^3}, \tag{3.5}$$

where R_1 is the singlet ratio; d_v and σ_g are the count median diameter and the geometric standard deviation of droplet size distribution generated by nebulisers. Based on the singlet ratio, the ratio of "empty" droplets to total droplets, called the "empty" droplet ratio, R_0, can be calculated. Raabe expressed the ratio as

$$R_0 \cong 1 - \frac{1 - R_1}{e^{9 \ln^2 \sigma_\mathrm{g}} \left(1 - 0.5\, e^{\ln^2 \sigma_\mathrm{g}}\right)}. \tag{3.6}$$

Equations 3.5 and 3.6 are valid for $\sigma_\mathrm{g} \leq 2.1$ and $R_1 \geq 90\%$.

The suspensions used in the calibration were prepared by diluting four stock suspensions, which contain monodisperse PSL beads and trace amount of surfactants. The surfactants were added by the suspension manufacturers to prevent the coagulation of the PSL beads. Some manufacturers specify the range of the surfactant mass fraction they added while others do not. The physical properties of the beads suspended in the stock suspensions as well as the range of surfactants mass fraction are listed in Table 3.1. Since the mass density of the beads, water and surfactant are similar, the mass fraction listed in the table can be approximated as the volume fraction of the beads and surfactants for the corresponding stock suspensions.

Table 3.1: Some physical properties of PSL beads and surfactants contained in the four stock suspensions used in the calibration. The refractive index of the beads is 1.59 and the mass density is 1.05 g cm^{-3}. The mass density of water in the suspensions is 1.005 g cm^{-3}. The mass density of the surfactant in the stock suspensions is not specified, however, commonly used surfactants to prevent PSL bead coagulation such as Triton$^{\mathrm{TM}}$ X-100 have a surfactant mass density of 1.07 g cm^{-3}.

Samp. code	**Product name**	**Suppliers**	**Mean size & std**		**Mass fract. (%)**	
			(nm)	**(%)**	**Bead**	**surfactant**
1	LB11	Sigma-Aldrich	1,100	5	10	up to 0.5
2	42744	ThermoFisher Sc.	1,800-2,200	3	2.6	trace amount
3	5200A	Duke Scientific	2,000	5	10	trace amount
4	LB30	Sigma-Aldrich	3,000	5	10	up to 0.5

Equations 3.5 and 3.6 can be used to illustrate the dilution factors for the four stock suspensions used in the calibration that can generate more than 90% singlet ratio when nebulising the diluted suspensions. In the calibration, a TOPAS ATM 220 nebuliser was used and it generated droplets whose sizes are distributed with d_v and σ_g around 240 nm and 2.1, respectively. Using these specifications along with the

stock properties listed in Table 3.1, the relation between the singlet ratio and dilution factors can be calculated using Equation 3.5. The results are shown in Figure 3.4. The corresponding "empty" droplet ratios was also calculated, based on Equation 3.6, and the results are shown in the same plot as the singlet ratio; its values can be read on the secondary vertical axis of the figure. As indicated by the figure, more than 90% of singlet and "empty" droplet ratio are likely to be generated when the four stock suspensions are diluted with dilution factors greater than 3.

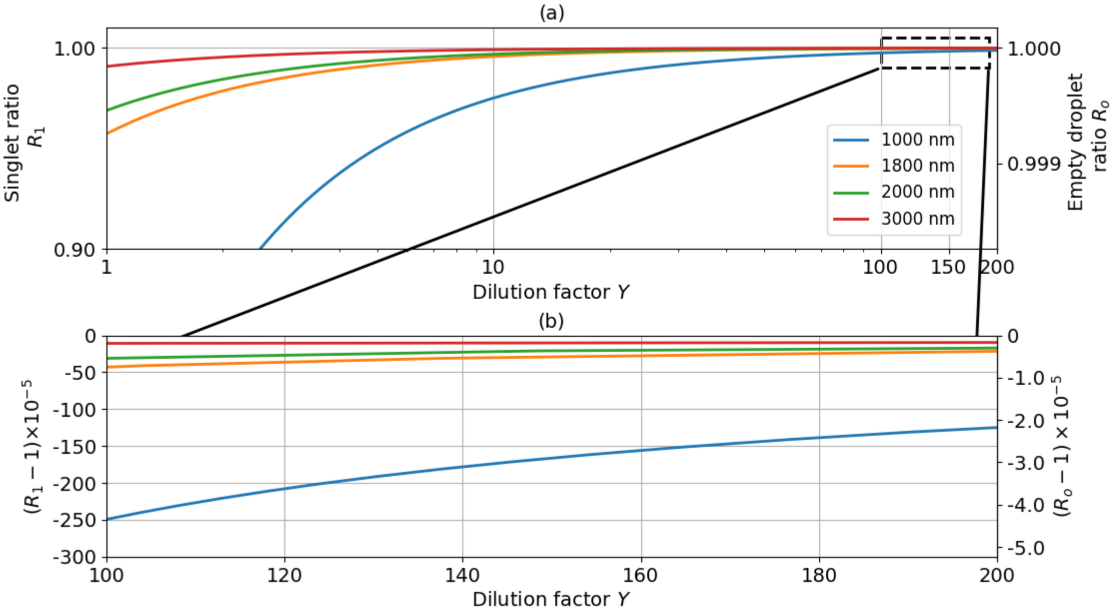

Figure 3.4: Singlet ratio and "empty" droplet ratio in nebulising suspensions diluted from four stock suspensions each containing PSL beads with the sizes : 1,000 nm, 1,800 nm, 2,000 nm and 3000 nm. The ratios are plotted as a function of dilution factors, Y. In (a), the singlet and "empty" droplet ratios are plotted for the dilution factors between 1 and 200. In (b), more detailed singlet and "empty" droplet ratios at dilution factors between 100 and 200 are plotted. In (a), the vertical scale is linear while the horizontal scale is logarithmic and in (b) both scales are linear.

Dilution factor is one of the factors that determine the size of residual particles. The selection of the dilution factor to be used in the calibration is based on the following relation. When "empty" droplets evaporate and are transformed into residual particles, the size of the residual particles is a function of the initial size of the "empty" droplets and the concentration of substances contained in the "empty" droplets. If the substances are only surfactants and the shape of the residual particles is assumed spherical, the size of the residual particles, d_{res}, generated from the evaporation of “empty” droplets with the size of d_{d0} is

$$d_{\mathrm{res}} = d_{\mathrm{d0}} \left\{ \frac{F_{\mathrm{stc}}}{Y} \right\}^{1/3} . \tag{3.7}$$

Equation 3.7 can be used to illustrate the size of residual particles generated in the nebulisation of suspensions diluted from stock suspensions listed in Table 3.1. In the illustration, residual particles are formed by evaporating three initial sizes of “empty” droplets: 1,000 nm, 9,000 nm, and 20,000 nm. The three sizes are selected as TOPAS 220 ATM nebuliser generates droplets whose sizes are mostly smaller than 20,000 nm. In the illustration, the volume fraction of the surfactants is assumed to be 0.5% and the stock suspensions are diluted with the dilution factors between 1 and 200. The results are shown in Figure 3.5. As indicated in the figure, higher dilution factors lead to smaller sizes of residual particles when evaporating “empty” droplets of the same size. It is essential to have residual particles that are much smaller than the PSL bead size contained in the diluted suspensions to avoid ambiguity when analysing the corresponding SPARCLE responses. As the smallest PSL bead used in the calibration is 1,000 nm, a dillution factor higher than 150 is essential in order to have residual particles smaller than 700 nm. However, some of the stock suspension manufacturers specify the surfactant volume fractions to be in the range between 0.1% and 0.5%, while other manufacturers only state the fraction as trace amount of surfactants. As a consequence, the actual size of residual particles might deviate from those shown in the figure.

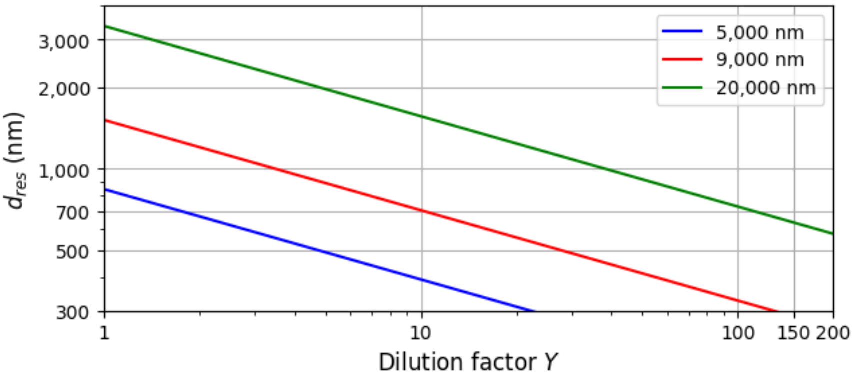

Figure 3.5: The size of residual particles generated from the evaporation of three sizes of “empty” droplets as a function of dilution factor. In this calculation, the dilution factor is between 1 and 200. It was assumed that the materials constituting the residual particles were surfactants added by suspension producers with the surfactant volume fraction of 0.5%.

If the dilution factors of the stock suspensions have been determined and the size as well as the volume fraction of the beads contained in the stock suspensions are known, the probability of generating “empty” droplets from nebulising the diluted stock suspensions can be calculated. Based on Equation 3.4, the probability is

$$P_{\mathrm{d}}(0) = e^{-\bar{N}_{\mathrm{s}}}, \tag{3.8}$$

where $P_{\mathrm{d}}(0)$ is the probability of a droplet to be an “empty” droplet and $\bar{N}_{\mathrm{s}}$ is calculated based on Equation 3.3. Equation 3.8 can be used to illustrate the probability of “empty” droplets generated in nebulising suspensions diluted from the four stock suspensions used in the calibration. In the illustration, the dilution factor of 150 and the bead volume fraction of the four stock suspensions listed in Table 3.1 are used. The probabilities are calculated as a function of droplet size and the results are shown as solid lines in Figure 3.6. As indicated in the figure, the probability of generating “empty” droplets smaller than 2,000 nm is high. Meanwhile, the probability decreases for generating “empty” droplets bigger than 2,000 nm decreases with the rate of decrease being determined by the size of the beads contained in the suspensions. As shown in the figure, the rate of decrease is higher when the nebulising suspensions contain smaller beads.

The probability discussed above can be used to derive the expected size distribution of residual particles generated from nebulising the suspensions and drying the generated droplets. The steps in the derivation are:

1. determining the expected size distribution of “empty” droplets by multiplying the probability of generating “empty” droplets as a function of droplet size with the size distribution of droplets generated by nebulisers,
2. determining the expected size distribution of residual particles by applying Equation 3.7 to the size distribution of “empty” droplets.

The size distribution of droplets generated by TOPAS 220 ATM nebuliser is shown as a dashed line in Figure 3.6. Based on the droplet size distribution, the expected size distribution of residual particles were calculated and the results are shown in Figure 3.7. The results are plotted for residual particle size between 300 nm and 1,000 nm as the detection limit of the OPC used in the calibration is 300 nm. As can be seen in the figure, smaller residual particle sizes are expected when nebulising suspensions containing smaller bead size.

The droplets generated from nebulisation should be perfectly dry in order to transform them into solid particles. The drying should be longer than the expected

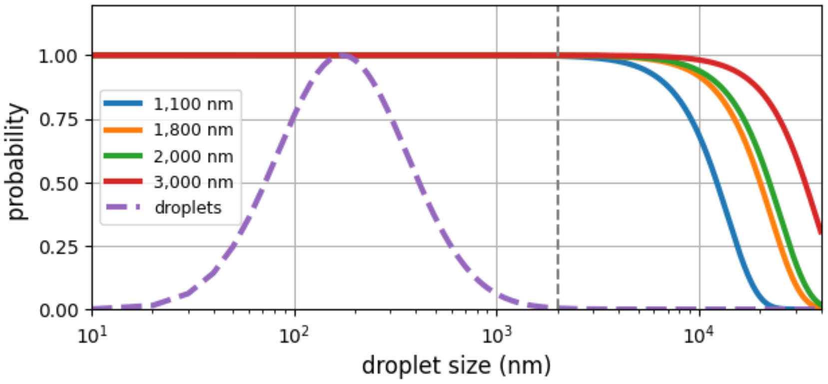

Figure 3.6: The probability of “empty” droplets as a function of droplet size. The probabilities are calculated based on droplets generated from four suspensions each containing different sizes of PSL beads. The dashed line is the size distribution of droplets generated using TOPAS 220 ATM nebuliser.

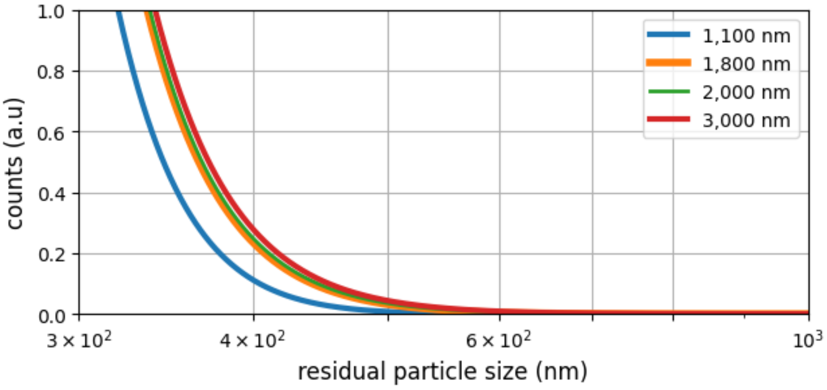

Figure 3.7: The expected size distribution of residual particles generated by nebulising suspensions each contains different size of PSL beads.

lifetime of the droplets. The lifetime of droplets is determined by their initial size as well as the temperature and relative humidity of the air around them. In this calibration, droplets were dried at ambient temperature, between 20° C and 25°C, and in relative humidity of less than 50%. In this condition, the lifetime of droplets with the size of 20,000 nm is around 0.3 s [Ferron and Soderholm, 1990]. As droplet sizes generated by TOPAS 220 ATM nebuliser are mostly smaller than 20,000 nm, the residence time of droplets in the dryers used in the calibration should be at least 0.3 s.

3.4 Calibration setup

The main components in the calibration of SPARCLE were a particle generator and a manufacturer calibrated OPC. The particle generator consisted of a nebuliser and two dryers which generates particles in two steps: by firstly, nebulising suspensions into droplets and then drying the droplets to produce solid aerosols. The solid aerosols were then delivered into SPARCLE and the OPC. The flow rate of solid aerosols flowing out of the nebuliser was higher than the sampling flow rate of SPARCLE and the sizer combined. The excess flow was then channeled into an overflow line. The nebuliser and the sizer as well as other devices used in the calibration are listed in Table 3.2. The setup of the calibration is depicted in Figure 3.8. Also shown in the figure are humidity sensors installed at each outlet of the dryers to monitor the humidity level of the air.

Table 3.2: The devices used in the SPARCLE calibration.

No	Devices	Series
1	Nebuliser or Atomiser	TOPAS ATM 220
2	Humidity sensor	HIH-4602-A/C
3	Dryers	Home made diffusion dryers
4	Particle sizer	Grimms OPC 1.108

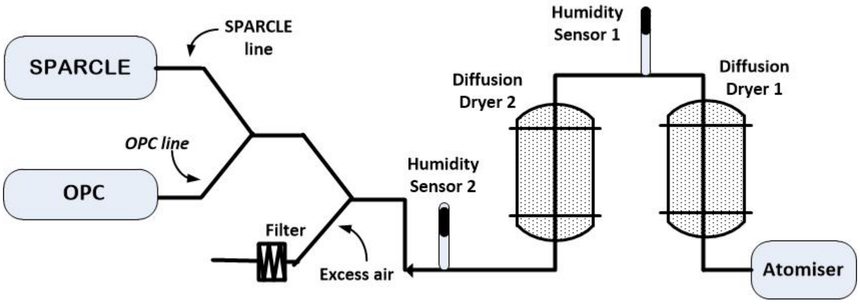

Figure 3.8: The experiment setup for the calibration of SPARCLE.

In the calibration, several parameters were acquired. Some parameters were acquired synchronously by trigger signals and others were acquired periodically with time interval of either one second or six seconds. The acquired parameters are summarised in Table 3.3.

During the calibration, the residence time of droplets in the dryers should be sufficient to perfectly dry the droplets. This time can be calculated based on the

Table 3.3: Parameters acquired during the calibration of SPARCLE.

No	**Parameter**	**Acquisition mode**	**Data format**
1	Humidity 1	Periodic	One value per second
2	Humidity 2	Periodic	
3	Aerosol size distribution	Periodic	One array per six seconds
4	Light scattering patterns	Sync.	2.000 values evenly distributed in 4 ms of acquisition time.
5	Trigger signals	Sync.	
6	Amplified PMT	Sync.	
7	SPARCLE flowrate	Sync.	
8	Laser power	Sync.	

dimension of the air path inside the dryers and the flow rate of the droplets. The flow rate was the same rate of air flowing out of the nebuliser outlet. In the calibration, the flow rate was fixed at 2 litres per minute or around $33.3 \times 10^{-6}\,\mathrm{m^3\,s^{-1}}$. This flow rate can be achieved by setting the air pressure at the nebuliser inlet of around 2 atm or 2.02×10^5 Pa. The time-of-flight of the droplets, t_d, can be expressed as

$$t_\mathrm{d} = \frac{\pi\, r_\mathrm{D}^2\, h_\mathrm{D}}{Q_\mathrm{a}}, \tag{3.9}$$

where Q_a is the flow rate of the droplets and r_D and h_D are the inner radii and the length of the dryers, respectively. As the inner radii of the dryers are around 7 mm and the total length of the dryers is around 1,000 mm, the time-of-flight was expected to be around 3 s. This time-of-flight is longer than 0.3 s, the minimum time-of-flight needed to perfectly evaporate droplets with the size of 20,000 nm as discussed in the previous section.

3.5 Particle loss in the calibration setup

In the calibration setup, particles can be lost while being transported to SPARCLE and the calibrated OPC. The loss is a combination of the losses in all transport segments that connect the nebuliser to the two instruments. The loss in each segment can be calculated using PLC software. Prior to the calculation, the transport segments were grouped into two lines: SPARCLE and OPC lines. A line is defined as a combination of transport segments that connect the nebuliser to an instrument. Some segments may be shared between the lines as illustrated in Figure 3.9. The segments of each line are tabulated in Table 3.4. The next step is to run the PLC software to calculate the loss in each segment and then calculate the combined losses in all the segments comprising the lines. The calculation was done for particles with sizes between 1 nm and 10,000 nm which are transported through the two lines. The results of the calculation are shown in Figure 3.10.a as percentages of the number of particles with sizes between 1 nm and 10,000 nm being lost at the end of the lines in comparison with the number of particles of the corresponding size entering the lines. As shown in the figure, particle loss of more than 35% was expected for particles with sizes bigger than 3,000 nm. Particle loss of more than 10% was expected for particles bigger than 2,000 nm transported through the two lines. The same percentage of loss was also expected for particles smaller than 40 nm transported through the OPC line and for particles smaller than 50 nm transported through the SPARCLE line. For particles in the size range between 100 nm and 2,000 nm, the loss was expected to be less than 10%.

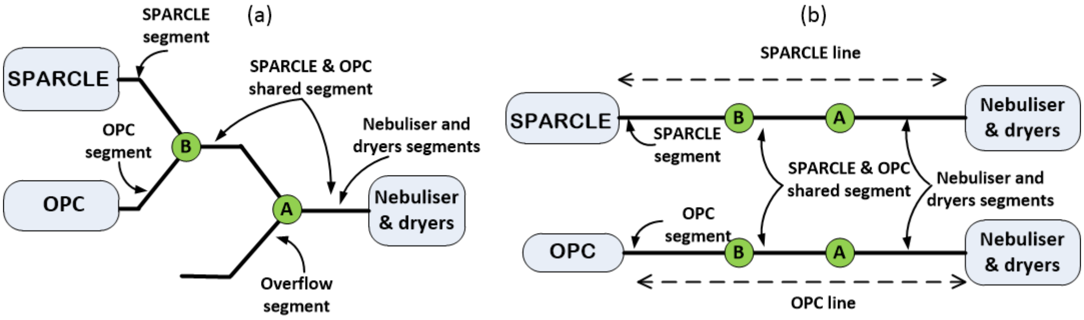

Figure 3.9: Transport line in the experiment setup

Since some segments are shared between the two lines, the size distribution of the particles flowing into the SPARCLE sensing volume can be derived from the corresponding distribution measured by the OPC. One shared segment is the segment at the outlet of the nebuliser. If the size distribution at this segment is $N_{\mathrm{A}}(d)$, then the particle size distributions at the end of the two lines are related through equations:

$$N_{\mathrm{S}}(d) = N_{\mathrm{A}}(d)\,[1 - \eta_{\mathrm{S}}(d)], \tag{3.10}$$

$$N_{\mathrm{O}}(d) = N_{\mathrm{A}}(d)\,[1 - \eta_{\mathrm{O}}(d)], \tag{3.11}$$

Section		**Flow rate** ($10^{-6}\,\mathrm{m^3\,s^{-1}}$)		**Tube length** (**m**)		**Tube dia.** ($10^{-3}\,\mathrm{m}$)		**Inclination** (°)		**Curvature** (°)	
OL	**SL**	**OL**	**SL**	**OL**	**SL**	**OL**	**SL**	**OL**	**SL**	**OL**	**SL**
1		33.3		0.03		6		90		0	
2				0.02		6		90		90	
3				0.16		3		0		0	
4				0.03		3		90		90	
5				0.1		3		90		0	
6				0.5		15		90		0	
7				0.1		3		90		0	
8				0.03		3		90		90	
9				0.05		3		0		0	
10				0.04		6		0		0	
11				0.11		3		0		0	
12				0.03		3		90		90	
13				0.1		3		90		0	
14				0.5		15		90		0	
15				0.4		3		90		180	
16				0.2		3		90		0	
17				0.05		3		0		90	
18				0.27		3		0		0	
19				0.05		3		90		90	
20				0.06		3		90		0	
21		20.0		0.06		3		70		0	
22		20.0	0.3	0.2	0.06	3	3	50	90	0	0
23		20.0	0.3	0.34	0.01	3	0.5	0	90	0	0
24	-	20.0	-	0.05	-	3	-	90	-	90	-

Table 3.4: Parameters of each segment of OPC Line (OL) and SPARCLE Line (SL) in the experimental setup. The tube diameter in each segment is considered to be constant from the beginning to the end of the segment.

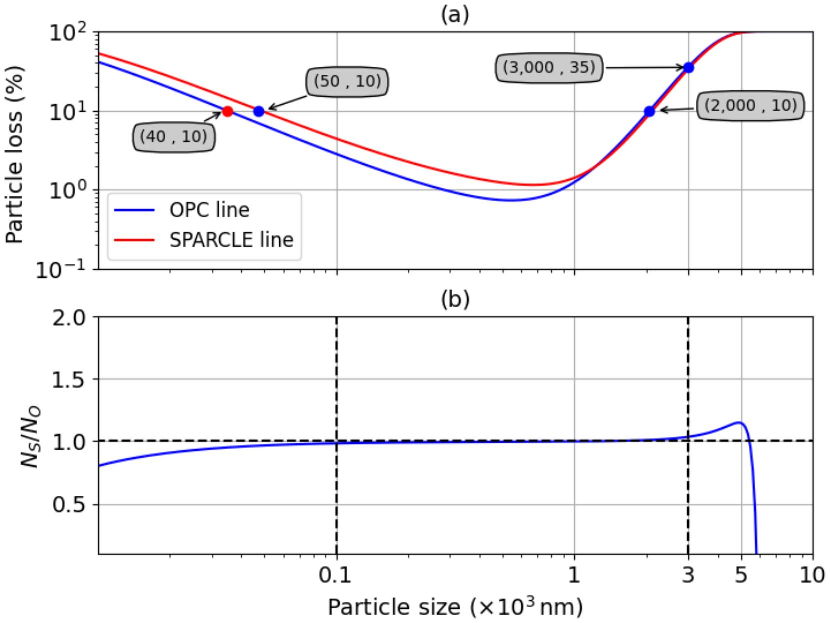

Figure 3.10: Particle loss calculation in the calibration setup. In (a) the loss of particles whose size is between 10 nm and 10,000 nm transported in the OPC and SPARCLE lines are plotted. (b) shows the number ratio of corresponding particles exiting the end of the both lines.

where $N_{\mathrm{O}}(d)$ and $N_{\mathrm{S}}(d)$ are the size distributions at the end of the OPC and SPARCLE lines, respectively; $\eta_{\mathrm{O}}(d)$ and $\eta_{\mathrm{S}}(d)$ are the percentage of particles lost when transported through the OPC and SPARCLE lines, respectively. Substituting the two equations to eliminate $N_{\mathrm{A}}(d)$ resulted in the number ratio of particles at the end of the two lines expressed as

$$\frac{N_{\mathrm{S}}(d)}{N_{\mathrm{O}}(d)} = \frac{[1-\eta_{\mathrm{S}}(d)]}{[1-\eta_{\mathrm{O}}(d)]}. \tag{3.12}$$

A plot of Equation 3.12 for particles with sizes between 10 nm and 10,000 nm is shown in Figure 3.10(b). As shown in the figure, the number ratio of particles with sizes between 100 nm and 3,000 nm is nearly equal to one. It means that within this size range, the size distribution of particles going into the SPARCLE sensing volume are nearly the same as those measured by the OPC.

3.6 Calibration procedure

Two main considerations in setting up the SPARCLE calibration procedure were:

1. to prepare nebulising suspensions which lead to high singlet ratio,
2. to ensure that generated aerosols were not contaminated by foreign materials.

The steps to prepare the nebulising suspensions were to disperse stock suspensions and dilute them. The dispersal was needed since prolonged storage of stock suspensions could lead to the deposition of PSL beads. The dispersal can be done by the ultra-sonication of stock suspensions for about one minute. After the dispersal, two drops of stock suspensions were diluted in grade-1 water with the volume of $80\,\mathrm{cm}^3$. The volume of the drops could not be precisely determined due to the relatively large size of the mouth of the stock suspension containers. The radius of the mouth is around 0.4 cm. If each drop could be approximated as spherical then the volume of each drop was approximated around $0.25\,\mathrm{cm}^3$. Using this estimation, the total volume for the two drops was estimated around $0.5\,\mathrm{cm}^3$. Hence, the dilution factor was $\frac{80}{0.5} = 160$. This dilution factor led to a high ratio of singlets as well as a high ratio of "empty" droplets as shown in Figure 3.4. There was an alternative to use an auto-pipette to sample the stock suspensions out of the container to have a better estimation of the drop volume. However, due to the risk of contamination, this alternative was not performed.

The step to prevent contamination was to clean both the nebuliser chamber and nozzle using grade-1 water prior to the measurements. The cleanliness of the chamber and the sprayer can be indicated by the ability to generate either zero or extremely low number of particles when nebulising grade-1 water. The contamination was considered to be minimum when less than 10 particles per 100 ml of air were detected during the nebulisation. On the other hand, if more than 10 particles per 100 ml were detected, the cleaning of the sprayer and the chamber was repeated. When the chamber and the sprayer had been cleaned, stock suspensions were then diluted in the chamber. The diluted suspensions were dispersed by gently shaking the chamber. Once the diluted suspensions were dispersed, measurements could be started. In addition to these steps, the background levels of the PMT and the CCD camera were recorded before and after the measurements by recording their outputs with an air filter installed in the SPARCLE inlet.

3.7 The calibration results and discussion

During calibration, SPARCLE was used to measure the responses to four monodisperse aerosols generated by nebulising four suspensions diluted from four stock suspensions listed in Table 3.1. The aerosols are encoded according to the code of the stock suspensions they were generated from. The suspensions were prepared as described in the calibration procedure. The results of the calibration are eight parameters acquired for each aerosols sample. The parameters are those listed in Table 3.3. The number of data for parameters which were acquired synchronously is 10,000 data.

3.7.1 Relative humidity

The relative humidity (RH) of the four monodisperse aerosols during the calibration runs are shown in Figure 3.11. The RHs on the outlets of the first and the second dryer are indicated by red and green lines, respectively. The RHs were less than 50% during all measurements. With these RH levels, droplets were expected to be perfectly dried as discussed in Section 3.4.

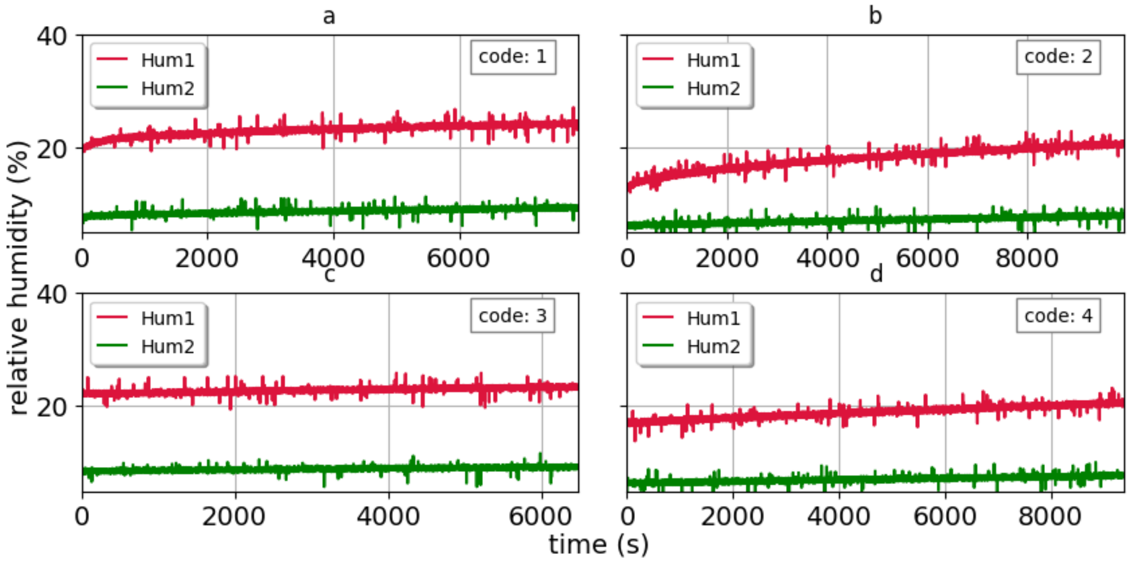

Figure 3.11: The relative humidity (RH) of the aerosols measured on the outlet of the dryers. The red lines are the RHs at the outlet of the first dryer and the green lines are those at the second dryer. The sample codes of the aerosols are shown in the top right of each plot.

3.7.2 The SPARCLE sampling flowrates

The SPARCLE sampling flowrates in measuring the aerosols during the calibration are shown in Figure 3.12. In general, the flowrates fluctuated with a standard deviation of less than 10% of the corresponding average flowrates. The average flowrates were not the same for all the aerosol measurements and this is to be expected as the pump flow is running without feedback control. For example, the average flow rates in measuring samples 1 and 4 are 161×10^{-9} m^{3}s^{-1} and 135×10^{-9} m^{3}s^{-1}. The discrepancies could be due to the slight differences in voltages applied to the pump, since the measurements were not done consecutively. Each measurement was undertaken in one working day and the power supply of the pump was switched off between measurements.

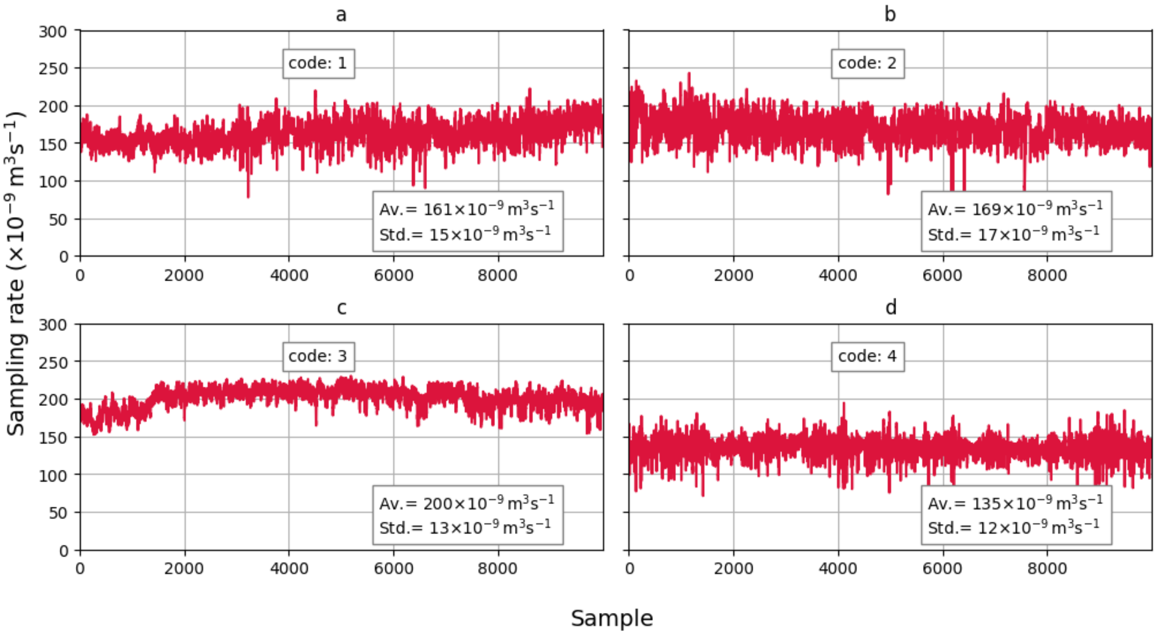

Figure 3.12: SPARCLE flow rates when measuring the four monodisperse aerosols.

3.7.3 Laser power stability

The power of a fraction of the laser beam was measured when measuring each aerosols to indicate the stability of the laser's power. The results are shown in Figure 3.13. As can be seen in the figure, the power was relatively stable with standard deviations of less than 1% of the average power.

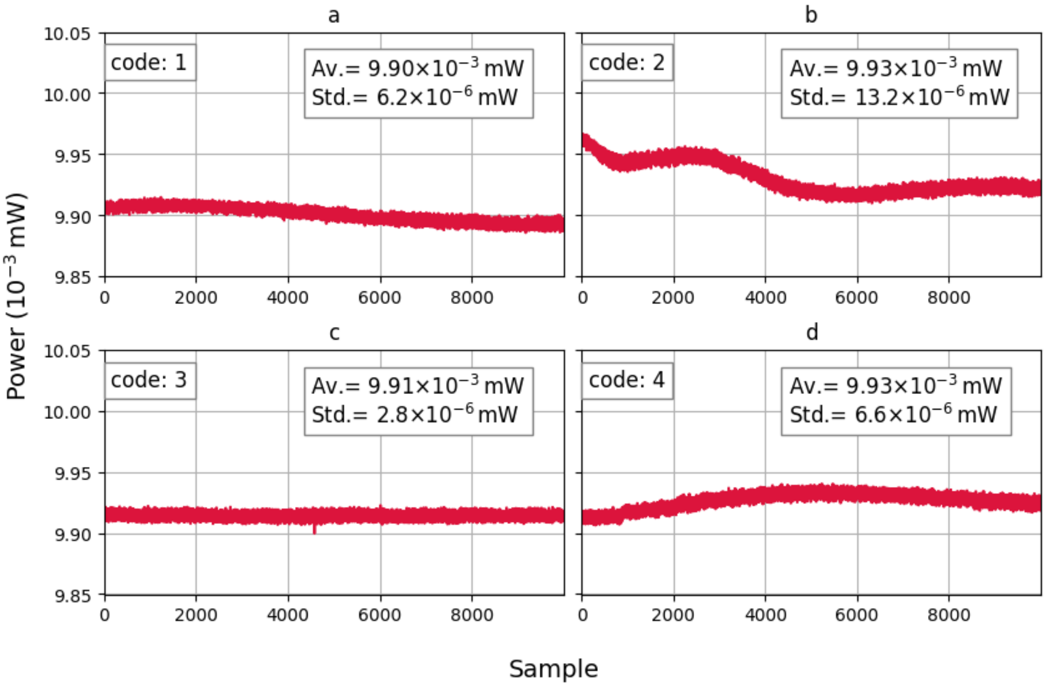

Figure 3.13: The power of a fraction of the laser beam when measuring the four monodisperse aerosols.

3.7.4 The size distribution of the monodisperse aerosols measured by the OPC

The average size distribution of the four monodisperse aerosols during the calibration are shown in Figure 3.14. Based on the figure, the distributions peaked around the corresponding PSL bead size. The distribution of particle size around PSL bead size were determined by at least three factors. First, there is a variation of the PSL bead size due to the manufacturing tolerance. Second, some amount of surfactants in singlets might be adsorbed on the surface of solid PSL beads when the singlets are perfectly dry. Third, the sizing resolution of the OPC around the size of PSL beads is low.

As shown in Figure 3.14, PSL aerosol particles of 1,800 nm, 2,000 nm, and 3,000 nm were generated. In addition to the PSL particles, small particles distributions due to solidification of empty droplets for three calibration runs encoded as 2, 3 and 4 were observed. Small particle distribution were not seen in the run encoded as 1. The small particles could be residual particles which were generated due to the solidification of “empty” droplets containing surfactants as explained in Section 3.3. The presence of the small particles resulted in the deviation of the geometric mean size, d_g, of the size distribution from the size of the PSL beads and widened the geometric standard deviation, σ_g. The absence of small particles in the aerosols containing PSL beads of size 1,100 nm might be due to the size of the corresponding residual particles which are smaller than the detection limit of the OPC. Smaller size residual particles are likely when the nebulising suspensions contain smaller beads as explained in Section 3.3. In the size distribution of the aerosols containing PSL beads of size 3,000 nm, the number of small particles is much larger than that of the PSL beads. This may be due to the nebuliser that generates only a small portion of droplets larger than 3,000 nm as indicated in the droplets size distribution shown in Fig. 3.6.

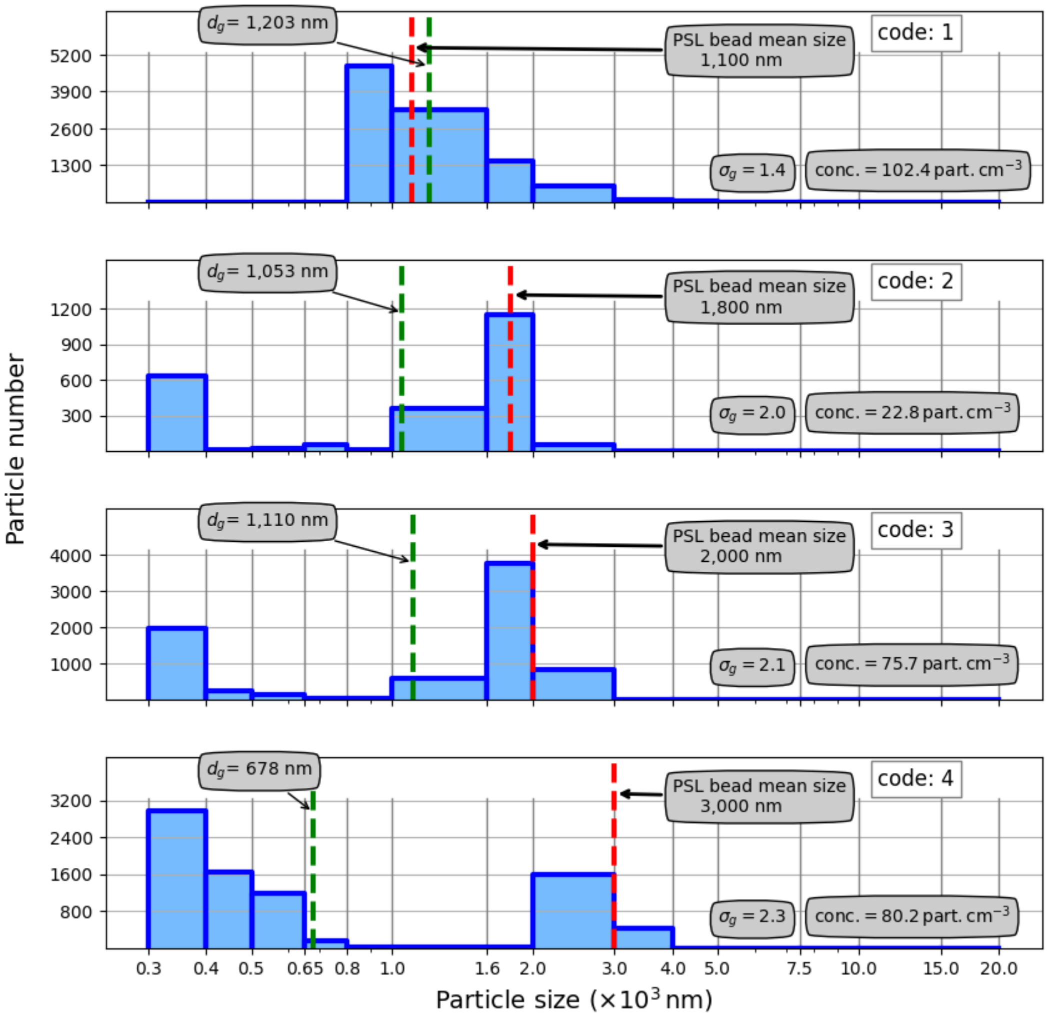

Figure 3.14: The average size distribution of the aerosols as measured by the GRIMM 1.108 OPC. The corresponding mean size of PSL beads contained in each aerosol are indicated by the red lines. The geometric mean size, d_g, of the size distribution are indicated by the green line. In addition to that, the geometric standard deviation, σ_g, and the particle number concentration of the aerosols are calculated and shown in the figure.

The OPC measures size distributions by sampling $100\,\mathrm{cm}^3$ volume of air sample. Based on this sample air volume, the particle number concentration of the four aerosols can be calculated from the measured size distributions. The calculations indicate that the number concentration for the four aerosols are around 100 particles cm^{-3} or less. As illustrated in Table 2.1, the SPARCLE coincidence error in detecting particles contained in the aerosols is expected to be around 2% or less.

3.7.5 PMT signals

One example of PMT signals measured during the calibration is shown as a red line in Figure 3.15. As shown in the figure, initially the PMT signals were at the background level. They then decreased for some time before the signals came back to the background level. This signal variation creates a pulse shaped signal distinguishable from the background. The pulse indicates an increase of light going into the PMT. The increase can be regarded as light scattered by particles transiting in the sensing volume, since the measurement of PMT signals when clean air was transported to the sensing volume did not produce pulse shaped signals. Hence, the pulse shape of the PMT signals provide indications of when particles are being illuminated by the laser beam and the intensity of the light they scatter. The pulses can be used to trigger the CCD camera to start integrating the scattering light. This is done by trigger signals which are generated when the pulses pass a threshold level. A threshold level is the level at which the pulses can be distinguished from the background. Since the variation in background can be as high as 0.4 V, based on 15-minute-observations of PMT signals when no particles were present in the sensing volume, the threshold level was set 0.4 V lower than background. One example of trigger signals generated based on the pulse which passed the threshold level is plotted as an orange line in Figure 3.15.

A pulse in PMT signals created by scattering light can be characterised by two parameters: pulse depth and pulse width. The pulse width can be associated with the time duration at which transiting particles scatter light with the scattering intensity distinguishable from the background. Meanwhile, the pulse depth can be associated with the highest intensity of scattering intensity. In determining the width and the depth of a pulse, the noise in the pulse was filtered out using the Savitzky-Golay method. A demonstration of the filtering is shown as a green line in Figure 3.15. The pulse width was determined by the duration at which the intensities of filtered pulses were at least 0.07 V lower than mean background. The voltage 0.07 V is chosen as the standard deviation of background is 0.07 V, as indicated in Figure 3.1.a. The pulse depth was determined by the highest difference between the filtered pulse and mean background. An illustration of pulse width and pulse depth determination is shown in Figure 3.15. The determination of the parameters using filtered signals can introduce biases. In the case of shot noise that trigger the data acquisition system, the corresponding pulse may be characterised by a shallow PMT pulse depth with the depth shallower than the threshold level.

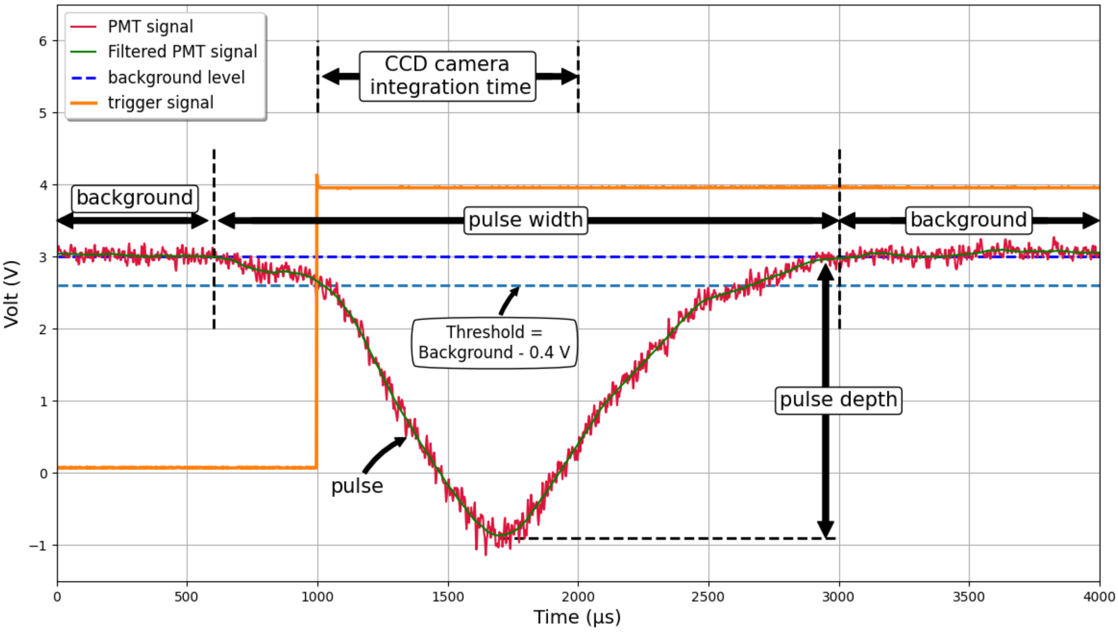

Figure 3.15: One example of PMT signals measured during the calibration. The signals are in the shape of pulses which can be characterised by pulse widths and pulse depths. The pulse is plotted as a red line and it contains noises in the form of very high frequency signals. The noise can be removed by applying a Savitzky-Golay filter. The filtered signals are plotted as a green line. Also shown in the figure, trigger signals which are generated when PMT signals are a threshold level smaller than background. The threshold level was set at 0.4 V. Once generated, trigger signals trigger the CCD camera to start integrating scattering light. The integration time is 1,000 µs and the timing of the integration is indicated in the figure.

During calibration, a data set of 10,000 PMT signals were recorded when measuring SPARCLE responses to each aerosol. The pulse width and depth of each signal was calculated with respect to the mean background measured before and after the aerosol measurement. The distribution of the pulse width and depth contained in the PMT signals for the four aerosols are shown in Figure 3.16 a-d. In each figure, the distribution of pulse width and pulse depth are shown in the top and right, respectively. The two-dimensional distribution governed by the distribution of pulse width and pulse depth is shown in the lower left in each figure. As can be seen in the top figures, the distributions of pulse width have a single peak, while the shapes of the distributions vary among data sets. The shapes are determined by at least two factors:

- sampling flow-rates. Sampling flow-rates determine the shape since the distribution of air speed in the sensing volume is a function of sampling flow-rates as discussed in Section 2.3.3,
- particle size and refractive index. Particle size and refractive index also determine the shapes since the determination of pulse width is based on scattering light intensity being distinguishable from background, and the aforementioned intensity is a function of particle size and refractive index.

The distribution of pulse depth as shown in each figure varies between data sets. In contrast to single-peak distributions seen in pulse width distributions, the pulse depth distributions have at least two peaks. The depths at which the distributions peaked also vary among the data set. For example, the distribution of pulse depth when measuring an aerosol with the mean particle size of 2,000 nm peaked at around the threshold and around 1.5 V, while when measuring an aerosol with the mean particle size of 3,000 nm, it peaked at around the threshold, around 2 V and around 4 V. There are at least three factors that determine pulse depth distributions:

- the spatial distribution of the beam intensity as discussed in Section 3.2. The distribution implies that scattering intensities are functions of the location at which particles are being illuminated,
- the variation of the particle size and refractive index contained in each aerosol. As specified by the manufacturers, the PSL bead size contained in the stock suspensions vary. Also, small particles were generated in the calibration and their refractive indices are not known,
- the bias introduced by the application of the threshold. The application filters out pulses whose depth is much smaller than the threshold, while those whose depth is slightly smaller than the threshold might still trigger the data acquisition system due to the variation of background.

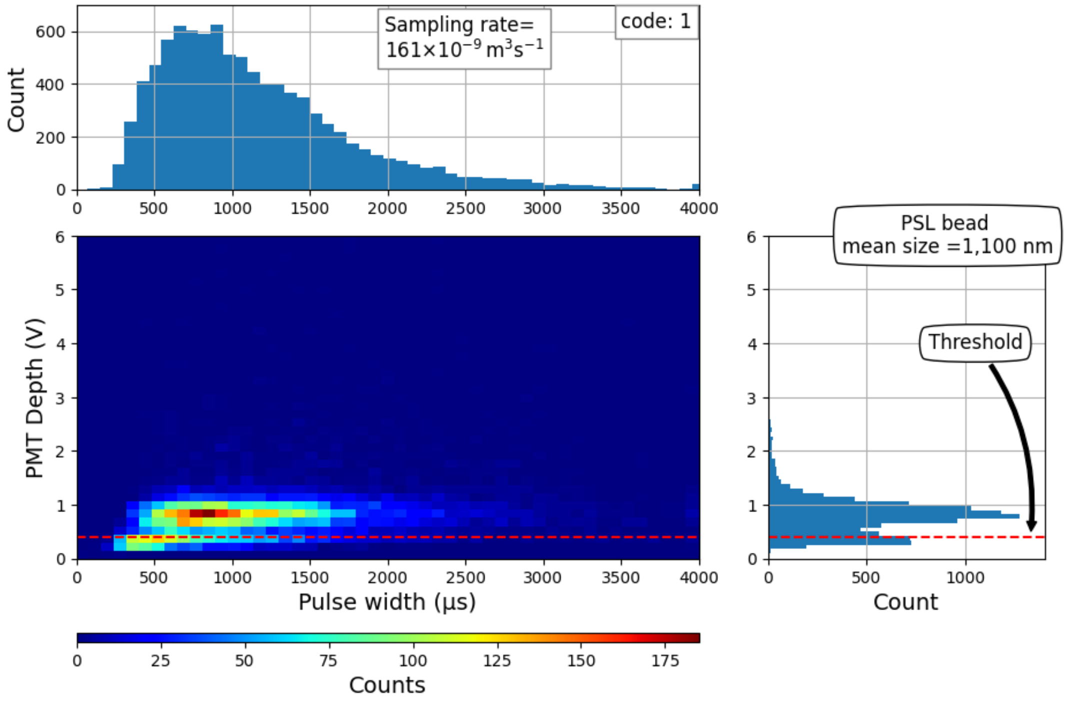

(a) Sample code 1

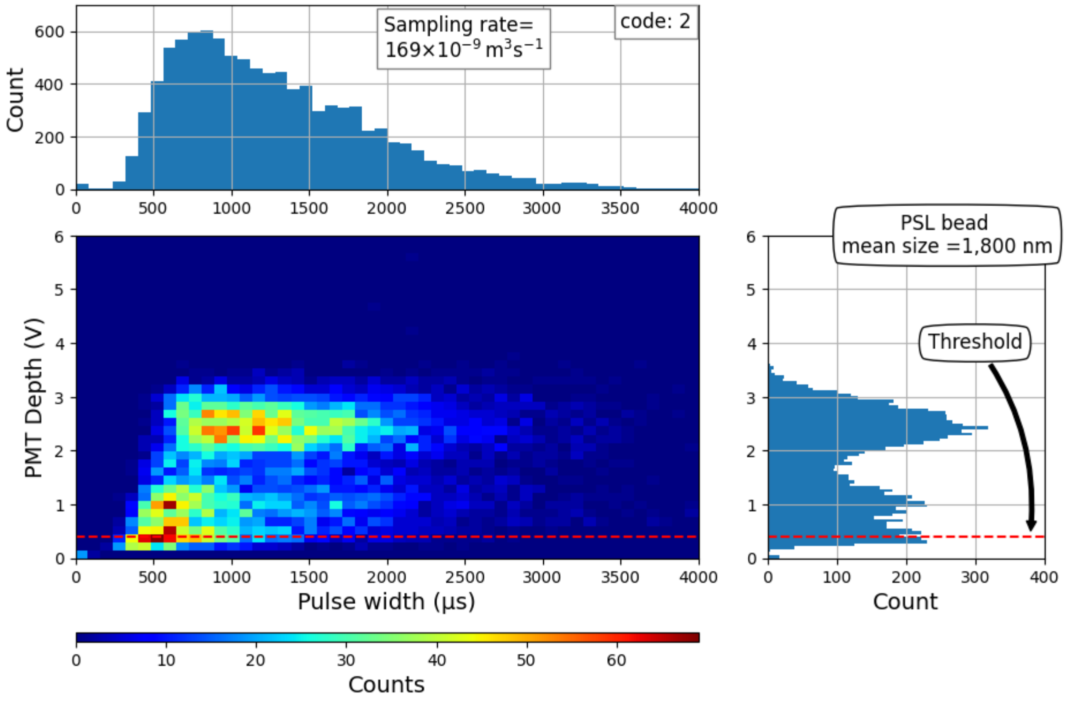

(b) Sample code 2

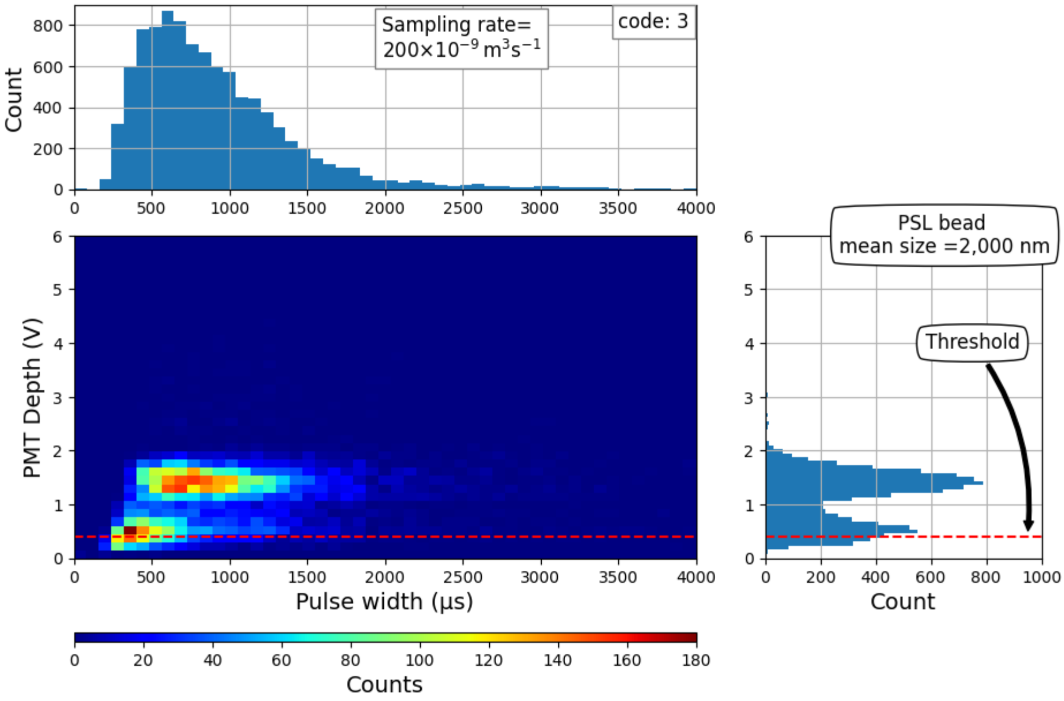

(c) Sample code 3

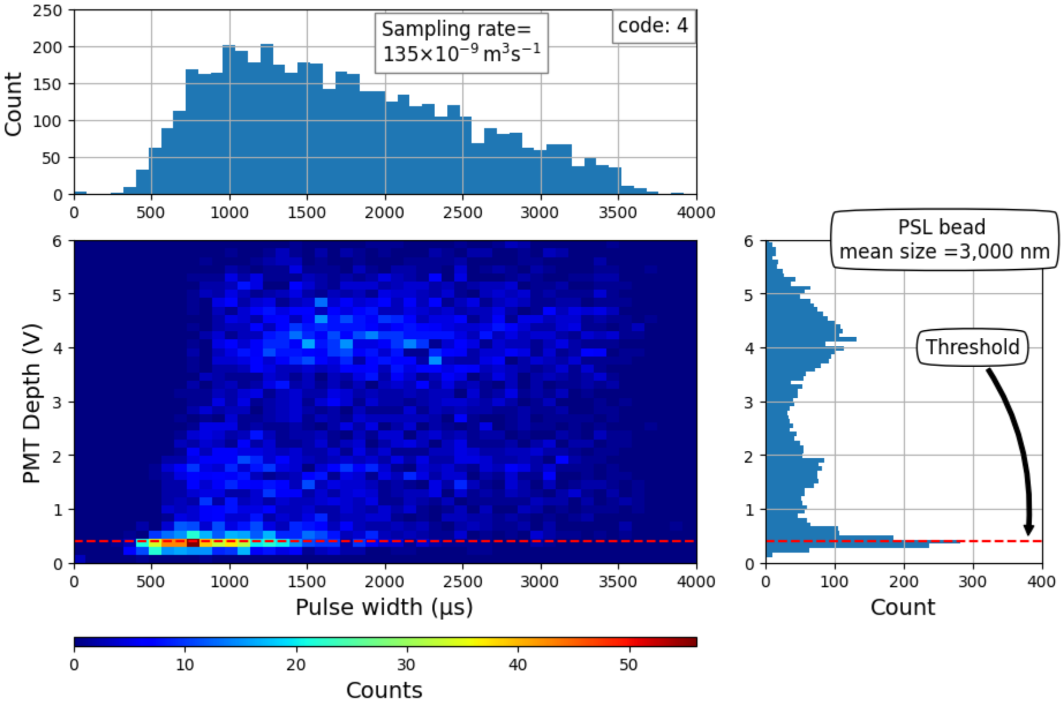

(d) Sample code 4

Figure 3.16: The two dimensional histogram of the pulse width and the pulse depth contained in PMT signals when measuring the four aerosols. The top figures and the right figures are pulse width and depth distributions, respectively.

3.7.6 CCD camera readings

Some examples of CCD camera readings when measuring the four aerosols in the calibration are shown on the right in Figures 3.18-3.21 and the corresponding PMT and trigger signals are shown on the left. In the figures, the background of the CCD camera readings have been removed. For further analysis, three parameters are defined based on the measurements by the PMT and the CCD camera. The first parameter is a fraction of the pulse area that spanned along the CCD camera integration time. The fraction of the pulse area is denoted by $\mathcal{A}$ and is shown as the green area in the figures on the left. The second parameter is the total scattered light measured by the CCD camera denoted by S and it is calculated by accumulating all the CCD camera pixels readings after the background is removed. The calculation can be expressed as

$$S = \sum_j \Big[\mathcal{V}(p_j) - \mathcal{V}_{\text{back}}(p_j)\Big], \tag{3.13}$$

where $\mathcal{V}(p_j)$ and $\mathcal{V}_{\text{back}}(p_j)$ are the readings of pixel p_j when measuring scattering light and background, respectively. In this work, $\mathcal{V}_{\text{back}}(p_j)$ is calculated by averaging CCD camera readings for 200 background measurements. The plot of $\mathcal{V}_{\text{back}}(p_j)$ is shown in Figure 3.17 as a blue line. In the same figure, CCD readings for a single measurement of background are plotted as a red line. The single measurement is denoted by $\mathcal{V}'_{\text{back}}(p_j)$. The third parameter is the signal-to-noise ratio, *SNR*, of the CCD camera readings. *SNR* is calculated by dividing S with the total readings of the CCD camera readings when measuring the background:

$$\mathit{SNR} = \frac{\sum_j \Big[\mathcal{V}(p_j) - \mathcal{V}_{\text{back}}(p_j)\Big]}{\sum_j \Big|\mathcal{V}'_{\text{back}}(p_j) - \mathcal{V}_{\text{back}}(p_j)\Big|}, \tag{3.14}$$

The S and $\mathcal{A}$ shown in the figures vary for each data set. As $\mathcal{A}$ and S are measured concurrently, it is expected that the two parameters are positively related. This type of relation is confirmed from the results shown in the figures where higher $\mathcal{A}$ leads to higher S. For example, the $\mathcal{A}$ in Figure 3.18.a is $44.8 \times 10^{-6}\,\text{V s}$ and the corresponding S in Figure 3.18.b is 1.00, while a higher $\mathcal{A}$ shown in Figure 3.18.m, with $\mathcal{A} = 990.3 \times 10^{-6}\,\text{V s}$, corresponds with a higher S which is $S = 8.23$ as shown in Figure 3.18.n.

The ratio *SNR* can be used to evaluate whether light scattering patterns measured by the CCD camera can be distinguished from the background. Visual evaluation of scattering patterns shown in Figures 3.18-3.21 suggests that the scattering patterns

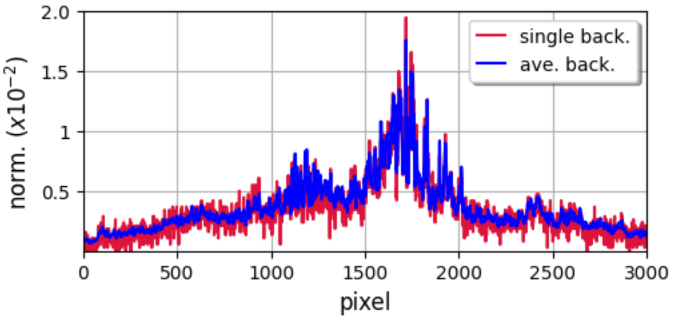

Figure 3.17: The CCD readings when measuring the background. The red line is the reading for single measurement of the background. The blue line is the average of CCD readings for 200 background measurements.

can be visually distinguished from the background when the *SNR* of the corresponding CCD camera readings are larger than 0.3. On the other hand, the patterns in CCD camera readings with *SNR* lower than 0.3 can hardly be distinguished from the background.

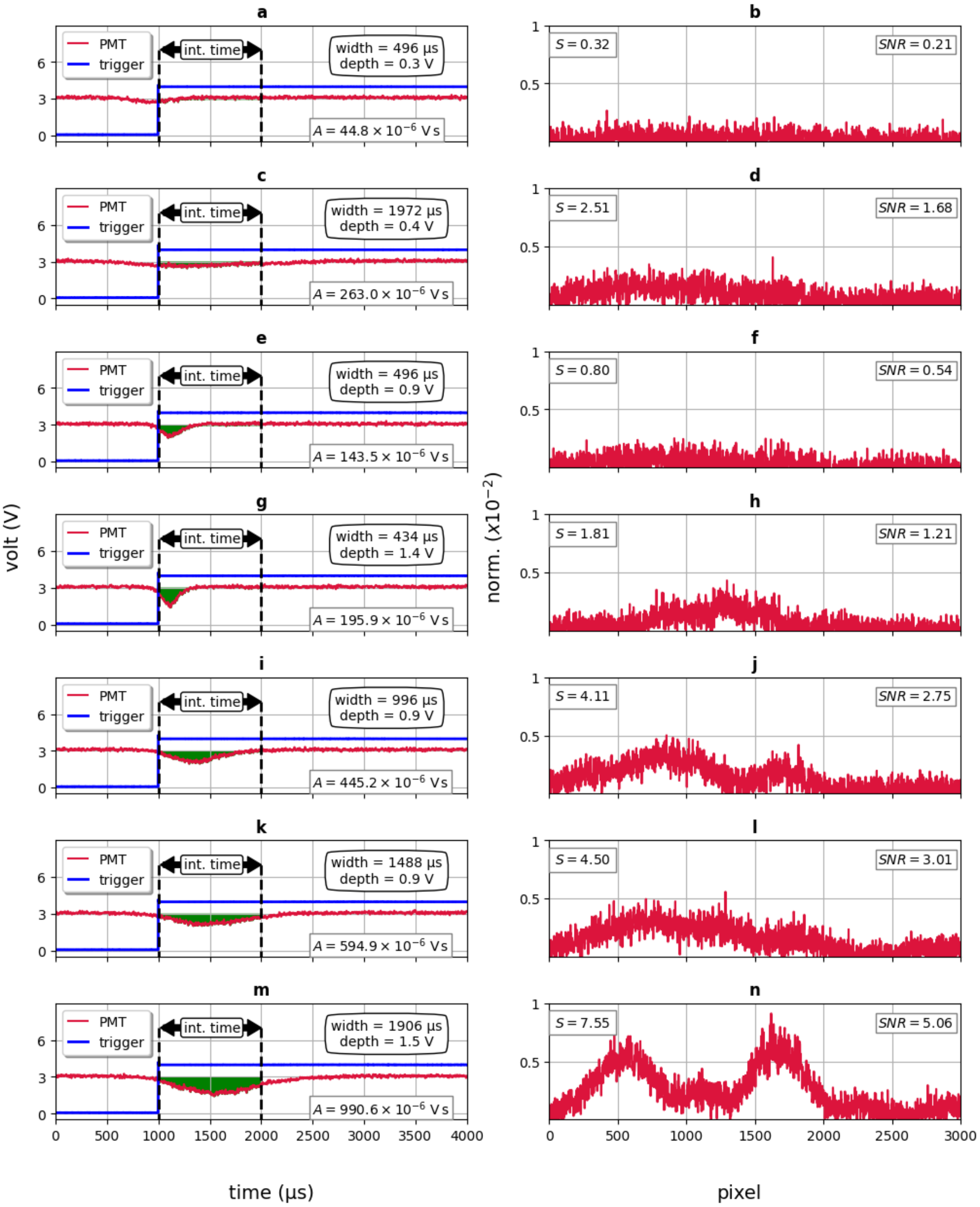

Figure 3.18: The CCD camera readings and the corresponding PMT signals measured as responses to the first aerosol particles. The mean size of the PSL bead in the aerosol is 1,100 nm.

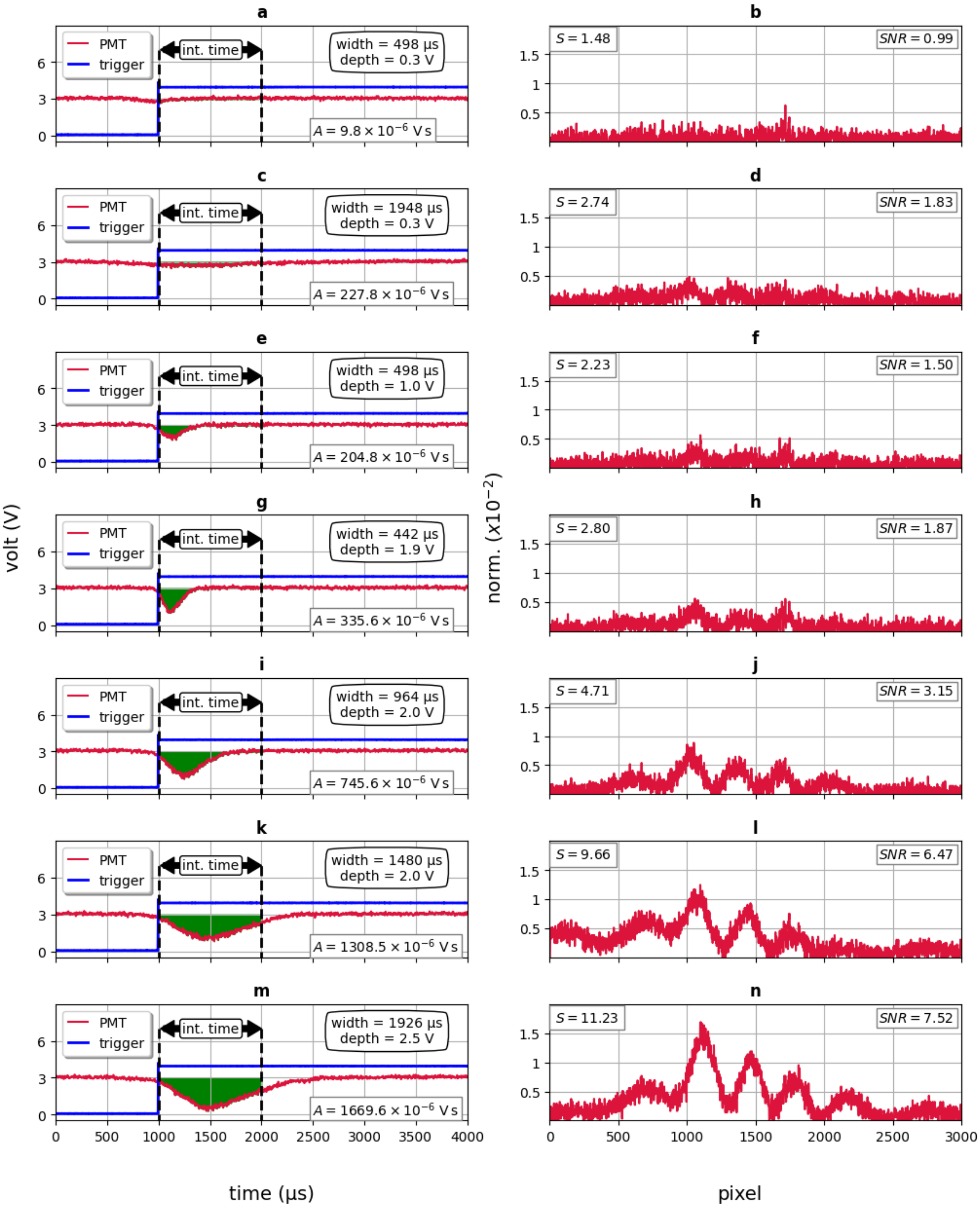

Figure 3.19: The CCD camera readings and the corresponding PMT signals measured as responses to the second aerosol particles. The mean size of the PSL bead in the aerosol is 1,800 nm.

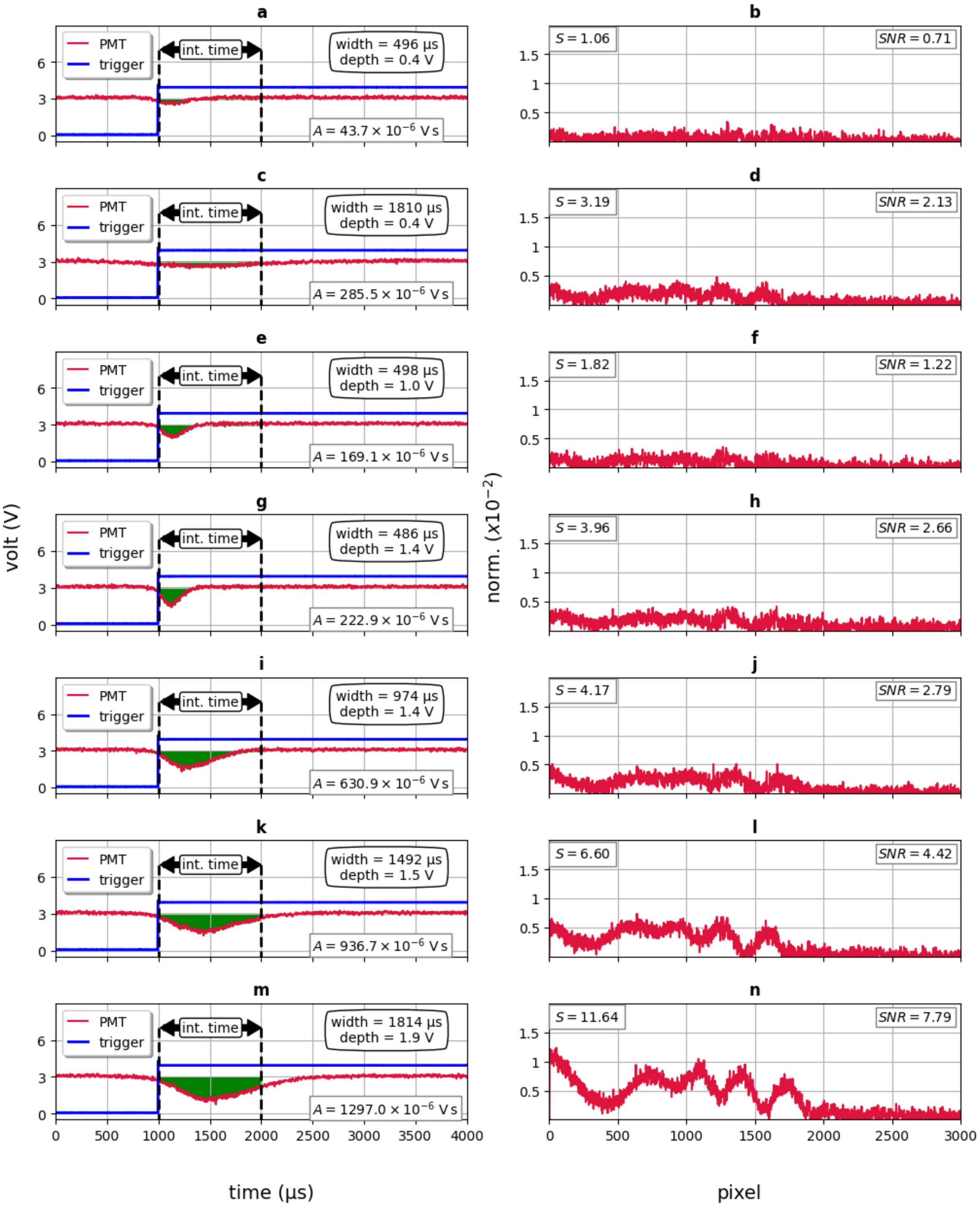

Figure 3.20: The CCD camera readings and the corresponding PMT signals measured as responses to the third aerosol particles. The mean size of the PSL bead in the aerosol is 2,000 nm.

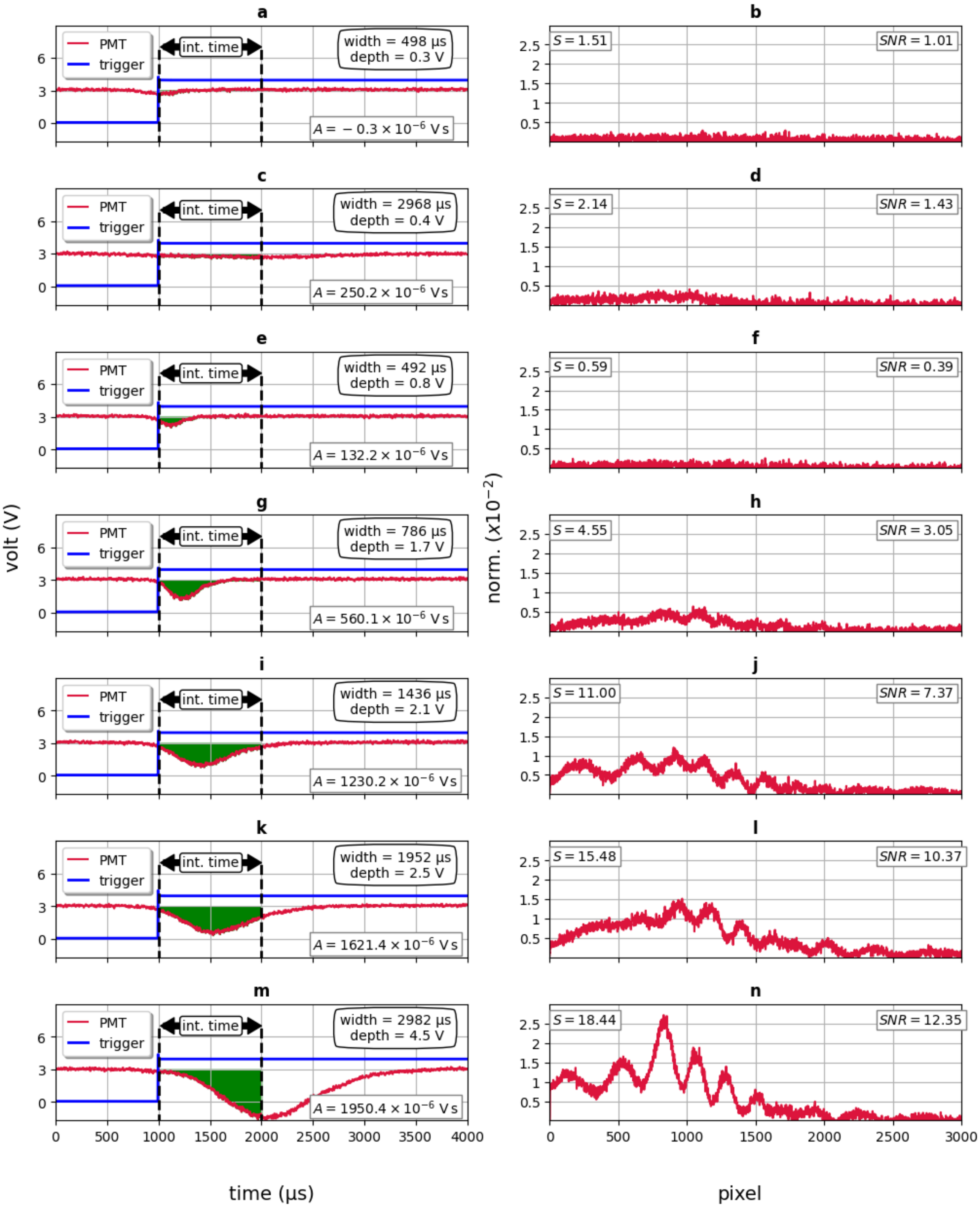

Figure 3.21: The CCD camera readings and the corresponding PMT signals measured as responses to the fourth aerosol particles. The mean size of the PSL bead in the aerosol is 3,000 nm.

To understand the relation between $\mathcal{A}$ and S, the two parameters were calculated for all data sets. The results are presented as two-dimensional histograms of $\mathcal{A}$ and S for each data set and are shown in Figure 3.22.a-3.22.d. As shown in the figures, a linear fit indicates that S is proportional to $\mathcal{A}$ with a different coefficient of proportionality for each data set. Linear correlation between $\mathcal{A}$ and S in data sets which contain various pulse widths suggests that the ratio of scattering light measured between the CCD camera and the PMT are slightly sensitive to the variation of the position of particles being illuminated in the sensing volume. Since the data sets were the results of the measurements of particles of difference size, the difference of the coefficient of proportionality among data sets could indicate that the coefficient is determined mainly by particle size. The indication is supported by the similarity between the coefficient of proportionality and the ratio of PMT signals and CCD camera readings discussed in Section 2.1.8. The similarity is summarised in Table 3.5.

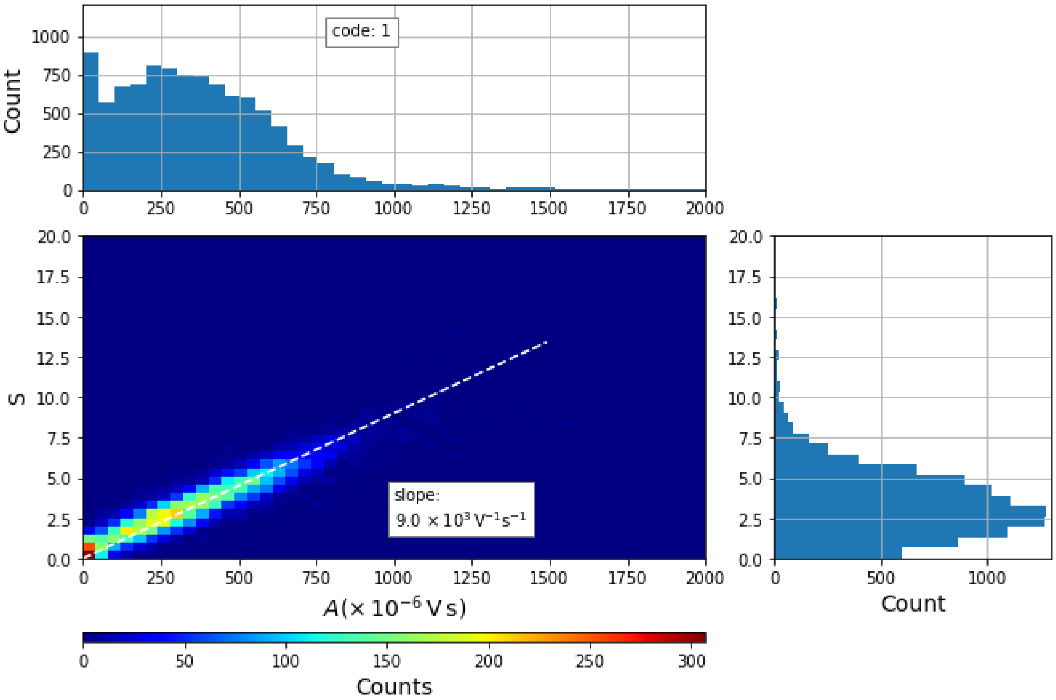

(a) The first aerosol measurements.

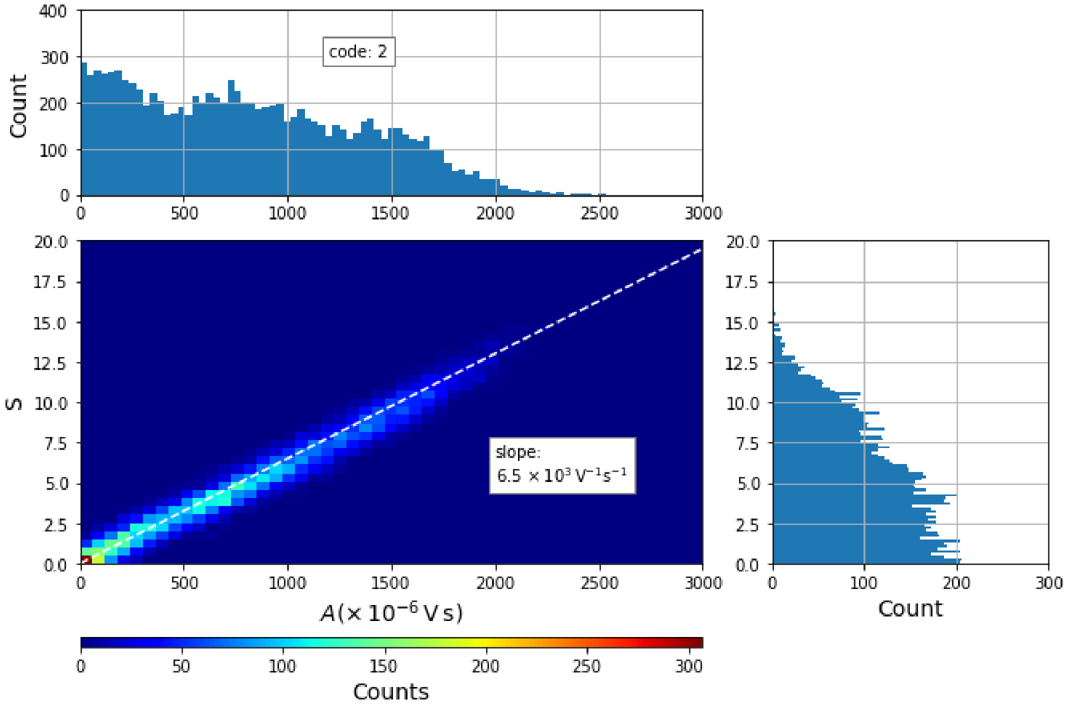

(b) The second aerosol measurements.

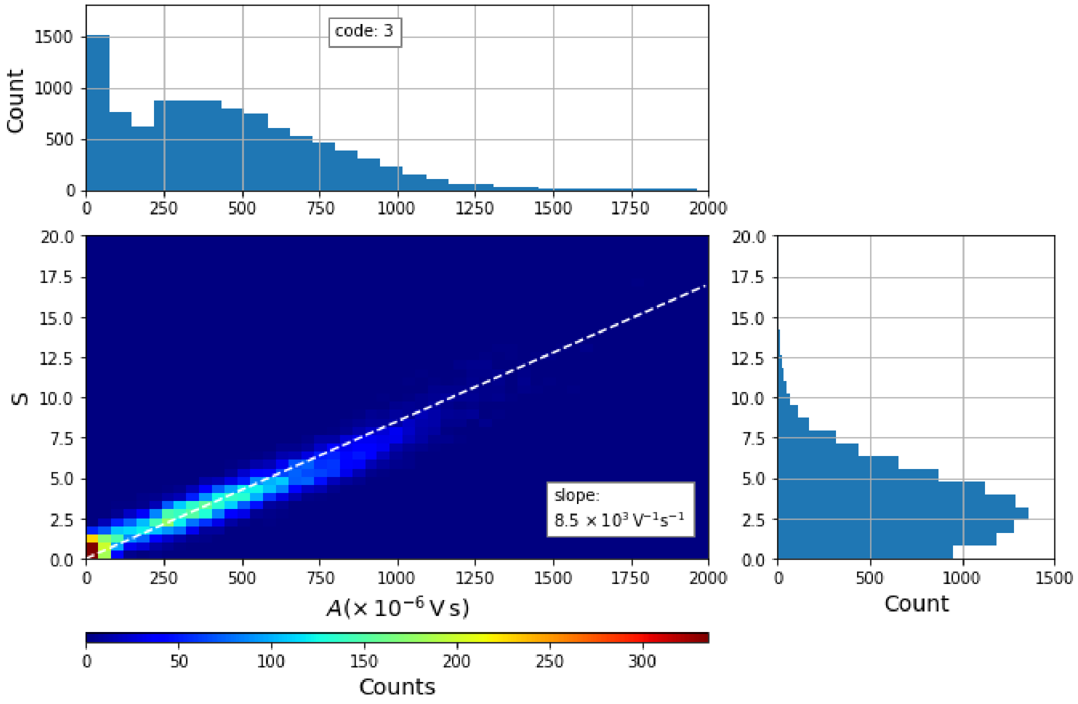

(c) The third aerosol measurements.

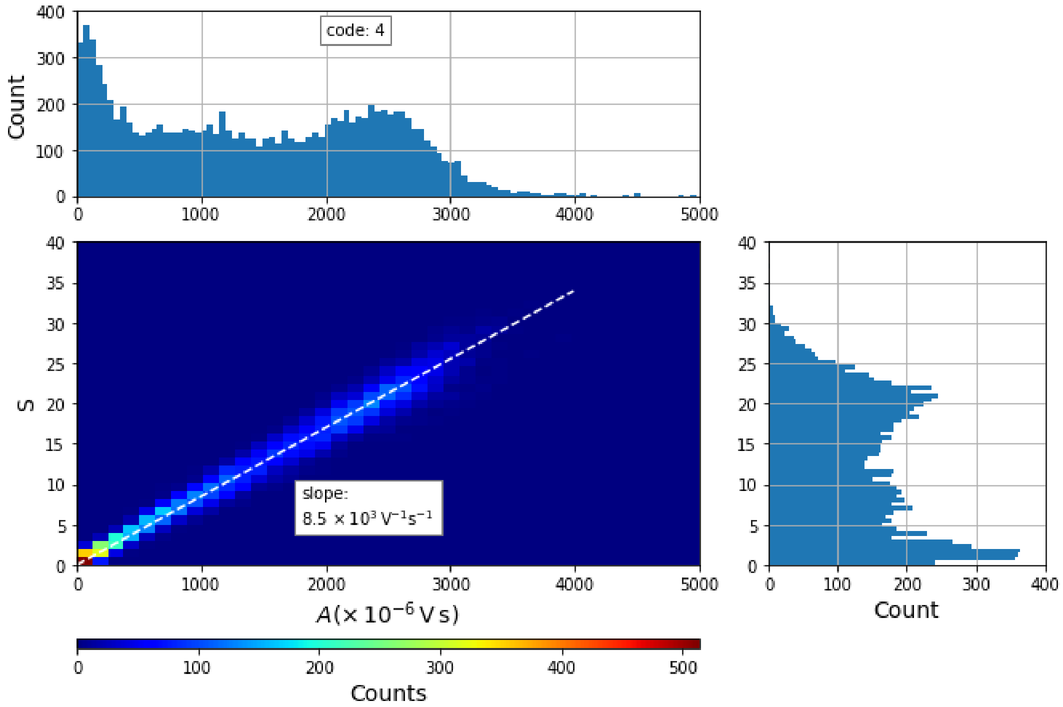

(d) The fourth aerosol measurements.

Figure 3.22: The two dimensional histograms of S and $\mathcal{A}$ calculated from the measurements of the four aerosols. In the top and right figures, the distribution of $\mathcal{A}$ and S are projected from the histogram, respectively.

PSL bead mean size (nm)	Slope $\times 10^3\ \mathrm{V}^{-1}\,\mathrm{s}$
1,100	9.0
1,800	6.5
2,000	8.5
3,000	8.5

Particle size (nm)	Ratio, see Sec. 2.1.9 $\times 10^3\ \mathrm{V}^{-1}\,\mathrm{s}$
1,080	9.0
1,785	6.5
2,000	8.5
2,990	8.5

Table 3.5: A comparison between the slope of $\mathcal{A}$-S two-dimensional histograms and the ratio of PMT signals and CCD camera readings calculated in Section 2.1.8.

3.8 A modified SPARCLE forward model

Some findings in the calibration require a modification to the SPARCLE model introduced in the second chapter. The model assumes that the beam intensity in the sensing volume is evenly distributed while the intensity measurement shows that it is not. The intensity varies along the x axis and, hence, the intensity that illuminates particles is a function of projected particle positions on the x axis. The modification was performed by accommodating the beam intensity distribution and introducing the probability of single particles traversing particular points in the x-z plane in the sensing volume. Since the beam intensity and the speed of air in the sensing volume are functions of locations, the positions at which single particles are illuminated is one of the factors that determine the intensity of the light they scatter and the duration of the scattering. If the probability of single particles traversing particular points is known, the distribution of pulse widths and depths can be simulated. In the modified model, the probability is modelled to be spatially distributed and proportional to the speed of air in which single particles are suspended. The spatial probability density function can be calculated as

$$p(x,z) = \mathcal{Q}\frac{v(x,z)}{Q_\mathrm{a}}, \tag{3.15}$$

where $p(x,z)$ and $v(x,z)$ are the probability density of single particles and the speed of air at a particular point (x,z), respectively; Q_a is the flow rate of air sample; $\mathcal{Q}$ is a normalisation factor. The integration of $p(x,z)$ for an infinite area is unity:

$$\int_{-\infty}^{\infty}\int_{-\infty}^{\infty} p(x,z)\,dx\,dz = 1. \tag{3.16}$$

The probability of particles passing through an infinitesimal area, $\mathrm{d}A = \mathrm{d}x\,\mathrm{d}z$, can be calculated as

$$P(\mathrm{d}A) = p(x,z)\,\mathrm{d}x\,\mathrm{d}z, \tag{3.17}$$

where $P(\mathrm{d}A)$ is the probability.

An illustration of the probability density across the x-z plane when sampling air with the sampling rate of $170\times10^{-9}\,\mathrm{m^3\,s^{-1}}$ are shown in Figure 3.23.a. The probability density shown in the figure was calculated based on the speed distribution as shown in Figure 2.17.b. The distribution of the beam intensity at the same plane is plotted in Figure 3.23.b. Note that single particles flow through the x-z plane. As shown in the figure, there is a high probability of single particles traversing points around the axis of the symmetry of the sampling pipe and, simultaneously, being illuminated by a high intensity of light. There is also the probability of single particles being illuminated by a low intensity of light, when single particles traverse points where coordinate components in the x axis are either bigger than around 0.25 mm or smaller than around -0.25 mm.

Based on the probability density, beam intensity, and air speed distributions in the sensing volume, SPARCLE responses to the four aerosols used in the calibration

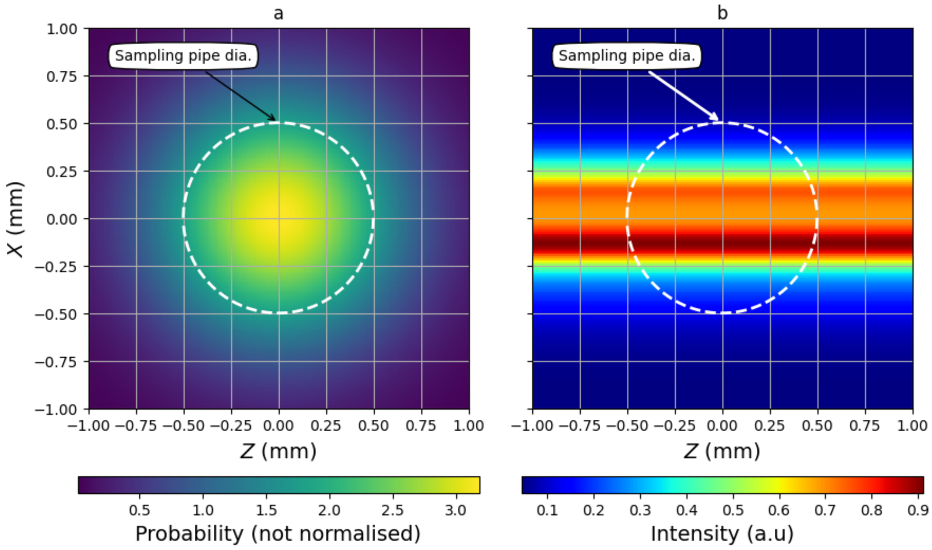

Figure 3.23: The probability density and beam intensity distribution across x-z plane in the sensing volume. The scale of the probability density is not normalised and the scale of the beam intensity distribution is an arbitrary unit. The projection of the sampling pipe in the plane is shown by the dashed line. The flow of single particles is through the plane.

can be simulated. The formula used in the simulation are detailed in Appendix A.4. The simulation can be summarised as follows:

- the simulations were done for the four data sets acquired in the calibration,
- the simulations were done for the points that are positioned in the plane and the position component in the x and the z axis are from -1 mm to 1 mm,
- at each point, the probability of single particles traversing the point is calculated based on Equation 3.17 using the mean flow rate of each data set.
- at each point, the scattering intensity measured by the PMT was calculated. To simplify the calculation, the distributions of particle size in the four aerosols are assumed to be bimodal distributions that peaked at the mean size of the PSL beads and a selected residual particle size contained in the aerosols. The bimodal distribution is shown in Figure 3.24 with the bimodal distribution plotted over the size distribution measured by the OPC. The uncertainty for PSL bead size is 5% of the mean size and it is included in the calculation. In the calculation, the refractive index of particles is 1.59 and the position of the PMT projected in the x axis is 6 mm,

- the temporal resolution of PMT measurements are modelled as a series of the measurement of light scattered by single particles while they travel parallel the y axis located before, at, and after the x-z plane. The temporal resolution can be simulated based on the distribution of the beam intensity in the y axis and the distribution of air speed at the point of interest. The speed of single particles is the same as the speed of air in which they are suspended and the speed is the same while they travel parallel the y axis in the sensing volume. The uncertainty of the flow rates is 10% and it is included in the calculation,
- based on the previous step, the pulse width and depth at each point can be determined,
- the distribution of pulse depths can be developed by accumulating the probability of pulses whose depths are within certain depth ranges. The same technique is applied in developing the distribution of pulse width.

The simulation results are shown in Figure 3.25 with the simulated distribution of pulse width and depth shown on the left and right, respectively. In the figures, the simulated distributions are scaled up to fit with the measurements. The results suggest that in general the distributions calculated from the simulation have the same shape as those generated from the measurements. Some slight deviations are identified and are summarised as follows:

- in Figure 3.25.h, a different number of peaks is identified between the simulated and the measured distribution. In the simulated distribution, more than three peaks are identified, while the measured distribution seems to have only three peaks. This deviation might be due to the uncertainty of photoelectrons being produced by the PMT which are not included in the simulation. This uncertainty is proportional to the square root of incoming photon number and, potentially, smears out peaks located at high voltages in pulse depth distributions,
- for the pulse depth distribution shown in the right figures, the measured distributions show lower number of counts compared to the simulated distribution for pulses with depths smaller than the threshold. This deviation is expected since applying the threshold in the measurements make pulses with depths shallower than the threshold less likely to be detected by the SPARCLE acquisition system.

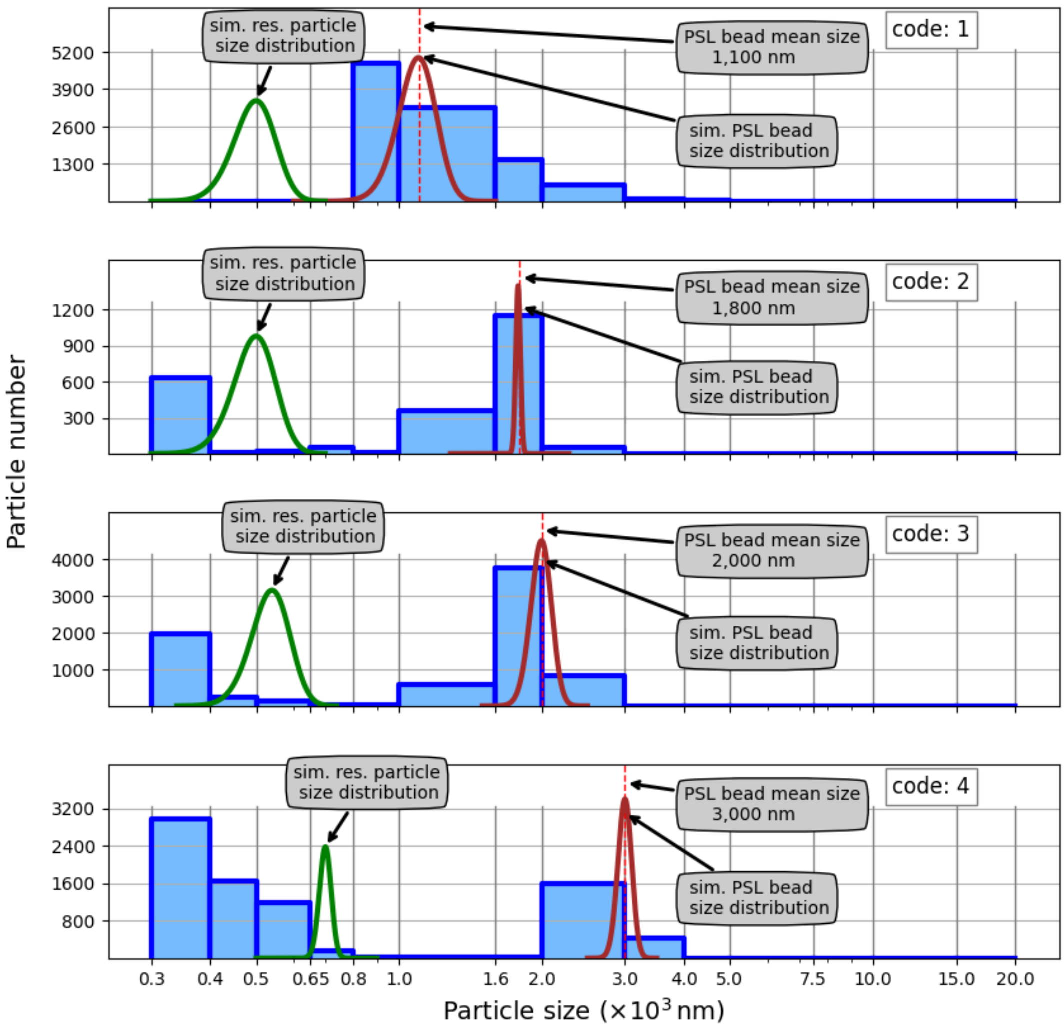

Figure 3.24: The bimodal distribution of PSL and residual particles used in the simulation of pulse depth and width. The size distribution of PSLs and residual particles is plotted as brown and green lines, respectively. To note, later calculations in the next section show that SPARCLE is not sensitive to particles smaller than 650 nm.

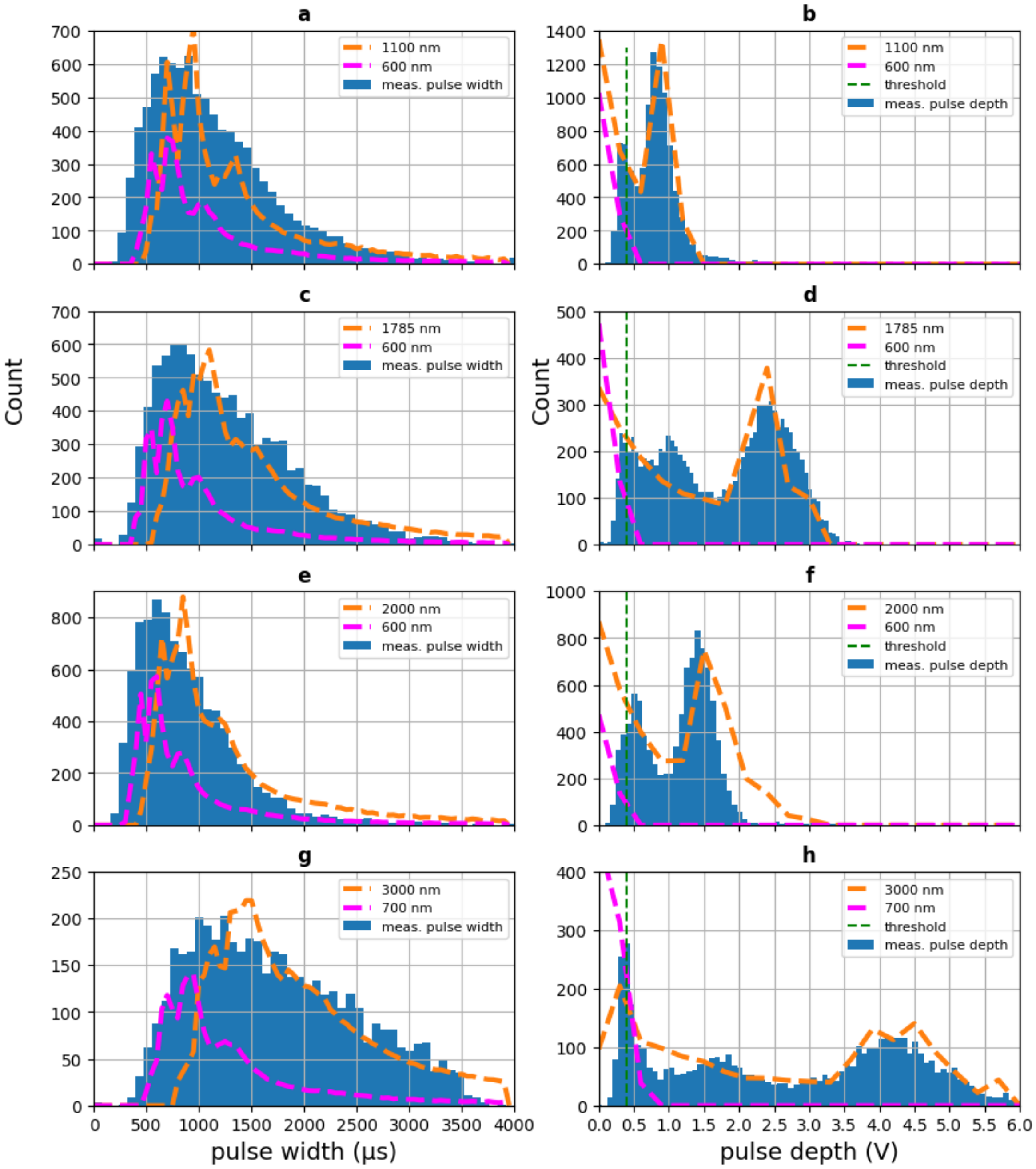

Figure 3.25: The distribution of pulse widths and pulse depths. The blue areas are the measured distributions generated from the calibration data. The dashed lines are the distributions calculated from the simulations. The simulated distributions have been scaled up to fit with the measured distributions. The scaling factor for each simulation was searched manually and the fit was evaluated visually. The simulations assumed that the size distributions of aerosol particles are bimodal distributions which peaked at two sizes. The measured distributions can be approximated as the combination of the simulated distributions for the two sizes. The two sizes are listed in the figure.

3.9 SPARCLE probability to detect particles

Using the forward model described in the section above, the probability of SPARCLE to detect particles with particular size and refractive index can be derived. The probability can be calculated by integrating the probability density of pulse depths deeper than the threshold level,

$$P(d, m) = \int_{V_\mathrm{T}}^{\infty} p(V_\mathrm{depth}) \, \mathrm{d}V_\mathrm{depth}, \tag{3.18}$$

where $P(d, m)$ is the probability of SPARCLE to detect a particle whose the size is d and the refractive index is m; $p(V_\mathrm{depth})$ is the probability density to generate pulse depth $V_\mathrm{depth}(d, m)$ as a response for light scattered by the particle. The probability density is expressed in Equation A.73; V_T is the threshold level. To illustrate, the probability density of pulse depth when a particle with the size of 2,000 nm and the refractive index of 1.59 sampled by SPARCLE is plotted in Figure 3.26. The plot was normalised that the area under the plot with pulse depth from 0 V to infinity is unity. The probability of detecting the particle can be calculated by integrating the area under the plot with pulse depth deeper than the threshold. Visually, the probability is the area in the figure colour-coded as yellow. In this illustration, the area is around 0.7. So, the probability of the SPARCLE detection system to detect a particle with the size of 2,000 nm and the refractive index of 1.59 is 0.7.

The probability of SPARCLE to detect particles whose sizes range from 100 nm to 3,000 nm was calculated. The probability of SPARCLE are plotted in Figure 3.27. As shown in the figure, the probability is zero for SPARCLE to detect particles smaller than 640 nm. This size is considered as the SPARCLE detection limit. The detection limit is slightly lower than the wavelength of the laser used in SPARCLE which is around 651 nm. Another implication of the probability is that there will be a bias in measured particle size distributions in comparison with actual size distributions.

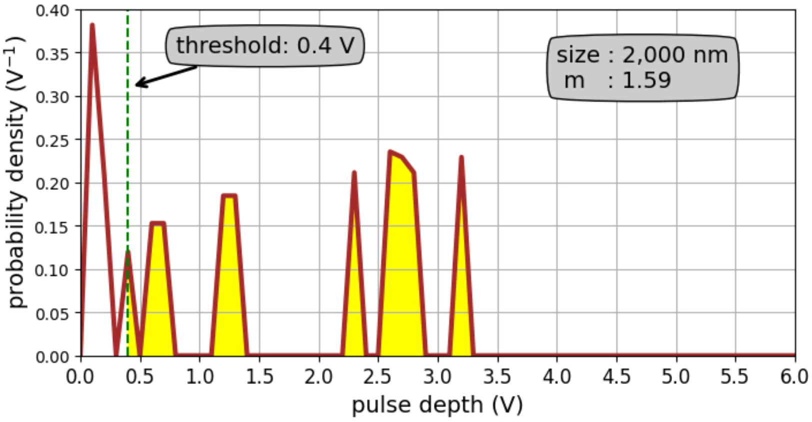

Figure 3.26: The probability density of pulse depth generated due to light scattered by a particle with the size of 2,000 nm and the refractive index of 1.59.

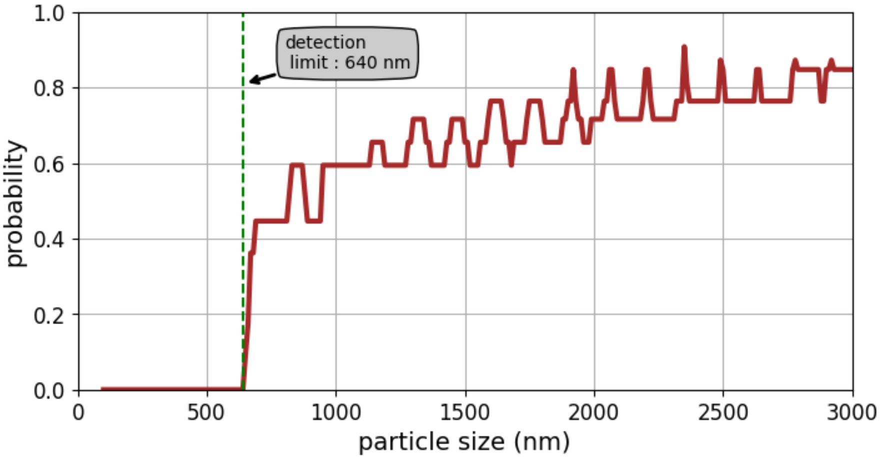

Figure 3.27: The probability of the SPARCLE detection system to detect particles whose sizes range from 100 nm to 3,000 nm. The detection limit of the SPARCLE detection system is defined as the smallest size that SPARCLE can detect. The detection limit is indicated as a green dashed line.

3.10 The particle detection rate of SPARCLE

The number of particles detected in a unit time when SPARCLE samples air is a function of the flow rate of the sampling and sampled aerosol concentration. Suppose that SPARCLE samples air with size distribution $N_\mathrm{o}(d)$ and total number N_o, the corresponding particle concentration of the air is

$$\rho_\mathrm{o} = \frac{N_\mathrm{o}}{V_\mathrm{o}}, \tag{3.19}$$

$$\rho_\mathrm{o} = \frac{\sum_d N_\mathrm{o}(d)}{V_\mathrm{o}}, \tag{3.20}$$

where ρ_o is the concentration; V_o is the volume of the air. Due to the particle lost in sampling and transporting the air to the SPARCLE sensing volume and the probability of detecting particles, the size distribution expected to be measured by SPARCLE, denoted by $N_\mathrm{S}(d)$, is

$$N_\mathrm{S}(d) = N_\mathrm{o}(d)\,[1 - \eta_\mathrm{s}(d)]\,[1 - \eta_\mathrm{t}(d)]\,P(d, m), \tag{3.21}$$

where $\eta_\mathrm{S}(d)$ and $\eta_\mathrm{t}(d)$ are the particle lost due to the sampling and transporting. Then, particle concentration expected to be measured by SPARCLE, denoted by ρ_S, can be calculated as

$$\rho_\mathrm{S} = \frac{\sum_d N_\mathrm{S}(d)}{V_\mathrm{o}}. \tag{3.22}$$

When the air is sampled over time period t_s with flow rate Q_S, the volume of air that being evaluated by SPARCLE is V_S which is equal to the difference between the volume of air being sampled by SPARCLE over t_s and the volume of air being "overlooked" by SPARCLE due to the dead time of the SPARCLE detection system in detecting N_s number of particles,

$$V_\mathrm{S} = Q_\mathrm{S}\,(t_\mathrm{s} - t_\mathrm{dead}\,N_\mathrm{S}). \tag{3.23}$$

So, ρ_S can also be expressed by

$$\rho_\mathrm{S} = \frac{N_\mathrm{S}}{V_\mathrm{S}}, \tag{3.24}$$

$$\rho_\mathrm{S} = \frac{N_\mathrm{S}}{Q_\mathrm{S}\,(t_\mathrm{s} - t_\mathrm{dead}\,N_\mathrm{S})}. \tag{3.25}$$

Using Equation 3.25 and 3.23, the detection rate of SPARCLE, denoted by Ψ_S, can be calculated as

$$\Psi_\mathrm{S} = \frac{N_\mathrm{S}}{t_\mathrm{s}}, \tag{3.26}$$

$$\Psi_\mathrm{S} = \frac{Q_\mathrm{S}\,\rho_\mathrm{S}}{1 + Q_\mathrm{S}\,\rho_\mathrm{S}\,t_\mathrm{dead}}. \tag{3.27}$$

Equations 3.21 and 3.27 were used to calculate the expected SPARCLE detection rate in the calibration runs. In the calculation, particle concentration ρ_S were calculated based on the size distribution measured by the OPC. During the calibration, particles were generated and channeled to the SPARCLE inlet hence, particle lost η_s can be omitted in the calculation using Eq. 3.21. According to Figure 3.10, the ratio between particle number flowing through the OPC and that flowing through SPARCLE are nearly unity or $\eta_{\mathrm{t}} \approx 0$. So, Equation 3.21 can be reduced into

$$N_{\mathrm{S}}(d) = N_{\mathrm{O}}(d)\, P(d). \tag{3.28}$$

Equation 3.28 was applied to the size distribution measured by the OPC and the results are shown in Figure 3.28. In the figure, the size distribution of the aerosols measured by the OPC is shown in blue while those of expected to be detected by SPARCLE is shown in red. Using the size distributions, ρ_{O} and ρ_{S} were calculated and listed in the same figure. Using calculated ρ_{S} and measured Q_{S}, the rate of detection was calculated using 3.27 and the results are listed in Table 3.6. The measured detection rates were also listed in the same table. Based on the table, the measured rates are in a good agreement with the calculated rates.

sample code	Q_{S} (cm^3 minute^{-1})	ρ_{S} (particles cm^3)	Ψ_{S}(particles minute^{-1})	
			calculated	measured
1	9.7	62	99.9	83.7 ± 23.5
2	10.2	11	57.8	61.6 ± 1.56
3	12.0	36	93.9	100.5 ± 1.43
4	8.1	17	64.1	66.0 ± 0.93

Table 3.6: The calculated and measured SPARCLE detection rate during the calibration runs.

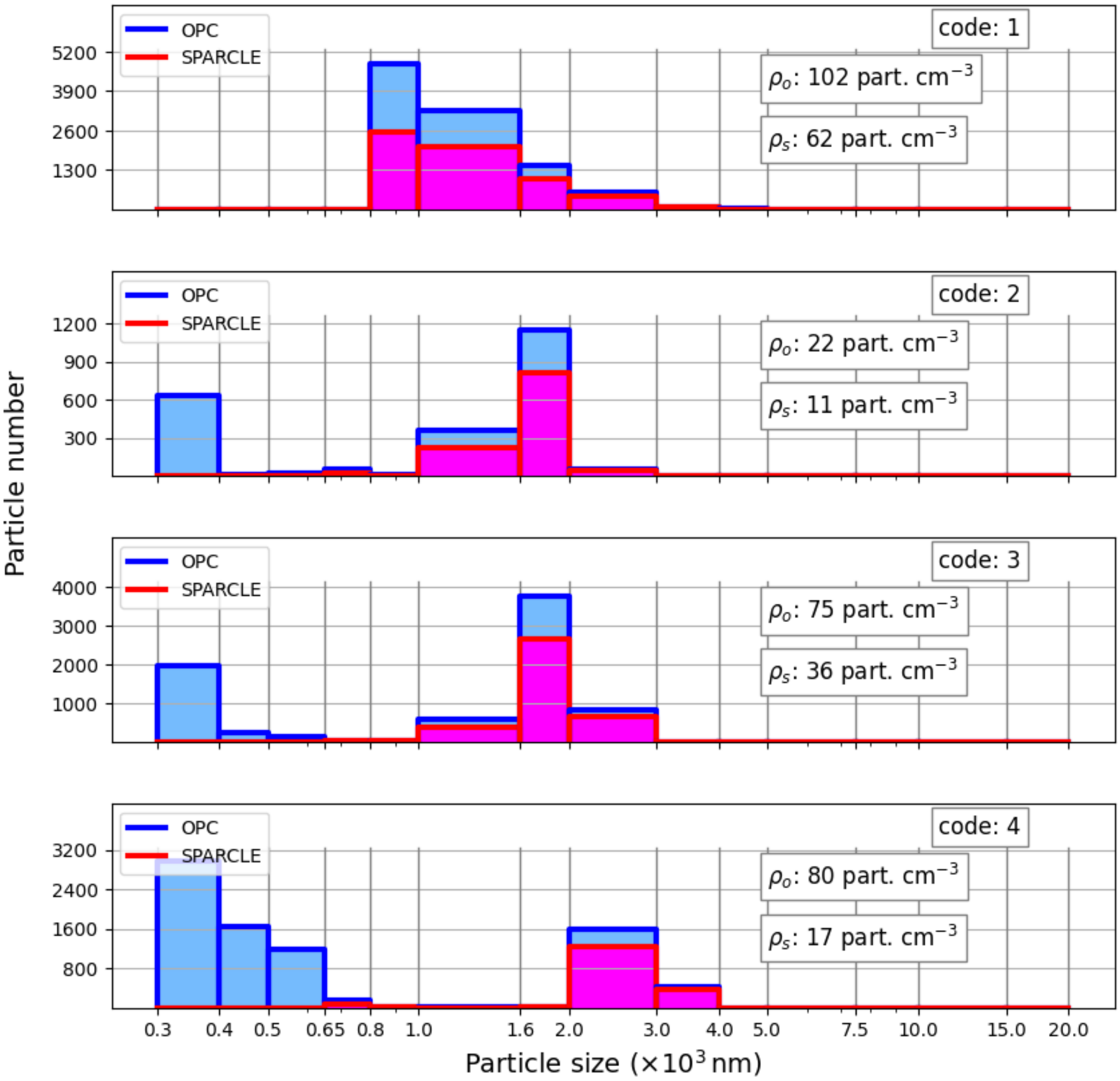

Figure 3.28: The size distribution of the aerosols measured by the OPC and the size distribution expected to be detected by SPARCLE. Note that the volumes of the air sample in the evaluation of the size distributions were $100\,\mathrm{cm}^{-3}$.

3.11 A demonstration of retrieving the size of particles from the selected calibration data

Based on the modified SPARCLE forward model described in Section 3.8, retrieving the sizes of particles from selected calibration data can be demonstrated. In the retrievals, a data sample is selected from each data set of the four measurements of aerosols in the calibration. The data samples are plotted as red lines in Figures 3.29 with the data of PMT signals plotted in the left figures while those of CCD camera readings are plotted in the right. The parameters of the forward model are varied so that the outputs of the model fit with the data samples. The parameters are particle size and the position of single particles in the x and z axis while the refractive indices of particles are set to be the same as those of the PSL beads. The goodness of the fit was determined from the standard deviation between measured and calculated CCD camera reading. The simulation of the PMT signals is as described in the previous section. The simulation of the CCD camera readings is based on the integration of scattering light for 1,000 µs, taking into consideration for the variation of illuminating light intensity during the integration time. The variation corresponds to the distribution of the beam intensity parallel with the y axis since single particles are travelling parallel with this axis during the integration time. This simulation is different from that in Chapter 2 where the illuminating light intensity was assumed to be constant during the integration time. The outputs of the modified model are expected PMT signals and CCD camera readings. The formulae used in the simulation of PMT outputs and CCD camera readings are detailed in Appendix A.1 and A.2. The outputs are plotted as blue lines in Figures 3.29 and the corresponding parameters used in the model are also indicated. The retrievals of the four data samples are summarised in Table 3.7. As shown in the table, the retrieved sizes slightly vary from the corresponding mean sizes of PSL beads with the variation from 0.5% to 3.6%. The errors in the retrieved sizes were estimated by evaluating the size range that lead to the standard deviation between measured and calculated CCD camera reading less than 0.0016.

Sample code	Mean bead size (nm)	Retrieved size (nm)	Deviation (%)
1	1,100	1,140±100	3.6
2	1,800	1,795±10	0.5
3	2,000	2,045±30	2.2
4	3,000	3,020±20	0.6

Table 3.7: Summary of the demonstration of particle size retrieval using four examples generated during the calibration.

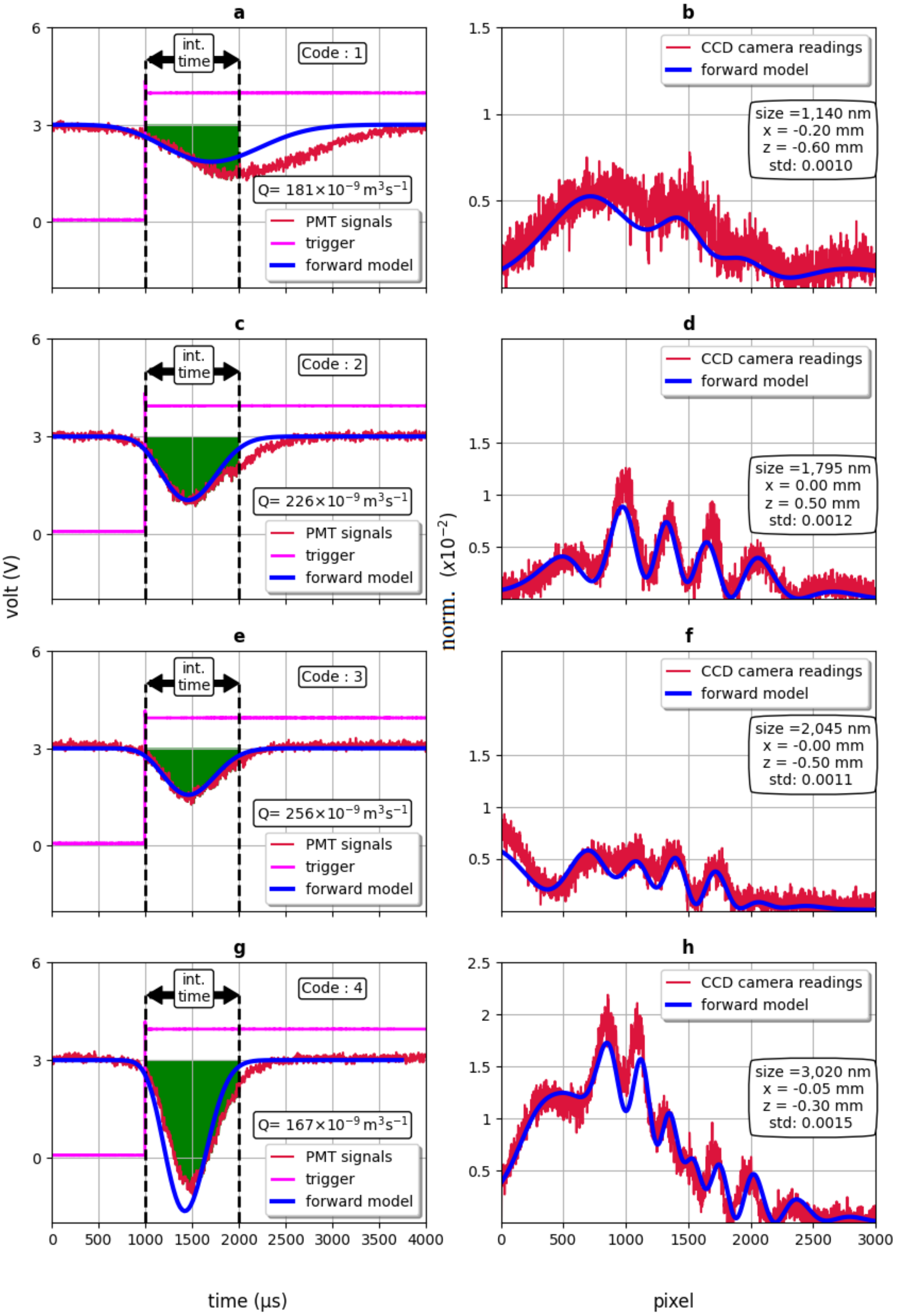

Figure 3.29: A demonstration of particle size retrieval using the four examples generated during the calibration. In this demonstration, the refractive index of the particles was assumed to be 1.59.

3.12 Summary

The calibration of SPARCLE was carried out to evaluate its performance. In the calibration, SPARCLE's responses to four monodisperse aerosols containing PSL beads with the mean size of 1,100 nm, 1,800 nm, 2,000 nm, and 3,000 nm were measured. The monodisperse aerosols were generated by nebulising suspensions resulting in droplets containing PSL beads. The droplets were then dried to form solid particles.

Prior to the calibration, the sensing volume was aligned and the distribution of the beam intensity illuminating the sensing volume was evaluated. The sensing volume was aligned slightly differently to that designed in Chapter 2, however, the effect of that difference to the intensity measured by the detectors is negligible. From the evaluation of the beam intensity, it was found that the cross-section of the beam in the sensing volume was not a simple rectangular shape as designed in Chapter 2. Based on this observation, the distribution of the beam intensity along the y axis can be modelled as a nearly Gaussian distribution which peaks at $y = 0$ with the standard deviation of 0.1 mm. Meanwhile, the intensity distribution along the x axis was measured.

During the calibration, several variables were acquired. Some of them were acquired periodically, while others were acquired synchronously. The latter was acquired from trigger signals generated when PMT outputs satisfy a threshold level. Simultaneously, the size distribution of the particles was also measured by a certified OPC.

Based on the calibration results, a revised forward model of SPARCLE is proposed to modify the model described in Chapter 2. The main changes in the revised model are:

- that the probability of single particles flowing through particular points in the x-z plane is not homogeneous but a function of the speed of the air in which the particles are suspended and,
- that the beam cross-section is not a simple rectangular shape but constructed based on the observation and measurement of the beam.

The outputs of the PMT and the CCD camera were simulated using the modified model and the results indicate that the simulations are generally in good agreement with the measured outputs.

Chapter 4

SPARCLE aerosol test measurement

After being calibrated, SPARCLE was used to sample and measure test aerosol suspended in a confined fume hood. The scheme of the sampling and measurements was straightforward: draw the test aerosol particles to the SPARCLE sensing volume and collect the corresponding SPARCLE responses. The test aerosol is droplets of a mixture of water and soap generated by spraying the mixture next to the SPARCLE inlet. The mixture was selected since it evaporated slower than droplets composed of pure water. The slow evaporation is due to the hydrophobic component of the soap molecules line up on top of the water to form a layer of hydrophobic components. This layer slows down the evaporation of water underneath. The confinement was necessary to ensure the aerosol did not disperse immediately after being generated. The size distribution of the test aerosols was monitored by a calibrated OPC. The temperature and the relative humidity during the measurements were 22° C and 45%, respectively.

4.1 The composition of the test aerosols

The soap used in the generation of the test aerosol is a commercial Fairy washing up liquid. The main ingredients of the liquid are listed in Table 4.1 [Fairy, 2021]. As listed in the table, the proportions of the solvents are not specified by the manufacturer and the refractive indices of the main ingredients vary between 1.33 and 1.44. The refractive index of the soap liquid was measured using HHTEC Refraktometer [HHTEC, 2021] and the measured refractive index was around 1.37.

no	ingredients	functions	prop. (%)	refractive index
1	water	solvents	not specified	1.33
2	ethanol			1.36
3	sodium dodecyl sulphate	cleaning agents	20 - 30	1.44 [Besio et al., 1988]
4	N,N-Dimethyldodecan-1-amine N-oxide		5 - 10	1.378 [Sigmaaldrich, 2021]

Table 4.1: The main ingredients of commercial Fairy washing liquid.

4.2 The size distribution of the test aerosol

The OPC measured the size distribution of the test aerosol continuously during the test aerosol measurement. The results of the OPC measurement were acquired every 6 seconds. The time series of the measurement results are depicted in Figure 4.1. As shown in the figure, the size distribution fluctuated during the measurements. This fluctuation corresponds to the spraying of the droplets which was done sporadically during the measurement. The average size distribution of the aerosol is shown in Figure 4.2. As can be seen from Figure 4.2, the majority of the particles were smaller than 1,000 nm, although particles with sizes between 1,000 nm and 3,000 nm were present in smaller particle number. On the other hand, there were relatively few particles bigger than 3,000 nm. The expected size distribution that can be detected by SPARCLE is shown in the same figure. The expected size distribution was calculated using Equation 3.21 based on the SPARCLE probability of detecting particles shown in Fig. 3.27 and the SPARCLE sampling and transport efficiency shown in Fig. 2.15.

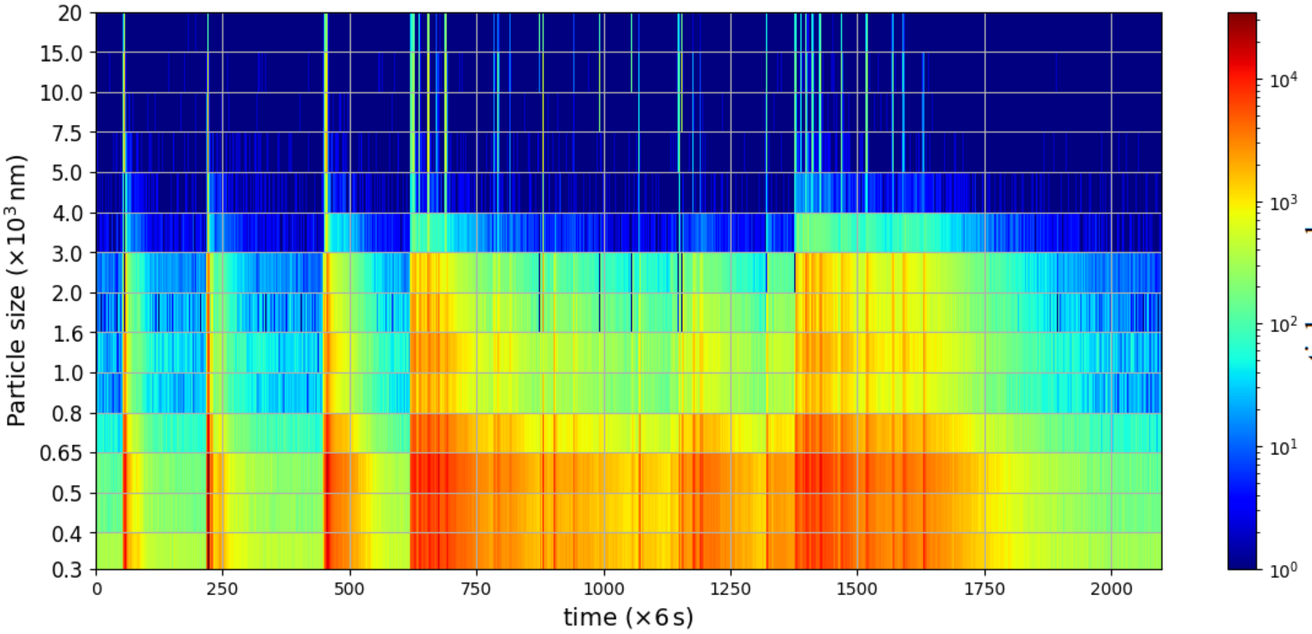

Figure 4.1: The distribution of the test aerosol as a function of time as measured by the OPC. The vertical axis is not linearly scaled. The axis is arranged according to the bin width of the OPC. The number of particles are colour coded based on the figure bar on the right.

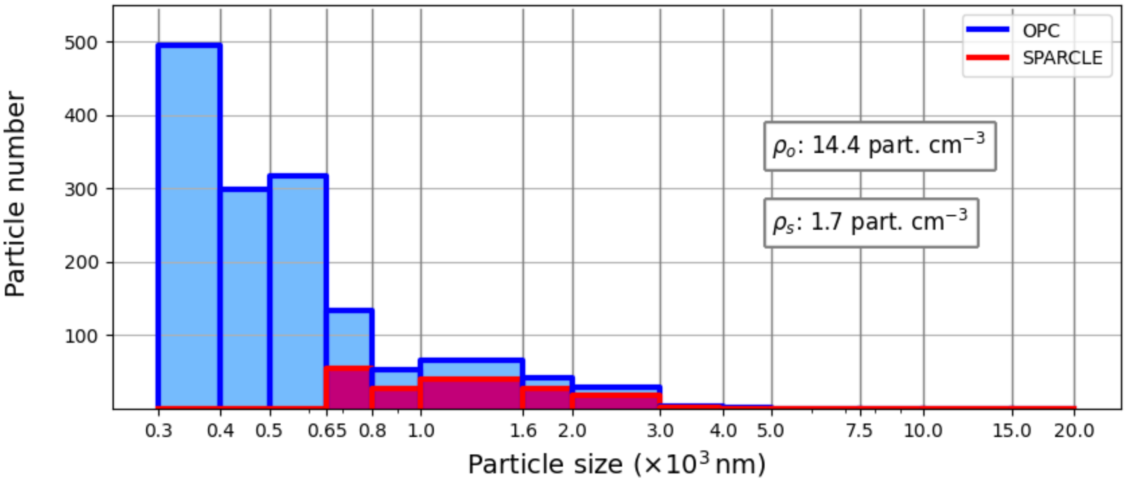

Figure 4.2: The average size distribution of the test aerosol as measured by the OPC and that of expected to be detected by SPARCLE. The air sample volume was 100 cm^3. The particle concentration as measured by the OPC and that of expected to be detected by SPARCLE are listed in the figure.

4.3 SPARCLE sampling flow rates and laser power stability

During the test aerosol measurement, SPARCLE sampled particles continuously. The number of samples collected by SPARCLE was 5430. The SPARCLE flowrate in sampling the particles was monitored and the results are presented in Figure 4.3.a. Based on the figure, the flow rate fluctuated with the average and the standard deviation of the flow rate $146 \times 10^{-9}\,\mathrm{m^3s^{-1}}$ and $25 \times 10^{-9}\,\mathrm{m^3s^{-1}}$, respectively. To determine the stability of the laser power during the measurement, the power of a fraction of the laser beam was measured. The results are presented in Figure 4.3.b. Based on the figure, the power fluctuated slightly with the average and the standard deviation of the measured power $9.97 \times 10^{-3}\,\mathrm{mW}$ and $12.7 \times 10^{-6}\,\mathrm{mW}$, respectively.

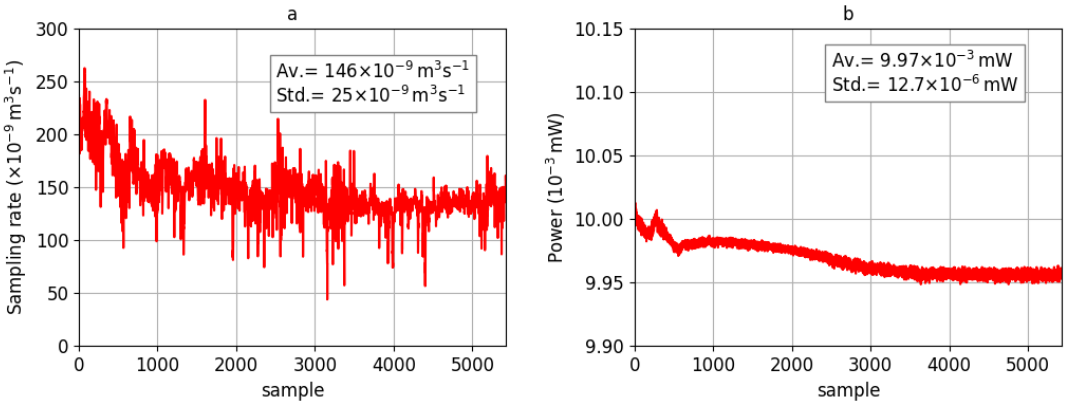

Figure 4.3: The sampling rates and the power of a fraction of the laser beam during the test aerosol measurement. The sampling rates and the power as a function of samples are shown in (a) and (b) respectively. The rate and the power fluctuated during the measurement. The average and the standard deviation of the rate and the power are indicated in the figure.

4.4 SPARCLE responses

The responses of SPARCLE for all samples in the test aerosol measurement were measured. The responses are composed of PMT outputs and CCD camera readings. The responses were then analysed in a similar manner to that of the calibration responses:

1. analyse the distribution of the width and the depth of pulses contained in the PMT outputs,

2. evaluate the relation between the total reading of the CCD camera, S, with the corresponding pulse area, A, measured at the same time frame with the CCD Camera readings.

4.5 The distribution of pulse width and depth

The distribution of the width and the depth of the PMT pulses are shown in Figure 4.4. The top figure projects the distribution of the width. As shown in the figure, the shape of the distribution is similar to that of the monodisperse aerosols measurement in the SPARCLE calibration shown in Figure 3.16. A small discrepancy is identified in the number of short pulses which are shorter than 500 µs. In contrast to the measurement of the monodisperse aerosols, the measurement of the test aerosol generated a larger number of these short pulses. One probable explanation is that these short pulses corresponded to the light scattered by very small particles that were smaller than the detection limit of SPARCLE. These short pulses can induce large variation in the background that occasionally lead to trigger the SPARCLE detection system. The test aerosol size distribution shown in Figure 4.2 indicates that a large portion of the test aerosol particles was smaller than 650 nm.

The distribution of the depth is projected in the right figure. The shape of the distribution is different from that of the monodisperse aerosol measurement. The distribution in the test aerosol measurement peaks around the threshold and then decreases smoothly as the depth increases. Meanwhile, those in the monodisperse aerosol measurement shown in Figure 3.16 peak at various pulse depths: one of them is around the threshold and the others are at depths deeper than the threshold.

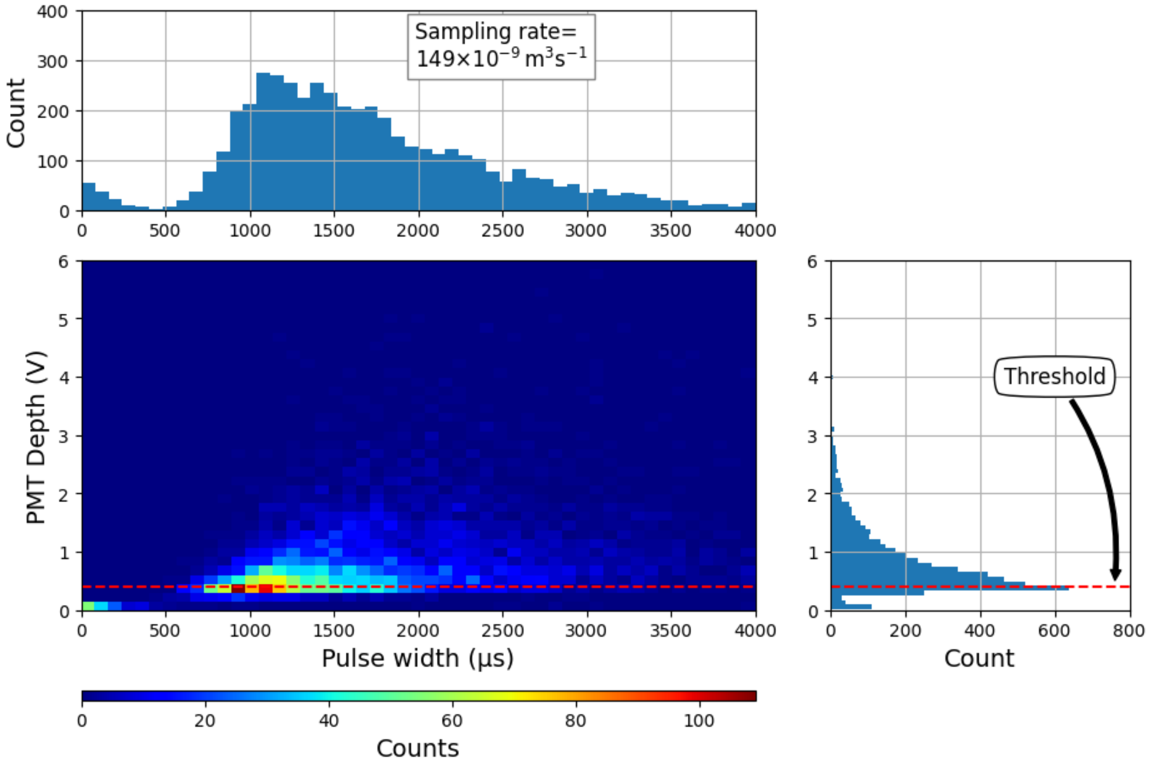

Figure 4.4: The two-dimensional histogram of the distribution of the width and the depth of pulses contained in the PMT outputs. The width distribution is projected on the top figure while the depth distribution is projected in the right.

4.6 The relation between S and A

As discussed in Chapter 2, the comparison between S and A for all data samples can be used to characterise SPARCLE measurements. The distributions of S and A in the test aerosol measurement were derived from the CCD Camera readings and the PMT outputs, respectively. The results are shown in Figure 4.5. As can be seen in the figure, the relation between the distribution of S and A fluctuates around a line. The fluctuation is higher than for the measurement of the monodisperse aerosols discussed in Chapter 3. The high fluctuation can be explained by the wide range of the particle size of the test aerosol as shown in Figure 4.2.

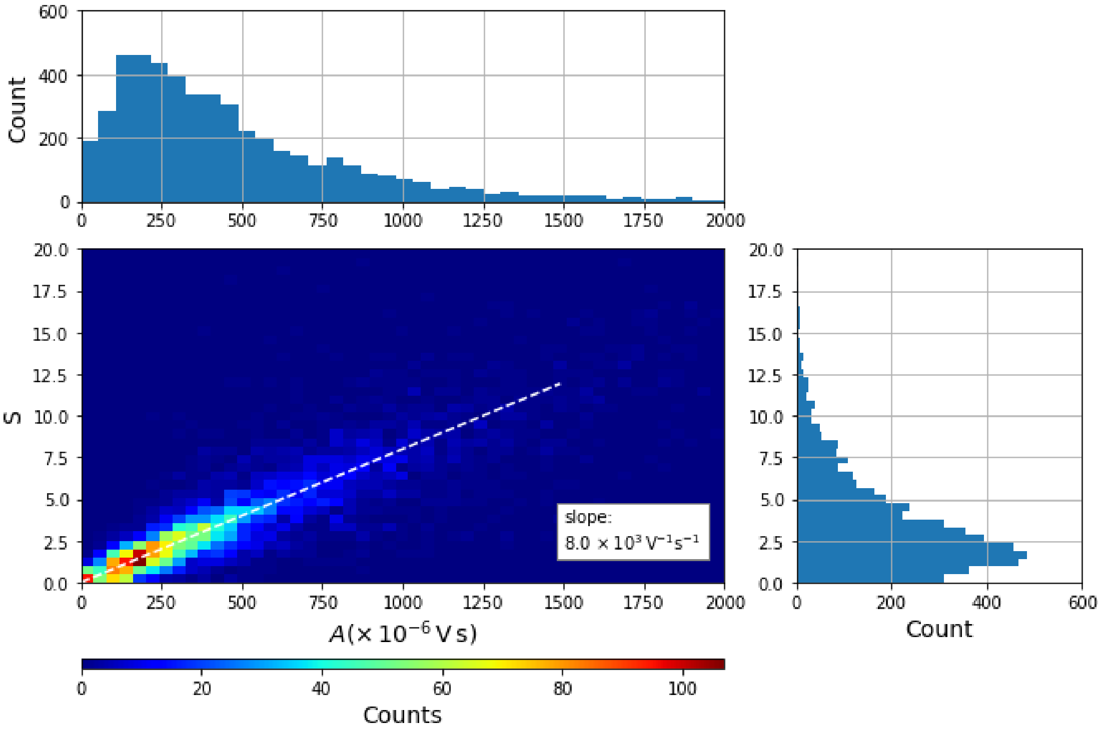

Figure 4.5: The two-dimensional histogram of the distribution of S and A. In the top and right figures, the distributions of A and S are projected from the two-dimensional histogram, respectively. A line is drawn and the slope of the line is indicated in the figure.

4.7 The particle detection rate of SPARCLE

The rates of SPARCLE in detecting particles in a unit of time during the test aerosol measurement were calculated using Equation 3.27. The calculation were done in each minute of the measurement. The results for the first 50 minutes of the measurement are shown in Figure 4.6. This limited time window was selected for visual clarity. In Fig 4.6.a, the particle concentrations of the test aerosol as measured by the OPC are shown as blue dots. The expected concentrations to be measured by SPARCLE are also shown in the same figure as red triangles. In Fig 4.6.b, the calculated and measured SPARCLE particle detection rate are shown as blue dots and red triangles, respectively. Based on the figure, the measured rate is in general inline with the calculated rate with deviations in some points. The results indicate that SPARCLE can measure transient aerosol distribution which last for few minutes particularly shown in the time between 40 and 50 minute.

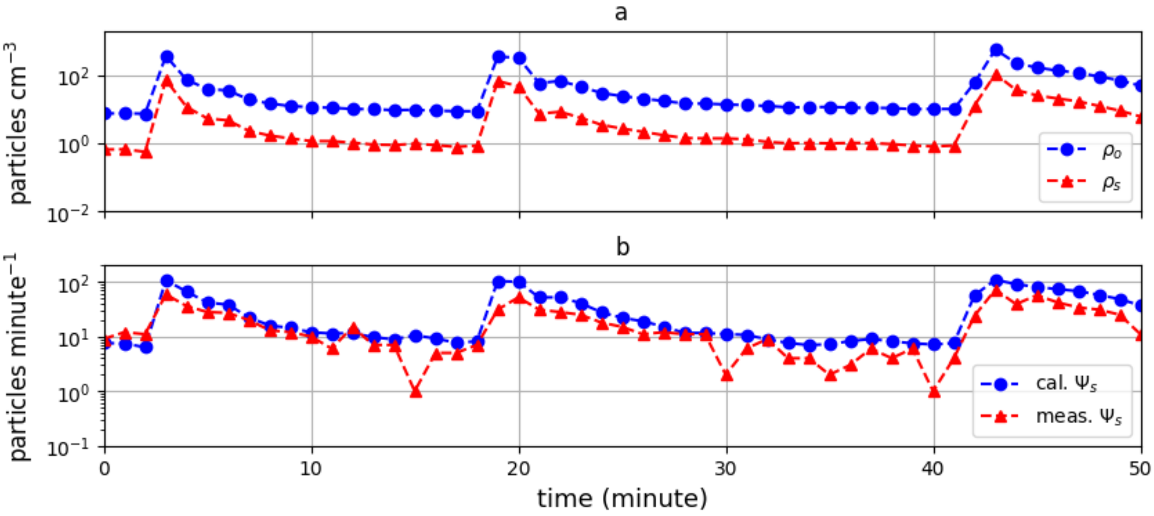

Figure 4.6: The particle detection rate of SPARCLE. (a). The particle concentration as measured by the OPC and that as expected to be detected by SPARCLE. (b) The calculated and measured SPARCLE detection rate.

4.8 The demonstration of the particle size and refractive index retrieval of the test aerosol measurement samples.

The retrieval of particle size and refractive index was performed using two samples of the SPARCLE test aerosol measurements. Using the modified forward model described in Chapter 3, the expected outputs of the PMT and the CCD Camera for various variables were calculated. The calculated outputs which fit the two samples were then selected. The measured and the calculated outputs of the PMT and the CCD Camera are depicted in Figure 4.7. As shown in the figure, the retrieved sizes of the two samples are 3,245 nm and 2,615 nm, while the retrieved refractive index is 1.44 for the two samples.

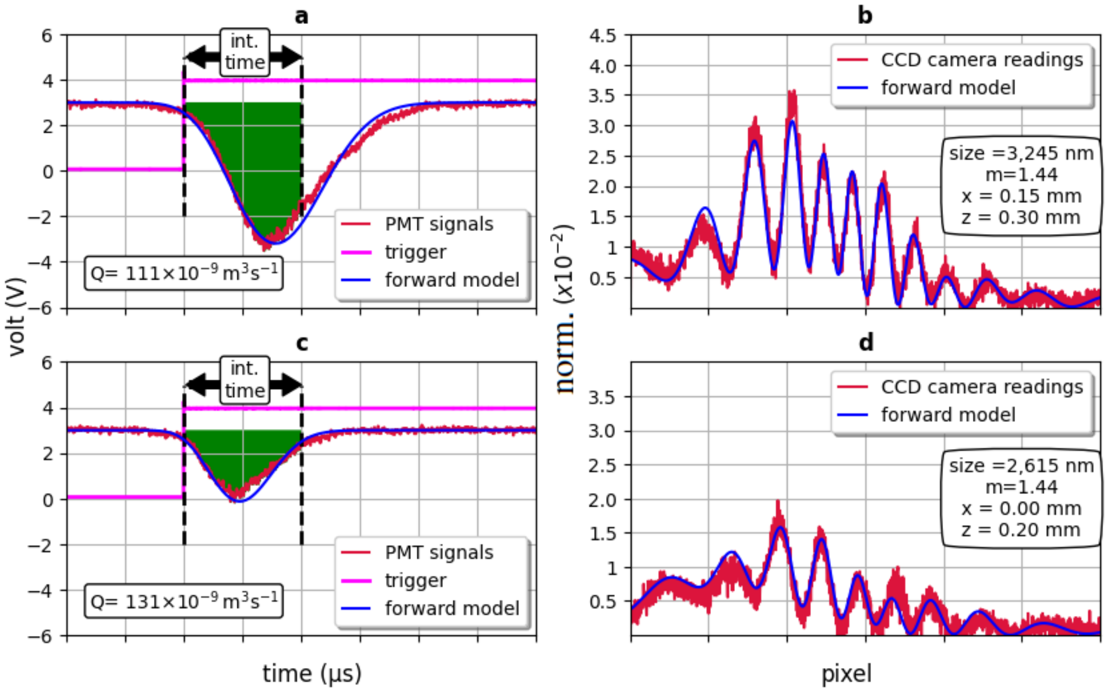

Figure 4.7: The demonstration of the size and refractive index retrieval from the test aerosol measurement. The variables to be varied in the calculation of the outputs are particles size and refractive index as well as the position of the particles on the **x-z** plane.

4.9 Summary

A measurement of test aerosol was carried out using SPARCLE. The test aerosol was manually generated by spraying a mixture of water and soap. The size distribution of the generated aerosols was monitored by the OPC. The result of the OPC monitoring show that the shape of the size distribution is a skewed distribution with a large proportion of small particles. The expected SPARCLE rates of detection were calculated based on the size distribution measured by the OPC. In general, the expected rates were in a good agreement with measured SPARCLE detection rates. A simple demonstration of retrieving particle size and refractive index from SPARCLE responses to the test aerosol was performed. The method of the retrieval was varying four variables in SPARCLE forward model manually and selecting the variables that lead to the best fit between SPARCLE responses and the output of SPARCLE forward model as the solutions. Two SPARCLE responses were selected for the retrieval and the solutions were found. The plots of the outputs of SPARCLE forward model calculated using the solutions indicates the fitness between the outputs and the responses.

Chapter 5

SPARCLE retrieval

The retrieval of particle properties using the measurement of light scattered by particles is not a trivial process. The relation between scattered light and particle properties is highly non-linear. In the case of homogeneous spherical particles, analytic retrieval of their size and refractive index can be performed if the Mie amplitudes of scattered light, $S_1(\theta, d, m)$ and $S_2(\theta, d, m)$, are known continuously from $\theta = 0°$ to $\theta = 180°$ [Ludlow and Everitt, 2000]. As SPARCLE measures scattered light with a different range of θ, the analytical retrieval is impractical. Therefore, numerical methods are considered in the retrieval of particle size and refractive index from SPARCLE measurements. Ideally, no prior assumption about a particle would be used in retrievals. For example, particle shape was retrieved from light scattering patterns (LSPs) measured as a function of azimuth and scattering angle at various particle orientations [Kim et al., 2014]. Retrievals based on other types of measurements require a priori assumption about particle properties, such as particle shape or composition.

There are at least three techniques to retrieve particle properties numerically: optimisation, machine learning, and parametric techniques. Optimisation is based on the comparison between a measurement and a forward model. The forward model includes the physics of light scattering as well as the instruments' expected response to the scattering. Particular particle properties are selected as the retrieval solution when the forward model fits the measurement. The computational cost of optimisation techniques can rapidly increase as a function of the number of particle properties [Strokotov et al., 2011; Wang et al., 2016]. One way to reduce the cost is by building look-up tables consisting of expected forward model for various particle properties [Kolesnikova et al., 2006; Wojtkiewicz et al., 2013]. The optimisation with pre-calculated look-up tables has been applied for the retrieval based on light scattered by non-spherical particles such as red blood cells [Caramanica, 2012] and rod-shaped bacteria [Konokhova et al., 2013].

One of the methods in machine learning that has been used in the retrieval of particle properties is the neural network method. This method does not include any knowledge of the physics involved but used a known set of scattering patterns to train the algorithm. It is expected that constructed neural networks are able to train themselves over a large set of measurement and solve high-dimensional problems [Galushkin, 2007]. However, the performance of neural networks is difficult to predict and the structure of a neural network may require laborious fine tuning [Berdnik and Loiko, 2015]. Neural networks have been applied to retrieve spherical particles [Ulanowski et al., 1998; Berdnik et al., 2006] and red blood cells [Apostolopoulos et al., 2013].

In the parametric approach, instruments' outputs are compressed into a small number of parameters. Parameters can be extracted from LSPs [Quist and Wyatt, 1985; Maltsev and Lopatin, 1997], from time-resolved signals [Zhang et al., 2016], or from Fourier transformed LSPs [Min and Gomez, 1996; Yu et al., 2012]. One widely-used parametric method is spectral sizing based on LSPs [Steiner et al., 1999; Jakubczyk et al., 2013]. This method builds a nearly linear relation between the size of spherical particles and the characteristic frequency of the LSP for a limited particle size range. Another study proposes an integral of the LSP as a second parameter to estimate the size and refractive index of spherical particles over a limited size and refractive index domain [Fiorani et al., 2008]. However, the accuracy of the approach has not been tested.

The retrieval of particle size and refractive index from SPARCLE measurements discussed in this chapter uses a simple optimisation method. In the optimisation, the solutions for the SPARCLE retrievals are searched over a particular domain defined based on a priori knowledge of the sampled particles. The sampled particles are assumed to be homogeneous, isotropic, and non-absorbing spherical particles. To reduce the computational cost of the retrievals, a look-up table of the PMT signals as a function of particle size and refractive index was pre-calculated.

5.1 The retrieval problem

The problem to retrieve target quantities from measurements can be divided into two distinct problems: the forward problem and the inverse problem. The forward problem is the calculation of the measurements based on the target quantities. The inverse problem is the estimation of the target quantities from the measurements with associated errors. The measurements are assembled into a measurement vector denoted by $\mathbf{y}$. The target quantities are assembled into a state vector denoted by $\mathbf{x}$. The elements of $\mathbf{x}$ and $\mathbf{y}$ are expressed as

$$\mathbf{x} =\{x_1, x_2, x_3, ...x_s\}, \tag{5.1}$$

$$\mathbf{y} =\{y_1, y_2, y_3, ...y_h\}, \tag{5.2}$$

where s is the number of the target quantities; h is the number of the measurements. The s-dimensional space and h-dimensional space of the state and measurement vectors are called state space and measurement space, respectively. The vectors $\mathbf{x}$ and $\mathbf{y}$ can be related as

$$\mathbf{y} = \mathbf{F}(\mathbf{x}, \mathbf{b}) + \boldsymbol{\epsilon}, \tag{5.3}$$

where $\mathbf{F}(\mathbf{x}$,$\mathbf{b})$ is the forward function that describes the physics of the measurements; $\boldsymbol{\epsilon}$ is the measurement errors; $\mathbf{b}$ is the known parameters of the forward function. Since $\mathbf{b}$ is already known, the dependency of $\mathbf{F}$ on $\mathbf{b}$ is not necessary explicitly shown and Equation 5.3 can be simplified into

$$\mathbf{y} = \mathbf{F}(\mathbf{x}) + \boldsymbol{\epsilon}. \tag{5.4}$$

A state vector is regarded as a retrieval solution, denoted by $\hat{\mathbf{x}}$, when $\hat{\mathbf{x}}$ minimises a cost function χ^2 defined by

$$\chi^2 = [\mathbf{y} - \mathbf{F}(\mathbf{x})]^{\mathrm{T}}\, \mathbf{S}^{-1}\, [\mathbf{y} - \mathbf{F}(\mathbf{x})], \tag{5.5}$$

where $\mathbf{S}$ is the measurement uncertainty covariance matrix [Rodgers, 2000]. The element of $\mathbf{S}$ is the covariance between the errors of two measurements:

$$S_{ij} = \mathrm{Cov}(\epsilon_i, \epsilon_j), \tag{5.6}$$

where ϵ_i and ϵ_j are the errors of y_i and y_j, respectively. There are various method to find $\hat{\mathbf{x}}$. The simplest method is a simple brute-force method where a range of each element of $\mathbf{x}$ is divided into p segments with equal increment so that state space is described by discrete points which form the vertices of p^s hypercubes. The value of χ^2 is then evaluated at the vertices of each hypercubes. This method yields a coarse map of the behaviour of χ^2 as a function of all elements of $\mathbf{x}$. The vertex whose χ^2 is minimum is selected as $\hat{\mathbf{x}}$. To indicate the goodness of the fit between $\mathbf{y}$ and $\mathbf{F}(\hat{\mathbf{x}})$, a parameter χ^2_v is introduced. The parameter is defined as

$$\chi^2_v = \frac{\chi^2}{v}, \tag{5.7}$$

where v is the number of the degree of freedom calculated by

$$v = h - s. \tag{5.8}$$

A vector $\mathbf{y}$ can be considered as a good approximation of $\mathbf{F}(\hat{\mathbf{x}})$ when χ^2_v evaluated at $\hat{\mathbf{x}}$ is between 1.0 and 1.5 [Bevinton and Robinson, 1992].

5.2 A state and a measurement vector in SPARCLE retrieval

A state vector in SPARCLE retrieval is assembled from the variables in the SPARCLE forward function. As discussed in Chapter 3, the variables are:

1. the position of the particle in the x-z plane denoted as (x, z),
2. the diameter and refractive index of the particle denoted as (d, m).

The depiction of the variables determining the light measured by the CCD camera and the PMT is shown in Figure 5.1. The state vector can be expressed as

$$\mathbf{x} = \{x, z, d, m\}. \tag{5.9}$$

A measurement vector in SPARCLE retrieval is assembled from the measurements by the PMT and the CCD camera. To reduce the computational cost, the PMT signals are represented by six signals that characterise the PMT signals. The first is the minimum PMT signal to represent the PMT pulse depth and the next five are the signals sampled at the same time-frame as the integration time of the CCD camera with equal time interval to represent the PMT pulse shape. The five signals are at 200 µs, 400 µs, 600 µs, 800 µs, and 1000 µs after the integration start time. Meanwhile, all CCD camera readings are included in the measurement vector. The elements of the measurement vector are summarised in Table 5.1.

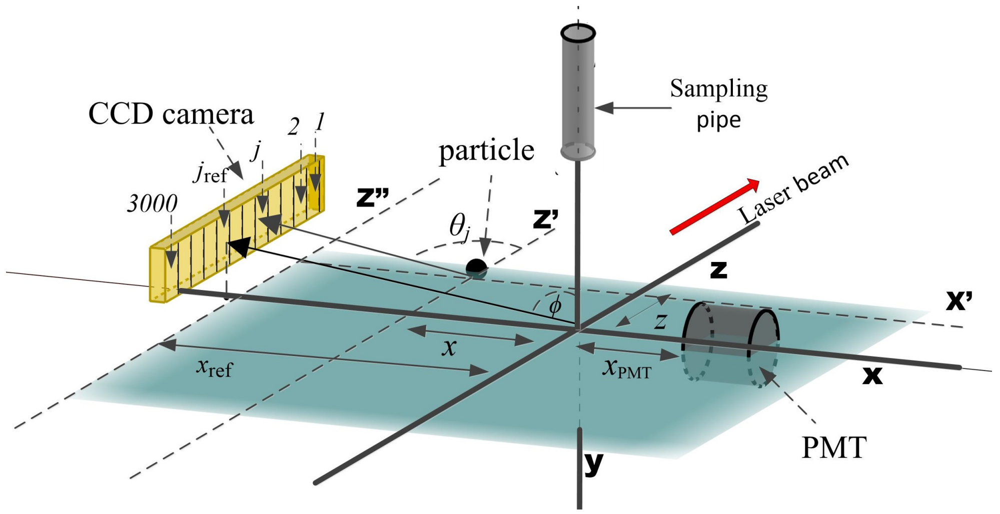

Figure 5.1: A depiction of the variables in the calculation of the outputs of the CCD camera. a particle with size d and refractive index m is located in the x-z plane. The plane is indicated by the transparent blue colour. The projection of the particle position in the x and z axis are denoted as x and z, respectively. There are 3,000 pixels in the CCD camera and the pixels are denoted by j with j as an integer number from 1 to 3,000. The vector position of pixel j is denoted as $\vec{r_j}$. The scattering angle of scattered light measured by pixel j is denoted by θ_j. The azimuthal angle of scattered light measured by the pixels are the same and is denoted by ϕ. Since the distance of the consecutive pixels are known, the position vector of all pixels can be derived from the position of a pixel which the location is precisely known. The pixel is denoted as j_{ref} and located in the x-y plane. The projection of the vector position of j_{ref} on the x axis is denoted by x_{ref}. The determination of j_{ref} and x_{ref} is detailed in Appendix B.

Table 5.1: The elements of a measurement vector

measurement	Description
y_1	a PMT pulse depth
y_2	a PMT signal sampled at 200 µs after the start of the integration time
y_3	a PMT signal sampled at 400 µs after the start of the integration time
y_4	a PMT signal sampled at 600 µs after the start of the integration time
y_5	a PMT signal sampled at 800 µs after the start of the integration time
y_6	a PMT signal sampled at 1000 µs after the start of the integration time
y_7	a CCD camera reading from the first pixel
y_8	a CCD camera reading from the second pixel
.	.
.	.
y_{3006}	a CCD camera reading from the 3000$^{\text{th}}$ pixel

5.3 The retrieval error vector

An error vector $\boldsymbol{\epsilon}$ is assembled using the errors associated with $\mathbf{y}$ and $\mathbf{F}(\mathbf{x})$. In this work, $\mathbf{F}(\mathbf{x})$ is assumed to be exact, hence only the errors associated with $\mathbf{y}$ are included. One way to calculate the errors is by analysing the PMT and the CCD camera measurements of known light intensity. The standard deviation of the measurements can be considered as the errors. In this work, the background light in the scattering chamber was used for the error analysis. The true intensity is approximated by averaging a number measurements of the background. The standard deviation of the measurements can be calculated with respect to this approximated true intensity. There might be a correlation between the error measurements of the PMT and the CCD camera since the two instruments were connected to the same power supply. However, for simplicity, the correlation was assumed to be negligible.

The PMT measurements of the background were used to determine the measurement error of the PMT. The error is denoted by ϵ_{PMT}. In the measurements, 2,000 PMT signals were sampled with the sampling time interval of 2 µs. The signals are plotted as a red line in Figure 5.2.a. The average of the signals is shown as a blue line in the same figure. The distribution of the signals with respect to the average is plotted as a blue histogram in Figure 5.2.b. The standard distribution of the histogram is 0.07 V. The standard deviation is regarded as the measurement error of the PMT: $\epsilon_{\mathrm{PMT}} = 0.07\,\mathrm{V}$.

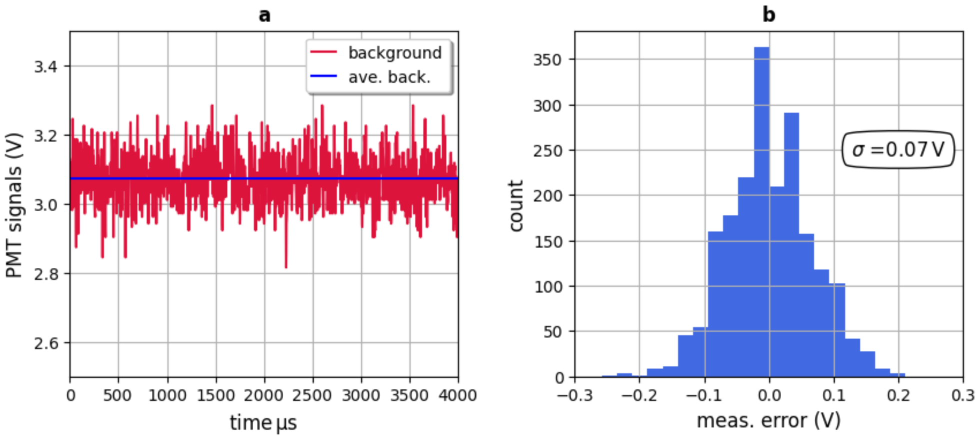

Figure 5.2: A determination of ϵ_{PMT} from a number PMT background measurements. In (a), the background and their average are plotted as a red line and a blue line, respectively. In (b), the distribution of the measurement error of the background is shown as a blue histogram. The standard distribution of the histogram is indicated in the figure.

The CCD camera measurements of the background were used to determine the measurement error of the CCD camera. The background was measured 100 times with the integration times of 1 ms. The average of the measurements is shown as a blue line in Figure 5.3.a. Single background measurements are plotted as a red line in the same figure. As shown in the figure, the readings in the single background measurements vary from those averaged from the 100 background measurements. To illustrate, the distribution of readings at 100^{th} pixel with respect to the average reading at the same pixel is shown in Figure 5.3.b. The standard deviation of the distribution is 0.06×10^{-2}. The standard deviation is regarded as the measurement error associated with 100^{th} pixel. Similar analysis were done for other pixels: $1,000^{\mathrm{th}}$ and $2,000^{\mathrm{th}}$ pixel. The results are shown in Figures 5.3.c and 5.3.d. The errors associated with the pixels are assembled into a vector and the vector is denoted by $\boldsymbol{\epsilon}_{\mathrm{CCD}}$ with its elements expressed as:

$$\boldsymbol{\epsilon}_{\mathrm{CCD}} = \{\epsilon'_1, \epsilon'_2, \epsilon'_3, .., \epsilon'_j, .., \epsilon'_{3000}\}, \tag{5.10}$$

where ϵ'_j is the error associated with j^{th} pixel. The errors are plotted in Figure 5.4.a with respect to the pixels. The distribution of the errors is plotted in Figure 5.4.b. As shown in the figure, the errors vary with the mean of the variation around 0.06×10^{-2}.

The measurement vector was obtained by removing the background content

$$\mathbf{y} = \mathbf{y}_{\mathrm{meas}} - \mathbf{y}_{\mathrm{back}}, \tag{5.11}$$

where $\mathbf{y}_{\mathrm{meas}}$ is a measurement vector that still contain background; $\mathbf{y}_{\mathrm{back}}$ is a background vector derived by averaging 100 background measurements. The vector $\mathbf{y}_{\mathrm{back}}$ can be approximated as a true background vector which does not contain errors. Hence, an error vector associated with $\mathbf{y}$ can be written as

$$\boldsymbol{\epsilon} = \boldsymbol{\epsilon}_{\mathrm{meas}}, \tag{5.12}$$

where $\boldsymbol{\epsilon}_{\mathrm{meas}}$ is an error vector associated with $\mathbf{y}_{\mathrm{meas}}$. The vector $\boldsymbol{\epsilon}_{\mathrm{meas}}$ can be estimated from the errors associated with the background $\boldsymbol{\epsilon}_{\mathrm{back}}$. If the source of the errors is assumed to be the uncertainty of the number of electrons generated by photons coming to the detectors, then the elements of $\boldsymbol{\epsilon}_{\mathrm{meas}}$ can be estimated as

$$\epsilon_i^{\mathrm{meas}} = \sqrt{\frac{y_i^{\mathrm{meas}}}{y_i^{\mathrm{back}}}}\, \epsilon_i^{\mathrm{back}} \quad \text{for } 1 \leq i \leq 3006, \tag{5.13}$$

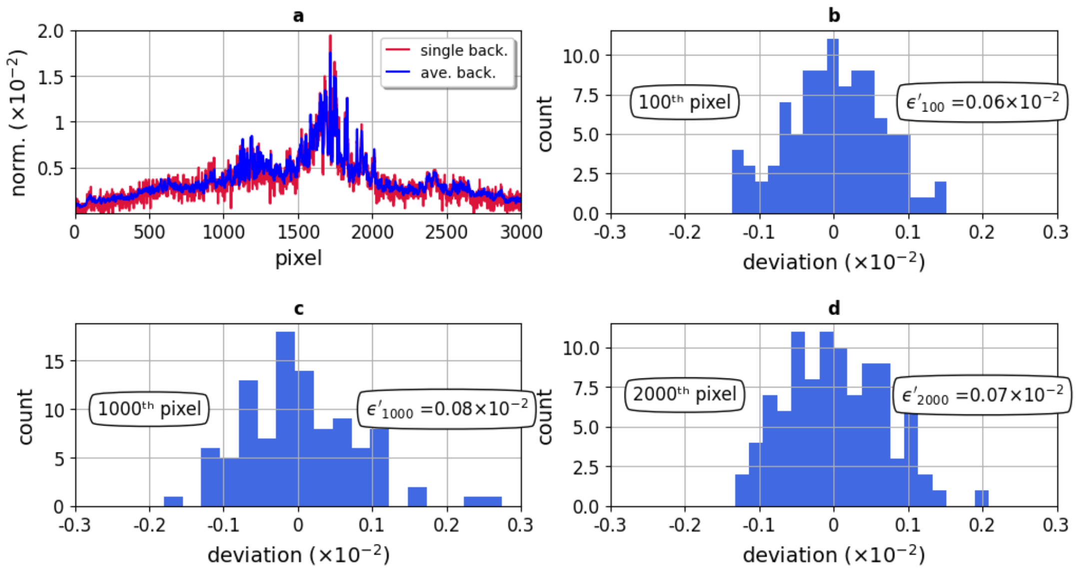

Figure 5.3: A determination of $\boldsymbol{\epsilon}_{\text{CCD}}$ from the background measured by the CCD camera. In (a), the approximated true background derived from 100 measurements of the background is plotted as a blue line. A single measurements of the background is plotted as a red line. In (b), (c) and (d), the distribution of the measurement errors associated with three pixels: 100th, 1000th, 2000th pixels. The standard deviation of the distribution is indicated in each figure.

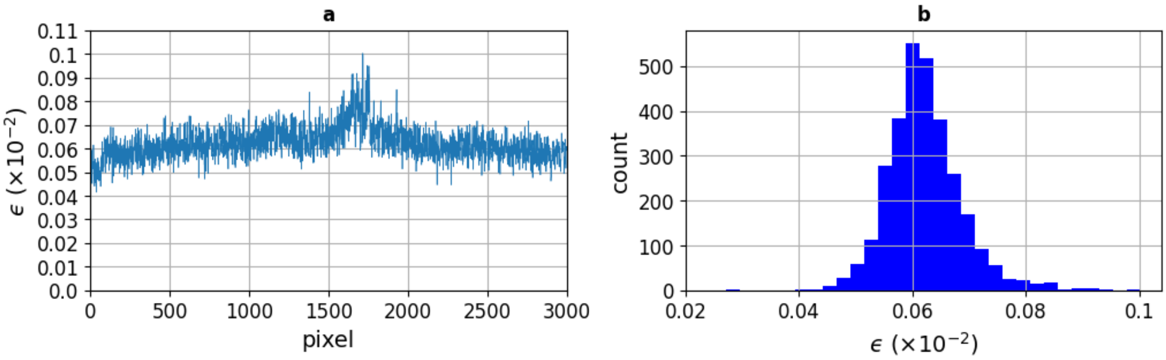

Figure 5.4: The elements of $\boldsymbol{\epsilon}_{\text{CCD}}$. In (a), $\boldsymbol{\epsilon}_{\text{CCD}}$ is plotted as a function of the pixel number. In (b), the distribution of $\boldsymbol{\epsilon}_{\text{CCD}}$ is shown a blue histogram.

where y_i^{meas} are the elements of $\mathbf{y}_{\text{meas}}$; y_i^{back} are the elements of $\mathbf{y}_{\text{back}}$; ϵ_i^{back} are the elements of $\boldsymbol{\epsilon}_{\text{back}}$. Vector $\boldsymbol{\epsilon}_{\text{back}}$ is assembled from the measurement errors of the detectors, and its elements are expressed by

$$\epsilon_i^{\text{back}} \begin{cases} \epsilon_{\text{PMT}} & \text{for } 1 \leq i \leq 6, \\ \epsilon'_{i-6} & \text{for } 7 \leq i \leq 3006. \end{cases} \tag{5.14}$$

The covariance of errors ϵ_i^{back} and ϵ_j^{back} for $1 \leq i, j \leq 6$ can be determined from the correlation between y_i^{back} and y_j^{back} sampled by the PMT. In SPARCLE measurements, the PMT signals were sampled with a sampling interval much longer than the response time of the PMT: the sampling interval is 2 µs while the response time is around 2 ns. Due to this large difference, each sampled signal can be considered as an independent measurement. Hence, the errors are uncorrelated to each other. The covariance of the errors can be written as

$$\mathrm{Cov}(\epsilon_i^{\text{back}}, \epsilon_j^{\text{back}}) \begin{cases} 0 & \text{if } i \neq j, \\ \epsilon_{\text{PMT}}^2 & \text{if } i = j, \end{cases} \text{ for } 1 \leq i, j \leq 6. \tag{5.15}$$

The covariance of errors ϵ_i^{back} and ϵ_j^{back} for $7 \leq i, j \leq 3006$ can be determined from the correlation of the errors associated with $(i-6)^{\text{th}}$ and $(j-6)^{\text{th}}$ pixels in the background measurements by the CCD camera. The covariance can be calculated by

$$\mathrm{Cov}(\epsilon_i^{\text{back}}, \epsilon_j^{\text{back}}) = \frac{1}{L}\sum_{\ell=1}^{L}(\epsilon_{i,\ell}^{\text{back}} - \bar{\epsilon}_i^{\text{back}})(\epsilon_{j,\ell}^{\text{back}} - \bar{\epsilon}_j^{\text{back}}) \text{ for } 7 \leq i, j \leq 3006, \tag{5.16}$$

where L is the number of the background measurements; ℓ is an integer number between 1 and L; $\epsilon_{i,\ell}^{\text{back}}$ and $\epsilon_{j,\ell}^{\text{back}}$ are the errors in ℓ^{th} measurement associated with $(i-6)^{\text{th}}$ and $(j-6)^{\text{th}}$ pixels, respectively; $\bar{\epsilon}_i^{\text{back}}$ and $\bar{\epsilon}_j^{\text{back}}$ are the mean errors associated with $(i-6)^{\text{th}}$ and $(j-6)^{\text{th}}$ pixels, respectively. The results are shown in Figures 5.5 as red and blue histograms for two cases: $i \neq j$ and $i = j$. As shown in the figure, the error covariance in the case of $i \neq j$ are small. For simplicity, the error covariance are regarded as zero. Hence, the covariance of the errors ϵ_i^{back} and ϵ_j^{back} for $7 \leq i, j \leq 3006$ can be written as

$$\mathrm{Cov}(\epsilon_i^{\text{back}}, \epsilon_j^{\text{back}}) \begin{cases} 0 & \text{if } i \neq j, \\ (\epsilon_j')^2 & \text{if } i = j, \end{cases} \text{ for } 7 \leq i, j \leq 3006. \tag{5.17}$$

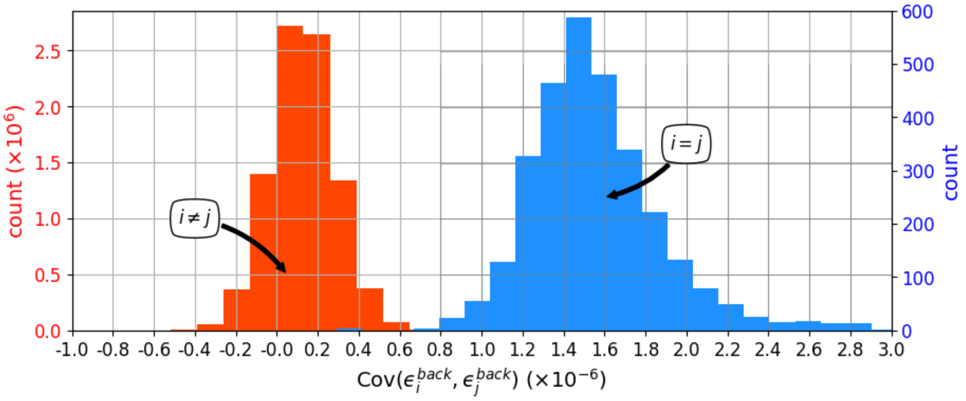

Figure 5.5: The distribution of $\mathrm{Cov}(\epsilon_i^{\mathrm{back}}, \epsilon_j^{\mathrm{back}})$ for two cases: $i \neq j$ and $i = j$ where $7 \leq i, j \leq 3006$.

5.4 The retrieval scheme

The scheme of the retrieval is a simple brute-force two-step method. A two-step procedure was used to reduce the overall computational cost. Applying a simple brute force to find $\hat{\mathbf{x}}$ that minimise χ^2 expressed in Eq. 5.5 can be computationally expensive when χ^2 is evaluated at large number of vertices in the 4-dimensional state space. The procedure for the cost reduction is focused on the reduction of the vertices number. The reduction is based on dividing χ^2 into independent components and χ^2 can be evaluated at the vertices that minimise one of the components. Finding the vertices should be computationally cheap. Moreover, the division can only be performed when the errors between the components are uncorrelated. It was decided that χ^2 was divided with one of the components related to the fit of PMT pulse depth. The value of χ^2 can be divided into two components: χ^2_{D} and χ^2_{S} written as

$$\chi^2 = \chi^2_{\mathrm{D}} + \chi^2_{\mathrm{S}}, \tag{5.18}$$

where χ^2_{D} is the component of χ^2 based on the fit of PMT pulse depth expressed as

$$\chi^2_{\mathrm{D}} = \frac{1}{\epsilon^2_{\mathrm{PMT}}}(y_1 - \mathrm{F}_1(\mathbf{x}))^2, \tag{5.19}$$

where $\mathrm{F}_1(\mathbf{x})$ is the first element of the forward function $\mathbf{F}$. The values of $\mathrm{F}_1(\mathbf{x})$ were computed prior to the retrieval. The evaluation of χ^2_{D} results in a coarse map of χ^2_{D} as a function of $\mathbf{x}$. The map may contain many local minima. Then, the values of χ^2 are evaluated at the vertices around the minima. The steps can be summarised as follows:

1. apply a brute-force method to find the minima of $\chi^2_{\rm D}$ in the 4-dimensional state space,

2. select the vertices around the minima whose the corresponding $\chi^2_{\rm D} \leq 9$. The criteria $\chi^2_{\rm D} \leq 9$ is derived by setting $y_1 - {\rm F}_1(\mathbf{x}) \leq 3\,\epsilon_{\rm PMT}$ assuming that y_1 is a measured pulse depth that distributed normally around ${\rm F}_1(\mathbf{x})$ with the standard deviation of the distribution is $\epsilon_{\rm PMT}$. The assumption implies that a state vector $\mathbf{x}$ is excluded in the solution searching when ${\rm F}_1(\mathbf{x})$ differ more than $3\,\epsilon_{\rm PMT}$ from the measured pulse depth. Since ${\rm F}_1(\mathbf{x})$ are pre-calculated, the determination of $\chi^2_{\rm D}$ can be quickly done. In this step, particle size and refractive index and the position of the particle at the x coordinate were estimated,

3. evaluate χ^2 at the vertices selected from step 2,

4. select the minimum χ^2, denoted as $*\chi^2$, and select the vertex corresponding to $*\chi^2$ as the retrieval solution $\hat{\mathbf{x}}$,

5. test the goodness of the fit by calculating a parameter $*\chi^2_v$ defined as

$$*\chi^2_v = \frac{*\chi^2}{v}. \tag{5.20}$$

The degree of freedom is calculated by

$$\begin{aligned} v &= h - s, \\ &= 3006 - 4, \\ &= 3002. \end{aligned} \tag{5.21}$$

5.5 An illustration of SPARCLE retrieval

The retrieval scheme described can be illustrated using a set of SPARCLE responses containing PMT signals and CCD camera readings. The PMT signals and the CCD camera readings are plotted as a red line in Figure 5.6.a and 5.6.b, respectively. The solution is searched over a limited range of 4-dimensional state space. The ranges of d and m are defined based on the ranges of PSL size and refractive index specified by the manufacturers. The range of x is limited to $|x| \leq 0.50\,\text{mm}$ since the laser beam intensity is very low for $|x| \geq 0.50\,\text{mm}$ as shown in Figure 3.22.b. The range of z is limited to $|z| \leq 0.75\,\text{mm}$ since the probability of single particles passing through a point in the x-z plane where $|z| \geq 0.75\,\text{mm}$ is very low as shown in Figure 3.22.a. The limited range of the state space is summarised in Table 5.2. The space is divided into discrete points which form the vertices of hypercubes with the length of the hypercubes in each x_i listed in the same table. There are no hard and fast rule for selecting the length of the hypercubes. A smaller length results in more computational cost while a larger length may overshoot the local minima. Various length had been trialled and those listed in the table are the length that optimised the computational cost and the ability to detect local minima. The value of χ^2_{D} is evaluated at the vertices of each hypercubes. This evaluations result in a map of χ^2_{D} as a function of $\mathbf{x}$. The plot of χ^2_D for various d and m and constant x and z is shown in Figure 5.7(a). The plot indicates that local minima can be identified when the lengths of the hypercubes in the dimensions d and m are 1 nm and 0.01, respectively.

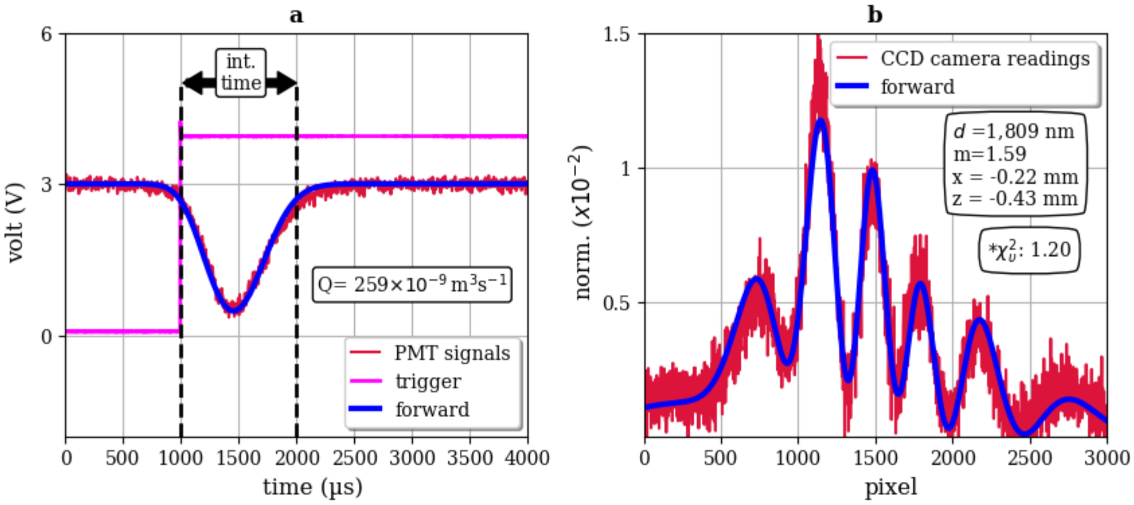

Figure 5.6: A pair of SPARCLE responses used to illustrate a SPARCLE retrieval. In (a), the measured and forward model PMT signals are plotted as a red line and a blue line, respectively. The sampling flow-rate of SPARCLE, Q, is indicated. In (b), the CCD camera measurements and forward model LSP are plotted as a red line and a blue line, respectively. The elements of the state vector that are used to model the LSP and the PMT signals are indicated. The values of $*\chi^2_v$ for the fit between the forward model and SPARCLE responses is also indicated.

The solution $\hat{\mathbf{x}}$ is searched by evaluating χ^2 at the vertices whose $\chi^2_{\mathrm{D}} \leq 9$. To illustrate, particle size range to be evaluated if the particle refractive index is 1.59 and the particle position is at -0.22 mm is between 1800 nm and 1825 nm since the corresponding χ^2_{D} are less than 9 as indicated in Fig. 5.7(b). The value of χ^2 is then evaluated at the size range and the vector $\mathbf{x}$ that lead to the minimum χ^2 is selected as $\hat{\mathbf{x}}$. To illustrate, the map of χ^2 for various d and m and constant x and z are shown in Figure 5.8(a). As seen in the figure, there are many minima identified with the global minima indicated at the cross-point of the two black dashed lines and a white

Table 5.2: The boundaries of the 4-dimensional state space and the length of the hypercubes for the retrieval illustration.

x_i	variables	min	max	hypercube length
x_1	x	-0.50 mm	0.50 mm	0.01 mm
x_2	z	-0.75 mm	0.75 mm	0.01 mm
x_3	m	1.45	1.65	0.01
x_4	d	1,000 nm	3,500 nm	1 nm

dashed line in the figure. The cross section of the map for the horizontal and vertical black dashed lines and the white dashed line are shown in the top, middle and bottom of Fig. 5.8(b), respectively. The minima at the figures are indicated and the vertex corresponding to the minima is selected as $\hat{\mathbf{x}}$. The values of $F_i(\hat{\mathbf{x}})$ for $1 \leq i \leq 6$ and $7 \leq i \leq 3006$ are plotted as a blue line in Figure 5.6.a and 5.6.b, respectively, with $*\chi_v^2$ indicated in Figure 5.6.b.

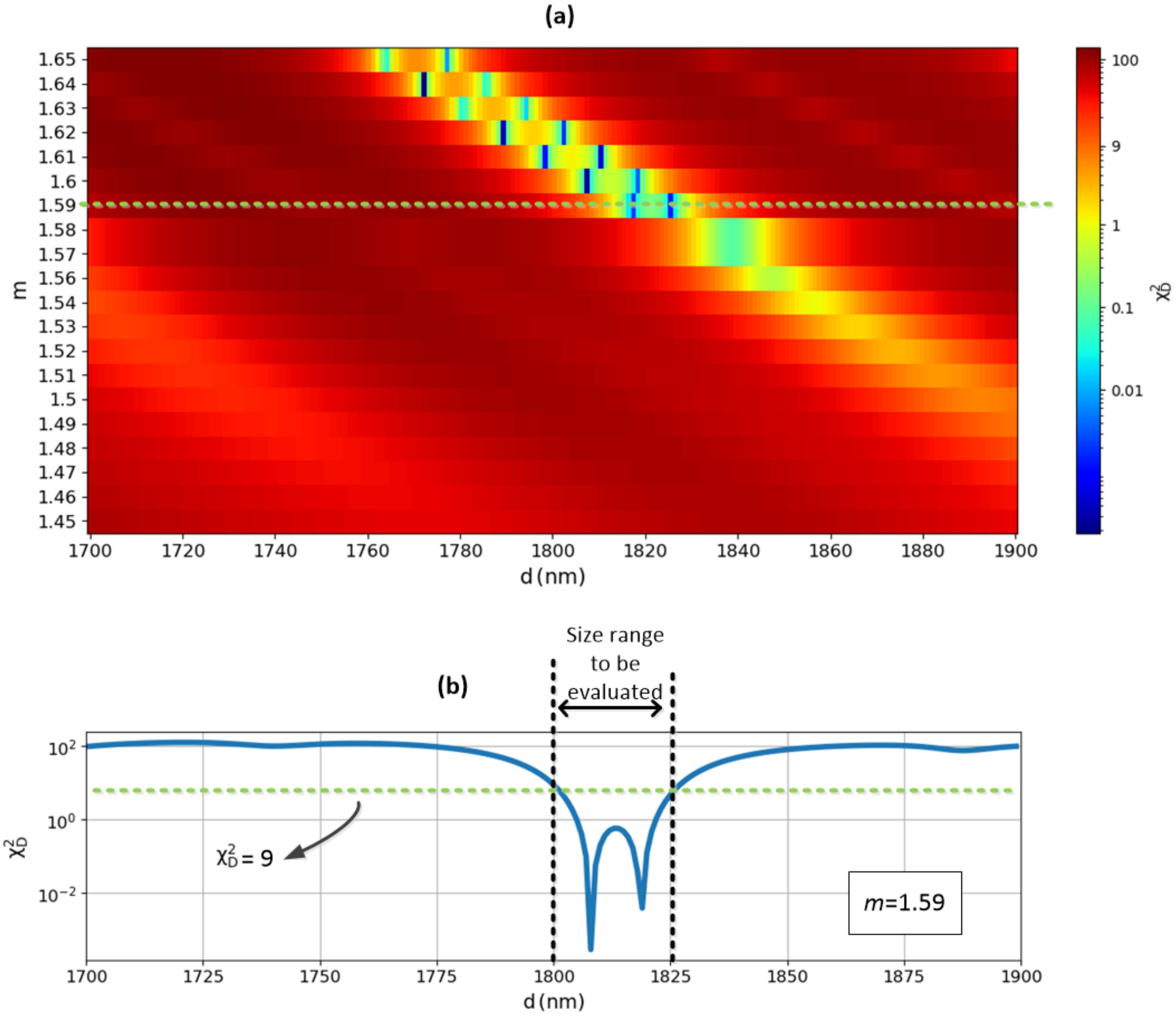

Figure 5.7: (a) The map of χ^2_{D} calculated from the fit of a PMT pulse depth shown in Figure 5.6.a with the forward model of PMT pulse depth for various particle size and refractive index located at a fixed particle position. For visual clarity, the size range is limited from 1,700 nm to 1,900 nm. The particles are positioned at $x = -0.22$ mm. The values of χ^2_{D} are approximated independent of z. (b) The cross section of the map at $m = 1.59$ indicated by a yellow dashed line in (a). The value of $\chi^2_{\mathrm{D}} = 9$ is indicated by a green dashed line. The size range to be evaluated is indicated by the range between the black dashed lines.

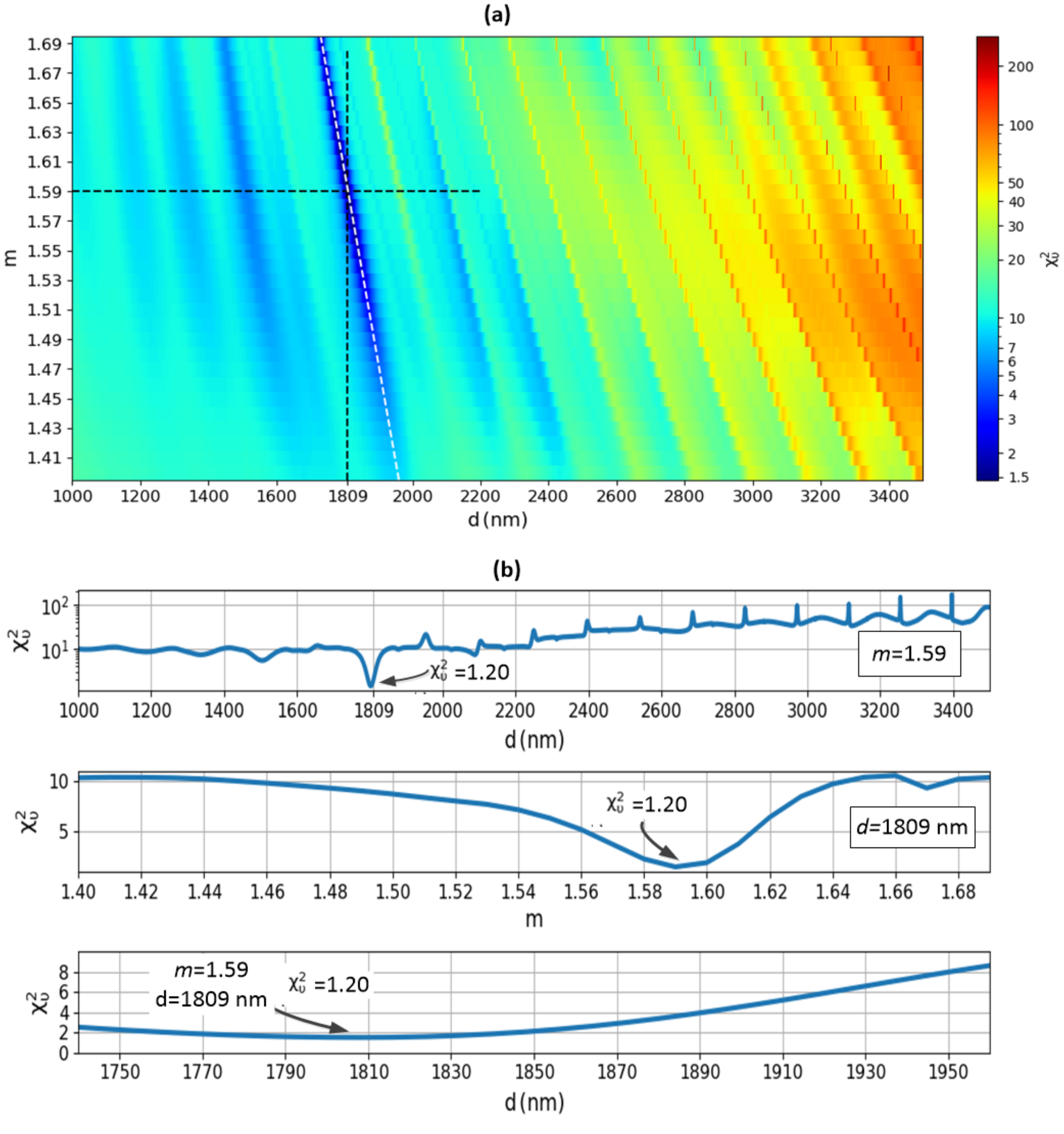

Figure 5.8: (a) The map of χ_{υ}^2 calculated from the fit of a pair of SPARCLE responses shown in Figure 5.6.a and 5.6.b with the forward model of SPARCLE responses for various particle size and refractive index located at a fixed particle position. The particles are positioned at $x = -0.22\,\mathrm{mm}$ and $z = -0.43$. (b) The cross sections of the map indicated by the horizontal and vertical black dashed lines and the white dashed line in (a).

5.6 Retrieving particle size and refractive index from SPARCLE calibration responses

The retrieval scheme was applied to retrieve particle size and refractive index from the responses of SPARCLE to the four solid aerosols in the calibration runs described in Chapter 3. The solutions were searched over different ranges of the 4-dimensional state space. The ranges are listed in Table 5.3. The state space were divided into hypercubes with the length of the hypercubes listed in the same table. Due to the time constraint in working this thesis, the retrievals were performed only for limited number of SPARCLE responses whose $SNR \geq 2.5$. The SNR limit 2.5 is selected due to apparent scattering signals for SPARCLE responses whose SNR higher than or equal to 2.5 as shown in Figures 3.18 - 3.21. The selection introduces a bias since SPARCLE responses whose SNR can be the responses to either residual particles or PSL particles illuminated by low light intensity.

Table 5.3: The boundaries of the 4-dimensional state space in retrieving particle size and refractive index from the responses to aerosols generated in the calibration runs and the length of the hypercubes in the state space.

x_i	variables	min	max	hypercubes length	applied in the retrieval from the responses to
x_1	x	-0.50 mm	0.50 mm	0.01 mm	all aerosols
x_2	z	-0.75 mm	0.75 mm	0.01 mm	all aerosols
x_3	m	1.55	1.65	0.01	all aerosols
x_4	d	1,000 nm	1,190 nm	1 nm	1st aerosol
		1,680 nm	1,900 nm	1 nm	2nd aerosol
		1,960 nm	2,140 nm	1 nm	3rd aerosol
		2,900 nm	3,150 nm	1 nm	4th aerosol

The values of $*\chi_v^2$ from the retrieval are presented as two-dimensional histograms as a function of the SNR of the SPARCLE responses. The histograms are shown in Figures 5.9.a - 5.9.d with the distributions of $*\chi_v^2$ and the SNR projected at the right and top, respectively. A dashed red line is plotted in each figure to indicate $*\chi_v^2 = 1$. The detail of the aerosols are indicated in the box at the top right of each figure. As seen in Figures 5.9.a and 5.9.b, most of $*\chi_v^2$ values are smaller than or equal to two. The two dimensional histograms in the figures indicate that the values of $*\chi_v^2$

is weakly affected by the *SNR*. This results indicate that the estimated $\boldsymbol{\epsilon}$ using the background measurements is a good approximation of true error. Meanwhile, most of $*\chi_v^2$ values as shown in Figures 5.9.c and 5.9.d are smaller or equal to twenty. The distribution of $*\chi_v^2$ values are greater for larger *SNR*. There are at least two possible explanation for this feature:

1. the particle size range of the aerosols are larger than the size range over which the solutions were searched,

2. a global minimal may be located off the vertices of the hypercubes. The hypercube size should be smaller for bigger particle size and refractive index due to higher sensitivity of LSPs to the changes of particle size and refractive index. Based on Mie theory, the derivative of scattering light amplitudes is a function of d and m [Grainger et al., 2004]. It implies that the patterns of light scattered by smaller particles with lower refractive index can be less sensitive to the changes of particle size and refractive index than those scattered by bigger particles with higher refractive index. The differences in the sensitivity are illustrated in Figure 5.10 which shows various LSPs generated from the light scattered by various size of particles with the same refractive index. In (a), the LSPs generated from the light scattered by three particles with the sizes 1.100 nm, 1.120 nm and 1,140 nm are nearly similar, while, in (b), (c) and (d), the LSPs generated from the light scattered by particles with sizes bigger than 1,800 nm can be easily distinguished,

Due to these possible caused, the retrieval of particle size and refractive index for some responses failed to find the solutions expressed by high values of $*\chi_v^2$. To illustrate, the values of $*\chi_v^2$ of some retrieval results are shown in Figures 5.11.a - 5.11.h. As shown in Figures 5.11.a and 5.11.d, the forward models fit with the measurements and the goodness of the fits are indicated by $*\chi_v^2$ lower than two. Meanwhile, other retrieval results show that the forward models do not fit with the measurements as shown in Figures 5.11.c and 5.11.d and the goodness of the fits are indicated by $*\chi_v^2$ bigger than five.

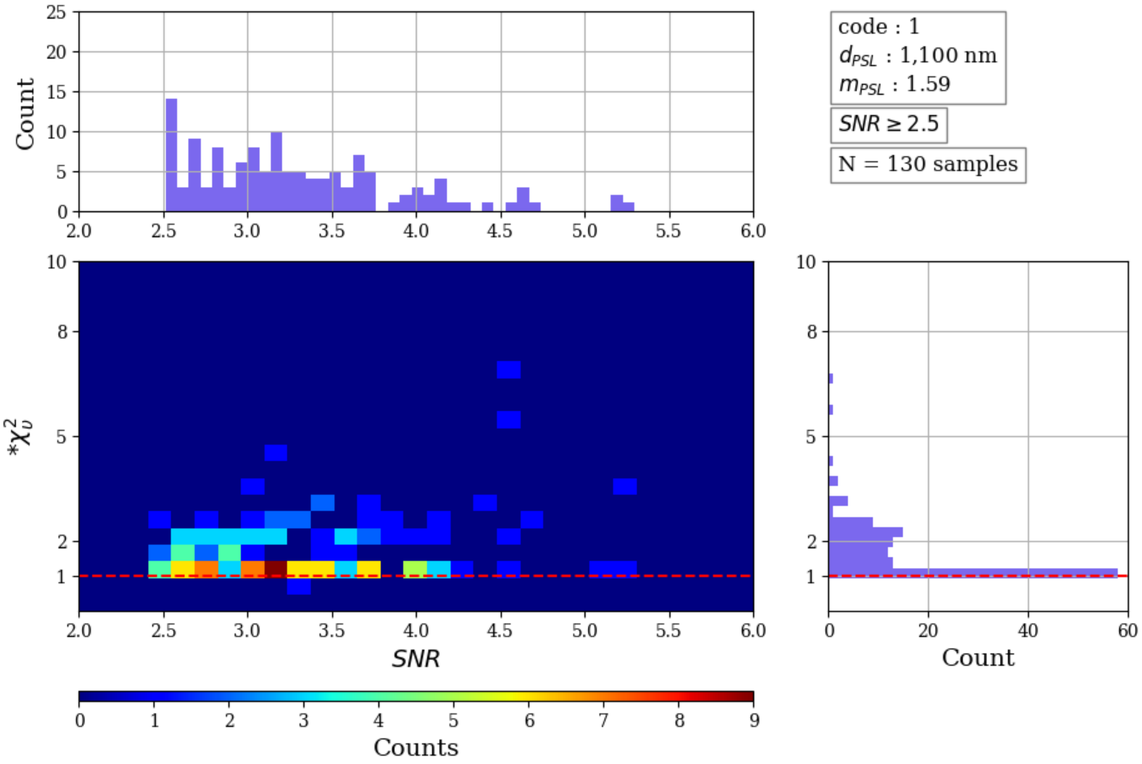

(a) the first aerosol

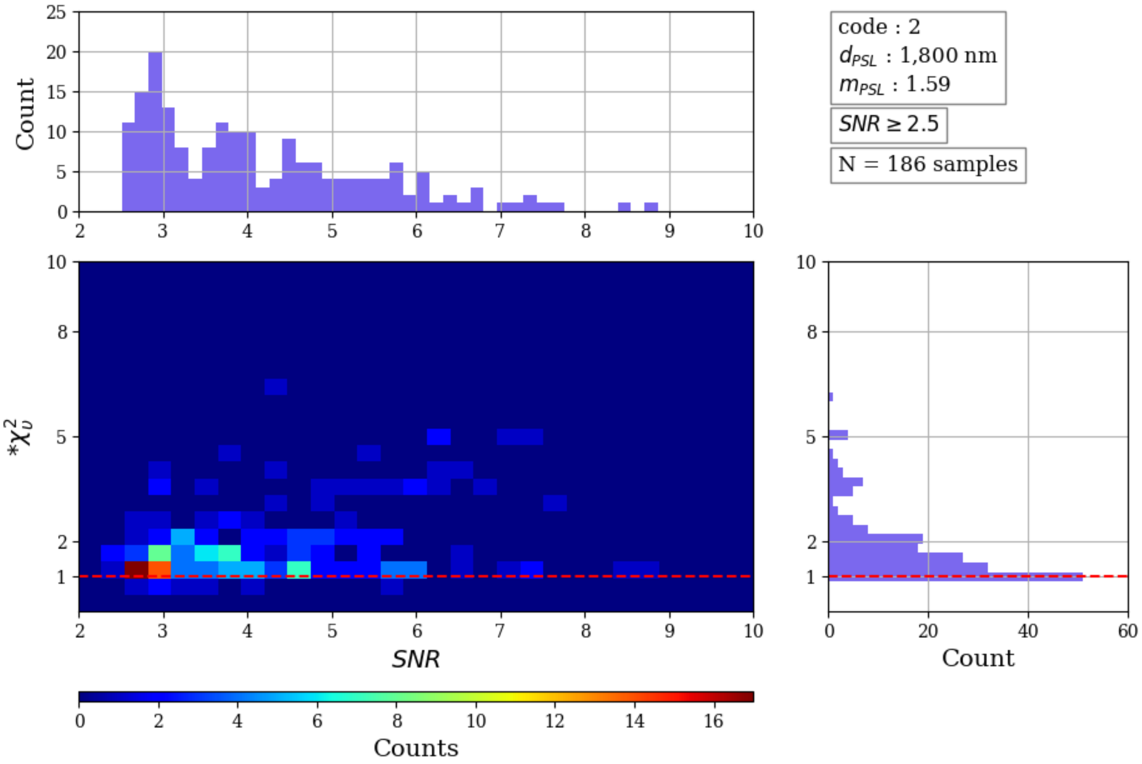

(b) the second aerosol

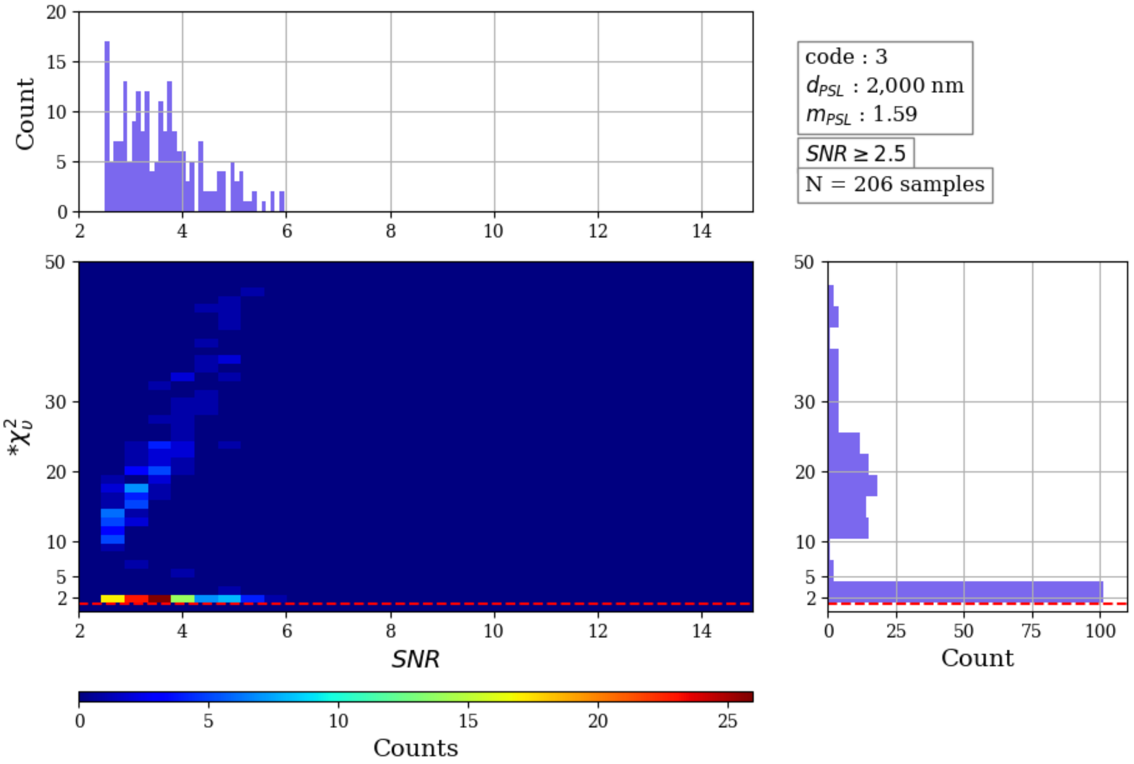

(c) the third aerosol

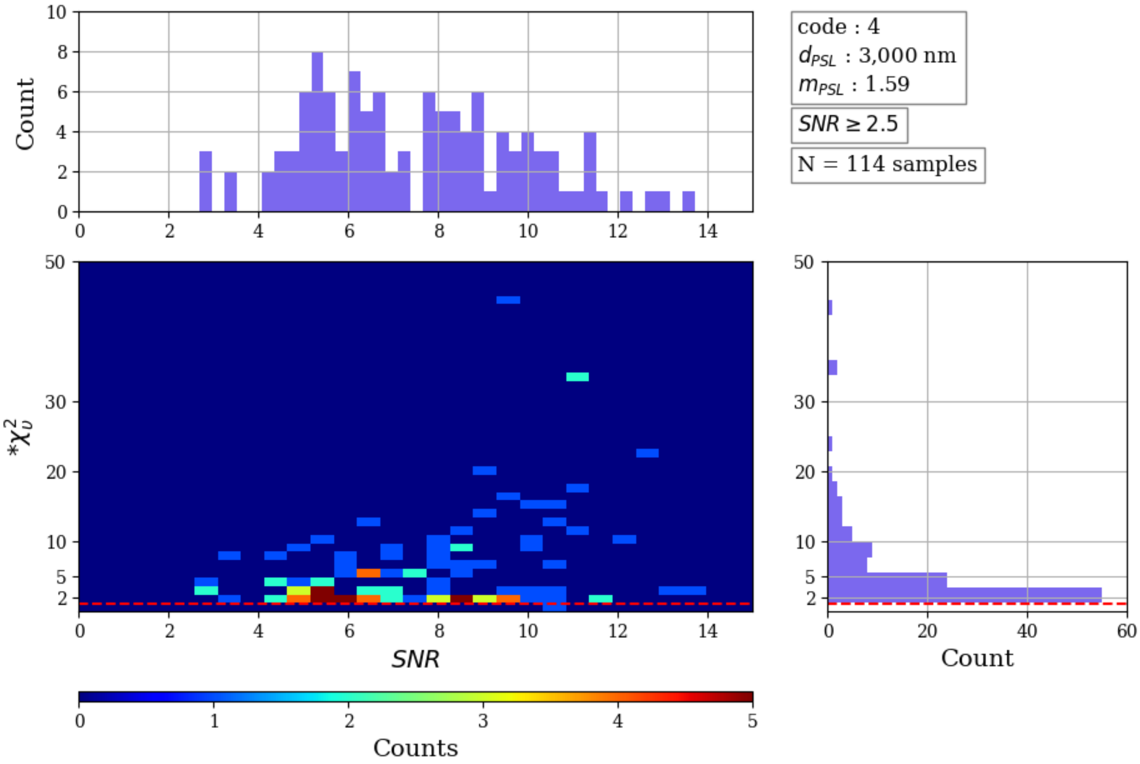

(d) the fourth aerosol

Figure 5.9: The histogram of SNR and the values of $*\chi_v^2$.

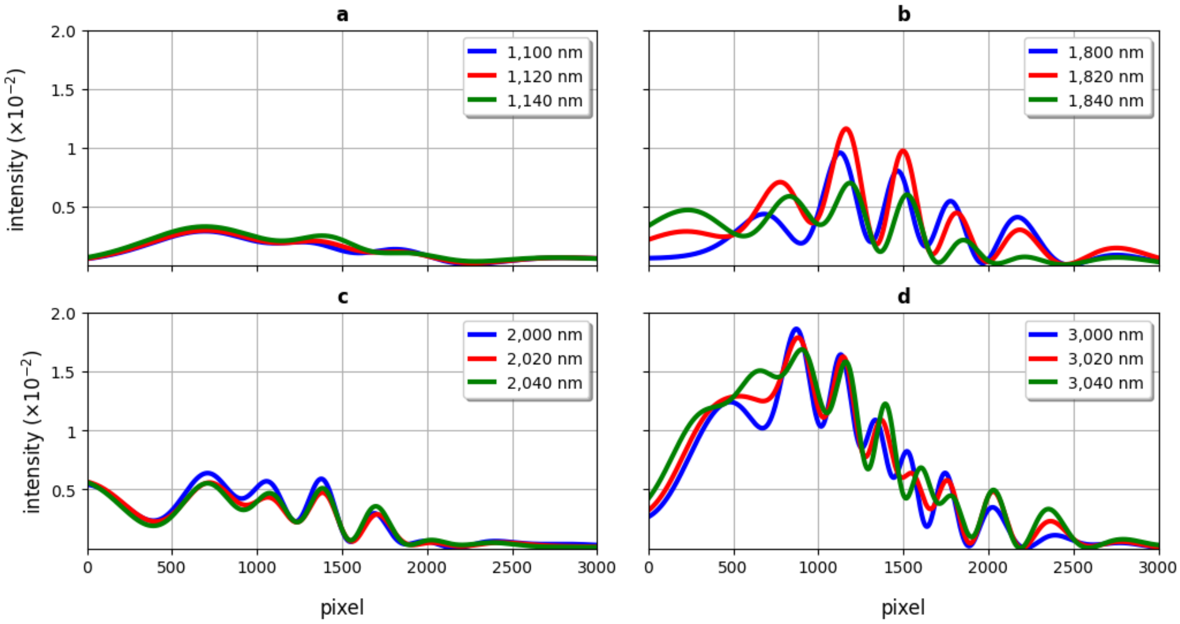

Figure 5.10: The forward model of the patterns of light scattered by various particle size with $m = 1.59$, $x = -0.22\,\mathrm{mm}$ and $z = -0.43\,\mathrm{mm}$.

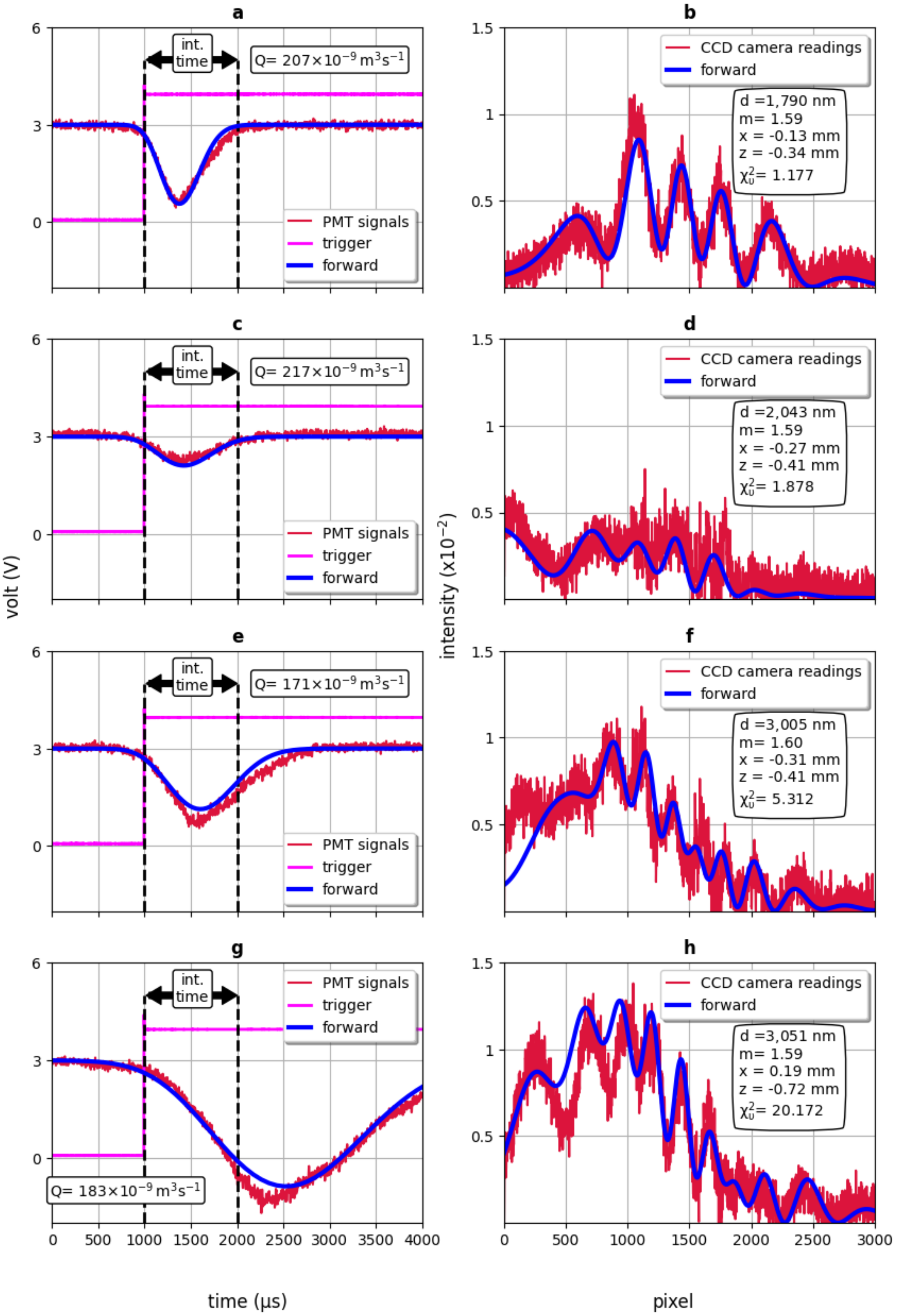

Figure 5.11: Some SPARCLE responses and the forward models calculated using retrieval solutions. The value of χ_v^2 is indicated in each figure

The retrieved d and m are presented as two-dimensional histograms shown in Figures 5.12.a - Figure 5.12.d with the distribution of retrieved d and m projected at the right and top, respectively. The detail of the aerosols are indicated in the box at the top right of each figure. The ranges of the values of d and m where the solutions for the retrievals were searched is indicated by the range between two red lines in the projected distributions. The mean d and m specified by the manufacturers are denoted as d_{PSL} and m_{PSL}, respectively, and they are indicated by the black lines in the projected distributions. To evaluate the distribution of retrieved d and m, two parameters are calculated: the mean of the distributions denoted by $\bar{d}$ and $\bar{m}$, respectively, and the standard deviation of the distributions denoted as σ_d and σ_m, respectively. In the figures, $\bar{d}$ and $\bar{m}$ are plotted as green lines while σ_d and σ_m are indicated. Additional parameters are derived from $\bar{d}$, $\bar{m}$, σ_d and σ_m for further evaluation of the distributions. The parameters are:

1. the ratios $\frac{|\bar{d}-d_{\mathrm{PSL}}|}{d_{\mathrm{PSL}}}$ and $\frac{|\bar{m}-m_{\mathrm{PSL}}|}{m_{\mathrm{PSL}}}$ that indicate the deviation of $\bar{d}$ and $\bar{m}$ from d_{PSL} and m_{PSL}, respectively,
2. the ratios $\frac{\sigma_d}{\bar{d}}$ and $\frac{\sigma_m}{\bar{m}}$ that indicate the the ratio of the standard deviation of retrieved d and m to $\bar{d}$ and $\bar{m}$, respectively. Ratio $\frac{\sigma_d}{\bar{d}}$ can be compared with ratio $\frac{\sigma_d}{d_{\mathrm{PSL}}}$ provided by the manufacturers.

The retrieval results are summarised in Table 5.4.

Table 5.4: A summary of the retrieval results.

aerosol details			retrieved properties							
aerosol code	d_{PSL} (nm)	m_{PSL}	$\bar{d}$ (nm)	σ_d (nm)	$\frac{|\bar{d}-d_{\mathrm{PSL}}|}{d_{\mathrm{PSL}}}$ %	$\lvert\frac{\sigma_d}{\bar{d}}\rvert$ %	$\bar{m}$	σ_m	$\frac{|\bar{m}-m_{\mathrm{PSL}}|}{m_{\mathrm{PSL}}}$ %	$\lvert\frac{\sigma_m}{\bar{m}}\rvert$ %
1	1,100	1.59	1,093	44	0.63	4.03	1.607	0.024	1.07	1.07
2	1,800		1,796	18	0.22	1.00	1.600	0.023	0.63	0.62
3	2,000		2,044	31	2.20	1.51	1.586	0.022	0.25	0.25
4	3,000		3,000	48	0.62	1.62	1.603	0.019	0.8	1.1

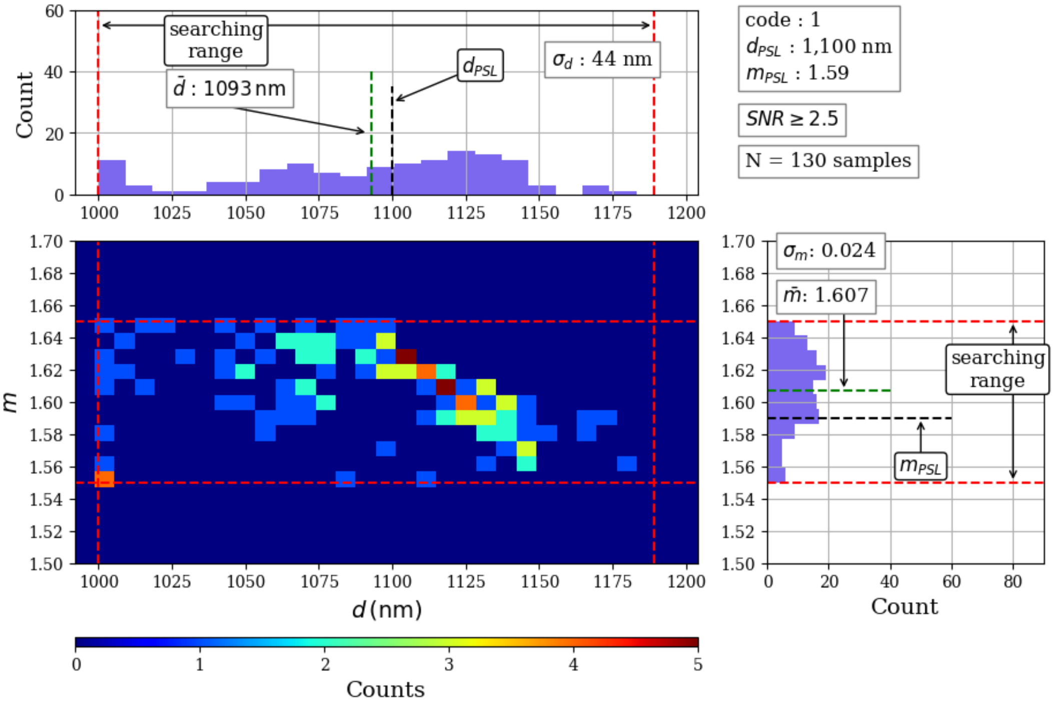

(a) the first aerosol

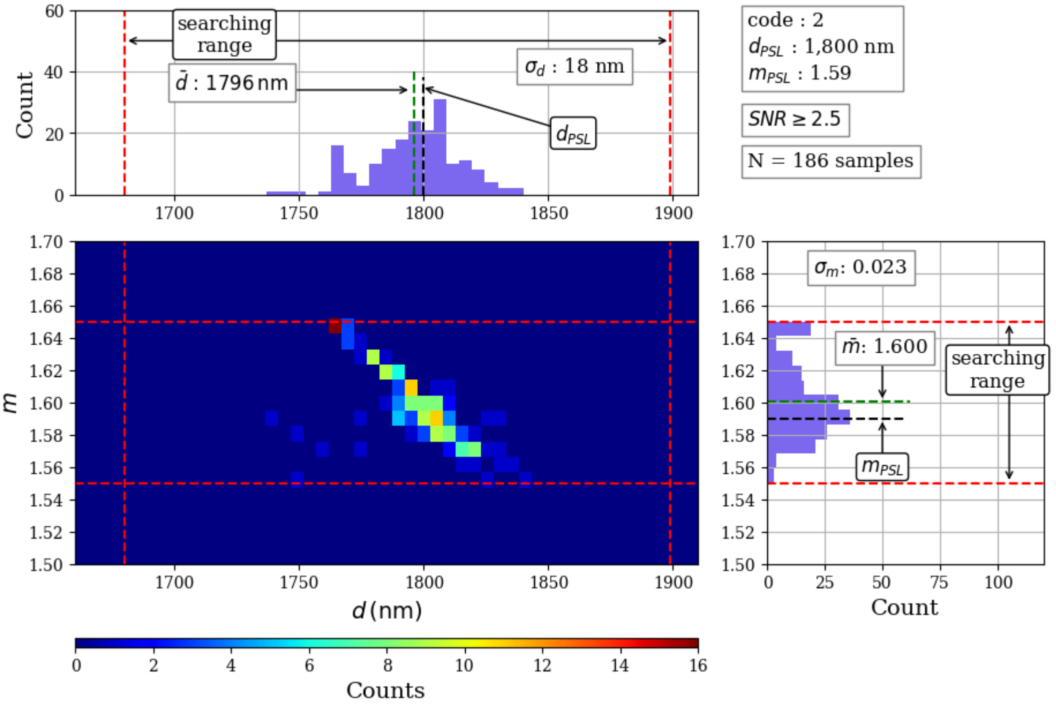

(b) the second aerosol

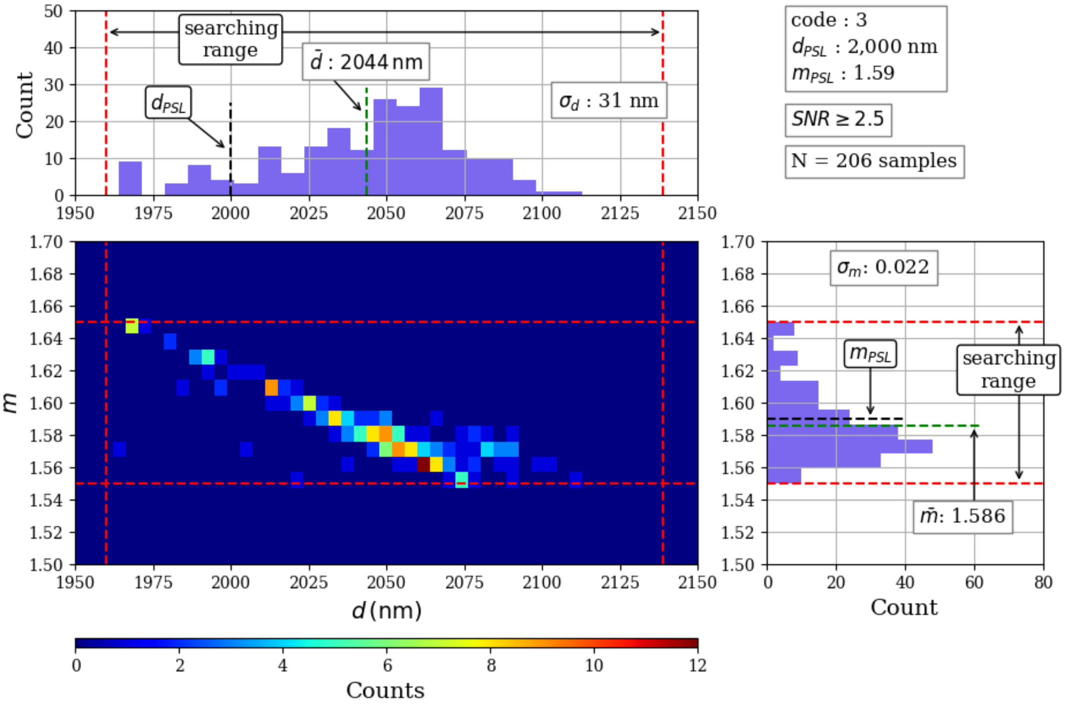

(c) the third aerosol

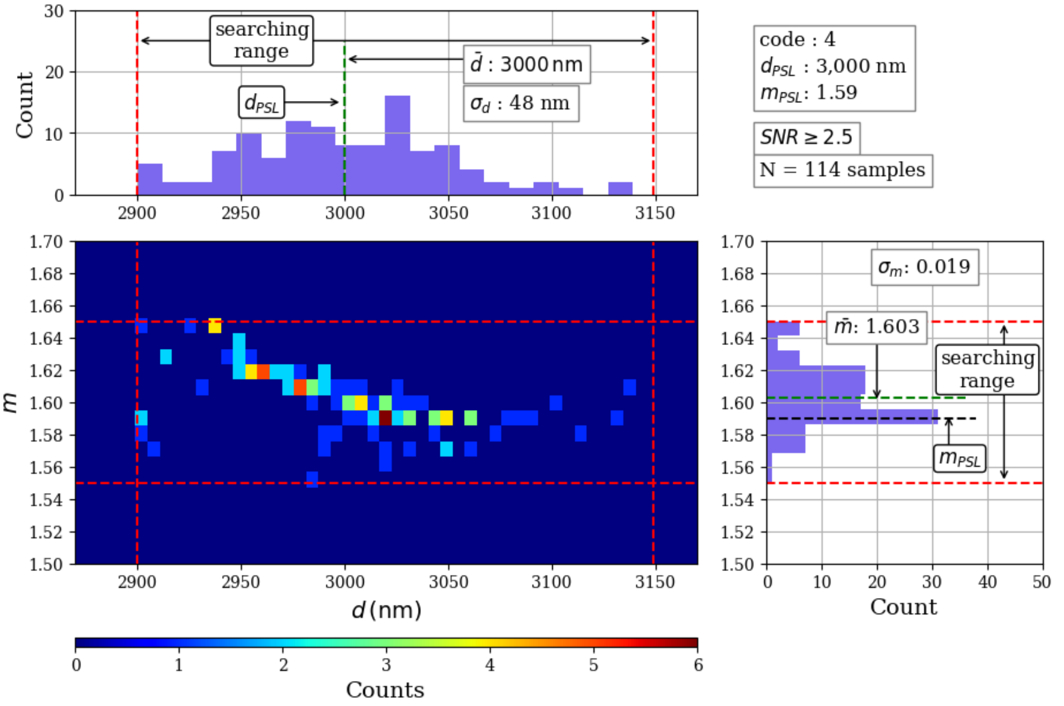

(d) the fourth aerosol

Figure 5.12: Retrieval results from the responses to aerosols generated in the calibration run.

The retrieval results from the responses to the aerosols encoded as 2, 3, and 4 are in agreement with those specified by the manufacturers. The shape of the distributions of the retrieval results are nearly symmetrical and peak around the means of the distributions. The deviation of $\bar{d}$ from d_{PSL} is less than 2.20% of d_{PSL}. The retrieved d distribute around $\bar{d}$ with the ratio $\frac{\sigma_d}{\bar{d}}$ less than 1.62%. This ratio is less than the uncertainties of d_{PSL} as specified by the manufacturers, which is less than 5% of d_{PSL}. The deviation of the retrieved $\bar{m}$ from m_{PSL} is less than 0.8% of m_{PSL}. The retrieved m distribute around $\bar{m}$ with the ratio $\frac{\sigma_m}{\bar{m}}$ less than 1.1%.

The retrieval results from the responses to the aerosol encoded as 1 show a large uncertainty. The shape of the distribution of the retrieval results are not symmetrical with the mean of the distribution further away from the peak of the distribution. The ratio $\frac{\sigma_d}{\bar{d}}$ is larger than 4%. This ratio is in the order of the uncertainty of d_{PSL} as specified by the manufacturer, which is less than 5% of d_{PSL}. Although the ratio is still within the specified uncertainty, the ratio is higher than those in the distribution of the retrieved d from SPARCLE responses to aerosol code 2, 3, and 4. The distribution of m also shows a similar feature: the ratio $\frac{\sigma_m}{\bar{m}}$ is higher than those in the distribution of the retrieved m from the SPARCLE responses to aerosol code 2, 3, and 4. The larger ratios can be resulted from the larger variation of particle size and refractive index of the aerosol. However, there may be a bias introduced by the retrievals. The retrieval used LSPs to retrieve particle size and refractive index and, as previously shown in Figure 5.10, the LSPs for various particle size around 1,100 nm are difficult to distinguished. This feature can result in a map of χ_v^2 that contains many local minima with similar values of χ_v^2.

5.7 Retrieving particle size and refractive index from the responses of SPARCLE to test aerosols

The retrieval scheme was applied to the SPARCLE responses to test aerosols from the measurement described in Chapter 4. Due to the time constraint of this thesis, the retrievals were only performed to limited number of the responses whose $SNR \geq 4.15$. The solutions were searched over particular ranges of state space. The ranges are summarised in Table 5.5. To note, the hypercube length in the size dimension is 10 nm. This length is longer than that used in the section above. The values of $*\chi_v^2$ from the retrieval are shown in Figure 5.13. As shown in the figure, most of the values are smaller than two. Some solutions failed to be found and it is indicated by large values of $*\chi_v^2$. Some examples of the solutions are illustrated in Figure 5.14

with the solutions and the values of χ_v^2 indicated in the figure. As seen in the figure, the forward models fit with the measurements with χ_v^2 between around 1.6 to around 1.8.

Table 5.5: The range of the state space and the hypercube length in the state.

x_i	variables	min	max	hypercube length
x_1	x	-0.50 mm	0.50 mm	0.01 mm
x_2	z	-0.75 mm	0.75 mm	0.01 mm
x_3	m	1.30	1.70	0.01
x_4	d	1,000 nm	3,500 nm	10 nm

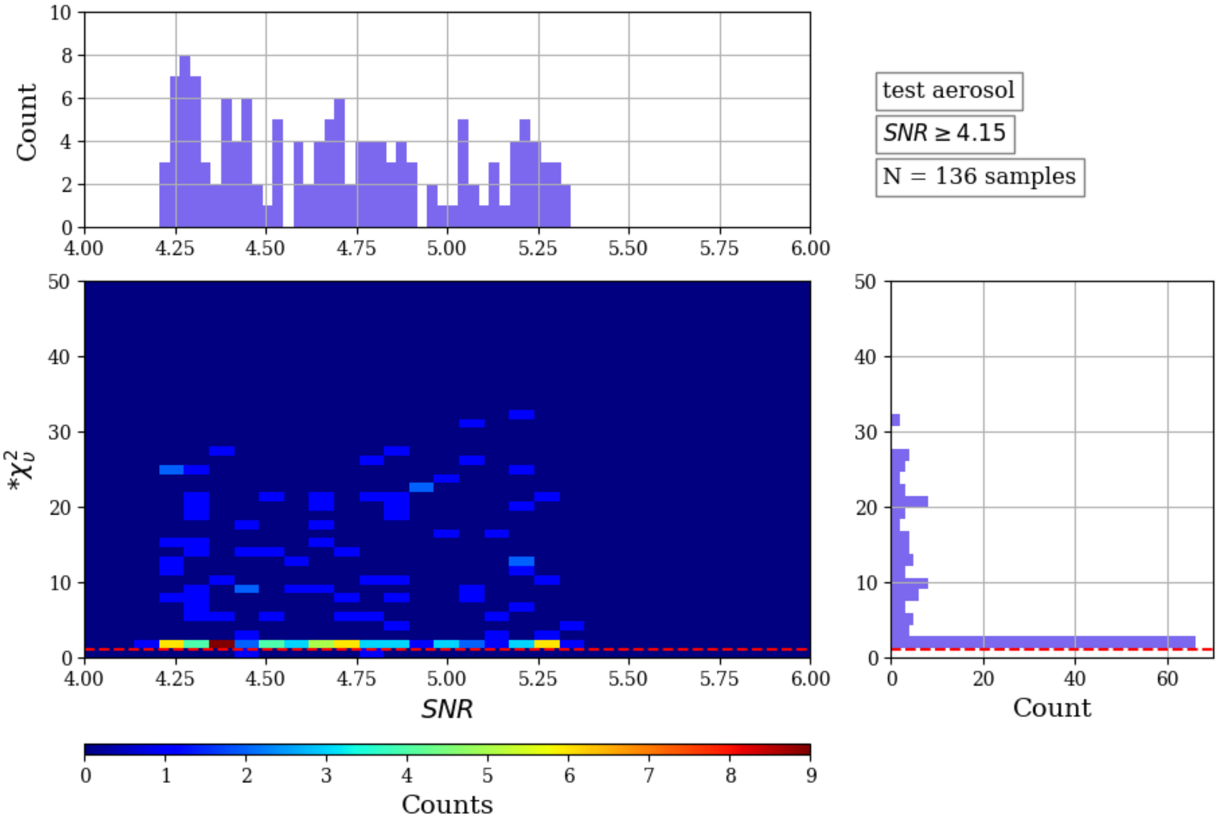

Figure 5.13: The histogram of *SNR* and the values of $*\chi_v^2$.

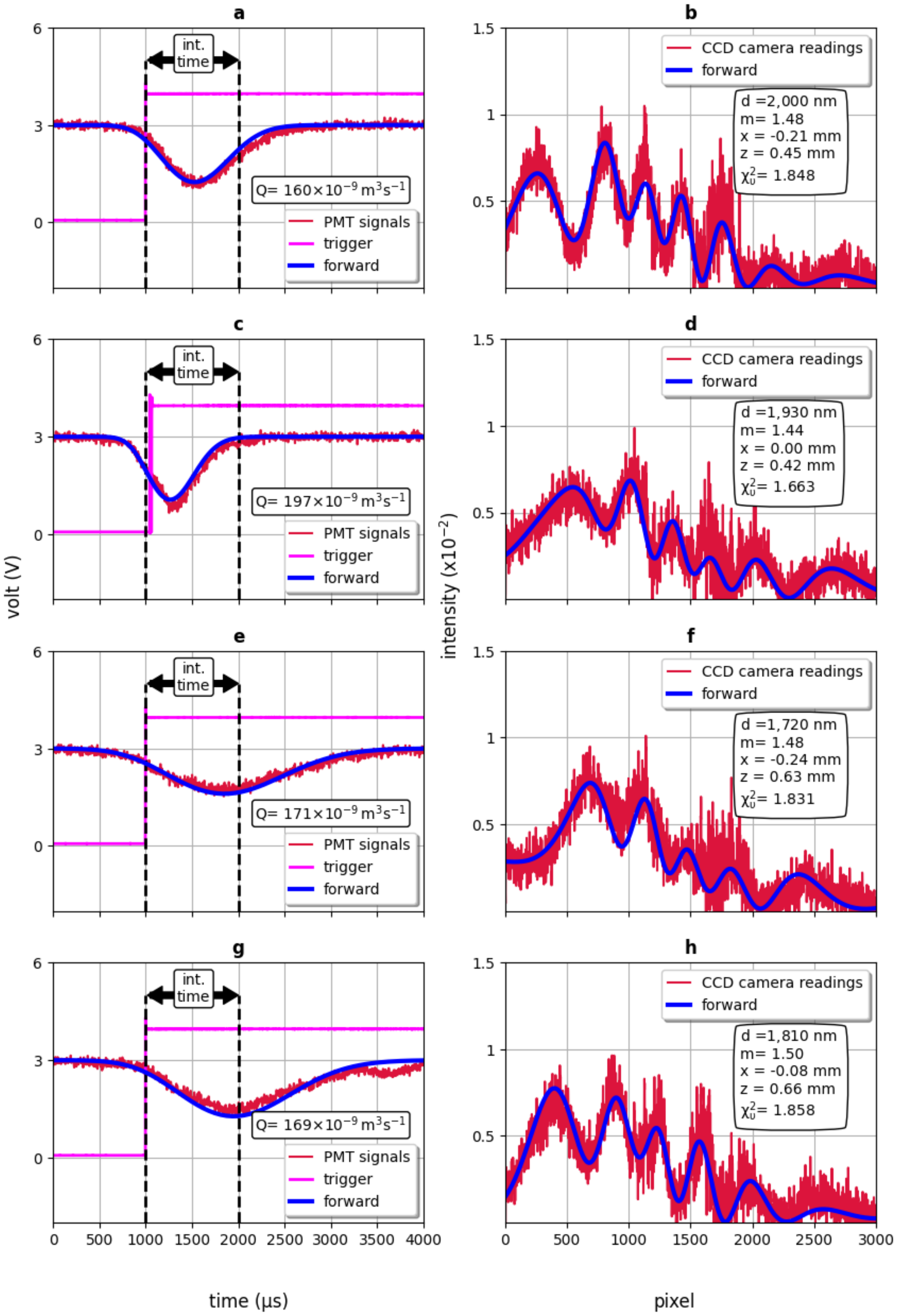

Figure 5.14: Some SPARCLE responses to test aerosols and the forward models calculated using retrieval solutions. The value of χ^2_υ is indicated in each figure

The distribution of retrieved d and m are shown in Figure 5.16. As seen in the figure, the shape of the distribution of retrieved m is nearly symmetrical with a peak easily identified at around 1.48. The mean and the standard deviation of the distribution are 1.47 and 0.060, respectively. The mean is close to the refractive index of sodium dodecyl sulphate, one of the main ingredients of the test aerosol listed in Table 4.1. The refractive index of sodium dodecyl sulphate is 1.44. One of the interpretation of the results is that the water and ethanol contents in the test aerosols quickly evaporated and solid particles formed which were mainly composed of sodium dodecyl sulphate. More investigation is needed to explain the difference between $\bar{m}$ and the refractive index of sodium dodecyl sulphate. One possible explanation is due to the bias in the retrieval that assuming the aerosols were non-absorbing aerosols. The patterns of light scattered by absorbing and non-absorbing particles can be significantly different as illustrated in Fig. 5.15. The colour of the liquid soap used to generate the aerosols was green suggesting that the aerosols might absorb a portion of the illuminating red laser beam.

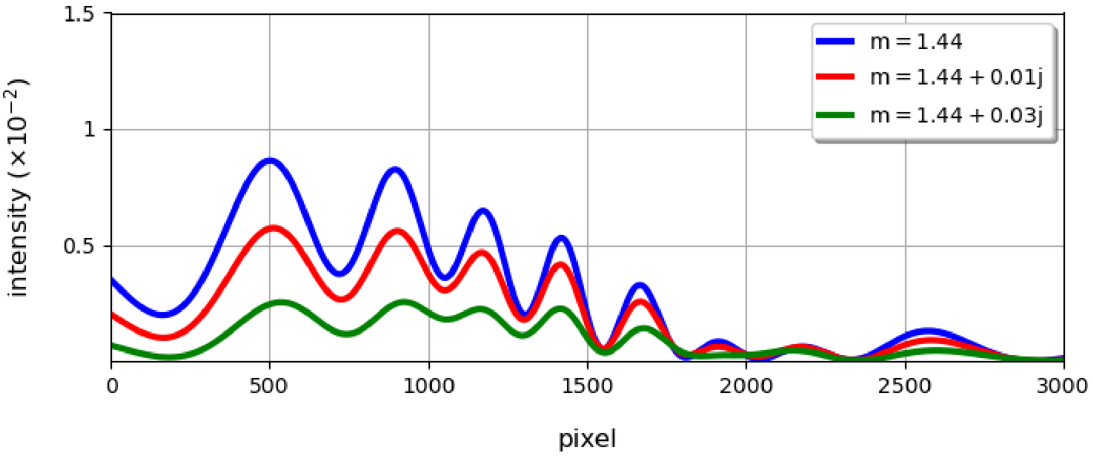

Figure 5.15: LSPs scattered by three particles of the same size and different refractive index. The size of the particles is 2,500 nm and the refractive indices are indicated.

The shape of the distribution of retrieved d seems to be different from the shape of the size distribution measured by the OPC shown in Figure 4.2. The difference may due to three reasons:

1. the size resolution of the histogram is different with the bin size of the OPC. In the size range between 1,000 nm and 1,600 nm, the bin size is 600 nm while the size resolution of the histogram is 100 nm,

2. the OPC was calibrated using dolomite particles whose refractive index is 1.60. This may introduced a bias when measuring particles with different refractive index,

3. the number of the responses in the retrievals are limited. In selecting responses with $SNR \geq 4.15$, a large portion of the responses which may correspond to the light scattered by particles smaller than 1,500 nm could have been omitted resulted in decreasing number of retrieved particle size smaller than 1,500 nm.

To compare the distribution of the retrieved d and the size distribution measured by the OPC, the retrieved d were distributed according to the bin size of the OPC. The distribution is plotted as a blue histogram in Figure 5.17. The expected size distribution to be detected by SPARCLE derived from the distribution measured by the OPC is plotted in the same figure as a red histogram. As seen in the figure, the shape of the distribution of retrieved d is similar to that of the expected distribution.

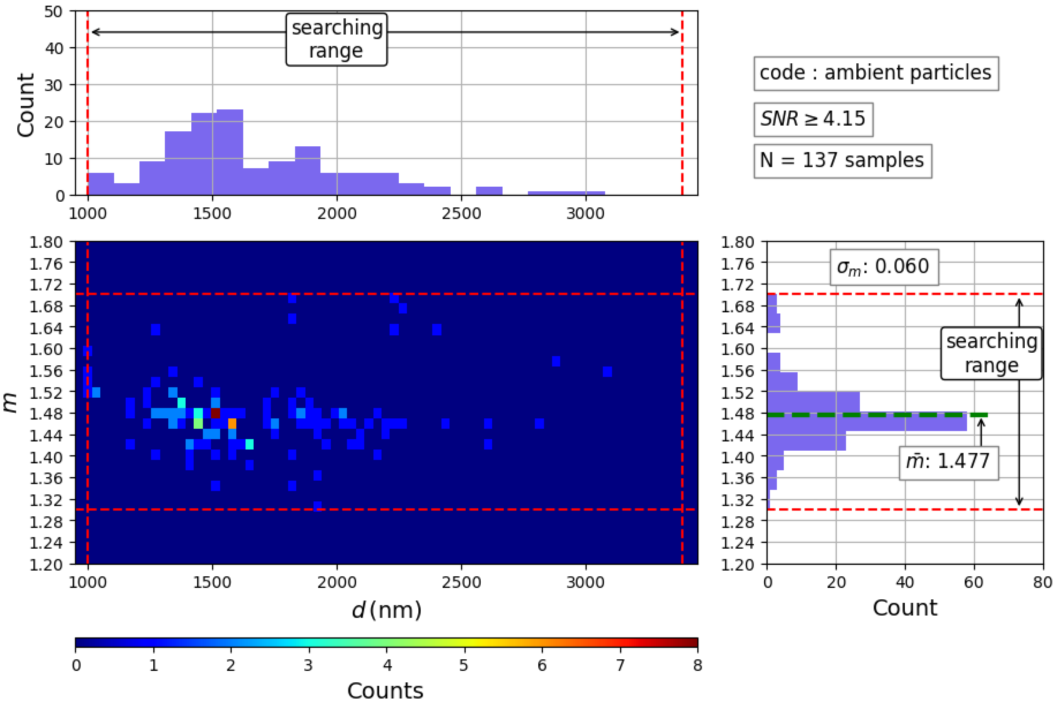

Figure 5.16: The distribution of d and m retrieved from SPARCLE responses to the test aerosol.

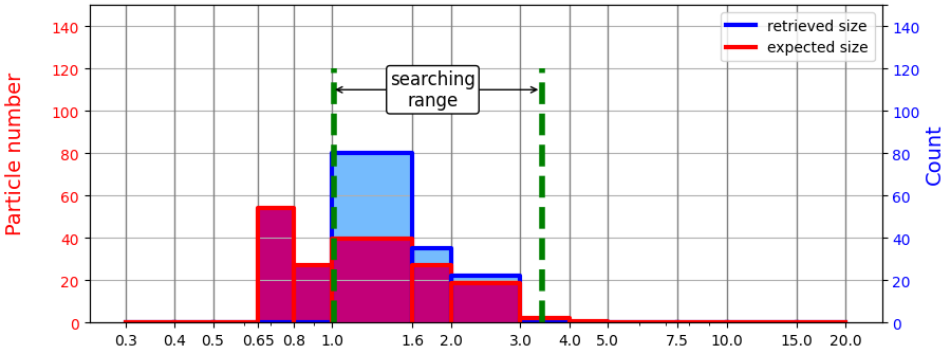

Figure 5.17: The retrieved d distributed according the bin size of the OPC and the expected size distribution detected by SPARCLE.

5.8 Summary

The problem to retrieve target quantities from measurements consists of two distinct problems: the calculation of SPARCLE measurements from target quantities called the forward problem and the estimation of the target quantities from the measurements with associated errors called the inverse problem. The target quantities are particle size and refractive index and the position of the particle on the x-z plane. The target quantities are assembled to form a state vector. The measurements by the PMT and the CCD camera were assembled to form a measurement vector. To reduce the computational cost, only six signals that characterise the PMT signals are included in the measurement vector. A state vector that minimises a cost function is selected as the solution. The cost function is calculated using the difference between the forward function and measurement vector with the associated errors.

A scheme to retrieve particle size and refractive index from SPARCLE responses has been developed. The scheme is a simple brute-force two-step method. The two-step procedure was used to reduce the overall computational cost. The first step is estimating the solution using the fit of PMT pulse depth. The second step is selecting the solution based on the estimation.

The retrievals were applied to the SPARCLE responses to the aerosols generated in the calibration runs whose *SNR* are higher than or equal to 2.5. The retrievals from the responses to aerosol particle size bigger than or equal to 1,800 nm result in the distributions that are nearly symmetrical with the mean of the distributions around the values specified by the manufacturers. The mean distributions of retrieved particle size are less than 2.20% of the size specified by the manufacturers. The mean distributions of retrieved refractive index are less than 0.8% of the refractive index specified the manufacturers. The standard deviation of the distributions of retrieved particle size is less than 1.62% of the mean of the distribution. The retrieval from the responses to aerosol particle size around 1,100 nm result in the distribution that is asymmetrical with the mean of the distribution further away from the peak of the distribution. The mean distributions of retrieved particle size is 0.63% of the size specified by the manufacturers. The mean distributions of retrieved refractive index is 1.07% of the refractive index specified the manufacturers. The standard deviation of the distribution of retrieved particle size is 4.03% of the mean of the distribution indicating a larger uncertainty of retrieved size compare to those in the retrieved size from the responses of the bigger aerosol particle size.

The retrievals scheme were also applied to limited number of the SPARCLE responses to the test aerosol whose *SNR* are higher than or equal to 4.15. The distribution of the retrieved particle size is in a good agreement with the expected size distribution derived from the size distribution measured by the OPC. The distribution of retrieved refractive index is nearly symmetrical with a clear peak at around 1.48. The mean and the standard deviation of the distribution are 1.47 and 0.060, respectively. The mean is close to the refractive index of sodium dodecyl sulphate, one of the main ingredients of the test aerosol. The refractive index is 1.44.

Chapter 6

Conclusion and future researches

6.1 Conclusion

This work demonstrates the ability of the second generation of SPARCLE to measure the size distribution and the refractive index of spherical homogeneous non-absorbing particles. Particle size and refractive index were retrieved simultaneously using a pair of SPARCLE responses consisting of the PMT signals and the CCD camera readings. The PMT is an extremely sensitive detector and in a simplified model where:

1. the illuminating light is evenly distributed in the sensing volume and the power of the illuminating light is around 4 mW,
2. the noise sources are limited to the Rayleigh scattering from air particles inside the scattering chamber and the dark currents of the detectors,

the PMT is expected to detect single particles as small as 300 nm with signal to noise ratio equal to 100. Based on the same model, the CCD camera can measure light patterns scattered by single particles as small as 800 nm with signal to noise ratio equal to 100. These limits are depicted in Figures 2.6 and 2.8. However, it was found that the illuminating light was not evenly distributed and, also the illuminating light was reflected by the sampling pipe contributed to higher background noise. The light distribution is shown in Figure 3.3 while the background noise is shown in Figure 3.1. The deviation to the simplified model results in the changes of the PMT detection limit: the smallest particle size it can detect is 640 nm.

Measurement biases introduced by SPARCLE instrument were identified. The dimensions of the sampling pipe and the rate of air sampling introduce biases in the sampling and transporting particles to the sensing volume. The efficiencies in the sampling and transporting particles are functions of particle size. The efficiencies are shown in Figure 2.15. Other bias is due to the distribution of the illuminating light and the air velocity in the sensing volume. The air velocity distribution is shown in Figure 2.18. The distribution lead to a probability distribution of particles being illuminated at a particular position in the sensing volume. The probability distribution is shown in Figure 3.23. Since the illuminating light is spatially distributed, the detection of a particle of particular size and refractive index depends on the particle position that the scattered light triggers the SPARCLE data acquisition system. The positions were calculated for particle size from 100 nm to 3000 nm with the refractive index of 1.59. By integrating the probability of particles being illuminated at these positions, the probability of detecting particles as a function of particle size can be developed. The probability of detecting particles is shown in Figure 3.27. Other bias is introduced due to the dimensions of the sensing volume. The dimensions determine the probability of more than one particle in the sensing volume at the same time called coincidence errors. The coincidence errors is expected to be less than 15% when sampling air with particle density less than 1,000 particles cm^{-3}. According to Table 1.5, SPARCLE is expected to measure particle size distribution of most types of troposphere regions with coincidence errors less than 15%.

To test its performance, SPARCLE was calibrated using four monodisperse solid aerosols. The aerosols contain PSLs beads whose the mean sizes as stated by the manufacturers are 1,100 nm, 1,800 nm, 2,000 nm and 3,000 nm. The refractive index of the PSLs is 1.59. By calibrating SPARCLE using these particle sizes, its performance to measure particles in the accumulation mode can be evaluated. The aerosols were generated by atomising liquid suspensions containing the PSLs and, then drying the droplets. The size distribution of the aerosols were monitored by the OPC. The OPC was calibrated by the manufacturer using Dolomite particles whose refractive index is 1.60. The size distributions as measured by the OPC are shown in Figure 3.28. Based on the figure, the aerosols were not only contain PSLs beads but also contain residual particles whose size is smaller than 800 nm. The residual particles were generated from the solidification of surfactants when “empty” droplets were completely dried. Particle size and refractive index were retrieved using limited number of SPARCLE responses to the aerosols. The results indicate that SPARCLE is able to measure the aerosols with the size deviation less than 2.2% and the refractive index deviation less than 1.07% of the size and refractive index specified by the manufacturers. The retrieval results are shown in Figure 5.12 These results are in the same order with the performance of DWOPS instrument described in Subsection 1.8.2. However, one of the main differences between SPARCLE and DWOPS is that SPARCLE does not require an *ad hoc* scaling factors to retrieve particle size and refractive index from its responses.

SPARCLE was used to measure a test aerosol. The test aerosol is a polydisperse aerosol generated by spraying a mixture of water and liquid soap. The measurement was performed in an enclosed fume hood. The refractive index of the liquid soap is 1.37. One of the main ingredients of the liquid soap was sodium dodecyl sulphate whose the refractive index is 1.44. The size distribution of the test aeorosol was monitored by the OPC. The retrieval of particle size and refractive index was performed using limited number of the responses of SPARCLE to the test aerosol. The distribution of the retrieved refractive index is nearly symmetrical and peaks at around 1.48. This result indicates that the test aerosol was dried shortly after it was generated and solid particles mainly composed of sodium dodecyl sulphate was formed. The distribution of the retrieved particle size is a skewed distribution with larger number of smaller particles. The shape is similar to the expected size distribution shape derived from the distribution measured by the OPC.

6.2 Future works

Based on the results in this work, there are several suggestions for future works. The future works can be divided into three types of developments. They are the development of

1. the instrument of the second generation of SPARCLE,
2. SPARCLE retrieval scheme,
3. the miniature of SPARCLE,
4. aerosol generation,

6.2.1 The development of the SPARCLE instrument

In this work, some limitations of SPARCLE instruments were identified. The limitations and their corresponding suggestions to improve the instrument are listed as follows:

1. the detection limit of SPARCLE was 640 nm when using a red laser diode whose wavelength was around 651 nm. The detection limit can be lowered down to detect particles smaller than 640 nm by using a light source with a shorter wavelength,

2. the distribution of the beam intensity in the scattering volume along the x-axis shown in Fig. 3.23(b) leads to the distribution of PMT pulse depth as a response to the light scattered by particles with particular size and refractive index as discussed in Sec. 3.8. Ideally, PMT pulse depth is a single value as a response to a particle of particular size and refractive index. This response characteristic can be used to constraint state vectors to be evaluated in retrieving particle size and refractive index. For example, PMT pulse depths as responses to particles illuminated with an homogeneous beam intensity can be similar to that shown in Fig. 2.6. As shown in the figure, a PMT pulse depth can be generated as a response to particles of various sizes. Then, the searching for the retrieval solution can be constraint into these particles sizes. If the beam is spatially distributed along the x-axis, then a large range of particle size should be included in the searching since bigger and smaller particles can lead to the same PMT pulse depth when they are illuminated by lower and higher light intensity, respectively. The single values of PMT pulse depth can be achieved by having an homogeneous beam intensity along the x-axis. The homogeneous beam can be approached by having a nearly homogeneous beam around the axis of the symmetry of the sampling pipe with sampled particles was designed to flow around the centre of axis. As shown in Fig 3.23, the beam used in SPARCLE was not homogeneous and sampled particles could flow further away from the axis of the symmetry as a function of SPARCLE sampling flow rate. There are at least two likely causes of the distribution of the beam:

    (a) it was caused by the characteristic of the laser diode beam. One way to alleviate this cause is by trying various laser diodes and use the one that leads to nearly homogeneous beam intensity around the axis of the symmetry,

    (b) it was caused by multiple reflections of the beam when propagating through the lenses and window glasses known as a ghosting effect. One way to alleviate this cause is by using non-reflective lenses and glass windows.

    Particles can be expected to flow around the axis of symmetry when SPARCLE is designed to operate in a relatively high sampling flow rate. As can be seen in Fig. 2.17, the distribution of particle speed is more concentrated around the axis of symmetry for higher sampling flow rate. However, this design leads to shorter particle transit time and higher laser diode power may be needed to increase the intensity of scattered light integrated by the CCD camera,

3. the CCD camera weakly measured the patterns of light scattered by particles whose size were 1,100 nm and refractive index was 1.59. This can be due to limited sensitivity of the CCD camera to detect the patterns. One option is to replace it with a new line sensor. The CCD camera was produced by Thorlab Inc. nearly 12 years ago. Since then, the technology of linear diode array has developed and become available with reasonable price.

4. the light scattered by particles smaller than 1,000 nm might be too weak to be measured by the CCD camera and retrieving particle size and refractive index using the scattered light may failed. One option is to use the responses of the PMT for the retrieval. However, the illuminating light is spatially distributed and this distribution introduces an ambiguity in retrieving particle size and refractive index using the responses: the responses to bigger particles illuminated by lower light intensity can be similar with the responses to smaller particles illuminated by higher light intensity. To alleviate the ambiguity, the illuminating light should be manipulated such that it evenly distributed in the sensing volume.

6.2.2 The development of SPARCLE retrieval scheme.

A simple retrieval scheme has been developed in this work. The simple retrieval suffers a main drawbacks: it was time consuming since the solution was searched by a brute-force method over a relatively large domain. In addition to that, the grid size for the search needs to adjusted as a function of particle size and refractive index to prevent overshooting the minima. One option to develop the retrieval scheme is to use a gradient-search method where the solution is searched by updating an initial guess of solution to the state along the direction of χ^2 gradient. This method can find the solution quickly provided a good initial guess. The initial guess may be derived from the PMT pulse depth, PMT pulse width and the characteristic frequency of the LSP.

6.2.3 Mini SPARCLE

The development of SPARCLE to the dimensions that can be carried by a simple unmanned aerial vehicle opens the possibility to measure the vertical distribution of particle size and refractive index in ambient air. This type of measurement can be a reference for the retrieval of particle size distribution based on satellite observation. One main component in the second generation of SPARCLE that is relatively heavy and takes a relatively large space is the PMT. In designing mini SPARCLE, the PMT can be replaced by PIN-25DP photovoltaic series produced by OSI Optoelectronics Inc. [Optoelectronics, 2021]. The photo sensitive area of the photovoltaic has a diameter around 28 mm, almost similar to the diameter of the PMT window. The photovoltaic can detect light as low as 10^{-10} W. This sensitivity makes the photovoltaic is expected to detect the power of light scattered by particles bigger than 500 nm as shown in Figure 2.6. The shape of the photovoltaic is nearly cylinder with the diameter around 30 mm and the length around 26 mm. The photovoltaic weighs less than 0.5 kg.

6.2.4 Aerosol generation

Some limitations of the aerosol generation in the SPARCLE calibration were identified. The limitations and their corresponding suggestions for the improvements are listed as follows:

1. the aerosols generated in the SPARCLE calibration still contained residual particles as shown in Fig. 3.14. This drawback can be alleviated by using PSL solution stocks which do not contain surfactants,
2. the OPC used to measure the aerosols had a relatively low size resolution in the size range between 1,000 nm and 4,000 nm. The low size resolution introduced a high uncertainty of the size distribution of the generated aerosols. An OPC with a high size resolution is currently available commercially,

Appendix A

The forward model of SPARCLE measurements

The forward model describes the light scattered by a particle in the sensing volume and the response of the detectors to the scattered light. The forward model is composed of two main steps:

1. calculating the power of the scattered light over the detectors' photo-active area,
2. convert the power into detectors' outputs based on detectors' specification and the SPARCLE data acquisition system setup.

In the calculation of the power in Step 1, variables to be considered are:

1. the position of the single particles in the sensing volume,
2. the size and refractive index of the single particles,
3. the wavelength and the intensity of the light that illuminates the single particles,
4. the area and the position of the detectors' photo-active area over which the power is evaluated,
5. the transit time of the single particles in the sensing volume. This variable is essential for the calculation of the measurements by the CCD camera.

Two coordinate systems are used in the forward models. The first coordinate system is the Cartesian coordinate system shown in Figure 2.3. The Cartesian coordinate system is centred at the intersection between the axis of the symmetry of the sampling pipe and the horizontal plane of the beam. The horizontal plane is the plane that divides the beam height in half. The second coordinate system is the Spherical coordinate system shown in Figure 1.9. The coordinate system is centred at the single particles travelling in the sensing volume. The two coordinates have different purposes. The Cartesian coordinate system is used to specify:

- the position of the single particles and the detectors,
- the distribution of the beam intensity,
- the distribution of the speed of air in the sensing volume.

While the Spherical coordinate is used to specify the direction of scattered light.

The response of the detectors to the scattered light is modelled as a result of the transfer of the power of scattered light to the detectors. The calculation of the power is done by integrating the scattered light Poynting vector which propagates perpendicular to the detectors' photo-active area. If the area is denoted as A_d, then the power of the scattered light transferred to the area, P_s, is calculated by

$$P_{\mathrm{s}} = \int_{A_{\mathrm{d}}} \vec{S}_{\mathrm{s}} . d\vec{A}_{\mathrm{d}}, \tag{A.1}$$

where $d\vec{A}_{\mathrm{d}}$ is the vector of the infinitesimal area of A_{d}; $\vec{S}_{\mathrm{s}}$ is the Poynting vector of scattered light and calculated as

$$\vec{S}_{\mathrm{s}} = \frac{1}{2} Re\left(\vec{E}_{\mathrm{s}} \times \vec{H}^{*}_{\mathrm{s}}\right), \tag{A.2}$$

where $\vec{E}_{\mathrm{s}}$ and $\vec{H}^{*}_{\mathrm{s}}$ are the electric field and the magnetic field conjugate of scattered light, respectively. The vectors $\vec{E}_{\mathrm{s}}$ and $\vec{H}^{*}_{\mathrm{s}}$ can be derived based on Mie theory and they are detailed in Appendix A.3. The formula for $\vec{E}_{\mathrm{s}}$ and $\vec{H}^{*}_{\mathrm{s}}$ are listed in Equation A.36. Applying the formula to Equations A.2 and A.1 resulted in

$$\begin{aligned} P_{\mathrm{s}}(r,\theta,\phi,\alpha,m) = \frac{|\vec{S}_{\mathrm{b}}|}{k^2} Re\Bigg[\int \frac{1}{r^2} \Big[&|S_1(\cos\theta,\alpha,m)|^2 \, \sin^2\phi + \\ &|S_2(\cos\theta,\alpha,m)|^2 \, \cos^2\phi \Big] \hat{r}.\hat{A}_{\mathrm{d}} \, dA_{\mathrm{d}} \Bigg] \end{aligned} \tag{A.3}$$

where:

- $\vec{S}_{\mathrm{b}}$ is the Poynting vector of the laser beam illuminating single particles;
- k is the wavenumber of the laser beam calculated as $k = \frac{2\pi}{\lambda}$ where λ is the laser wavelength;

- r, θ and ϕ represent the direction of the scattered light scattered over dA_d. They also represent the location of the detectors' photo-active area in the Spherical coordinate. While $\hat{r}$ is the unit vector of r;

- S_1 and S_2 are the angular distributions of the scattered light calculated based on Mie theory;

- α is the size parameter of single particles calculated by $\alpha = \frac{\pi\, a}{\lambda}$, where a is particle size;

- m is the refractive index of single particles;

- $\hat{A_\mathrm{d}}$ is the unit vector of surface A_d.

Since the beam propagated parallel with the z axis, the $\vec{S}_\mathrm{b}$ can be calculated from the beam intensity distribution on the x-y plane and the measured power of the beam. The $\vec{S}_\mathrm{b}$ is formulated as

$$|\vec{S}_\mathrm{b}|(x, y) = \frac{I_\mathrm{xy}(x, y)}{\int I_\mathrm{x}(x, y)\, dx\, dy} P_\mathrm{b}, \tag{A.4}$$

where $I(x, y)$ is the beam intensity distribution on the x-y plane; P_b is the measured power of the beam. The distribution $I_\mathrm{x}(x, y)$ is modelled as separable in the x and y axis as described in Chapter 3:

$$I_\mathrm{x}(x, y) = I_\mathrm{x}(x)\, I_\mathrm{y}(y), \tag{A.5}$$

where $I_\mathrm{x}(x)$ is the measured distribution along the x axis as shown in Figure 3.3 and $I_\mathrm{y}(y)$ is the distribution along the y axis modelled by Equation 3.1. Inserting Equations A.4 and A.5 into Equation A.3 results in

$$P_\mathrm{s}(x, y, r, \theta, \phi, \alpha, m) =$$
$$\frac{I_\mathrm{x}(x)\, I_\mathrm{y}(y)\, P_\mathrm{b}}{A_\mathrm{b}\, k^2} Re\left[\int \frac{1}{r^2}\Big[|S_1(\cos\theta, \alpha, m)|^2 \sin^2\phi + |S_2(\cos\theta, \alpha, m)|^2 \cos^2\phi\Big]\hat{r}.\hat{A_\mathrm{d}}\, dA_\mathrm{d}\right], \tag{A.6}$$

where A_b is equal to $\int I_\mathrm{xy}(x, y)\, dx\, dy$.

The particle is modelled to travel in the sensing volume parallel with the y axis. As described in Chapter 2, the speed is distributed normally around the axis of the symmetry of the sampling pipe. The distribution is expressed as

$$v(x, z) = a_\mathrm{v}\, e^{\frac{-(x^2+z^2)}{2\, \sigma_\mathrm{v}{}^2}}, \tag{A.7}$$

where $v(x, z)$ is the speed of single particles; a_v is the maximum speed; σ_v is the speed standard deviation. Modelling the air flow in the sensing volume by OpenFOAM software results in various a_v and σ_v for various SPARCLE sampling flow rates. The results are summarised in Table A.1. The modelling also indicates that the speed of single particles in the sensing volume is approximately constant. Based on the speed, the travelling time of single particles for a distance Δy can be calculated as

$$\Delta t(x, z) = \frac{\Delta y}{v(x, z)}. \tag{A.8}$$

No	Flow rates		a_v	σ_v
	$(\times 10^{-9}\mathrm{m}^3\mathrm{s}^{-1})$	(sccm)	$(\mathrm{m\,s^{-1}})$	(mm)
1	306	18.3	1.03	0.36
2	170	10.2	0.53	0.4
3	56	3.8	0.16	0.48

Table A.1: The speed distribution of air in the sensing volume as expressed in Equation A.7. The unit sccm is standard centimetre cube per minutes unit, a unit of the outputs of the flow meter used in the calibration.

SPARCLE samples the air with the rate varied from the flow rates shown in Table A.1. The speed distributions for the sampling are linearly projected from the distribution of similar flow rates shown in the table. For example, the sampling flow rates in the calibration vary slightly from $170 \times 10^{-9}\,\mathrm{m}^3\,\mathrm{s}^{-1}$. The speed distribution of the sampling flow rates are then approximated by linear projection of the a_v for the similar flow rate $170 \times 10^{-9}\,\mathrm{m}^3\,\mathrm{s}^{-1}$. Similar flow rates are called reference flow rates denoted by Q^ref while the corresponding a_v are denoted by $a_\mathrm{v}^\mathrm{cal}$. The projection is expressed as

$$a_\mathrm{v}^\mathrm{cal} = \frac{Q^\mathrm{cal}}{Q^\mathrm{ref}}\, a_\mathrm{v}^\mathrm{ref}. \tag{A.9}$$

The speed distribution of the flow rates used in the calibration is summarised in Table A.2

Sample code	Q^{cal}		$a_{\text{v}}^{\text{cal}}$	σ_{v}
	$(\times 10^{-9}\,\text{m}^3\,\text{s}^{-1})$	(sccm)	$(\text{m}\,\text{s}^{-1})$	(mm)
1	161	9.66	0.50	0.4
2	169	10.14	0.53	0.4
3	200	12.0	0.62	0.4
4	135	8.1	0.42	0.4

Table A.2: The speed distribution of air in the sensing volume for the sampling rates in the calibration. The flow rates are derived from Equation A.9 with $Q^{\text{ref}} = 170$ and $a_{\text{v}}^{\text{ref}} = 0.53$.

A.1 The forward model of the PMT signals

The PMT in the SPARCLE design is set to continuously measure the power of light scattered over the PMT window and to convert the power into electrical currents. The SPARCLE data acquisition system then converts the currents into voltages and samples the voltages with a particular sampling time. The PMT signals can be denoted by voltages as a function of time:

$$V(t). \tag{A.10}$$

The conversion of the power of scattered light into the voltages can be denoted by

$$V(t) = P(t) \left[\frac{\lambda\, \eta_{\text{PMT}}}{1.24}\right] G_{\text{PMT}}\, R_{\text{lo}}\, G_{\text{amp}}, \tag{A.11}$$

where

- $P(t)$ is the power of light scattered over the PMT window;
- η_{PMT} is the quantum efficiency of the photo-cathode on the PMT window;
- $\frac{\lambda\, \eta_{\text{PMT}}}{1.24}$ is the conversion factor of light power into electrical currents with the unit of λ is nm,
- G_{PMT} is the gain of the PMT;
- R_{lo} is the load resistor installed on the PMT outlet;
- G_{amp} is the amplification factor of the amplifier.

Some events during the PMT measurements can be expressed using the notation $V(t)$. For example, the event of triggering the CCD camera is denoted by $V(t = t_{\mathrm{T}})$ where t_{T} is the time when a PMT signal reaches a threshold voltage V_{T}.

The notation is used to denote the sampled and calculated PMT signals. Once triggered, the SPARCLE data acquisition samples 2,000 number of PMT signals with the sampling time interval: $\Delta t = 2\,\mu\mathrm{s}$. The data acquisition is programmed to sample 499 PMT signals before the trigger. The sampled PMT signals are numbered in the order of when they are sampled and the PMT signal which triggers the data acquisition is programmed to be the signal number 500. In the time domain, the PMT signals span from 1,000 µs before the trigger and 3,000 µs after the trigger. The notation of sampled PMT signals using integer numbers p is

$$V_{\mathrm{mea}}(t_p),$$

where

$$p = 1, 2 \ldots, 2000;$$

$$t_p = 2\,\mu\mathrm{s}, 4\,\mu\mathrm{s} \ldots, 4000\,\mu\mathrm{s}.$$

The sampled signal which triggers the data acquisition system is denoted by

$$V_{\mathrm{mea}}(t_{\mathrm{T}}),$$

where

$$V_{\mathrm{mea}}(t_{\mathrm{T}}) = V_{\mathrm{mea}}(t_{p=500});$$

$$V_{\mathrm{mea}}(t_{p=500}) = V_{\mathrm{T}}.$$

Sampled signals before and after triggers are denoted by $V_{\mathrm{mea}}(t_{p<500})$ and $V_{\mathrm{mea}}(t_{p>500})$, respectively.

The PMT signals can be calculated based on the light scattered by single particles which travel parallel with the y axis in the sensing volume. In the calculation, the single particles travel from points $(x, y = -0.5\,\mathrm{mm}, z)$ to points $(x, y = +0.5\,\mathrm{mm}, z)$ and the power is calculated when the single particles are illuminated at the points where coordinate y is linearly distributed with spatial interval $\Delta y = 0.01\,\mathrm{mm}$. With $\Delta y = 0.01\,\mathrm{mm}$ along the path of -5 mm< y <5 mm, the number of points to be evaluated is 101 points. The time needed for single particles to travel between the points, Δt, can be calculated based on the speed of single particles flowing parallel with the y axis using Equation A.8. Once Δt is known, the plot of calculated signals as a function of time between the points can be done. Then, the calculated PMT signals can be overlaid to the sampled PMT signals if a triggering voltage can be identified from the calculated PMT outputs. The overlay can be done by coinciding the triggering voltage with $V_{\text{mea}}(t_{\text{T}})$. If calculated PMT signals do not fit with sampled PMT outputs, then the calculation is repeated by using various particle position coordinates x and z, size parameter α, or refractive index m until they fit.

Mathematical notations are introduced based on the description in the previous paragraph. With calculated PMT signals indexed using integer numbers q, the signals are denoted by

$$V_{\text{cal}}(x, z, \alpha, m; y(t'_q)),$$

where

$$\begin{gathered} q = 1, 2 \ldots, 101; \\ t'_q(x, z, q) = t_{\text{T}} + (q - q_{\text{T}})\frac{\Delta y}{v(x, z)}; \\ -0.500\,\text{mm} < y(t_q) < -0.500\,\text{mm}; \quad \Delta y = 0.01\,\text{mm}; \end{gathered} \tag{A.12}$$

In the calibration, t_{T} was equal to 1000 µs; Index q_{T} is the index when

$$V_{\text{cal}}(x, z, \alpha, m; y(t'_{q_{\text{T}}})) \approx V_T.$$

The above expression means that at time t'_{q_T}, the data acquisition system is calculated to be triggered. However, $V_{\text{cal}}(x, z, \alpha, m; y(t'_q)) \approx V_T$ may not be unique as a function of t'_q. As a consequence, t'_{q_T} should be selected from a set of $t'_{q \in u}$ where u is a set of integer numbers that leads to $V_{\text{cal}}(x, z, \alpha, m; y(t'_u)) \leq V_T$. Since the system is triggered once V_T is reached, t'_{q_T} is selected as the earliest time in the set of $t'_{q \in u}$. In mathematical notation, the selection is expressed as

$$q_T = \min\{u \in \mathbb{Z}\}, \tag{A.13}$$

where $\mathbb{Z}$ is a set of all integers. Once q_{T} has been determined, the time frame of the calculation, t'_q, can be determined by applying q_{T} to Equation A.12. Then, $V_{\text{cal}}(x, z, \alpha, m; y(t'_q))$ can be overlaid on $V_{\text{mea}}(t_p)$.

The algorithm to calculate $V_{\text{cal}}(x, z, \alpha, m; y(t'_q))$ is detailed as follows:

1. get the sampling rate when sampled PMT signals,
2. select particular x, z, α, and m,
3. generate y_q with $y_1 = -0.5\,\text{mm}$ and $y_{101} = +0.5\,\text{mm}$ and $\Delta y = 0.01\,\text{mm}$,
4. calculate the power of light scattered to the PMT window, $P_{\text{s}}^{\text{PMT}}(x, z, \alpha, m; y(t'_q))$. The calculation is computationally expensive and an approximation is applied to reduce the computational cost. The approximation is based on $P_{\text{s}}^{\text{PMT}}(x, z, \alpha, m; y(t'_q))$ that are slightly invariant by the variation of z. The details of the calculation and the approximation will be discussed in the next paragraph,

5. convert $P_\mathrm{s}^\mathrm{PMT}(x, z, \alpha, m; y(t'_q))$ into $V_\mathrm{cal}(x, z, \alpha, m; y(t'_q))$ using Equation A.11
6. determine q_T using Equation A.13,
7. calculate $v(x, z)$ using Equation A.7,
8. calculate $t'_q(x, z)$ using Equation A.12,
9. overlay the plot of $V_\mathrm{cal}(x, z, \alpha, m; y(t'_q))$ as a function of t'_q with the plot of $V\mathrm{mea}(t_p)$,
10. if the two plots do not fit to each other, repeat the calculation with various x, z, α and m until they fit.

As mentioned in Step 3, the calculation of $P_\mathrm{s}^\mathrm{PMT}(x, z, \alpha, m; y(t'_q))$ is computationally expensive and an approximation is applied to the calculation. The algorithm of the calculation as well as the approximation is detailed as follows:

1. the area of the PMT window is divided into a grid comprising N number of squares and the power of scattered light over the PMT window is approximated as the summation of all of the power of light scattered over the squares,
2. the area of each square is
$$\Delta A = \frac{A_\mathrm{PMT}}{N}, \tag{A.14}$$
where A_PMT and ΔA are the area of the PMT window and each square, respectively,
3. in the calculation, N is set to be a large number, hence, the area of each square will be very small. Due to this very small area, the intensity of light scattered over the area can be approximated to be homogeneous,
4. each square is indexed by j with j is integer numbers from 1 to N,
5. the Spherical coordinates of square j are r_j, θ_j and ϕ_j,
6. the power of scattered light falls over square j is:
$$P_j(x, z, \alpha, m; y(t'_q)) = \frac{I_\mathrm{x}(x)\, I_\mathrm{y}(y)\, P_b}{A_\mathrm{b}\, k^2}\, Re\Bigg[\frac{1}{r_j^2}\Big[|S_1(\alpha, m, \cos\theta_j)|^2 \sin^2\phi_j + |S_2(\alpha, m, \cos\theta_j)|^2 \cos^2\phi_j\Big]\hat{r}_j.\hat{A}_j\, \Delta A\Bigg], \tag{A.15}$$

where Spherical coordinate variables r_j, θ_j and ϕ_j can be calculated based on Cartesian coordinate variables: x, y, and z since the position of the PMT is fixed; $\hat{A_j}$ is the unit vector of the area of square j; $\hat{r_j}$ is the position vector of the midpoint of square j,

7. the power of scattered light over the PMT window is approximated as

$$P_{\mathrm{PMT}}(x, z, \alpha, m; y(t'_q)) \approx \sum_{j=1}^{N} P_j(x, z, \alpha, m; y(t'_q)). \tag{A.16}$$

8. the calculation of $P_{\mathrm{PMT}}(x, z, \alpha, m; y(t'_q))$ for particular x, y, z is computationally expensive, therefore, the calculation of $P_{\mathrm{PMT}}(x, z, \alpha, m; y(t'_q))$ for all $y(t'_q)$ will be overwhelmingly expensive. An approximation to reduce the computational cost is applied by considering that the variation of the scattering solid angles subtended by the PMT window for various single-particle positions in the sensing volume is very small. The variation is less than 3%. The variation was calculated by considering that:

    - the boundaries of the coordinates (x, y, z) of any point in the sensing volume are -0.5 mm$< x <$0.5 mm, -0.04 mm$< y <$0.04 mm, and -0.5 mm$< z <$0.5 mm,
    - the centre of the PMT window is placed at $x = 6$ mm and the area vector of the PMT window is parallel with the x axis. The diameter of the window is around 25 mm,

9. since the variation of the scattering solid angle is very small, coordinates (r_j, θ_j, ϕ_j) in Equation A.16 can be approximated to be invariant to the variation of x, y, z. The approximation can be written as

$$P_{\mathrm{PMT}}(x, z, \alpha, m; y(t'_q)) = I_{\mathrm{x}}(x)\, I_{\mathrm{y}}(y_q)\, P_{\mathrm{sum}}(\alpha, m), \tag{A.17}$$

   where

$$\begin{aligned} P_{\mathrm{sum}}(\alpha, m) = \frac{P_{\mathrm{b}}}{A_{\mathrm{b}}\, k^2} \sum_{j=1}^{N} Re \Bigg[\frac{1}{r_j^2} \Big[|S_1(\alpha, m, \cos\theta_j)|^2 \, \sin^2\phi_j + \\ |S_2(\alpha, m, \cos\theta_j)|^2 \, \cos^2\phi_j \Big] \hat{r}_j . \hat{A}_j \, \Delta A_j \Bigg]. \end{aligned} \tag{A.18}$$

   To empasize, $P_{\mathrm{sum}}(\alpha, m)$ is invariant for the variation of x, y, and z.

A.2 The forward model of CCD camera readings

In the SPARCLE design, CCD camera is set to measure the angular distribution of the power of light scattered by single particles travelling in the sensing volume. The measurement of the angular distribution is performed by 3,000 photo-active pixels contained in the line sensor of the CCD camera. The line sensor integrates the light and converts it into electrical voltages ranging from 0 V to -2,3 V. Then the voltages are normalised by the CCD camera into values between 0 and 1 with 0 and 1 corresponding to voltages 0 V and -2.3 V, respectively. The normalised voltages are CCD camera readings that can be denoted as

$$\mathcal{V}_{\text{mea}}(p)|_{t_T}^{t_T+t_{\text{int}}}, \text{ where } \{p \in \mathbb{Z}|1 \geq p \geq 3000\}, \tag{A.19}$$

where t_{T} is the time the CCD camera is triggered to start integrating scattered light; t_{int} is the integration time.

The voltage $\mathcal{V}_{\text{mea}}(p)|_{t_T}^{t_T+t_{\text{int}}}$ can be calculated by calculating expected CCD camera readings for light scattered by single particles travelling parallel with the y axis in the sensing volume. The calculated reading is denoted by

$$\mathcal{V}_{\text{cal}}(p)|_{t_T}^{t_T+t_{\text{int}}}. \tag{A.20}$$

The conversion of the light integrated by the line sensor into normalised voltages is expressed by

$$\mathcal{V}_{\text{cal}}(p)|_{t_T}^{t_T+t_{\text{int}}} = W(p)|_{t_T}^{t_T+t_{\text{int}}} \frac{K(\lambda)\,\mathcal{S}^{\text{CCD}}(\lambda)}{A_{\text{p}}\,\mathcal{n}} \tag{A.21}$$

where

- $W(p)|_{t_T}^{t_T+t^{int}}$ is the energy of scattered light integrated by pixel p.
- λ is the wavelength of the laser. The wavelength is 651 nm,
- $K(\lambda)$ is photopic luminous efficacy and $K(\lambda = 651\,\text{nm}) \approx 73$ lumens Watt^{-1},
- $\mathcal{S}^{\text{CCD}}(\lambda)$ is the sensitivity of the line sensor in the CCD camera. For $\lambda = 651\,\text{nm}$, $\mathcal{S}^{\text{CCD}}(\lambda = 651\,\text{nm}) \approx 3700\,\text{V}\,\text{lux}^{-1}\,\text{s}^{-1}$,
- A_{p} is the area of each pixel,
- $\mathcal{n}$ is the normalisation factor of the CCD camera. For the CCD camera, $\mathcal{n} = 2.3\,\text{V}$.

The calculation of $V_{\rm cal}(p)|_{t_T}^{t_T+t_{\rm int}}$ is coupled with $V_{\rm cal}(x, z, \alpha, m; y(t'_q))$. The coupling is apparent due to:

- the two detectors measure the light that is scattered by the same single particles,
- the CCD camera is triggered to integrate the light based on the PMT output that satisfies the threshold.

This coupling can be used to determine various intensities of the laser beam that illuminates single particles during the CCD camera integration time. The determination is based on the sampled PMT signals that can be mapped into the location where the single particles are illuminated.

The power of scattered light measured by each pixel can be denoted by

$$P_{\rm s}(x, y, z, \alpha, m; r_p, \theta_p, \phi_p).$$

The pixels are lined up parallel with the propagating direction of the illuminating light, so $\phi_p = \phi$ for all pixels. Since the location of the CCD camera is fixed, parameter r_p can be calculated for particular θ_p and ϕ. Parameter r_p can be expressed as

$$\vec{r_p} = x_{\rm ref}\,\hat{x} + y_{\rm ref}\,\hat{y} + z_{\rm ref}(p)\,\hat{z} \tag{A.22}$$

where

- $x_{\rm x}$ is the projection of the pixel position on the x axis,
- $y_{\rm y}$ is the projection of the pixel position on the y axis. In this setup, $R_{\rm y} \approx 0.4\,{\rm mm}$,
- $z_{\rm z}(p)$ is the projection of the pixel location on the z axis. The $z_{\rm z}(p)$ can be calculated based on the pixel whose z coordinate is zero. If the pixel is denoted as $j^{\rm mid}$ then

  $$z_{\rm ref}(p) = (j^{\rm mid} - j)\,w \tag{A.23}$$

  where w is the width of each pixel.

The determination of $x_{\rm ref}$ and $j^{\rm mid}$ is detailed in Appendix B. The notation of the angular distribution of the power can be simplified as:

$$P_{\rm s}(x, y, z, \alpha, m; \theta_p).$$

Once triggered, the CCD camera integrates P_s and the energy collected from the integration can be denoted as

$$W(x, z, \alpha, m; \theta_p)|_{t_\mathrm{T}}^{t_\mathrm{T}+t_\mathrm{int}} = \int_{t_\mathrm{T}}^{t_\mathrm{T}+t_\mathrm{int}} P_\mathrm{s}(x, y(t), z, \alpha, m; \theta_p)\, dt. \tag{A.24}$$

The calculation of $W(x, z, \alpha, m; \theta_p)|_{t_\mathrm{T}}^{t_\mathrm{T}+t_\mathrm{int}}$ as shown in Equation A.24 can be approximated numerically,

$$W(x, z, \alpha, m; \theta_p)|_{t_\mathrm{T}}^{t_\mathrm{T}+t_\mathrm{int}} = \sum_i P_\mathrm{s}(x, y(t_i), z, \alpha, m; \theta_p)\, \Delta t, \tag{A.25}$$

where

$$\{i \in \mathbb{Z} | i * \Delta t \leq t_\mathrm{int} \wedge i \geq 0\}. \tag{A.26}$$

If Δt in Equation A.25 is the same with the time interval used in the calculation of $V_\mathrm{cal}(x, z, \alpha, m; y(t'_q))$, Equation A.25 can be written as

$$W(x, z, \alpha, m; \theta_p)|_{t_\mathrm{T}}^{t_\mathrm{T}+t_\mathrm{int}} = P_\mathrm{s}(x, z, \alpha, m; \theta_p)\, \Delta t \sum_i I_\mathrm{y}(y'_{q=i+q_T}), \tag{A.27}$$

where

- $y'_{q=i+q_T}$ is the various y coordinates used in the calculation of $V_\mathrm{cal}(x, z, \alpha, m; y(t'_q))$ that represent the coordinates of single particles projected on the y axis when the CCD camera is integrating scattered light,
- $P_\mathrm{s}(x, z, \alpha, m; \theta_p)$ is calculated based on the consideration that the pixel dimension is small relative to distance to the sensing volume so the intensity of light scattered to each pixel is homogeneous. $P_\mathrm{s}(x, z, \alpha, m; \theta_p)$ can be calculated as

$$\begin{aligned} P_\mathrm{s}(x, z, \alpha, m; \theta_p) = \frac{I_\mathrm{x}(x)\, P_\mathrm{b}}{A_\mathrm{b}\, k^2}\, Re \Bigg[\frac{1}{r_p^2} \Big[|S_1(\alpha, m, \cos\theta_p)|^2 \, \sin^2\phi + \\ |S_2(\alpha, m, \cos\theta_p)|^2 \, \cos^2\phi \Big] \hat{r}_p . \hat{A}\, A \Bigg], \end{aligned} \tag{A.28}$$

  where A and $\hat{A}$ is the pixel area and the unit vector of the area. In the SPARCLE design, $\hat{A} = \hat{x}$. Note, A in Equation A.28 and A.21 will cancel out.

Some corrections to Equation A.21 may be needed since a slab of glass is installed in front of the line sensor. The corrections are the power reduction and the lateral displacement of scattered light propagating through the glass. The power reduction can be calculated by evaluating the transmittance of scattered light through the glass.

Meanwhile, the lateral displacement shifts θ_p into θ'_p. The corrections are applied to A.21 where the correction due to the transmittance is applied first:

$$\mathcal{V}^{\mathrm{tr}}_{\mathrm{cal}}(x, z, \alpha, m; \theta_p)|_{t_\mathrm{T}}^{t_\mathrm{T}+t_\mathrm{int}} = \mathcal{V}_{\mathrm{cal}}(x, z, \alpha, m; \theta_p)|_{t_\mathrm{T}}^{t_\mathrm{T}+t_\mathrm{int}}\, \mathcal{T}(\theta_p, m^{\mathrm{g}}), \tag{A.29}$$

and the lateral displacement correction:

$$\mathcal{V}^{\mathrm{cor}}_{\mathrm{cal}}(x, z, \alpha, m; \theta'_p)|_{t_\mathrm{T}}^{t_\mathrm{T}+t_\mathrm{int}} = \mathcal{V}^{\mathrm{tr}}_{\mathrm{cal}}(x, z, \alpha, m; \mathcal{R}(\theta_p))|_{t_\mathrm{T}}^{t_\mathrm{T}+t_\mathrm{int}}, \tag{A.30}$$

where $\mathcal{T}$ is the transmittance of scattered light; m^{g} is the refractive index of the glass; $\mathcal{R}$ is the lateral displacement function that maps θ_p into θ'_p.

The transmittance of light when incident on an interface of two mediums is a function of light polarisation, the refractive index of the two mediums and the incident angle of light defined as the angle between the propagation direction of light and the normal of the interface. In the SPARCLE design, the light scattered to the line sensor is polarised perpendicular to the scattering plane. The incident angle of the light on the surface can be calculated as

$$\theta^{\mathrm{i}}_p = |90^\circ - \theta_p|. \tag{A.31}$$

The propagation of the light through the glass passes two interfaces. The first interface is between the air and the glass then the second interface is between the glass and the air. In each interface, the transmittance of light is calculated. The calculation is done based on Fresnell equation:

$$\mathcal{T}(\theta^{\mathrm{i}}_p, m^{\mathrm{g}}) = \left[1 - \left|\frac{cos\,\theta^{\mathrm{i}}_p - \sqrt{(m^{\mathrm{g}})^2 - (sin\,\theta^{\mathrm{i}}_p)^2}}{cos\,\theta^{\mathrm{i}}_p + \sqrt{(m^{\mathrm{g}})^2 - (sin\,\theta^{\mathrm{i}}_p)^2}}\right|^2\right]^2. \tag{A.32}$$

During their propagation through the glass, scattered light is laterally displaced and the propagation direction with respect to scatterer is changed. The displacement affects the mapping of pixels to scattering angles. With no displacement, the mapping is expressed as

$$cos\,\theta_p = \frac{\vec{r}_p\,.\,\hat{z}}{|\vec{r}_p|}. \tag{A.33}$$

Due to the displacement, the mapping is altered into

$$cos\,\theta'_p = \frac{(\vec{r}_p + \Delta\vec{r}_p)\,.\,\hat{z}}{|(\vec{r}_p + \Delta\vec{r}_p)|}, \tag{A.34}$$

where $\Delta\vec{r}_p$ is the lateral displacement of scattered light propagating toward pixel p. The lateral displacement can be calculated based on Snell's law and resulted in

$$\Delta\vec{r}_p = D\, sin\, \theta_p^{\mathrm{i}} \left[1 - \frac{\sqrt{1 - (sin\, \theta_p^{\mathrm{i}})^2}}{\sqrt{(m^{\mathrm{g}})^2 - (sin\, \theta_p^{\mathrm{i}})^2}} \right] \hat{z}, \tag{A.35}$$

where D is the thickness of the glass. Note, the thickness of the glass is 0.7 mm and the distance between the glass and the line sensor is not specified and, for this correction, is assumed to be 1 mm; the refractive index of the glass is 1.5. The algorithm to calculate $\mathscr{V}_{\mathrm{cal}}(x, z, \alpha, m; \theta_p)|_{t_{\mathrm{T}}}^{t_{\mathrm{T}}+t_{\mathrm{int}}}$ is detailed as follows:

1. use the same x, z, α, and m as well as Δt, y'_q, Δy and q_T as those used in the calculation of $V_{\mathrm{cal}}(x, z, \alpha, m; y(t'_q))$,
2. generate integer numbers p from 1 to 3,000,
3. set $\phi = 8°$ and $t_{\mathrm{int}} = 1000\,\mu\mathrm{s}$,
4. calculate r_p and θ_p, using Equations A.22, A.23, and A.33,
5. determine $\{i\}$ based on equation A.26,
6. calculate $\Delta t \sum_i I_y(y'_{q=i+q_T})$,
7. calculate $P_{\mathrm{s}}(x, z, \alpha, m; \theta_p)$ based on Equation A.28,
8. calculate $\mathscr{W}(x, z, \alpha, m; \theta_p)|_{t_{\mathrm{T}}}^{t_{\mathrm{T}}+t_{\mathrm{int}}}$ using Equation A.27,
9. calculate $\mathscr{V}_{\mathrm{cal}}(x, z, \alpha, m; \theta_p)|_{t_{\mathrm{T}}}^{t_{\mathrm{T}}+t_{\mathrm{int}}}$ based on Equation A.21,
10. overlay $\mathscr{V}_{\mathrm{cal}}(x, z, \alpha, m; \theta_p)|_{t_{\mathrm{T}}}^{t_{\mathrm{T}}+t_{\mathrm{int}}}$ with $\mathscr{V}_{\mathrm{mea}}(\theta_p)|_{t_{\mathrm{T}}}^{t_{\mathrm{T}}+t_{\mathrm{int}}}$,
11. if the two plots do not fit, $\mathscr{V}_{\mathrm{cal}}(x, z, \alpha, m; \theta_p)|_{t_{\mathrm{T}}}^{t_{\mathrm{T}}+t_{\mathrm{int}}}$ and $V_{\mathrm{cal}}(x, z, \alpha, m; y_q(t'_q))$ calculations are repeated with various x, z, α and m.

A.3 Mie scattering theory

SPARCLE is designed based on the measurement of light scattered by single particles. In this report, it is assumed that the particle is an homogenous spherical particle. The light scattered by such particles can be explained by the Mie scattering theory developed by Gustav Mie in 1908 Mie [1908]. In his derivation, Maxwell's equations were applied to derive the electromagnetic field of scattered light as a result of interaction between plane wave incident light and a particle. The solution is in the form of an infinite series of spherical harmonic functions. An excellent mathematical treatment of this theory can be found in Bohren and Huffman [1983] and is reproduced below.

A.3.1 Mie amplitude

The transverse component of scattering electric (E) and magnetic (M) field by a spherical particle with size a as a function of the distance from the particles r, scattering angle θ, azimuthal angle ϕ, size parameter $\alpha = \frac{\pi d}{\lambda}$ and refractive index m is derived as:

$$\begin{aligned} E_{s\theta} &\sim E_o \frac{e^{i\mathcal{P}}}{-i\mathcal{P}} \cos(\phi) S_2(\theta,\alpha,m), \\ E_{s\phi} &\sim E_o \frac{e^{i\mathcal{P}}}{-i\mathcal{P}} \sin(\phi) S_1(\theta,\alpha,m), \\ H_{s\phi} &\sim E_o \frac{e^{i\mathcal{P}}}{-i\mathcal{P}} \frac{k}{\omega\mu} \cos(\phi) S_2(\theta,\alpha,m), \\ H_{s\theta} &\sim E_o \frac{e^{i\mathcal{P}}}{-i\mathcal{P}} \frac{k}{\omega\mu} \sin(\phi) S_1(\theta,\alpha,m), \end{aligned} \tag{A.36}$$

where $\mathcal{P} = kr$; $S_1(\theta,x,M)$ and $S_2(\theta,x,M)$ are infinite series expressed as:

$$S_1(\theta,x,M) = \sum_{n=1}^{\infty} \frac{2n+1}{n(n+1)} \left[a_n\pi_n(\cos\theta) + b_n\tau_n(\cos\theta)\right], \tag{A.37}$$

$$S_2(\theta,x,M) = \sum_{n=1}^{\infty} \frac{2n+1}{n(n+1)} \left[b_n\pi_n(\cos\theta) + a_n\tau_n(\cos\theta)\right], \tag{A.38}$$

where the angular functions π and τ are Legendre polynomials defined as:

$$\begin{aligned} \pi_n(\cos\theta) &= \frac{P_n^1(\cos\theta)}{\sin\theta}, \\ \tau_n(\cos\theta) &= \frac{d}{d\theta} P_n^1(\cos\theta), \end{aligned} \tag{A.39}$$

and Mie coefficients are given by

$$\begin{aligned} a_n &= \frac{\psi_n(x)\psi_n'(Mx) - M\psi_n'(x)\psi_n(Mx)}{\zeta_n(x)\psi_n'(Mx) - M\zeta_n'(x)\psi_n(Mx)}, \\ b_n &= \frac{M\psi_n(x)\psi_n'(Mx) - \psi_n'(x)\psi_n(Mx)}{M\zeta_n(x)\psi_n'(Mx) - M\zeta_n'(x)\psi_n(Mx)}, \end{aligned} \tag{A.40}$$

where ψ and ζ are the Ricatti-Bessel functions, defined as:

$$\psi_n(x) = \sqrt{\frac{\pi x}{2}} J_{n+\frac{1}{2}}(x), \tag{A.41}$$

$$\zeta_n(x) = \sqrt{\frac{\pi x}{2}} H_{n+\frac{1}{2}}(x), \tag{A.42}$$

with $J_{n+\frac{1}{2}}(x)$ is the half-integral-order spherical Bessel function, and $H_{n+\frac{1}{2}}(x)$ is the half-integral-order Hankel function of the second kind. In this work, the calculation of S_1 and S_2 were done by writing Phyton codes based on the IDL codes written by [Grainger et al., 2004].

A.3.2 Poynting vector

The magnitude and the direction of the energy of electromagnetic wave are specified by the wave Poynting vector. The Poynting vector is expressed as

$$\vec{S} = \vec{E} \times \vec{H}^*. \tag{A.43}$$

Most instruments are not sensitive to the high oscillation of the instantaneous Poynting vector. They respond to the time averaged Poynting vector expressed by

$$\vec{S} = \frac{1}{2} Re\Big[\vec{E} \times \vec{H}^*\Big]. \tag{A.44}$$

The time-averaged Poynting vector of scattered light can be expressed using the amplitude in Equation A.36:

$$\begin{aligned}
\vec{S}_s &= \frac{1}{2} Re\left(\vec{E}_s \times \vec{H}_s^*\right), \\
\vec{S}_s &= \frac{1}{2} Re\left[(E_{s\theta}\hat{e}_\theta + E_{s\phi}\hat{e}_\phi) \times \left(H_{s\theta}^*\hat{e}_\theta + H_{s\phi}^*\hat{e}_\phi\right)\right], \\
\vec{S}_s &= \frac{1}{2} Re\left[\left(E_{s\theta}H_{s\phi}^* - E_{s\phi}H_{s\theta}^*\right)\hat{e}_r\right].
\end{aligned} \tag{A.45}$$

The power of scattered light P_s transferred to detector active area A can be calculated as

$$P_s = \int_A \vec{S}_s . d\vec{A}. \tag{A.46}$$

A.4 Modelling the distribution of the pulse depth and width

As described in Section 3.8, the distribution of the PMT pulse depth and width during the calibration can be modelled by the probability of generating the pulses which is a function of the PMT pulse depth and width. The probability can be developed by the following steps:

1. mapping the probability density of single particles traversing each point in the sensing volume. The probability density is denoted by $p(x, y, z)$. Since single particles are flowing parallel with the y axis, the probability can be reduced into two-dimensional probability which is denoted as $p(x, z)$,

2. calculating $V_{\text{cal}}(x, z, \alpha, m; y(t'))$ at each point in the sensing volume,

3. identifying the pulses in $V_{\text{cal}}(x, z, \alpha, m; y(t'))$ and calculating their depth and width. The depth and width are denoted by $V_{\text{depth}}(x, z, \alpha, m)$ and $T_{\text{width}}(x, z, \alpha, m)$, respectively,

4. calculating the probability density of generating pulses with the depth V by accumulating the probability density of particles traversing points where particle illumination leads to generating pulses with the depth V. This accumulation can be denoted by

$$p(V_{\text{depth}}(\alpha, m) = V) = \mathcal{Q}_{\text{depth}} \int p(x, z) \sum_{i} \delta(x - x_i)\, \delta(z - z_i)\, \mathrm{d}x\, \mathrm{d}z, \quad \text{(A.47)}$$

   where the integration is evaluated over the x-z plane; $\mathcal{Q}_{\text{depth}}$ is the normalisation factor; δ is delta Dirac function; (x_i, z_i) is a set of the coordinate positions of single particles projected on the x-z plane where particle illumination leads to

$$V_{\text{depth}}(x_i, z_i, \alpha, m) = V. \quad \text{(A.48)}$$

   To note, the integration of $p(V_{\text{depth}})$ from zero to infinity is unity

$$\int_0^\infty p(V_{\text{depth}}) \mathrm{d}V = 1, \quad \text{(A.49)}$$

5. calculating the probability of generating pulses with the width t by similar technique described in the previous step: the probability of particles traversing points where particle illumination leads to generating pulses with the width t accumulated. The accumulation can be denoted by

$$p(T_{\text{width}}(\alpha, m) = t) = \mathcal{Q}_{\text{width}} \int p(x, z) \sum_{j} \delta(x - x_j)\, \delta(z - z_j)\, \mathrm{d}x\, \mathrm{d}z, \quad \text{(A.50)}$$

   where $\mathcal{Q}_{\text{width}}$ is the normalisation factor; (x_j, z_j) is a set of the coordinate positions of single particles projected on the x-z plane where

$$T_{\text{width}}(x_j, z_j, \alpha, m) = t. \quad \text{(A.51)}$$

   To note, the integration of $p(T_{\text{width}})$ from zero to infinity is unity

$$\int_0^\infty p(T_{\text{width}}) \mathrm{d}t = 1. \quad \text{(A.52)}$$

However, calculating $V_{\text{cal}}(x, z, \alpha, m; y(t'))$ for all coordinates (x, y, z) in the sensing volume and then evaluating the corresponding pulse depth, $V_{\text{depth}}(x, z, \alpha, m)$, and width, $T_{\text{width}}(x, z, \alpha, m)$, are computationally expensive. An approximation to reduce the cost of the computation can be done by identifying features in the beam intensity distribution.

The distribution of the beam intensity parallel with the y axis, $I_{\text{y}}(y)$, is modelled to peak at x-z plane and, as single particles are travelling parallel with the y axis, the light intensity they scatter is highest when they are at the x-z plane. The highest intensity corresponds to the pulse depth in PMT outputs. Hence, the depth of pulses contained in PMT outputs can be determined by evaluating $V_{\text{cal}}(x, z, \alpha, m; y = 0)$. Furthermore, the beam intensity is constant in the direction parallel with the z axis and this constant reduces the dependance of the depth on the z component. In mathematical notation, the pulse depth distribution across the x-z plane denoted by V_{depth} can be expressed as

$$V_{\text{depth}}(x, \alpha, m) = V_{\text{cal}}(x, \alpha, m; y = 0). \tag{A.53}$$

$V_{\text{cal}}(x, \alpha, m; y = 0)$ can be calculated by

$$V_{\text{cal}}(x, \alpha, m; y = 0) = P_{\text{PMT}}(x, \alpha, m; y = 0) \left[\frac{\lambda\, \eta_{\text{PMT}}}{1.24}\right] G_{\text{PMT}}\, R_{\text{lo}}\, G_{\text{amp}}, \tag{A.54}$$

where

$$P_{\text{PMT}}(x, \alpha, m; y = 0) = I_{\text{x}}(x)\, I_{\text{y}}(0)\, P_{\text{sum}}(\alpha, m). \tag{A.55}$$

As $I_{\text{y}}(0) = 1$, Equation A.55 can be simplified into

$$P_{\text{PMT}}(x, \alpha, m; y = 0) = I_{\text{x}}(x)\, P_{\text{sum}}(\alpha, m). \tag{A.56}$$

So,

$$V_{\text{depth}}(x, \alpha, m) = I_{\text{x}}(x)\, P_{\text{sum}}(\alpha, m) \left[\frac{\lambda\, \eta_{\text{PMT}}}{1.24}\right] G_{\text{PMT}}\, R_{\text{lo}}\, G_{\text{amp}}. \tag{A.57}$$

An interesting feature in Equation A.57 is that once $P_{\text{sum}}(\alpha, m)$ is calculated for single particles with size parameter α and refractive index m then the corresponding $V_{\text{depth}}(x, \alpha, m)$ for various x can be generated by using $I_{\text{x}}(x)$.

Another feature of $I_{\text{y}}(y)$ can be used to simplify the calculation of the width of pulses as a function of the points on the x-z plane where single particles are being illuminated. Since single particles are travelling parallel with the y axis, the width of pulses corresponds to how long the single particles being illuminated with the intensity of the illuminating light proportional to $I_{\text{y}}(y)$. In this work, $I_{\text{y}}(y)$ is modelled to be nearly Gaussian. However, in the determination of the width of pulses, the distribution can be approximated as Gaussian distribution. To reflect the measurements done by SPARCLE, the pulses that are included in the calculation of pulse width distribution are those whose depth is deeper than or equal to threshold V_{T}. Other pulses whose depths are shallower than V_{T} are considered to be overlooked by SPARCLE.

The width of pulses can be determined by identifying two special positions of single particles during their travelling in the sensing volume. The two positions are the positions where particle illumination lead to PMT outputs which can be statistically distinguished from background. The statistical criteria for the distinction is when the difference between the outputs and background is equal to the standard deviation of the background. The positions are denoted by y_{L} and y_{H} and are shown in Figure A.1. The difference with background is denoted by V_{b}. The width of pulses are determined based on evaluating the travelling time between the two points. With pulse width denoted as T_{width}, the determination of T_{width} is expressed as

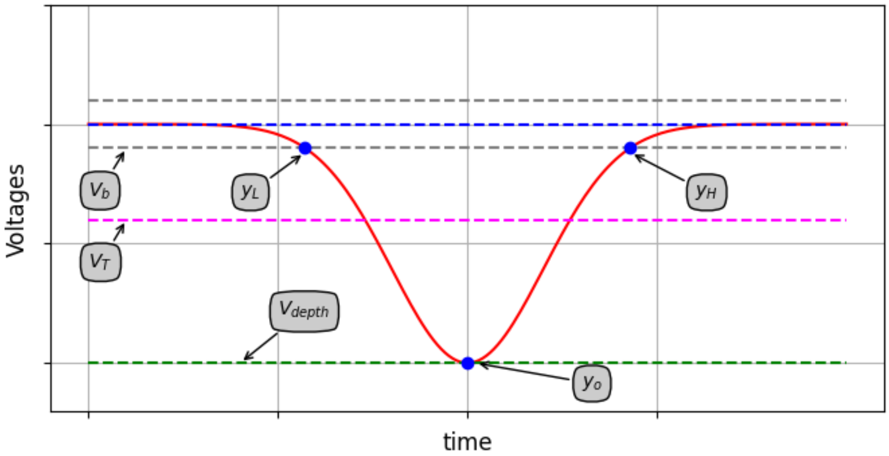

Figure A.1: The scheme of PMT pulses. The points related to pulse width calculation are indicated. The pulse is shown as a red line while the background is shown by a dashed blue line.

$$T_{\mathrm{width}}(x, z, \alpha, m) = \frac{\Delta y_{\mathrm{p}}(\alpha, m)}{v(x, z)}, \tag{A.58}$$

where

$$\Delta y_{\mathrm{p}} = y_{\mathrm{H}} - y_{\mathrm{L}}. \tag{A.59}$$

The determination of y_{L} and y_{H} as demonstrated in the figure can be expressed mathematically as

$$y_{\mathrm{L}} = \min\{Y\} \text{ and } y_{\mathrm{H}} = \max\{Y\}, \tag{A.60}$$

where y_p is the various position of single particles projected on the y axis which satisfying

$$V_\mathrm{cal}(x, z, \alpha, m; y \in y_\mathrm{p}) \geq V_\mathrm{b}. \tag{A.61}$$

Also, the pulses should trigger the data acquisition system and the triggering requires

$$V_\mathrm{cal}(x, z, \alpha, m; y = 0) \geq V_\mathrm{T}. \tag{A.62}$$

Since the pulses are approximated to be symmetrical with respect to the time when the pulses valleyed at $y = 0$, Δy_p can be calculated as

$$\Delta y_\mathrm{p}(\alpha, m) = 2 y_H(\alpha, m). \tag{A.63}$$

y_H can be determined through the comparison between PMT outputs when single particles at $y = y_H$ and $y = 0$:

$$\begin{aligned}
\frac{V_\mathrm{cal}(x, z, \alpha, m; y = y_H)}{V_\mathrm{cal}(x, z, \alpha, m; y = 0)} &= \frac{V_\mathrm{b}}{V_\mathrm{depth}(x, \alpha, m)}, \\
I_\mathrm{y}(y = y_H) &= \frac{V_\mathrm{b}}{V_\mathrm{depth}(x, \alpha, m)}, \\
e^{-\frac{1}{2}\left[\frac{y_H(\alpha, m)}{\sigma_\mathrm{y}}\right]^2} &= \frac{V_\mathrm{b}}{V_\mathrm{depth}(x, \alpha, m)}, \\
-\frac{1}{2}\left[\frac{y_H(\alpha, m)}{\sigma_\mathrm{y}}\right]^2 &= \ln\left[\frac{V_\mathrm{b}}{V_\mathrm{depth}(x, \alpha, m)}\right], \\
y_H(\alpha, m) &= \sigma_\mathrm{y}\sqrt{2\ln\left[\frac{V_\mathrm{depth}(x, \alpha, m)}{V_\mathrm{b}}\right]}.
\end{aligned} \tag{A.64}$$

Hence, pulse width is formulated as

$$T_\mathrm{width}(x, z, \alpha, m) = \frac{2\,\sigma_\mathrm{y}\sqrt{2\ln\left[\frac{V_\mathrm{depth}(x, \alpha, m)}{V_\mathrm{b}}\right]}}{v(x, z)}. \tag{A.65}$$

The interesting feature in equation A.65 is that once the distribution of pulse depth over the x-z plane is calculated, the corresponding distribution of pulse width can be derived.

The distribution of pulse width as a function of the position where particles being illuminated can be used to calculate the probability density of generating pulses as a function of pulse width using Equation A.50. A numerical formula is derived from the equation to developed a histogram of the probability density as a function of pulse width. The first step in developing the histogram is to divide the entire range of pulse width into a series of successive pulse width interval and determine the probability in each pulse width interval. The interval must be contiguous and cover the entire pulse width. The upper width limit of each interval coincides with the lower width limit of the next-higher interval. If pulse width fall exactly on the interval limit, it is grouped in the higher interval. The numerical formula is expressed as

$$p(T_j(\alpha, m)) = \mathcal{Q}_{\text{width}} \sum_{j'} p(x_{j'}, z_{j'}) \, \Delta x \, \Delta z, \tag{A.66}$$

where j is the integer numbers to index pulse width intervals; j' is the integer numbers to index the points on the x-z plane which particles illumination lead to generate pulses with width between the interval limit and, mathematically, j' can be expressed as

$$\{j' \in \mathbb{Z} | T_j^{\text{L}} < T_{\text{width}}(x_{j'}, z_{j'}, \alpha, m) < T_j^{\text{H}}\}, \tag{A.67}$$

where T_j^{L} and T_j^{H} are the lower and upper limit of the pulse width interval j, respectively.

The probability density of generating pulses as a function of pulse depth can be developed with techniques similar to that described in the previous paragraph. A numerical formula derived from Equation A.47 to develop a histogram of the probability density of generating pulses as a function of pulse depth is

$$p(V_i(\alpha, m)) = \mathcal{Q}_{\text{depth}} \sum_{i'} p(x_{i'}, z_{i'}) \, \Delta x \, \Delta z, \tag{A.68}$$

where i is the integer numbers to index pulse depth intervals; i' is the integer numbers to index the points on the x-z plane which particles illumination lead to generate pulses with depth between the interval limit and, mathematically, i' can be expressed as

$$\{i' \in \mathbb{Z} | V_i^{\text{L}} < V_{\text{width}}(x_{i'}, \alpha, m) < V_i^{\text{H}}\}, \tag{A.69}$$

where V_i^{L} and V_i^{H} are the lower and upper limit of the pulse depth interval i, respectively.

The size of PSL beads contained in the stock suspension varies around specified mean size and this variation should be included in the calculation of pulse depth and width distribution. The variation can be denoted by $F(\alpha - \alpha_{\text{o}}; \sigma_{\text{o}})$ where α_{o} and σ_{o} are the size parameter and its variation calculated based on the spesified mean size and size variation of PSL beads, respectively. Using this notation, the probability of generating pulses with width T can be expressed as:

$$p(T_{\mathrm{width}}(\alpha_{\mathrm{o}}, m) = T) = \mathcal{Q}_{\mathrm{width}} \int \left[\int p(x,z) \sum_{j'} \delta(x - x_{j'})\, \delta(z - z_{j'})\, dx\, dz \right] F(\alpha - \alpha_{\mathrm{o}}; \sigma_{\mathrm{o}})\, d\alpha, \tag{A.70}$$

The numerical expression for the above equation to develop the histogram of the probability density of generating pulses is expressed as:

$$p(T_j(\alpha_{\mathrm{o}}, m)) = \mathcal{Q}_{\mathrm{width}} \sum_{\alpha} \left[\sum_{j'} p(x_{j'}, z_{j'}) \Delta x\, \Delta z \right] F(\alpha - \alpha_{\mathrm{o}}; \sigma_{\mathrm{o}})\, \Delta\alpha, \tag{A.71}$$

The similar techniques is applied to pulse depth and resulted in equation

$$p(V_{\mathrm{depth}}(\alpha_{\mathrm{o}}, m) = V) = \mathcal{Q}_{\mathrm{depth}} \int \left[\int p(x,z) \sum_{i'} \delta(x - x_{i'})\, \delta(z - z_{i'})\, dx\, dz \right] F(\alpha - \alpha_{\mathrm{o}}; \sigma_{\mathrm{o}})\, d\alpha, \tag{A.72}$$

The numerical expression would be:

$$p(V_i(\alpha_{\mathrm{o}}, m)) = \mathcal{Q}_{\mathrm{depth}} \sum \left[\sum_{i'} p(x_{i'}, z_{i'}) \Delta x\, \Delta z \right] F(\alpha - \alpha_{\mathrm{o}}; \sigma_{\mathrm{o}})\, \Delta\alpha. \tag{A.73}$$

SPARCLE sampling flow rates during the calibration varied as mentioned in Chapter 2 and this variation affected the distribution of pulse width measured in the calibration. The calculation of pulse width as expressed in Equation A.74 need to be modified to inclused the sampling rate variation. The modified equation is

$$p(T_j(\alpha_{\mathrm{o}}, m, Q)) = \mathcal{Q}_{\mathrm{width}} \sum_{Q} \sum_{\alpha} \left[\sum_{j'} p(x_{j'}, z_{j'}) \Delta x\, \Delta z \right] F(\alpha - \alpha_{\mathrm{o}}; \sigma_{\alpha})\, F(Q - Q_{\mathrm{o}}; \sigma_{Q})\, \Delta\alpha\, \Delta Q, \tag{A.74}$$

where Q is SPARCLE sampling flow rates; Q_{o} and α_Q are mean flow rates and their variation, respectively.

Appendix B

Determining the position of the PMT and the CCD camera

As discussed in Chapter 2, the detectors in SPARCLE are designed to be placed with the mid-point of the detectors around 6 mm from the sensing volume. However, more precise position in the order of sub-millimetre for the position of the CCD camera is needed since the LSPs measured by the CCD camera are sensitive to the uncertainty of the CCD camera position in the order of sub-millimetre. Meanwhile, the same level of precision for the PMT position may not be needed since the measurement of scattering light by the PMT is not sensitive to the uncertainty of the PMT position in the order of sub-millimetre. The insensitivity is due to a small variation of the solid angle of scattering light subtended by the PMT window for the variation of the PMT position in the range from 5.5 mm to 6.5 mm. The variation is less than 5%. The small variation can be qualitatively explained by the diameter of the PMT which is much larger than the distant between the PMT and the sensing volume.

Practically, the sub-millimetre precision of the CCD camera position is difficult to achieve through spatial measurements. The first reason is that the centre of the Cartesian coordinate, which is created by the cross-section between the sampling pipe axis of symmetry and the laser beam, can not be determined precisely. The second reason is that the thickness of the sealing layer installed between the CCD camera and the scattering chamber can not be determined precisely as well. The thickness of the glass window installed in the CCD camera is specified by the manufacturer as 0.6 mm, however, the distant between the surface of the glass window to the line sensor may not be the same value.

The relevant position of the CCD camera is the position of a pixel in the line sensor used as a reference to determine other pixel positions. The pixel is located at the x-y plane and indicated as j_{ref} in Figure 5.1. The projection of the position of j_{ref}

in the x axis is denoted as x_{ref} and indicated in the same figure. The sub-millimetre precision of the projection of the position of j_{ref} on the y axis is not necessary since the uncertainty of the projection in the order of sub-millimetre has negligible effect to the uncertainty of the azimuth angle of scattering light. For example, the projection located between $-0.5\,\text{mm}$ and $+0.5\,\text{mm}$ on the y axis is related to the azimuth angle of scattering light between $0°$ and $8°$. This small range of azimuth angle has a negligible effect to the pattern of scattering light.

One way to obtain the precise position of the CCD camera is by retrieving it through a retrieval method similar to that described in Section 5.4 with x_{ref} and j_{ref} included as state vector elements in addition to x, z, d and m. The retrieval is applied to search the solution for a pair of SPARCLE responses to the aerosol generated in the calibration with the mean size of the aerosol 1,800 nm. The variation of the values of x_{ref}, j_{ref}, x, z, d, and m over which the solutions were searched are summarised in Table B.1. To illustrate, the map of χ_v^2 for various x_{ref} and j_{ref} with $d = 1,809\,\text{nm}$, $m = 1.59$, $x = -0.22$ and $z = -0.43$ in the searching of the solution for a SPARCLE response shown in Figure 5.6. The map is plotted in Figure B.1. The values $x_{\text{ref}} = 7.3$ and $j_{\text{ref}} = 1420$ indicated by the crosspoint of the two dashed lines shown in the figure are selected as the solution. The retrieval is also performed to other 99 responses to the same aerosol with $SNR > 4.15$. The solutions were obtained and the mean of x_{ref} and j_{ref} are 6.9 mm and 1419, respectively. The position of the CCD camera and the PMT used in SPARCLE forward model is summarised in Table B.2.

Table B.1: The range of variables in the searching for j_{ref} and x_{ref}.

variables	min	max	hypercube length
x	-1 mm	1 mm	0.01 mm
z	0 mm	1 mm	0.01 mm
j_{ref}	1300	1696	4
x_{ref}	6.0 mm	7.9 mm	0.1 mm
d	1,760 nm	1,840 nm	1 nm
m	1.55	1.65	0.01

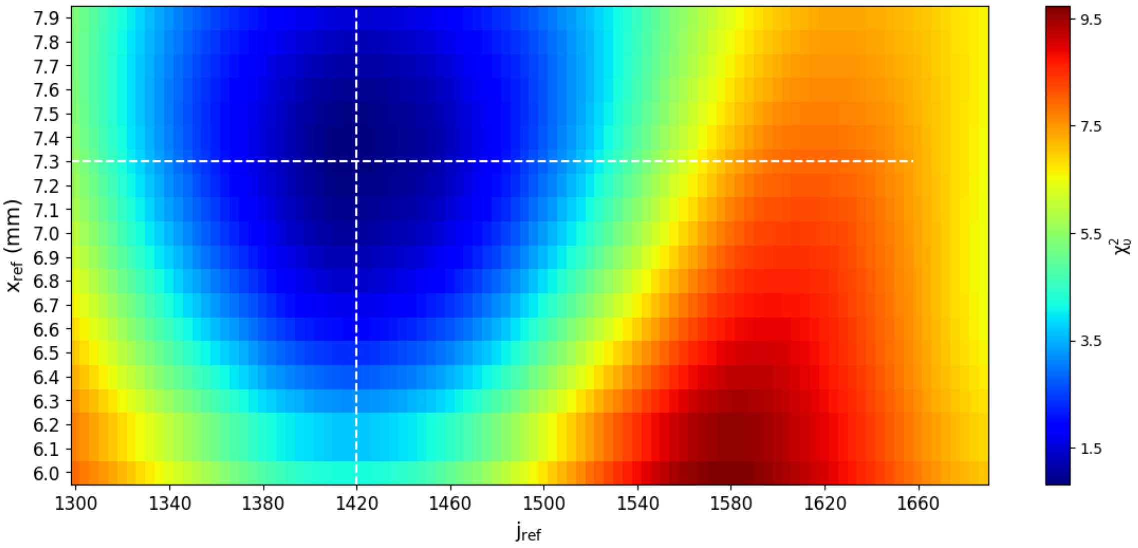

Figure B.1: The map of χ_v^2 for determining j_{ref} and x_{ref}.

Table B.2: The position of the detectors installed in SPARCLE.

variables	values	description
x_{PMT}	6.0 mm	the position of the PMT window projected on the x axis
p_{ref}	1419	a reference pixel illustrated in Fig. 5.1
x_{ref}	6.9 mm	the projection of p_{ref} on the x axis illustrated in Fig. 5.1

Appendix C

The amplifier circuit

In the SPARCLE detection system, the PMT signals were filtered and amplified before sampled by the digital oscilloscope. The filter is a four pole low-pass filter with a cut-off frequency of approximately by 20 kHz which removes the higher frequencies of shot noise produced by the PMT. The signals was then amplified to provide the -10 to 10 V voltage range expected by the digital oscilloscope. The amplification includes turn adjustment pots for both zero-offset and gain to allow for changes in background light levels. The amplifier circuit is shown in Figure C.2. The transfer function of the amplifier was tested using sinusoidal signals whose frequencies from 100 Hz to around 200 kHz. The tranfer function is shown in Figure C.1. As shown in the figure, the gain of the amplifier for the signals whose frequencies lower than 20 kHz is around 500.

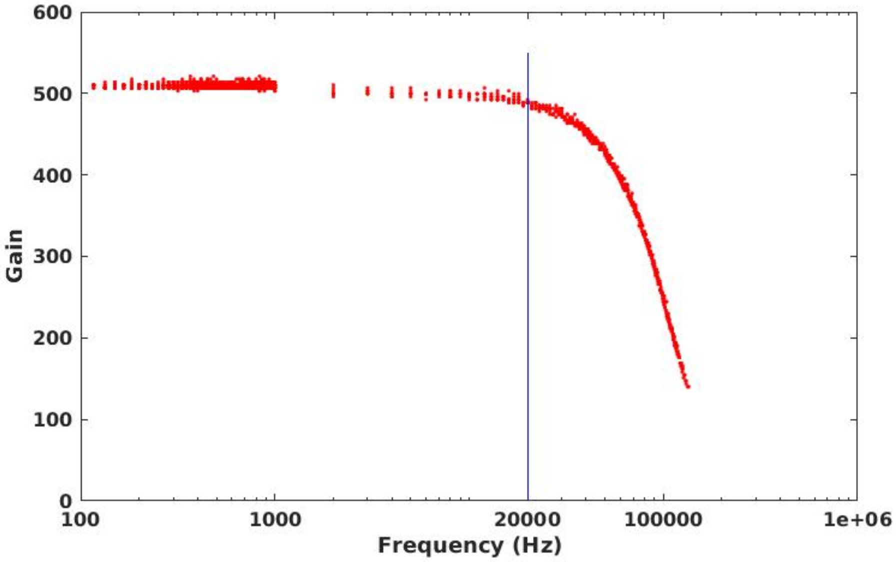

Figure C.1: The transfer function of the amplifier.

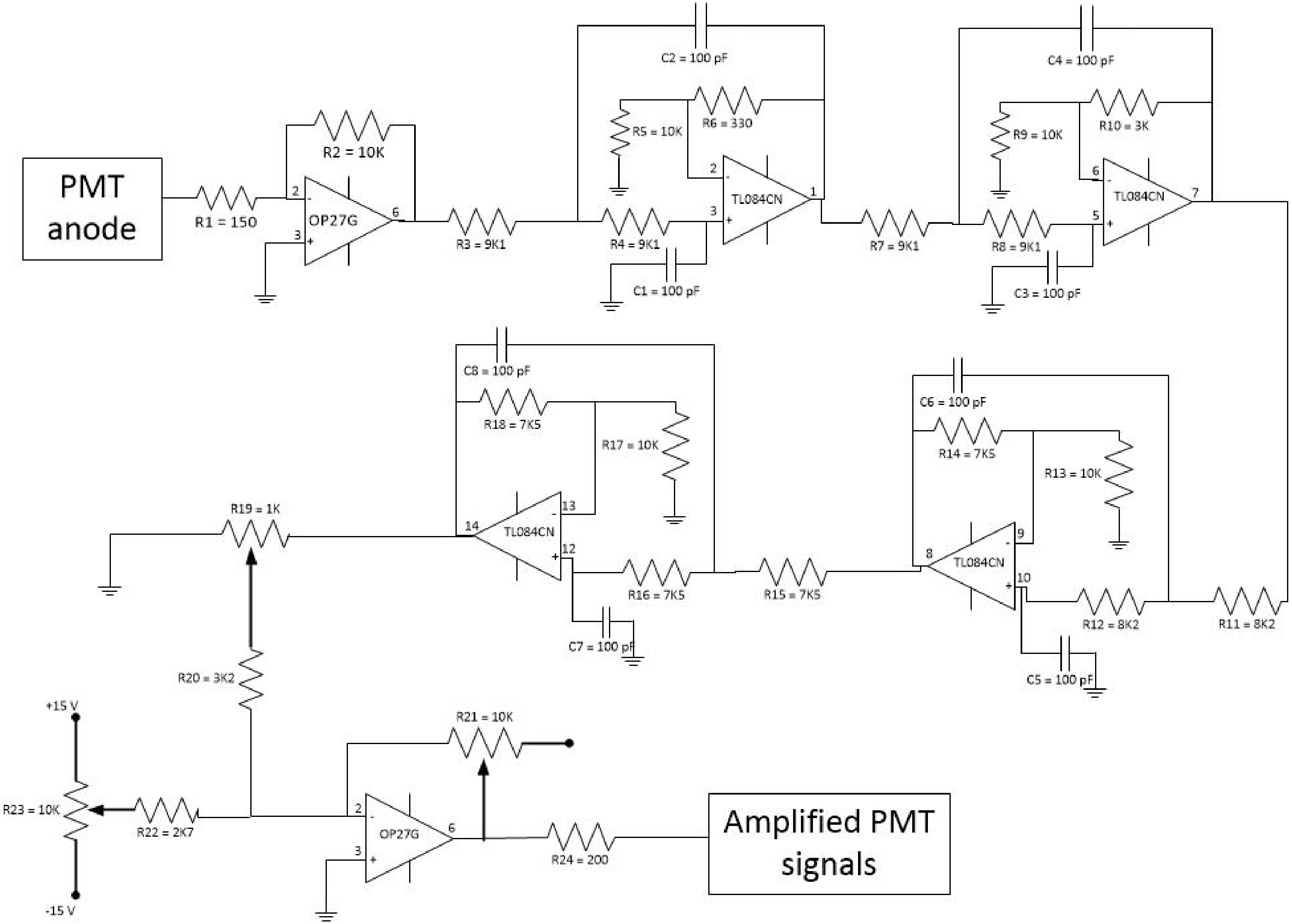

Figure C.2: The amplifier circuit.

Bibliography

Apostolopoulos, G., Tsinopoulos, S. V., and Dermatas, E. (2013). A methodology for estimating the shape of biconcave red blood cells using multicolor scattering images. *Biomed. Signal Process. Control*, 8(3):263–272.

Aptowicz, K. B., Pinnick, R. G., Hill, S. C., Pan, Y. L., and Chang, R. K. (2006). Optical scattering patterns from single urban aerosol particles at Adelphi, Maryland, USA: A classification relating to particle morphologies. *J. Geophys. Res. Atmos.*, 111(12).

Berdnik, V. V., Gilev, K., Shvalov, A., Maltsev, V., and Loiko, V. A. (2006). Characterization of spherical particles using high-order neural networks and scanning flow cytometry. *J. Quant. Spectrosc. Radiat. Transf.*, 102(1):62–72.

Berdnik, V. V. and Loiko, V. A. (2015). Neural networks for particle parameter retrieval by multi-angle light scattering. In *Light Scatt. Rev. 10 Light Scatt. Radiat. Transf.*, pages 291–340. Springer Berlin Heidelberg.

Besio, G. J., Prud'homme, R. K., and Benziger, J. B. (1988). Ellipsometric Observation of the Adsorption of Sodium Dodecyl Sulfate. Technical report.

Bevinton, P. and Robinson, D. (1992). *Data reduction and error analysis for the physical sciences.* McGraw-Hill, 2 edition.

Birmili, W. and Wiedensohler, A. (2000). New particle formation in the continental boundary layer: Meteorological and gas phase parameter influence. *Geophys. Res. Lett.*, 27(20):3325–3328.

Blackford D., A., D.Y., H., Pui, Kinney, P., and Ananth, G. (1988). Details of recent work towards improving the performance of the TSI Aerodynamic Particle Sizer. In *2nd Annu. Meet. aerosol Soc.*, Bournemouth.

Blanchard, D. C. and Woodcock, A. H. (1957). Bubble Formation and Modification in the Sea and its Meteorological Significance. *Tellus*, 9(2):145–158.

Bohren, C. F. and Huffman, D. R. (1983). *Absorption and Scattering of Light by Small Particles*, volume 1. John Wiley & Sons Inc.

Boucher, O. and Lohmann, U. (1995). The sulfate-CCN-cloud albedo effect. *Tellus B Chem. Phys. Meteorol.*, 47(3):281–300.

Brook, R. D., Franklin, B., Cascio, W., Hong, Y., Howard, G., Lipsett, M., Luepker, R., Mittleman, M., Samet, J., Smith, S. C., and Tager, I. (2004). Air Pollution and Cardiovascular Disease A Statement for Healthcare Professionals From the Expert Panel on Population and Prevention Science of the American Heart Association. 109:2655–2671.

Brook, R. D., Rajagopalan, S., Pope, C. A., Brook, J. R., Bhatnagar, A., Diez-Roux, A. V., Holguin, F., Hong, Y., Luepker, R. V., Mittleman, M. A., Peters, A., Siscovick, D., Smith, S. C., Whitsel, L., and Kaufman, J. D. (2010). Particulate Matter Air Pollution and Cardiovascular Disease: an update to the scientific statement from the American Heart Association. *Circulation*.

Buseck, P. R. and Schwartz, S. E. (2003). Tropospheric Aerosol. In *Treatise on geochemistry*, chapter 4, pages 91–95.

Caramanica, F. (2012). A method based on particle swarm optimization to retrieve the shape of red blood cells: A preliminary assessment. *Prog. Electromagn. Res. M*, 27:109–117.

Chang, H., Okuyama, K., and Szymanski, W. W. (2003). Experimental Evaluation of the Optical Properties of Porous Silica/Carbon Composite Particles. *Aerosol Sci. Technol.*, 37(9):735–751.

Charell, P. R. and Hawley, R. E. (1981). Characteristics of water adsorption on air sampling filters. *Am. Ind. Hyg. Assoc. J.*, 42(5):353–360.

Chen, B. and Cheng, Y. (1984). Optical diameters of aggregate aerosols. *J. Aerosol Sci.*, 15(5):615–623.

Chow, J. C., Watson, J. G., Egami, R. T., Frazier, C. A., Lu, Z., Goodrich, A., and Bird, A. (1990). Evaluation of Regenerative-air Vacuum Street Sweeping on Geological Contributions to PM 10. *Waste Manag. Assoc.*, 40(8):1134–1142.

Chung, S. H. and Seinfeld, J. H. (2002). Global distribution and climate forcing of carbonaceous aerosols. *J. Geophys. Res. Atmos.*, 107(19):AAC 14–1–AAC 14–33.

Colbeck, I. and Lazaridis, M. (2014). *Aerosol Science: Technology and Applications*. John Wiley {&} Sons Ltd.

Cooke, D. D. and Kerker, M. (1975). Response Calculations for Light-Scattering Aerosol Particle Counters. *Appl. Opt.*, 14(3):734.

Eatough, J., Lewis, L. J., Eatough, M., and Lewist, E. A. (1995). Sampling Artifacts in the Determination of Particulate Sulfate and S02<g) in the Desert Southwest Using Filter Pack Samplers DELBERT. Technical report.

Erlick, C., Ynelisa, Abbatt, J. P., and Rudich, Y. (2011). How different calculations of the refractive index affect estimates of the radiative forcing efficiency of ammonium sulfate aerosols. *J. Atmos. Sci.*, 68(9):1845–1852.

Faiola, C. L., Buchholz, A., Kari, E., Yli-Pirilä, P., Holopainen, J. K., Kivimäenpää, M., Miettinen, P., Worsnop, D. R., Lehtinen, K. E., Guenther, A. B., and Virtanen, A. (2018). Terpene Composition Complexity Controls Secondary Organic Aerosol Yields from Scots Pine Volatile Emissions. *Sci. Rep.*, 8(1):3053.

Fairy (2021). Fairy Product Ingredients Explained | Supersavvyme | Supersavvyme.

Ferron, G. and Soderholm, S. C. (1990). ESTIMATION OF THE TIMES FOR EVAPORATION OF PURE WATER DROPLETS AND FOR STABILIZATION OF SALT SOLUTION PARTICLES *. *J. Aerosol Sci.*, 21(3):415–429.

Fiorani, L., Maltsev, V. P., Nekrasov, V. M., Palucci, A., Semyanov, K. A., and Spizzichino, V. (2008). Scanning flow cytometer modified to distinguish phytoplankton cells from their effective size, effective refractive index, depolarization, and fluorescence. *Appl. Opt.*, 47(24):4405–4412.

Fitzgerald, J. W. (1991). Marine aerosols: A review.

Galushkin, A. I. (2007). *Neural network theory*. Springer Berlin Heidelberg.

Garvey, D. M. and Pinnick, R. G. (1983). Response Characteristics of the Particle Measuring Systems Active Scattering Aerosol Spectrometer Probe (ASASP–X). *Aerosol Sci. Technol.*, 2(4):477–488.

Gebhart, J. and Zerull, R. (1986). RESPONSE OF OPTICAL PARTICLE COUNTERS TO PARTICLES OF IRREGULAR SHAPE. pages 623–627. Pergamon Press.

Gong, S. L., Barrie, L. A., Blanchet, J. P., von Salzen, K., Lohmann, U., Lesins, G., Spacek, L., Zhang, L. M., Girard, E., Lin, H., Leaitch, R., Leighton, H., Chylek, P., and Huang, P. (2003). Canadian Aerosol Module: A size-segregated simulation of atmospheric aerosol processes for climate and air quality models 1. Module development. *J. Geophys. Res. Atmos.*, 108(1):AAC 3–1.

Grainger, D., Peters, D., Clarisse, L., and Herbin, H. (2020). Aerosol refractive index archive (ARIA).

Grainger, R. G., Lucas, J., Thomas, G. E., and Ewen, G. B. (2004). Calculation of Mie derivatives. *Appl. Opt.*, 43(28):5386–5393.

Griffin, D., Kellogg, A., Garrison, V., and Shinn, E. A. (2002). The Global Transport of Dust: An intercontinental river of dust, microorganisms and toxic chemicals flows through the Earth's atmosphere.

GRIMM (2020). EDM180.

Gucker, F. T., Pickard, B., Pitts, J. N., and Vol, J. (1947a). A Photoelectronic Counter for Colloidal Particles. *J. Am. Chem. Soc.*, 69(10):2422–2431.

Gucker, F. T., Pickard2, H. B., and O'konski, C. T. (1947b). A Photoelectric Instrument for Comparing the Concentrations of Very Dilute Aerosols and Measuring Low Light Intensities. Technical report.

Gucker, F. T. and Rose, D. G. (1954). A photoelectronic instrument for counting and sizing aerosol particles. *Br. J. Appl. Phys.*, 5(S138).

HHTEC (2021). HHTEC Official Home.

Hinds, W. and Kraske, G. (1986). Performance of PMS model LAS-X optical particle counter. *J. Aerosol Sci.*, 17(1):67–72.

Hinds, W. C. (1999). *Aerosol Technology: Properties, Behavior, and Measurement of Airborne Particles.*

Hobbs, P. V., Bowdle, D. A., and Radke, L. F. (1985). Particles in the Lower Troposphere over the High Plains of the United States. Part I: Size Distributions, Elemental Compositions and Morphologies. Technical Report 12.

Husar, R. B., Tratt, D. M., Schichtel, B. A., Falke, S. R., Li, F., Jaffe, D., Gassó, S., Gill, T., Laulainen, N. S., Lu, F., Reheis, M. C., Chun, Y., Westphal, D., Holben, B. N., Gueymard, C., McKendry, I., Kuring, N., Feldman, G. C., McClain, C., Frouin, R. J., Merrill, J., DuBois, D., Vignola, F., Murayama, T., Nickovic, S., Wilson, W. E., Sassen, K., Sugimoto, N., and Malm, W. C. (2001). Asian dust events of April 1998. *J. Geophys. Res. Atmos.*, 106(D16):18317–18330.

IARC (2013). AIR POLLUTION AND CANCER. Technical report, World Health Organization, Lyon.

IPCC (2014). CLIMATE CHANGE 2014: Synthesis Report. Technical report, Geneva.

Jaenicke, R. (1993). Tropospheric aerosols. In *Aerosol-Cloud_Climate Interact.* Academic Press Inc., San Diego, CA.

Jakubczyk, D., Derkachov, G., Kolwas, M., and Kolwas, K. (2013). Combining weighting and scatterometry: Application to a levitated droplet of suspension. *J. Quant. Spectrosc. Radiat. Transf.*, 126:99–104.

Jia, G. (2014). Atmospheric Residence Times of the Fine-aerosol in the Region of South Italy Estimated from the Activity Concentration Ratios of 210Po/210Pb in Air Particulates. *J. Anal. Bioanal. Tech.*, 5(6):1–9.

Kiehl, J. and H., R. (1995). Modeling geographical and seasonal forcing due to aerosols. In Charlson, R. and Heintzenberg, J., editors, *Aerosol Forcing Clim.*, pages 281–296. New York.

Kim, Y., Shim, H., Kim, K., Park, H. J., Jang, S., and Park, Y. K. (2014). Profiling individual human red blood cells using common-path diffraction optical tomography. *Sci. Rep.*, 4.

Kolesnikova, I. V., Potapov, S. V., Yurkin, M. A., Hoekstra, A. G., Maltsev, V. P., and Semyanov, K. A. (2006). Determination of volume, shape and refractive index of individual blood platelets. *J. Quant. Spectrosc. Radiat. Transf.*, 102(1):37–45.

Konokhova, A. I., Gelash, A. A., Yurkin, M. A., Chernyshev, A. V., and Maltsev, V. P. (2013). High-precision characterization of individual E. coli cell morphology by scanning flow cytometry. *Cytom. Part A*, 83 A(6):568–575.

Krarnes, J., Büttner, H., and Ebert, F. (1991). Submicron particle generation by evaporation of water droplets. *J. Aerosol Sci.*, 22(SUPPL. 1):S15–S18.

Labusov, V. A., Selyunin, D. O., Zarubin, I. A., and Gallyamov, R. G. (2008). Measuring the quantum efficiency of multielement photodetectors in the spectral range between 180 and 800 nm. *Optoelectron. Instrum. Data Process.*, 44(1):19–26.

LaFranchi, B. W., Knight, M., and Petrucci, G. A. (2003). Leaching as a source of residual particles from nebulization of deionized water. *J. Aerosol Sci.*, 34(11):1589–1594.

Liao, H., Adams, P. J., Chung, S. H., Seinfeld, J. H., Mickley, L. J., and Jacob, D. J. (2003). Interactions between tropospheric chemistry and aerosols in a unified general circulation model. *J. Geophys. Res. D Atmos.*, 108(1):AAC 1–1.

Liao, H., Seinfeld, J. H., Adams, P. J., and Mickley, L. J. (2004). Global radiative forcing of coupled tropospheric ozone and aerosols in a unified general circulation model. *J. Geophys. Res. Atmos.*, 109(16).

Lide, D. R. e. (2005). *Handbook of Chemistry and Physics, Internet Version.* Boca Raton, Florida.

Liousse, C., Penner, J. E., Chuang, C., Walton, J. J., Eddleman, H., and Cachier, H. (1996). A global three-dimensional model study of carbonaceous aerosols. *J. Geophys. Res. Atmos.*, 101(14):19411–19432.

Liu, B. Y., Szymanski, W. W., and Pui, D. Y. (1986). RESPONSE OF A LASER OPTICAL PARTICLE COUNTER TO TRANSPARENT AND LIGHT-ABSORBING PARTICLES. In *ASHRAE Trans.*, volume 92, pages 518–538. ASHRAE.

Liu, B. Y. H., Marple, V. A., Whitby, K. T., and Barsic, N. J. (1974). Size Distribution Measurement of Airborne Coal Dust by Optical Particle Counters.

Ludlow, I. K. and Everitt, J. (2000). Inverse Mie problem. *J. Opt. Soc. Am. A*, 17(12):2229.

Maltsev, V. P. and Lopatin, V. N. (1997). Parametric solution of the inverse light-scattering problem for individual spherical particles. *Appl. Opt.*, 36(24):6102.

McMurry, P. H. (2000). A review of atmospheric aerosol measurements. *Atmos. Environ.*, 34(12-14):1959–1999.

Mie, G. (1908). Beiträge zur Optik trüber Medien, speziell kolloidaler Metallösungen. *Ann. Phys.*, 330(3):377–445.

Min, S. L. and Gomez, A. (1996). High-resolution size measurement of single spherical particles with a fast Fourier transform of the angular scattering intensity. *Appl. Opt.*, 35(24):4919.

Mischenko, M. I. (2004). Scattering, Absorption, and Emission of Light by Small Particles.

Monahan, E. C., Fairall, C. W., Davidson, K. L., and Boyle, P. J. (1983). Observed inter-relations between 10m winds, ocean whitecaps and marine aerosols. *Q. J. R. Meteorol. Soc.*, 109(460):379–392.

Myhre, G., Samset, B. H., Schulz, M., Balkanski, Y., Bauer, S., Berntsen, T. K., Bian, H., Bellouin, N., Chin, M., Diehl, T., Easter, R. C., Feichter, J., Ghan, S. J., Hauglustaine, D., Iversen, T., Kinne, S., Kirkevåg, A., Lamarque, J.-F., Lin, G., Liu, X., Lund, M. T., Luo, G., Ma, X., Van Noije, T., Penner, J. E., Rasch, P. J., Ruiz, A., Seland, Ø., Skeie, R. B., Stier, P., Takemura, T., Tsigaridis, K., Wang, P., Wang, Z., Xu, L., Yu, H., Yu, F., Yoon, J.-H., Zhang, K., Zhang, H., and Zhou, C. (2013). Sciences ess Atmospheric Chemistry and Physics Climate of the Past Geoscientific Instrumentation Methods and Data Systems Radiative forcing of the direct aerosol effect from AeroCom Phase II simulations. *Atmos. Chem. Phys*, 13:1853–1877.

Nagy, A., Szymanski, W., Gál, P., Golczewski, A., and Czitrovszky, A. (2007). Numerical and experimental study of the performance of the dual wavelength optical particle spectrometer (DWOPS). *J. Aerosol Sci.*, 38(4):467–478.

Okazaki, K., Wiener, R., W., and Willeke, K. (1987). The combined effect of aspiration and transmission on aerosol sampling accuracy for horisontal isoaxial sampling. *Atmos. Environ.*, 21(5):1181–1185.

OpenFoam (2019). *OpenFOAM ® Basic Training.*

Optoelectronics, O. (2021). Photovoltaic Series Planar Diffused Silicon Photodiodes. Technical report, https://www.osioptoelectronics.com/application-notes/OSI_Parts_Catalog.pdf.

Peters, A., Dockery, D. W., Muller, J. E., and Mittleman, M. A. (2001). Increased particulate air pollution and the triggering of myocardial infarction. *Circulation*.

Peters, D., Grainger, D., and Smith, A. (2009). Local Air Quality.

Pinnick, R., Pan, Y., S.C., H., Aptowicz, B., and Chang, R. (2011). Laser-induced Fluorescence Spectra and Angular elastic Scattering Patterns of Single Atmospheric Aerosol Particles. In Signorell, R. and Reid, J., editors, *Fundam. Appl. Aerosol Spectrosc.* Taylor {&} Francis, New York.

Pinnick, R. G. and Auvermann, H. J. (1979). Response characteristics of knollenberg light-scattering aerosol counters. *J. Aerosol Sci.*, 10(1):55–74.

Pinnick, R. G. and Hofmann, D. J. (1973). Efficiency of Light-Scattering Aerosol Particle Counters. *Appl. Opt.*, 12(11):2593.

Pinnick, R. G., Rosen, J. M., and Hofmann, D. J. (1973). Measured Light-Scattering Properties of Individual Aerosol Particles Compared to Mie Scattering Theory. *Appl. Opt.*, 12(1):37.

Pramod, K. and Baron, P. (2011). Aerosol Measurement. In Pramod, K., Paul, B., and Klaus, W., editors, *Aerosol Meas. Princ. Tech. Appl.*, chapter 5.

Prospero, J. M., Charlson, R. J., Mohnen, V., Jaenicke, R., Delany, A. C., Moyers, J., Zoller, W., and Rahn, K. (1983). The atmospheric aerosol system: An overview. *Rev. Geophys.*, 21(7):1607.

Querry, M. R. (1987). Optical constants of minerals and other materials from the millimeter to the ultraviolet: Report CRDEC-CR-88009. Technical report, US Army, Aberdeen.

Quist, G. M. and Wyatt, P. J. (1985). Empirical solution to the inverse-scattering problem by the optical strip-map technique. *J. Opt. Soc. Am. A*, 2(11):1979.

Raabe, O. G. (1968). The Dilution of Monodisperse Suspensions for Aerosolization. *Am. Ind. Hyg. Assoc. J.*, 29(5):439–443.

Raes, F., Van Dingenen, R., Vignati, E., Wilson, J., Putaud, J. P., Seinfeld, J. H., and Adams, P. (2000). Formation and cycling of aerosols in the global troposphere.

Reed, B. E., Peters, D. M., McPheat, R., and Grainger, R. G. (2018). The Complex Refractive Index of Volcanic Ash Aerosol Retrieved From Spectral Mass Extinction. *J. Geophys. Res. Atmos.*, 123(2):1339–1350.

Riccobono, F., Schobesberger, S., Scott, C. E., Dommen, J., Ortega, I. K., Rondo, L., Almeida, J., Amorim, A., Bianchi, F., Breitenlechner, M., David, A., Downard, A., Dunne, E. M., Duplissy, J., Ehrhart, S., Flagan, R. C., Franchin, A., Hansel, A., Junninen, H., Kajos, M., Keskinen, H., Kupc, A., Kürten, A., Kvashin, A. N., Laaksonen, A., Lehtipalo, K., Makhmutov, V., Mathot, S., Nieminen, T., Onnela, A., Petäjä, T., Praplan, A. P., Santos, F. D., Schallhart, S., Seinfeld, J. H., Sipilä, M., Spracklen, D. V., Stozhkov, Y., Stratmann, F., Tomé, A., Tsagkogeorgas, G., Vaattovaara, P., Viisanen, Y., Vrtala, A., Wagner, P. E., Weingartner, E., Wex, H., Wimmer, D., Carslaw, K. S., Curtius, J., Donahue, N. M., Kirkby, J., Kulmala, M., Worsnop, D. R., and Baltensperger, U. (2014). Oxidation products of biogenic emissions contribute to nucleation of atmospheric particles. *Science (80-.).*, 344(6185):717–721.

Rocha-Lima, A., Martins, J. V., Remer, L. A., Todd, M., Marsham, J. H., Engelstaedter, S., Ryder, C. L., Cavazos-Guerra, C., Artaxo, P., Colarco, P., and Washington, R. (2018). A detailed characterization of the Saharan dust collected during the Fennec campaign in 2011: in situ ground-based and laboratory measurements. *Atmos. Chem. Phys.*, 18(2):1023–1043.

Rodgers, C. (2000). *Inverse methods for atmospheric sounding.* World Scientific Publishing Co.

Rosen, J. (1968). Simultaneous dust and ozone soundings over North and central America. *J. Geophys. Res.*, 73(2):479–486.

Rosen, J. M. (1964). The vertical distribution of dust to 30 kilometers. *J. Geophys. Res.*, 69(21):4673–4676.

Sachweh, B., Umhauer$, H., Ebert, F., Biittner, H., and Friehmelt, R. (1998). IN SITU OPTICAL PARTICLE COUNTER WITH IMPROVED COINCIDENCE ERROR CORRECTION FOR NUMBER CONCENTRATIONS UP TO lo7 PARTICLES cme3. Technical Report 9.

Savoie, D. L. and Prospero, J. M. (1989). Comparison of oceanic and continental sources of non-sea-salt sulphate over the Pacific Ocean. *Nature*, 339(6227):685–687.

Seinfeld, J. H. and Pandis, S. N. (2006). *Atmospheric chemistry and physics.* John Wiley & Sons Inc, New Jersey, 2 edition.

Sigmaaldrich (2021). N,N-Dimethyldodecylamine N-oxide solution | Sigma | CAS No.1643-20-5 (principal component).

Smith, M., O'Dowd, C., and Lowe, J. (1996). Observations of cloud-induced aerosol growth. In Kulmala, M. and Wagner, P. E., editors, *Nucleation Atmos. Aerosols*, pages 937–940. Oxford.

Sorensen, C., Gebhart, J., O'Hern, T., and Rader, D. (2011). Optical measurement techniques: fundamentals and application. In Pramod, K., Paul, B., and Willeke, K., editors, *Aerosol Meas. Princ. Tech. Appl.*, chapter 13. A John Wiley {&} Sons.

Steiner, B., Berge, B., Gausmann, R., Rohmann, J., and Rühl, E. (1999). Fast in situ sizing technique for single levitated liquid aerosols. *Appl. Opt.*, 38(9):1523.

Strokotov, D. I., Moskalensky, A. E., Nekrasov, V. M., and Maltsev, V. P. (2011). Polarized light-scattering profile-advanced characterization of nonspherical particles with scanning flow cytometry. *Cytom. Part A*, 79 A(7):570–579.

Sullivan, R. C. and Prather, K. A. (2005). Recent Advances in Our Understanding of Atmospheric Chemistry and Climate Made Possible by On-Line Aerosol Analysis Instrumentation.

Szymanski, W. W. and Liu, B. Y. (1986). ON THE SIZING ACCURACY OF LASER OPTICAL PARTICLE COUNTERS. *Part. Charact.*, 3(1):1–7.

Szymanski, W. W., Nagy, A., and Czitrovszky, A. (2009). Optical particle spectrometry-Problems and prospects. *J. Quant. Spectrosc. Radiat. Transf.*, 110(11):918–929.

Szymanski, W. W., Nagy, A., Czitrovszky, A., and Jani, P. (2002). Measurement Science and Technology A new method for the simultaneous measurement of aerosol particle size, complex refractive index and particle density. Technical report.

Thomas, G. (2003). *A New Instrument for Atmospheric Aerosol Measurement.* PhD thesis, University of Canterbury.

TSI (2020). Aerodynamic Particle Sizer (APS) Spectrometer 3321 -.

Tsuda, A., Henry, F. S., and Butler, J. P. (2013). Particle transport and deposition: Basic physics of particle kinetics. *Compr. Physiol.*, 3(4):1437–1471.

Ulanowski, Z., Wang, Z., Kaye, P. H., and Ludlow, I. K. (1998). Application of neural networks to the inverse light scattering problem for spheres. *Appl. Opt.*, 37(18):4027.

Umhauer, H. and Bottlinger, M. (1991). Effect of particle shape and structure on the results of single-particle light-scattering size analysis. *Appl. Opt.*, 30(33):4980.

Valenzuela, A., Reid, J. P., Bzdek, B. R., and Orr-Ewing, A. J. (2018). Accuracy Required in Measurements of Refractive Index and Hygroscopic Response to Reduce Uncertainties in Estimates of Aerosol Radiative Forcing Efficiency. *J. Geophys. Res. Atmos.*, 123(12):6469–6486.

Vincent J., H. (2007). *Aerosol sampling; Science, Standards, Instrumentation and Applications.*

Von Der Weiden, S.-L., Drewnick, F., and Borrmann, S. (2009). Atmospheric Measurement Techniques Particle Loss Calculator-a new software tool for the assessment of the performance of aerosol inlet systems. Technical report.

Walcek, C. J., Stockwell, W. R., and Chang, J. S. (1990). Theoretical estimates of the dynamic, radiative and chemical effects of clouds on tropospheric trace gases. *Atmos. Res.*, 25(1-3):53–69.

Wales, M. and Wilson, J. N. (1961). Theory of Coincidence in Coulter Particle Counters. *Residual Drag Torque Magn. Suspended Rotating Spheres Rev. Sci. Instruments*, 32(10):1413.

Wang, A., Garmann, R. F., and Manoharan, V. N. (2016). Tracking E coli runs and tumbles with scattering solutions and digital holographic microscopy. *Opt. Express*, 24(21):23719.

Warneck, P. (2000). *Chemistry of the Natural Atmosphere,2nd Edition.* Academic Press Inc., 2th edition.

Whitby, K. T. (1978). The physical characteristics of sulfur aerosols. *Atmos. Environ.*, 12(1-3):135–159.

WHO (2013). Review of evidence on health aspects of air pollution-REVIHAAP Project Technical Report. Technical report, Bonn.

Wiedensohler, A., Wehner, B., and Birmili, W. (2002). Aerosol Number Concentrations and Size Distributions at Mountain-Rural, Urban-Influenced Rural, and Urban-Background Sites in Germany. Technical Report 2.

Wojtkiewicz, S., Sawosz, P., Kostecki, M., and Sokolowska, A. (2013). Optical method for characterization of nanoplates in lyosol. *Microelectron. Eng.*, 108:121–126.

Ye, Y. and Pui, D. Y. H. (1990). PARTICLE DEPOSITION IN A TUBE WITH AN ABRUPT CONTRACTION*. Technical Report 1.

Yu, S., Zhang, J., Moran, M. S., Lu, J. Q., Feng, Y., and Hu, X.-H. (2012). A novel method of diffraction imaging flow cytometry for sizing microspheres. *Opt. Express*, 20(20):22245.

Zarzana, K. J., Cappa, C. D., and Tolbert, M. A. (2014). Sensitivity of Aerosol Refractive Index Retrievals Using Optical Spectroscopy. *Aerosol Sci. Technol.*, 48(11):1133–1144.

Zender, C. S., Bian, H., and Newman, D. (2003). Mineral Dust Entrainment and Deposition (DEAD) model: Description and 1990s dust climatology. *J. Geophys. Res. Atmos.*, 108(14).

Zhang, L., Chen, X., Zhang, Z., Chen, W., Zhao, H., Zhao, X., Li, K., and Yuan, L. (2016). Scattering pulse of label free fine structure cells to determine the size scale of scattering structures. *Rev. Sci. Instrum.*, 87(4).

Zhu, Y., Hinds, W. C., Kim, S., Shen, S., and Sioutas, C. (2002). Study of ultrafine particles near a major highway with heavy-duty diesel traffic. *Atmos. Environ.*, 36(27):4323–4335.